WINDERFUL
Wind and INfrastructures: Dominating Eolian Risk For Utilities and Lifelines

Edited by
Gianni Bartoli, Francesco Ricciardelli, Vincenzo Sepe

Firenze University Press

WINDERFUL
Wind and INfrastructures: Dominating Eolian Risk For Utilities and Lifelines

Edited by
Gianni Bartoli, Francesco Ricciardelli, Vincenzo Sepe

Firenze University Press

WINDERFUL
Wind and INfrastructures: Dominating Eolian Risk For Utilities and Lifelines

Edited by
Gianni Bartoli, Francesco Ricciardelli, Vincenzo Sepe

Firenze University Press
2004

WINDERFUL : Wind and INfrastructures : Dominating Eolian Risk For Utilities and Lifelines / Edited by Gianni Bartoli, Francesco Ricciardelli, Vincenzo Sepe. – Firenze : Firenze university press, 2004.
http://digital.casalini.it/8884531381

ISBN 88-8453-138-1 (online)
ISBN 88-8453-137-3 (print)
624.175 (ed. 20)
Building Aerodynamics – Wind effects – Structural Dynamics

WINDERFUL is the title of a Research Project on Wind Engineering co-financed by the Italian Ministry for Education, University and Research (MIUR), carried out by eight Italian Universities for two years (Nov. 2001- Nov. 2003).
This book reports the main results obtained in the project, that was mainly devoted to the reliability of structural elements of life-lines, on whose integrity and functionality during and after windstorms the quality of the city life is depending.

Project Co-ordinating Institution:

CRIACIV

Centro di Ricerca Interuniversitario di
Aerodinamica delle Costruzioni ed Ingegneria del Vento

Università di Firenze, Università di Roma "La Sapienza", Università di Perugia,
Università di Trieste, Università IUAV di Venezia, Università di Chieti-Pescara

Cover photo:
9 May 2001: Storm in southern Minnesota

Università degli Studi di Firenze
Borgo Albizi, 28
50122 Firenze
Italy
http://espress.unifi.it

Printed in Italy

WINDERFUL
Wind and INfrastructures:
Dominating Eolian Risk For Utilities and Lifelines

INDEX

FOREWORD

Within the PRIN (Progetti di Ricerca di Interesse Nazionale) cofinanced by the MIUR (the Italian "Ministero dell'Istruzione, dell'Università e della Ricerca), some University Departments, which are active in the field of Building Aerodynamics and Wind Engineering promoted in 2001 the launch of a wide research project called on "**W**ind and **IN**frastructures: **D**ominating **E**olian **R**isk **F**or **U**tilities and **L**ifelines", aimed to coordinate and create synergies and interactions amongst the main research activities carried out in the field in Italy. 10 Research teams from 8 Universities have joined the project, which had its official start in November 2001.

The present volume, which is going to be presented at the IN-VENTO-04, the 8th (Italian) National Conference of Wind Engineering, hosted by the University "Mediterranea" of Reggio Calabria, June 2004, is the main tool for the presentation and dissemination of the scientific outcomes: the present book aims to give a complete perspective on the topics dealt with by the research teams on the different aspects of the wind action on the built environment, whose effects are very diverse.

Out of the many open questions in this young and developing science, the WINDERFUL project has focused on 9 Themes which are deemed to be vital in view of specific needs. These broad scientific and engineering themes have been considered within the 10 research teams, any of them dealing with one or more of the themes, in a truly intense cooperation network.

More than 50 researchers from the 10 participating Universities in the project have been involved in one or more of the scheduled activities: some 65 published papers, in international/national journals, scientific conferences or seminars, 1 originally developed *remote monitoring* equipment, 6 plenary meetings, many cross visits of young researchers carried out for scientific exchanges and/or experimental works, 3 specially devoted sessions/papers at major Conferences and, lastly, a final dissemination session at the 8th IN-VENTO-2004. These are the positive figures of the overall amount of the work carried out during the 24 months of contract of the WINDERFUL project, which shall be therefore considered as a completely successful one, giving rise to a sense of proud for the entire staff that has managed and coordinated it.

ACKNOWLEDGMENTS

The Scientific Coordinator wishes to gratefully acknowledge the commitment of all involved actors during the entire project life: the local team coordinators/Chair persons (G. Augusti, P. D'Asdia, V. Gusella, M. Majowiecki/G. Matildi, S. Noè, M. Pieraccini, F. Ricciardelli/E. D'Amore, G. Serino & P. Spinelli) as well as all team members. A special recognition goes to the Editorial Board of the project (G. Bartoli, F. Ricciardelli and V. Sepe) for the editorial work of issuing the present volume; the precious advices of Dr. C. Bullo (Firenze University Press, publisher of the volume) during the overall editing of the manuscripts is also gratefully acknowledged.

Last but not least, many personal thanks are due to the Secretariat of the project, in the person of Mrs. Serena Cartei.

Finally, the financial contribution of the MIUR (Ministero dell'Istruzione, dell'Università e della Ricerca) is gratefully acknowledged.

Firenze, May 23rd, 2004

Claudio BORRI
CRIACIV c/o Dipartimento di Ingegneria Civile
Università di Firenze
Scientific Coordinator of the Project

*

1 Introduction

Claudio Borri
University of Firenze

1.1 SUMMARY

This Introduction aims to give an overall outline on the contents and main outcomes of the WINDERFUL project (acronym for “Wind and INfrastructures: Dominating Eolian Risk For Utilities and Lifelines”), run from Nov. 2001 until Nov. 2003 amongst the Research Projects of National Interest (PRIN) of the Italian Ministry of Education, University and Research (MIUR). To properly introduce the reader into the project, Sect. 1.2 will first describe the overall objectives and project structure, with the allocation of tasks amongst the different research teams, based upon the available resources; the organization and project management will be dealt with, which will be followed by a last Sect. devoted to national and international links with other similar activities. Sect. 1.3 introduces an overview on the main activities and results, with some transversal information about the structure of the final report and synthesis reports from the teams; it will also present an overall outline of the following Chapters of this final report/book of the project. Sections 1.4 & 1.5 will shortly introduce the dissemination activities and performances, including some future perspectives through follow-up projects.

1.2 PROJECT STRUCTURE AND DESCRIPTION

1.2.1 Project summary

In a country that is still considered a region with “well behaving climate”, atmospheric wind and its effects on utilities & infrastructures are not yet considered as a priority hazard. As a matter of fact, according to the insurers’ total claims from natural disaster, windstorms are by far 1st with about 70% of the claims, while earthquakes account for about 18%, flood 6% and other 6% relates to forest fire and volcanic eruptions.

In the recent past, two previous national research Projects (PRIN) have already focused on: a) establishment of research facilities and laboratories and definition of analysis tasks (RESACIV, 1997-99; 6 research teams) and b) the evaluation of eolian risk and the measures for its control and investigation (ACME CUE, 1999-2001; 10 research teams).

The WINDERFUL project has mainly focused the target of avoiding “major fatalities” occurring to engineering facilities and main infrastructures: i.e. to guarantee quality of life and of the society after & during a major natural phenomena, like a heavy windstorm. This was the declared target in the application proposal, very well in line with a keyword of the 6th Framework Programme of the EU (quality of life and sustainable development), whose concepts were in preparation and discussion at that time (summer 1999). To focus more suitably the aim of the present proposal, one could shortly synthesize like following: “To keep a city running and ensuring quality services during & after a major windstorms”.

WINDERFUL has developed along two main lines: L 1, i.e. evidencing the “wind vulnerable” networks of infrastructures & facilities, whose reduced (or annulled) service ability would induce temporary or permanent failures in the entire network, and L 2: producing a kind of “white book” on the reliability/vulnerability of networks and complex systems to wind effects, containing useful & synthetic criteria for a “good practice”. In addition to these main two lines, WINDERFUL has interacted also with other activities in the field of environmental engineering (which is part of a research project on the study of pollutants dispersion on complex terrains), in order to ensure the interdisciplinary character of the concerned field (across the disciplines of structural engineering, fluid dynamics, physics of the atmosphere, networks & complex systems, etc.). As a matter of fact, WINDERFUL reflects only a part of a wide range of activities carried out by partners involved and focuses on the purely “structural engineering & quality of life” aspects, while the above mentioned research project mainly deals with “environmental and sustainability” aspects.

The project has been carried out, partly, as the Italian contribution to the wide COST[1] C14 Action in the domain “Urban Civil Engineering” on “Impact of wind and storms on city life and built environment”, grouping 16 European countries and chaired by the same coordinating Institution as the WINDERFUL one. As, notably, COST finances exclusively the coordination & the dissemination costs, it is important that nationally funded projects guarantee the continuity of the research activity. This has revealed as a good synergy effect and follows the principle of subsidiarity in research amongst the EU and the other associated countries.

1.2.2 Research objectives

Damages induced by windstorms have been very severe in the last years, so that both local Authorities as well as financial and economic operators have had to face with huge costs. The increase of losses caused by windstorms can be only partially ascribed to climatological aspects (changes in environmental climatology), but it can be due to increasing complexity and vulnerability of buildings and structures which have been built in the last years; more specifically, one of the most vulnerable structural category is represented by those necessary for the correct functioning of infra-structural lines (life-lines) such as roads, highways, airport sites, electricity and transmission lines, and so on.

The major part of losses is often due to elements directly related to life-lines, such as components of electrical power-plants (cooling towers, pylons, chimneys), components of transmission lines (towers and cables), and components of road and highway lines (mainly bridges). But it is to be remarked that the huge level of costs is mainly due to “indirect” costs, such as those deriving from temporary stops on life-lines functionality (such as black-outs induced by a collapse of some branches of electrical lines). Eight severe windstorms hit at least 10 different European Countries only in 1990. In December 1999 the two windstorms Lothar and Martin hit South-West Europe, from Denmark to France, causing more than one hundred victims and estimated losses of about 14 Billion Euros. Moreover, extended black-outs have been experienced in several big cities. It is

---

[1] European Cooperation in the field of Scientific and Technical Research programme

then evident the growing interest in the field of “eolian risk” showed by economists and researchers; the research is then not only addressed to assess wind effects on structures, but mainly to investigate real effects on the city life and on the whole built environment.

Among other research programmes, the recently established European COST Action C14 (entitled “Impact of wind and storms on city life and built environment”, Sept. 2000 - May 2004) has to be recalled here; the action has been promoted (and it is at present chaired) by the proposer of this project and, till today, 13 different European Countries joined it, offering the support of several different researchers. The main objective of the COST Action is the investigation of new techniques and planning activities aimed to mitigate wind effects during severe windstorms, in order to ensure a correct working of the built environment. The WINDERFUL project was thought as inserted within this general framework. According to the above sketched research lines, the research project developed on two different scales: the first scale is related to the evaluation of the eolian risk connected to the “direct” damaging of elements being part of life-lines; the second scale has considered the influence that the damaging or the collapse of a certain component can have on a complex network, such as the life-lines system of a city (so analyzing the reliability of the whole system under severe windstorm conditions). From the viewpoint of the correct working of a complex life-lines system, not only the collapse of one component can lead to some stops, but also other circumstances could lead to serious effects: as an example, severe wind induced oscillations could lead a suspended bridge to be closed to traffic, as well as strong winds could lead to excessive oscillations in cables of electrical lines so that the power-supply must be stopped. Accordingly to these considerations, the project has split into two parts:

1. *singling out of all the life-lines connected to urban environment* and, within these, characterization of wind-sensitive elements, which, due to a reduced functionality, can lead to reductions as well as temporary (or final) stops of supply of some services (transport, electricity, etc.);
2. *evaluation of results from several wind researches from the viewpoint of the estimation of the risk* and reliability of life-lines and other complex systems.

The final objective of WINDERFUL is intended as the assessment of the “eolian risk” with a specific reference to life-lines, by analyzing both single components as well as the system as a whole.

The strong interdisciplinary approach of the project, involving network management experts and experts in several other research fields (fluid-dynamics, atmospheric physics, structural engineering), is very innovative for the field concerned. Among all aspects analyzed within the research activity, those which are more specifically connected with structural aspects have been taken into account, so aiming at two different objectives: 1. definition of “eolian risk” for specific structural elements from both the ultimate limit state (collapse) and the serviceability limit state (large oscillations), evaluating their instability thresholds; for some of these elements, an investigation on monitoring and mitigating devices (by using active, passive and semi-active control systems) has been performed, in order to evaluate a possible increase in the performances of such elements under strong wind loading; 2. evaluation of the vulnerability of certain life-lines as a function of the vulnerability of single components, in order to assess the whole “eolian risk” for a built environment on for the quality of city lifes.

1.2.3 Project structure, research teams & allocation of tasks

The project WINDERFUL has dealt with definition and reduction of “eolian risk”, with a specific reference to life-lines, i.e. lines for transport and supply serving a built environment. Each single component of life-lines has been analyzed, relating its performances in networking with those of the other elements of the whole life-lines system.

Both theoretical and experimental methods are used to analyze the problems related with the research programme. Main research topics can be assembled into two different themes:

1. *vulnerability evaluation of some specific component of life-lines* under severe wind loading conditions. Specific reference has been intended to structural elements and components which are part of a life-line (as described in the following) and to elements which constitutes the so called "street architecture" (such as bill-boards, traffic signs and traffic lights, lighting poles, news-stands, bus stop shelters), which often suffer huge damage from windstorms;

2. *vulnerability evaluation of the whole life-lines system* under severe wind loading conditions. The research results have contributed to ensure the possibility of the correct working of these systems even during and after windstorms, especially for those of primary relevance with respect to the life of cities and built environments.

Experimental tests will be mainly carried out at Boundary Layer Wind Tunnel located in Prato, managed by CRIACIV (Inter-University Research Centre on Building Aerodynamics and Wind Engineering), i.e. the co-ordination Unit of the present project. Within these two research themes several sub-themes were singled out and allocated to the 10 research teams (Units) participating into the project, namely

Unit #1: Univ. of Roma "La Sapienza", Dipartimento di Ingegneria Strutturale e Geotecnica
(Coord.: Prof. G. Augusti)

Unit #2: Univ. of Firenze, CRIACIV, c/o Dipartimento di Ingegneria Civile
(Coord.: Prof. C. Borri, Project Coordinator)

Unit #3: Univ. "Mediterranea" of Reggio Calabria, Dipartimento di Meccanica e Materiali
(Coord.: Prof. F. Ricciardelli/Ing. E. D'Amore)

Unit #4: Univ. of Chieti-Pescara "G. D'Annunzio", Dipartimento di Progettazione, Riabilitazione e Controllo delle Strutture Architettoniche
(Coord.: Prof. P. D'Asdia)

Unit #5: Univ. of Perugia, Dipartimento di Ingegneria Civile ed Ambientale
(Coord.: Prof. V. Gusella)

Unit #6: Univ. of Bologna, Dipartimento di Ingegneria delle Strutture, Trasporti, Acque, Rilevamento del Territorio
(Coord.: Prof. M Majowiecki/ G. Matildi)

Unit #7: Univ. of Trieste, Dipartimento di Ingegneria Civile
(Coord.: Prof. S. Noè)

Unit #8: Univ. of Firenze DET, Dipartimento di Elettronica e Telecomunicazioni
(Coord.: Ing. M. Pieraccini)

Unit #9: Univ. of Napoli "Federico II", Dipartimento di Analisi e Progettazione Strutturale
(Coord.: Prof. G. Serino)

Unit #10: Univ. of Firenze DIC, Dipartimento di Ingegneria Civile
(Coord.: Prof. P. Spinelli)

In the following, each one of the research themes is listed, together with all Units involved on the specific topic.

Theme 1 – Reliability of specific structural life-lines elements under severe wind conditions

1.1 – *Vertical structures*

Theme 1.1 groups all the structural elements which are parts of lifelines and that, for their particular conformation, result as highly sensitive to wind actions. These can be elements directly belonging to life-lines (such as bridge pylons, electricity lines pylons) or located into important plants or systems (such as chimneys and cooling towers in power plants, airport control towers). Within all the vertical elements belonging to life-lines, three different typologies have been singled out: chimneys (vertical slender cylindrical elements), cooling towers and antennas (mainly broadcasting ones).

The study of chimneys (which will be performed by the Units of Trieste, Chieti-Pescara and CRIACIV) is focused to the evaluation of actions which, in the lock-in range, can arise due to alternate vortex shedding. The analysis covers both theoretical aspects (tuning of the numerical model worked out by the Unit of Trieste), experimental “full-scale” tests (monitoring of the oscillations of the chimney of the new waste treatment plant: the new measurement system set-up by the Firenze-DET Unit within this project could be employed together with the GPS system already in use) and experimental wind tunnel tests (performed by the Units of Trieste and CRIACIV).

Natural draft cooling towers represent systems whose shape and thickness make them very sensible to wind actions. The study, performed by the Units of Firenze-DIC and CRIACIV, consists in experimental studies and numerical studies, these latter performed both in a linear-elastic range and in a non-linear one, leading, f.e., to define reliable “design loads” for these structures, as well as to estimate the actual vulnerability and safety level under different severe load conditions.

As last point included in Theme 1.1, the study of vertical antennas has been performed by the unit Perugia. A full-scale experimental antenna (built some years ago) will be used as specimen to be tested: full-scale measurements and numerical simulation will be performed in order to assess a reliable active or passive control system, in order to minimize the wind response of these structural elements. Radar techniques set up by the Unit Firenze-DET were usefully employed during the experimental tests.

1.2 – *Horizontal & sub-horizontal structures*

Within the framework of WINDERFUL project, the behaviour of some horizontal structures that are part of lifelines (such as viaducts or suspended and stayed bridges) were investigated. The research aimed to deepen the study of their safety, mainly on the side of the aerodynamic stability; the study took into account the control and mitigation of their oscillations under strong winds. The research involved four different Units with the aim of: 1) defining the “structure” of aeroelastic and aerodynamic forces acting on the deck sections of large suspended bridges, by wind tunnel model tests (Units of Reggio Calabria and CRIACIV); 2) improving the available numerical tools to predict the structural response of large bridges under severe wind conditions (Units of Roma “La Sapienza” and Chieti-Pescara); 3) evaluating the efficiency of some possible upgrading measures aimed to reduce the oscillatory regime during the life of the structure (Units of Roma “La Sapienza”, Chieti-Pescara and Reggio Calabria).

Edited by Gianni Bartoli and Francesco Ricciardelli, WINDERFUL: Wind and INfrastructures: Dominating Eolian Risk
For Utilities and Lifelines, ISBN 88-8453-138-1, ©2004 Firenze University Press

1.3 – Suspended structural elements (cables and stays)

The structural elements within this research theme are of particular importance: either they directly constitute parts of life-lines (transmission of and electrical lines) or they to have to carry other main structures composing life-lines (such as bridge hangers or stays). These structural elements were studied with the aim of controlling and mitigating their possible oscillations under strong winds as well as with the aim of evaluating their safety level against aeroelastic instability. In details, following research themes were addressed: 1) data collecting and set-up of a data-base about the whole Italian high and medium voltage electric network aimed to a further eolian risk analysis (Unit at Napoli); 2) experimental and numerical analysis of some actual cable configurations with respect to vortex shedding and galloping instability (units of Bologna and CRIACIV); 3) experimental and numerical analysis aimed to single out the most suitable protection devices and to define suitable design strategies (units of Bologna and Napoli).

1.4 – “Street architecture” elements

This research theme groups a series of “secondary” elements that normally result as the most suffering when severe windstorms hit built environments. Reference are made to a series of elements (such as bill-boards, traffic signs and traffic lights, lighting poles, news-stands, bus stop shelters) which are often seriously damaged by winds (then leading to high economic losses) but they are seldom studied and investigated.

In this research Theme, the Units Reggio Calabria and Roma “La Sapienza” have dealt with following problems: 1) the characterization of wind fields in the lower atmospheric layer (i.e. the one closest to the ground), which is often completely different with respect to the one adopted in usual structural calculations; 2) the aerodynamic characterization of the most usual elements; 3) the assessment of suitable techniques aimed to define their structural response; 4) the definition of some guidelines and interventions intended to mitigate wind effects on them.

The field of “street architecture” also includes some aspects dealt with by the Unit at Univ. of Bologna, aimed to reduce the risk connected to the joint action of several atmospheric events. The snow-wind interaction has been object of a series of theoretical studies performed in the framework of a previous research program. These results were integrated by wind-tunnel experimental tests on either some typical roofing elements and some simple reference cases. This part of the research programme, which is often completely neglected when dealing with wind engineering studies, has contributed to a more accurate definition of design criteria for the investigated structural elements.

Theme 2 – Reliability of life-lines under severe wind conditions

The topic addressed by the second research Theme was related to the observation that most of the losses caused by windstorms are not only represented by “direct” costs (i.e. due to failures or collapses of structures, structural elements and buildings) but mainly by “indirect” costs (i.e. due to stops or breakdowns of some essential life-lines). As an example, reference can be made to all the induced damages caused by black-outs, by the poor performances of transmission lines, by the interruption of roadways, highways and railways.

In the second part, the project developed tools and proper procedures to enable the maintaining of a correct working level of life-lines even during and after the windstorm event. The research has analysed the vulnerability of several life-lines (transport, electrical lines, communication networks), taking into consideration the interaction between different networks. Starting from well-assessed procedures developed by the researchers of the Unit at Roma “La Sapienza” in the field of the evaluation of network performances under seismic events, the research aimed to develope the most suitable preventive upgrading operations on vulnerable components of the network, in order to increase their performances according to some “objective functions”.

More specifically, following aspects were taken into account: the reliability of the network system (probability that the connections between a source node and a destination node will remain still active under a wind storm of given intensity); the expected value of the out-of-service time of the network determined by the occurrence of a windstorm; the expected value of the flow (i.e., the electrical power) between the source and the destination nodes in the emergency period that follows the storm. Analyses performed within the above mentioned research Theme 1. were used to give information on the vulnerability of each single component of the life-line, in order to obtain a correct estimation of the reliability level of the whole network.

Moreover, some data-base information on life-lines (such as the one that will be developed by the Unit of Napoli on the whole Italian high and medium voltage electric network) allowed to analyze the “eolian risk” in some particular Italian situations.

Summarizing, following allocation of tasks has been set amongst the project partners:

Theme 1. Reliability of specific structural life-lines elements under severe wind conditions

Theme 1.1: vertical structures. Units involved in the project: CRIACIV, Chieti-Pescara, Perugia, Trieste, FI-DET, FI-DIC

Theme 1.2: horizontal structures. Units involved in the project: CRIACIV, Chieti-Pescara, Roma “LS”, Reggio Calabria

Theme 1.3: suspended structural elements (cables and stays). Units involved in the project: CRIACIV, Napoli, Bologna

Theme 1.4: “street architecture” elements. Units involved in the project: CRIACIV, Chieti-Pescara, Roma “LS”, Bologna

Theme 2. Reliability of life-lines under severe wind conditions

Units involved in the project: Roma “LS”, Napoli, FI-DIC

(List of abbreviations: Roma “LS”: Roma “La Sapienza”, FI-DIC: Firenze, Dipartimento di Ingegneria Civile, FI-DET: Firenze, Dipartimento di Elettronica e Telecomunicazioni)

1.2.4 National & International activities & participation

As already mentioned before, the WINDERFUL project has been carried out, partly, as the Italian contribution to the wide COST[2] C14 Action in the domain “Urban Civil Engineering” on “Impact of wind and storms on city life and built environment”, grouping 16 European countries and chaired by the same coordinating Institution as the WINDERFUL one. The project has also acted as potential “Center of Excellence” in the field of “Risk Management”, being involved in the higher post-graduate education, amongst others, within:

---

[2] European Cooperation in the field of Scientific and Technical Research programme

- the International Doctoral Course on “Risk Management in the built Environment” and Graduiertenkolleg 802 of the DFG, between the Univ. di Firenze and the TU “Carolo Wilhelemina” Braunschweig (Germany);
- within a Master course in “Emergency Engineering”, Univ. di Roma “La Sapienza” especially on eolian risk and its reduction.

The project participants have been actively participating in all main scientific events (conference, workshops, etc.) in Europe and world-wide. It is worth to mention here the participation at the 11th International Conference on Wind Engineering, Lubbock, Texas, June 2003; 3rd East European Conference on Wind Engineering, Kiev, Ukraine, May 2002; 3rd World Conf. on Structural Control, Como, Italy, April 2002; 7th Convegno Nazionale di Ingegneria del Vento IN-VENTO-2002, Milan, September 2002; 16th Congress of Associazione Italiana di Meccanica Teorica e Applicata AIMETA’03, Ferrara, Italy, September 2003; 5th European Conference on Structural Dynamics Eurodyn 2002, Munich, Germany, September 2002; “Alan G. Davenport” Wind Engineering Symposium, London, Canada, June 2002; Final Conference of COST Action C14 “Urban Wind Engineering & Building Aerodynamics”, Von Karmán Institute, Belgium, May 2004; 12th European Conference on Earthquake Engineering, London, U.K., September 2002; 2nd International Conference on Structural and Construction Engineering ISEC-02, Rome, Italy, September 2003; 5th International Symposium on Cable Dynamics, Santa Margherita Ligure, Italy, September 2003.

At the next IN-VENTO-04 (8th Italian Conference on Wind Engineering, Reggio Calabria, June 2004), a special session devoted to the dissemination of the results of WINDERFUL project is also scheduled.

1.3 ACTIVITIES AND RESULTS

1.3.1 The final report: outline

WINDERFUL, i.e. “Wind and INfrastructures: Dominating Eolian Risk For Utilities and Lifelines”: one can surely state that the assigned topic has been well pursued and the main targets have been totally matched. The description of the research activity and general results are presented in the following together with the major contributions of the teams/Units involved. At a very overall level it can be said that the project was fully satisfactory, from both points of view: the cooperation amongst the different Units and the realization of a common objective.

It is evident, in fact, that the synergy effect created by sharing the resources of a common laboratory of excellence makes impossible to waste energies and efforts amongst the research groups. On the contrary, all contributions actually converge to the same target.

The WINDERFUL project had a wide resonance, both nationally as well as internationally: entire sessions within scientific conferences and workshops (IN-VENTO-2002, Milan; IN-VENTO-2004, Reggio Calabria; 11th ICWE, Lubbock; 3rd EACWE, Eindhoven; Workshop of COST Action C14 in “Urban Civil Engineering”, Nantes) have reported on progresses and advances in the research activities, achieved by the project teams. Future activities within 6th European Framework Programme of RTD, like ERA-NET (Network of project nationally funded) are still in progress at the present.

To summarize the results, some overall figures appear very significant and give a precise dimension of the workload carried out: about 600 man × months is the global involvement of human resources entirely devoted to the project, which produced some 25 scientific papers published in international journals, 40 presentations at international and national conferences, about 90 participations to workshops and congresses and 10 other products.

1.3.2 Reports by the research Units

The research program of the **Unit #1 (at Roma "La Sapienza")** has been devoted to the assessment of reliability of large structures (in particular long span bridges) and elements of "street architecture" under the action of wind loads. The investigation of this topic has been integrated with an accurate theoretical-experimental analysis of the urban boundary-layer wind structure.

1 – ASSESSMENT OF RELIABILITY OF LARGE STRUCTURES (IN PARTICULAR LONG-SPAN BRIDGES). The attention has been focused on the detuning of large amplitude oscillations induced by vortex shedding in long span bridges. A first analysis, in combined effort with the Unit at Chieti-Pescara, as a conclusion of the previous PRIN works, has been addressed to the investigation of large vibrations with relative cables-deck motion, with lacking of suspension systems: a paper on this subject has been published on an international journal. A second report has been developed on TMD (Tuned Mass Dampers) system for the mitigation of the elastic oscillations of an existing suspended pedestrian bridge of 252 m span. The time-domain response has been evaluated within the framework of a finite-element model, able to account the second-order effects in terms of displacements. The correlated results are detailed in some papers and in a Degree Thesis.

2 – ELEMENTS OF "STREET ARCHITECTURE" UNDER THE ACTION OF WIND LOADS. About the aspect of the impact of wind effects on urban environments, some experimental work has been done on elements of "street architecture". Pertaining to this subject, a consistent description of the vertical wind profile in urban surroundings has been proposed, after measuring the boundary layer characteristics in three different landscapes identified by different roughness. A further test campaign has been dedicated to the identification of the wind action on a model of a framed signboard. Two cases have been analyzed: the first model was an isolated one, while a second model was immersed in a regular group of buildings with different incoming wind directions. These experimental tests have been the subject of a Ph. D. thesis and of some papers.

The Unit at Roma "La Sapienza" has also carried out some complementary work, i.e.: (i) a compound study of methodologies for the risk reduction in highway networks, with different vulnerability elements; the results have been summarized in a short cycle of lessons hold by the Responsible of the Unit in an important international Institution; (ii) a multimedia presentation, very useful to display the activity of the group, has been realized by the Responsible of the Unit, thanks to the experience achieved within a Master course in "Emergency Engineering", especially on eolian risk and its reduction.

The **Unit #2** (**at Firenze-CRIACIV**) has actively cooperated within all research activities, besides its own projects, especially by arranging different experiments in the wind tunnel managed by CRIACIV. In particular, the unit has technically supported the work and given all the assistance to the model design, following the experimental tests and analyzing the obtained results. Within the Unit Firenze-CRIACIV following specific research activities have been carried out:

1 – EVALUATION OF THE EOLIAN RISK ON COOLING TOWERS. Several efforts of the research Unit have been devoted to the study of the dynamic behavior of an isolated cooling tower immersed in a typical boundary layer of a suburban area, to obtain an estimate of the design static-equivalent wind loads. The pressure field on such tower has been measured: the complexity of the fluid-structure interaction phenomenon requires experimental investigations, to put in evidence the pressure distribution around the body due to the incoming turbulent wind field. Such experimental analyses are strongly suggested also by technical standards, considering that a large variability of wind loads need to be accounted for in different structural solutions.

2 – EVALUATION OF THE EOLIAN RISK ON CABLES AND SUSPENDED BRIDGES. The evaluation of the eolian risk on suspended bridges has been pursued by carrying on a wide

parametric analysis on different bridges. The goal has been achieved through a complete wind tunnel experimental campaign conducted on a set of aeroelastic section models to examine the flutter mechanisms for long span suspended bridges.

Also in this case, the complete research program has been developed in different steps, described in details in the final report to the Ministry.

At the **Unit #3 (at Reggio Calabria),** the definition of the aerodynamic loads on the bridge decks has been performed following the classical approaches in time and frequency domains as the Proper Orthogonal Decomposition technique. The analyses in time and frequency domain have been carried out on experimental data obtained from wind tunnel tests by using both a system constituted of load cells, laser displacement transducers, accelerometers and a set of pressure taps. This latter system allowed the evaluation of the pressure distribution along the transversal axis of the bridge deck section.

Through the Orthogonal Decomposition method, the excitation frequencies have been evidenced, and for each of them, a component in-phase of the wind force and one out-of-phase have been identified, by using only a relatively small number of vibration modes.

Moreover, a carbon fiber bridge model with rectangular section has been designed and built, with the purpose of analyzing aerodynamic and aeroelastic wind loads on a simple and well-documented section. The effect of turbulence on the vibrating model will be investigated within such new experimental campaign. The wind action on elements of “street architecture” has been investigated with two different experimental models, in order to characterize the flow field in urban areas, in terms of turbulence and gust factors. With the first set of experiments, a qualitative flow behavior and a first estimate of the Reynolds stress have been obtained: in particular it has been attained that the leeward Reynolds stress can overpass by three times the same amount measured windward.

At the **Unit # 4 (at Chieti-Pescara),** following four themes have been considered, of which only the first two were originally scheduled:

1 – THEORETICAL MODELS AND EXPERIMENTAL TESTS IN WIND TUNNEL MODEL FOR VIBRATION CONTROL OF LONG-SPAN BRIDGES. The problem of control and mitigation of aerodynamic and aeroelastic vibrations of cable-stayed and suspended bridges has been addressed; in fact, comfort and traffic capacity problems can arise due to the unexpected vibrations, even if the collapse of the structure can be excluded. In cooperation with researchers of the Unit at Trieste and Roma "La Sapienza”, a wide set of experimental tests have been set up. In parallel, a finite-element code (TENSO), developed in the last ten years, has been employed. This program is able to simulate not only the various aspects of geometrical and mechanical non-linearity, but also the different significant types of fluid-structure interactions (aerodynamic and aeroelastic forces, vortex shedding, etc.) acting contemporary on structural members. In particular the role of wind turbulence has been investigated, through a comparison of the structural response with different combinations of power spectral densities and correlation functions proposed in scientific literature. Moreover, the theme of the passive control of the vibrations induced by the vortex shedding on bridge decks has been followed. Different active, semi-active and passive control disposals for bridges and pedestrian bridges have been analyzed and compared, considering their range of applicability. In particular classical Tuned Mass Dampers (TMD) have been compared with multiple disposals of the same kind (MTMD), able to mitigate the induced vibrations in a wider frequency range of the acting forces.

2 – THEORETICAL MODELS AND NUMERICAL PROCEDURES FOR THE EVALUATION OF THE EFFECTS OF VORTEX SHEDDING ON SLENDER STRUCTURES. Wind tunnel tests have allowed a detailed description of the synchronization phenomenon and of its effects on the wind load acting on the structure. In collaboration with the Trieste unit, an accurate

study of the experimental results obtained in the experimental campaign carried out with the model built at the Boundary Layer Wind Tunnel Laboratory, University of Western Ontario, has been performed, in particular focusing attention on the variating ratio among the main parameters of the lock-in phenomenon. The experiments with a second model have been continued at the CRIACIV wind tunnel. Free vibration tests have been carried out, in laminar and turbulent flow, with different turbulence intensities. With the Unit at Trieste, a new numerical formulation of the aeroelastic loads due to vortex-shedding has been proposed for the lock-in condition, both for slender structures and bridge decks. This formulation completes the numerical model built in these last years with the use of experimental observations.

3 – STRUCTURAL IDENTIFICATION: Beside the described topics, a research activity on structural identification has been carried with the contribution of researchers of the Units Roma “La Sapienza” and Napoli. In this case the main goal of the activity has been the setting of a robust structural identification system for actions not directly or non completely measurable, as it happens often for wind-induced loads. This topic is strictly related to the others, especially to the aspects of structural control.

4 – STREET ARCHITECTURE: Lastly, during the first two years of PRIN, several studies on the wind effects on elements of street architecture have been performed. In particular, some measurements of the wind field in urban areas have been carried out on a scale model of a signboard at the CRIACIV wind tunnel in Prato.

The research activity at **Unit #5 (at Perugia)** has dealt with the design, the construction and the application of active control systems to full-scale structures under the wind action, with particular attention to systems for telecommunication networks. The results obtained are related to different aspects of the problem of correct estimating the eolian risk. As a first step, the structural vulnerability has been evaluated, for support structures devoted to transmission and/or telecommunication systems (antennas, etc.). The estimation of the reliability of such structures under the action of extreme wind loads, has been investigated in wind tunnel tests with model built with full-scale elements, with regard to the safety of the structure itself, to its efficiency and maintenance. Aerodynamic loads and drag and lift coefficients variable with the system configuration and with the wind direction have been evaluated through these experiments. Considering the eolian vulnerability, the identification of the stochastic characters of the wind pressures and the simulation of the corresponding loads has been performed. These analyses have been carried out on industrial building roofs that can evidence strong sensitivity to the wind action. An interesting comparison among the recommendations of different standards has been made. Experimental wind tunnel data have been analyzed, to characterize statistically the time histories for the calibration of a probabilistic model for the numerical simulation of pressure histories. Finally, a first experimental campaign on cables has been carried out at the CRIACIV wind tunnel, to obtain a first load estimate. Considering the structural response, the numerical simulation methods have been utilized within a Database-Assisted-Design, to investigate the stochastic characters of the response of a typical small building under the action of wind flow. Moreover, a procedure for the evaluation of the peak response of strong non-linear systems has been developed. Using previous results, the problem of the mitigation of the structural response has been addressed, using active control systems. For this purpose, a prototype antenna has been designed by the Unit, and an experimental campaign in situ has been carried out to evaluate the efficiency of proportional/ derivative control systems (PD). A second, cable-stayed & tubular, antenna has been realized, for the contemporary measures of the wind velocities. The efficiency of the procedure has been validated through a comparison of the structural response under the wind action in two different cases: a configuration with the control disposal, and a non-controlled one. The efficiency of the active PD system has been evidenced by the relevant decrease of the peaks in the fluctuating response component.

The problem of cables and cable structures under the wind action has been addressed at **Unit #6** (**at Bologna),** with particular attention to the response to aerodynamic action and interaction with suspended elements. ***Damping systems for stays***: the efficiency of distributed damping disposals for the ending part of a cable has been analyzed. Such systems are more effective in the mitigation of wide spectrum vibrations than the concentrated damping ones. ***Excitation of stays under the combined action of wind and rain***: a new experimental campaign has been launched at the wind tunnel CRIACIV in Prato, to definitely characterize a numerical predictive model (already published) with the calibration of some parameters affected by uncertainties. ***Large roofs supported by cables and cable systems***: an application of the recent techniques for the definition of the wind loads has been developed in the analysis of the roof of the Braga Stadium (Portugal). The eolian forces have been analyzed with the orthogonal decomposition of signals. The response has been numerically evaluated, with different techniques in the frequency domain and with a complete analysis in time domain; a monitoring system of pressures and wind velocities has been set up. ***Response to the wind action for roofs containing closed volumes:*** in the present research a simplified model for the interaction of structure and enclosed gas has been proposed. This model can be an useful tool for the simulation of the damping induced by the fluid on the structure. The model is based on two physical assumptions: (1) the motion of a portion of structure is damped by a local pressure variation; (2) the local pressure peaks are propagating in a finite time interval in the structural volume.

Unit #7 (**at Trieste)** has carried out the research activities as briefly pointed in the following sections:

1 – DETAILED DESCRIPTION, BY MEANS OF WIND-TUNNEL BASED MATH MODELS, OF THE PHENOMENON OF THE SYNCHRONIZATION AND ITS EFFECTS ON THE LOAD ACTING ON THE STRUCTURE. A detailed study of the results obtained from the tests executed in the BLWT Laboratory of the University of the Western Ontario has been carried out. Attention has been placed to the relationships between the main parameters of the phenomenon of lock-in. According to the second model, tests of free oscillation in conditions of laminar flow and with various values of the intensity of turbulence have been executed in the BLWT Laboratory of CRIACIV.

2 – COLLECTION OF THE EXPERIMENTAL DATA ON A REAL CHIMNEY. It has been continued the campaign of measures on the chimney of the new system of refusal burning plant of the province of Trieste.

3 – DEVELOPMENT OF THE NUMERICAL MODEL OF THE LOAD DUE TO THE VORTEX SHEDDING. It has been set up a new numerical formulation of the aerolastic load due to the separation in condition of lock-in. Both the amplitude of the lock-in band and the value of the lift coefficient depends on the oscillation amplitude, coherently to how much has been experimentally investigated.

4 – STUDY OF THE RESPONSE OF SLENDER STRUCTURES TO THE SEPARATION OF THE VORTICES. In collaboration with the Unit of Chieti-Pescara, it has been lead a wide parametric survey with TENSO code, taking into account the geometric and mechanical nonlinearity, including the unilateral behavior of hangers and the fluid-structure interactions (mean and aeroelastic actions, vortex shedding, etc).

Four main streamlines of research activity have been pursued at **Unit #8** (**at Firenze-DET**):

1 – VALIDATION, BY MEANS OF EXPERIMENTAL TESTS ON PROTOTYPE, OF THE INSTRUMENTATION ALREADY AVAILABLE AT DET, previously to the activities of this research project. In agreement with the partner, it a test-site suitable to the validation of the radar

technique has been selected. Therefore, in July 2002 an experimentation in-situ has been performed in the Department of Civil and Environmental Engineering of the University of Perugia, where a steel structure, 15 meters tall and instrumented by means of a hydraulic jack on the top. The dynamic behavior of the structure has been evaluated under the excitation of the hydraulic jack, and under a low-speed wind action. In both cases goods results, in terms of frequency and amplitude of oscillations have been carried out with an accuracy comparable to the conventional instrumentation. The measure without artificial excitation has been particularly meaningful: the system has been able to operate a distant measure the natural frequency of a structure movement in a few minutes. The applicative impact of such a technique is remarkable, as, for example, the possibility to monitor a large number of structures (quickly and non-destructively). Thanks to the rapidity and simplicity of the method, with a single instrumentation a lot of monitoring in a day could be executed controlling wide urban areas.

2 – DEVELOPMENT OF A SYSTEM RADAR WITH A SAMPLING TIME LOWER THAN 60 SECONDS. In the present project it has been completed a first prototype of radar not based on laboratory instrumentation, but entire realized with discrete members operating in X band (approximately 10 GHz). This prototype has the main scope to constitute a test bench for the technology and the know-how to be developed in the present project. The prototype is not directly applicable to monitor structures in dynamic conditions but happening like penetrating radar (GPR has been applied with: Ground Penetrating Radar). The adopted technological solutions and the experimental tests on a wall realized in laboratory have been object of a discussion in an international conference.

3 – DEVELOPMENT OF A SYSTEM WITH A SAMPLING TIME OF THE ORDER OF THE FRACTION OF A SECOND, able to follows the transitory phenomena induced by the wind. The most cumbersome activity in terms of resources and engagement has been the design and the realization of a prototype radar based on advanced technical solutions and technologies at the state of the art. The system operates in K_u band (approximately 17 GHz) with one bandwidth of 400 MHz. The architecture of such system is based on the direct digital synthesis (DDS: Direct Digital Synthesis) that constitutes a meaningful innovation in the field of the radar technology. Moreover the architecture of the communications between the devices is based on protocol USB, also this is one important innovation that allows high speeds of communication between the system and the Personal Computer. The realized system is currently able to log one single radio frequency in 10 microseconds, as also verified from laboratory measures. Since an image radar is constituted typically of 1000 radio frequencies, the system is able to acquire an image every 10 milliseconds. This speed is widely able to sample the transitory of the wind in the architectonic structures. About the accuracy of measure carried out from the laboratory tests on a target able to make calibrated movements, it turns out that the system can appreciate movements lower than one-tenth of millimeters as for distances of some hundred of meters.

4 – ADDITIONAL EXPERIMENTATIONS. The radar system developed according to the previous point, able to acquire an image in a fraction of a second, has been used on large viaduct near the city of Florence (the Indiano Bridge, a steel bridge 200 meters long over the Arno river). The driving surface is approximately at 10 meters elevation over the measurement level, and a pedestrian footbridge is hanging under the driving surface. The radar was installed on a river bank of the river in proximity of a pillar of the bridge and has been headed at the downstairs of the same bridge. The bridge was excited from wind and intensive traffic, and measured movements have been of approximately 2.5 cm in the central part and of fractions of millimeter near the pillars. The frequency of vibration of the natural mode was well characterized, like the dynamic deformation of the bridge: these are very original results, as currently, it does not exist anything

comparable to this system for the non-destructive/distant survey of the dynamic behavior of one large structure.

The research activities of the **Unit #9 (at Napoli "Federico II")** have concerned :

1 – THE DEVELOPMENT OF TECHNIQUES FOR REDUCING THE DYNAMICS RESPONSE OF THE ELEMENTS OF ELECTRICAL NETS AND INDUSTRIAL SYSTEMS. For the electrical nets, two arrangements of passive protection for a switch of 420 kV of one substation of transformation, have been proposed and analyzed (with determinist and probabilistic procedures). For the industrial systems, elements with prevailing vertical development (chimneys, cooling towers, etc) have been studied, with particular interest to the problem of vortex shedding, estimating the benefits derive from tuned masses with semi-active systems, also proposing a simplified design methodology.

2 – THE DEVELOPMENT OF ALGORITHMS BASED ON ENERGETIC CONSIDERATIONS FOR THE SEMI-ACTIVE CONTROL SYSTEMS. Some control algorithms based on energetic considerations have been proposed and characterized. These algorithms leads to a reduction of the response under eolian action up to the 50% of that would be possible in the case of systems based on traditional passive technologies. The obtained results have been applied also in the seismic field.

3 – THE DEVELOPMENT OF ANALYTICAL MODELS SIMULATING THE MECHANICAL BEHAVIOUR OF SEMI-ACTIVE MAGNETORHEOLOGIC-FLUID SYSTEMS, and their validation based on experimental tests. The study, first analytical and then experimental, of the mechanical and dynamic property of the dissipation devices based on the employment of magneto-rheologic fluids has lead to the development of analytical models subsequently applied to a steel test-model of a building tested on vibrating table.

4 – THE DEVELOPMENT AND THE IMPLEMENTATION OF CONTROL SYSTEMS OF THE DYNAMICS RESPONSE OF PEDESTRIAN BRIDGE INDUCED BY THE ACTION OF THE TRANSIT OF THE PEDESTRIANS. The advantages deriving from the substitution of the passive dampers of the tuned masses with semi-active systems have been demonstrated. These advantages consists in a greater total robustness of the system of control as for the variation of the characteristics of mass and rigidity of the structure and the content in frequency of acting loads.

At the **Unit #10 (at Firenze DIC)** two main research activities have been carried out on:

1 – EOLIAN RISK ANALYSIS OF COOLING TOWERS. Cooling towers are structures particularly sensitive to the action of the wind, and so they are critical points inside of the production- distribution chain of the electric power. Their particular sensibility to the eolian action derived from their dimensions and from the load conditions; actually, if the regular flow of the wind is disturbed from elements contiguous to the towers, the natural symmetry of the eolian pressure gets lost on the shell of the same tower and dangerous bending moments, removing the conditions of structural operation from the theoretical membrane condition, are generated in the structure. The research activities had been programmed according to five different steps, that is: 1 - execution of tests in wind tunnel, in collaboration with unit CRIACIV; 2 - non Gaussian pressure histories simulations; 3 - structural analyses; 4 – Eolian risk assessment of one or more cooling towers; 5 - definition of design wind loads on the single cooling tower. Experimental tests have been carried out in wind tunnel in collaboration with unit CRIACIV with the aim of measuring the wind pressures on towers surfaces varying the incidence direction of the wind as regards to the towers, theirs distance, their slenderness (defined like the relationship between their height and their base diameter), the average speed of the flow. In the CRIACIV boundary layer wind tunnel a test-model 1:300 scaled has been tested. A similar experimental campaign have been previously carried out on a model with a lower number of pressure taps. The pressure taps have been placed on 8 different levels equally spaced of 30°. A new software for the acquisition of pressure taps

have been implemented allowing to log data with a sampling frequency up to 1075 Hz. The wind pressure histories have been simulated by means of two approaches: the first one deals with Radial-Basis-Function Artificial-Neural-Networks (RBFANN) , developed in DIC improving the simulations methods based on parametric models; the second is based on the use of opportune transfer functions. Finite-Element models of the cooling tower have been implemented, and the equations of motion have been integrated with the pressure histories generated in the previous step. The models have been implemented with codes able of modelling at least the simplest characteristics of the reinforced-concrete, because the structural collapse heavy depend on the formation of cracks in the structure. An automatic code (MORE) for the assessing of the structural response with a strongly nonlinear behavior (like reinforced concrete structure in flexural regime) have been implemented. Such procedure is based on the decomposition of the field of structural motion on the space generated from the modal shapes of the actual structural system with a linearization around the mean deformed configuration The application of this procedure reduces the times of calculation being necessary for a dynamics analysis in flexural regime, drastically limiting the error in respect to the complete procedure, and simply leading to the next step of the research, which deals with the assessment of the eolian risk of one or more towers.

2 – DETERMINATION OF DESIGN WIND LOADS. Concerning the definition of design wind loads, the study has been organized as follows: Pressure coefficient have been carried out and characterized; Extend simulations of such coefficients have been carried out; Stresses induced in the structures from the wind pressures acting on the structural surface have been estimated; for this purpose: wind loads reproducing the worst stresses conditions have been computed by means of LRC method (load – response- correlation); Since the obtained design wind loads distributions are qualitatively very similar to the mean one, the internal stresses of the structure have been maximized (or minimized) by means of the GRF (Gust Response Factor) method which consists in multiplying the mean wind load by the GRF coefficient. In the present research value of GRF between 2 and 3 have been founded. The theoretical justification of such results are still in phase of elaboration, like the structural analysis.

1.4 DISSEMINATION EVENTS

Results have been disseminated, during the project life, within all main scientific conferences (in Italy, Europe and worldwide; s. 1.2.4): the present final publication will be officially presented during a special devoted session of the 8th Italian Congress of Wind Engineering, IN-VENTO-04, Reggio Calabria, June 2004.

1.5 FUTURE PERSPECTIVES

An immediate follow-up of the project has already started his activity and is lifely continuing some of the research streamlines initiated by WINDERFUL: this *follower* project, which has been approved and co-financed within the PRIN (Research Projects of National Interest) in Nov. 2003 for the two years 2003-2005, deals with: LIFE-CYCLE PERFORMANCE, INNOVATION AND DESIGN CRITERIA FOR STRUCTURES AND INFRASTRUCTURES FACING EOLIAN AND OTHER NATURAL HAZARDS, and aims to introduce a new “PERformance Based Approach to Construction Cost Optimization” (PERBACCO, which the new acronym of the project). Besides the great impact that WINDERFUL has had on the European developments in the field, and especially on the results of the COST action C14 in “Urban Civil Engineering”, it is likely that a new COST action will be launched in the immediate future, which will be based on this new approach. The heritage of WINDERFUL, both at National as well as European/international level, is therefore ensured.

ACKNOWLEDGMENTS

The Author is grateful to Carlotta Costa and Stefano Pastò for the help provided in the revision of the paper; the financial contribution of MIUR, Min. dell'Istruzione, Università Ricerca (PRIN WINDEFUL, Cofin 2001) is also gratefully acknowledged.

The Project Coordinator wishes also to thank all colleagues, local Unit responsibles, researchers, staff members and technicians who contributed with their personal engagement and competence to the success of the project and to its adfirmation in the scenario of the technological competition. A special thank is due to Ing. Lorenzo Procino (Chief technician at the CRIACIV - BLWT laboratory in Prato) and to Mrs. Serena Cartei, of CRIACIV Secretariat, for their concrete help in all phases of the project.

1.6 RESEARCH UNITS

Unit #1

Dipartimento di Ingegneria Strutturale e Geotecnica – Università degli Studi di Roma "La Sapienza"

Research Theme: **Reliability under wind actions of (1) elements of transportation infrastructures (horizontal structures like viaducts and suspended or cable-stayed bridges, and "street architecture" components like roadway and railway signs, bus stops, etc.) and (2) lifeline networks, in order to keep utilities and cities running during and after windstorms**

Coordinator:	Giuliano AUGUSTI	Full Professor
Components:	Marcello CIAMPOLI	Associate Professor
	Carlo PAULOTTO	PhD student
	Furio Lorenzo STAZI	PhD student

Unit #2

CRIACIV (Centro di Ricerca Interuniversitario di Aerodinamica delle Costruzioni ed Ingegneria del Vento) – Università degli Studi di Firenze

Research Theme: **Evaluation of the eolian risk on cooling towers, cables and suspended bridges**

Coordinator:	Claudio BORRI	Full Professor
Components:	Gianni BARTOLI	Associate Professor
	Serena CARTEI	Secretary
	Carlotta COSTA	PhD student
	Claudio MANNINI	PhD student
	Lorenzo PROCINO	Technician
	Michele RIGHI	PhD student

Unit #3
Dipartimento di Meccanica e Materiali – Università degli Studi di Reggio Calabria

Research Theme: **Evaluation of the response of wind sensitive structures and its reduction: from long-span bridges to street architecture**

Coordinators:	Enzo D'AMORE	Assistant Professor
	Francesco RICCIARDELLI	Associate Professor
Components:	Enrico Tullio DE GRENET	PhD student
	Giulio NICOLOSI	Full Professor (Univ. of Napoli)
	A. David PIZZIMENTI	PhD student
	Raffaele PUCINOTTI	Technician
	Aldo RAITHEL	Full Professor (Univ. of Napoli)

Unit #4
PRICOS (Dipartimento di Progettazione Riabilitazione e Controllo delle Strutture Architettoniche) – Università degli Studi di Chieti-Pescara

Research Theme: **Analysis and control of the wind risk for infrastructures formed by flexible structures**

Coordinator:	Piero D'ASDIA	Full Professor
Components:	Salim FATHI	PhD student
	Vincenzo SEPE	Associate Professor
	Massimo TARQUINI GUETTI	Consulting Engineer
	Alberto VISKOVIC	Assistant Professor

Unit #5
Dipartimento di Ingegneria Civile ed Ambientale – Università degli Studi di Perugia

Research Theme: **Wind hazard reduction for telecommunication networks by means of control systems**

Coordinator:	Vittorio GUSELLA	Full Professor
Components:	Marco BRECCOLOTTI	PhD student
	Federico CLUNI	PhD student
	Massimilano GIOFFRÈ	PhD
	Annibale Luigi MATERAZZI	Full Professor

Unit #6

Dipartimento di Ingegneria delle Strutture, Trasporti, Acque, Rilevamento del Territorio – Università degli Studi di Bologna

Research Theme: **Dynamic behaviour of cables under wind actions: cable response and structural interaction**

Coordinators:	Massimo MAJOWIECKI	Associate Professor
	Giuseppe MATILDI	Associate Professor
Components:	Nicola COSENTINO	PhD student
	Stefano PINARDI	Consulting Engineer
	Roberto TREVISAN	Consulting Engineer

Unit #7

Dipartimento di Ingegneria Civile – Università degli Studi di Trieste

Research Theme: **Vulnerability of slender structures to vortex shedding**

Coordinator:	Salvatore NOÈ	Associate Professor
Components:	Boris SOSIC	Technician
	Franco TREVISAN	Technician
	Tatiana SLUGA	PhD
	Luca CARACOGLIA	Consulting Engineer

Unit #8

DET (Dipartimento di Elettronica e Telecomunicazioni) – Università degli Studi di Firenze

Research Theme: **Interferometric radar for remote monitoring of large structure vibrations caused by wind**

Coordinator:	Massimiliano PIERACCINI	Assistant Professor
Components:	Davide LEVA	PhD student
	Linhsia NOFERINI	PhD student
	Paolo CLEMENTE	Researcher (ENEA)

Unit #9
DAPS (Dipartimento di Analisi e Progettazione Strutturale) – Università degli Studi “Federico II” di Napoli

Research Theme: **Development of methodologies for the reduction of aeolic vulnerability of electric networks and industrial plants**

Coordinator:	Giorgio SERINO	Full Professor
Components:	Carlo BAGGIO	Associate Professor
	Manuela DI DONNA	Consulting Engineer
	Renato GIANNINI	Full Professor
	Alessio LUPOI	PhD
	Fabrizio PAOLACCI	Technician
	Tommaso PUOPOLO	Consulting Engineer
	Lorena SGUERRI	PhD
	Maria Cristina SPIZZUOCO	PhD

Unit #10
DIC (Dipartimento di Ingegneria Civile) – Università degli Studi di Firenze

Research Theme: **Eolian risk analysis for cooling towers and evaluation of design loads**

Coordinator:	Paolo SPINELLI	Full Professor
Components:	Michele BETTI	PhD
	Luca FACCHINI	Associate Professor
	Maurizio ORLANDO	Assistant Professor
	Stefano PASTÒ	PhD student

2 Long-span bridges

Francesco Ricciardelli
University of Reggio Calabria

2.1 INTRODUCTION

Long-span bridges, are one of the most, if not the most wind-prone of all structures, and many of the achievements in Wind Engineering are more or less related to large bridge projects or failures. Even though not always recognised, bridge aerodynamics and aeroelasticity have a two-century-long history, which started when the first pioneering, few metres long suspension bridges happened to be blown down by the wind. Then since, suspension bridges have multiplied their spans by a factor of one hundred, and longer projects are presently under consideration, which increase the need for an always deeper understanding of their static and dynamic behaviour in wind.

Static deformations, buffeting- and shedding-induced stable response, lock-in and flutter unstable behaviour of the deck on one side; buffeting- and shedding-induced response of the towers, shedding-induced response and galloping (including wind-rain response) of the cables on the other side are the major pathologies. Wind tunnel testing, analytical and numerical models and computational fluid dynamics are the diagnostic tools.

2.2 WIND TUNNEL TESTING OF LONG SPAN BRIDGES IN THE CRIACIV WIND TUNNEL

2.2.1 Tests on section models

Two different setups are presently used in the CRIACIV boundary layer wind tunnel for the testing of bridge deck sectional models. The first setup is based on the use of two end plates placed inside the wind tunnel, with the suspension system also placed inside the tunnel. The end plates are used (figure 2.1) to ensure a two-dimensional flow condition in the area of interest, but they reduce the maximum length of the model, which cannot exceed 100 cm. In the second setup, the suspension system is placed outside the tunnel, which makes it possible to test models up to 240 cm long. To do so, two holes have been made in the tunnel walls to let the model shaft out, together with tubing and lines. This second setup is more versatile when the span-wise coherence of the excitation is of relevance.

Tests have been performed, using setup #1, on rectangular prisms (figure 2.2) with two

Edited by Gianni Bartoli and Francesco Ricciardelli, WINDERFUL: Wind and INfrastructures: Dominating Eolian Risk
For Utilities and Lifelines, ISBN 88-8453-138-1, ©2004 Firenze University Press

Figure 2.1 Aeroelastic section model in the CRIACIV boundary layer wind tunnel

slenderness ratios of *B/D*=12.5 and *B/D*=5, which will be discussed in Section 2.5. The models are 92 cm long (*L*), 37.5 cm and 20 cm wide (*B*), and 3 cm and 4 cm deep (*D*), respectively. The geometry chosen is not that of a real bridge deck, but rather a reference geometry, which allows most of the aeroelastic phenomena to be investigated, and the results to be compared with those from other authors. The maximum allowable length of the model was determined by the width of the tunnel test section, and by the size of the end plates; to obtain a satisfactory two-dimensional behaviour, the *L/B* ratio needs to be at least 2.5, where a value of 3 is usually adopted [a]. Once *L* is chosen, values for *B* and *D* are calculated.

The models were made of a plywood skin, stiffened by a lightweight wooden core; a stainless steel shaft, 16 mm in diameter and 1.5 mm thick was used to connect the model to the supporting aluminium arms. The model was supported by eight vertical helical spring (figure 2.3), whose

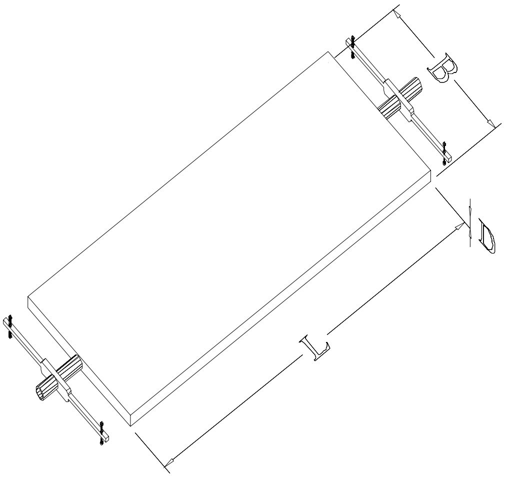

Figure 2.2 Sketch of the aeroelastic section model

Figure 2.3 Elastic supporting system

eccentricity could be adjusted so to obtained the desired ratio between the natural frequencies of the heaving and torsional modes.

The role of the end plates is to ensure a two-dimensional wind flow, then a correct dimensioning of their geometry is fundamental in order to obtain reliable results from section model tests. Only empirical guidelines are available in the literature. In [b] the results of several tests on cylinders are reported, aimed at optimising the end plates design. Given D_c, the cylinder diameter and X_c, its distance from the end plates leading edge, Stansby found that if X_c/D_c is large the flow is practically unaffected by the end plates, whereas if the ratio is small the effect is restricted to a small area around the edge. The optimal values of X_c/D_c vary between 2.5 and 3.5, which bring a uniform pressure distribution along the longitudinal axis of the cylinder. The design of the end-plates used in the tests was done according to these guidelines.

The alongwind vibration of the model was restrained by a system of stays attached to the model axis and to the tunnel walls upstream and downstream the model; the inclination of the stays was such to prevent them from acting as a vertical restraint; ball bearings were installed to the axis head to avoid additional friction, so to allow an undisturbed torsional and heaving motion. Undesired lateral motion was also restrained via additional stays connected to the tunnel walls.

A second run of tests has been recently started on a carbon fiber rectangular model 240 cm long, using setup #2. The lightweight model has a slenderness ratio B/D=5, and is equipped with 7 arrays of 30 pressure taps. The tests are aimed at a characterisation of the aeroelastic interaction, including span-wise coherence.

2.2.2 Flow characteristics

Tests have been performed both in smooth and turbulent flow; the reference wind speed U_{ref} was measured with a Pitot tube positioned above the end plates, while the mean and RMS wind speed profiles were measured via an x-probe hot-wire anemometer (figure 2.4).

During the aeroelastic tests the wind speed at deck level cannot be measured directly with the hot-wire anemometer, as the sensor would interfere with the deck motion; what is measured instead is the above mentioned U_{ref}, then a relation between U_{ref} and the actual wind speed at deck level must be found. Several wind profiles have been measured with U_{ref} =5, 10, 11.50, 15, 20 and

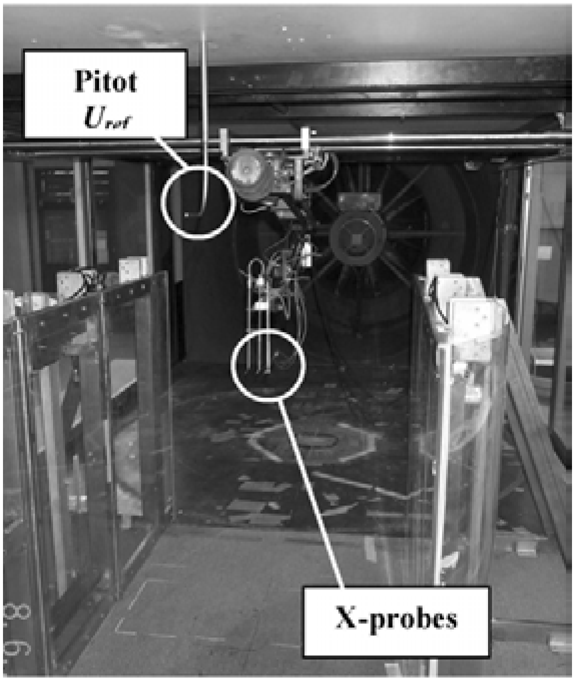

Figure 2.4 Pitot tube and X-probe hot-wire anemometers in the tunnel

25 m/s, in order to calculate the ratio U_{deck}/U_{ref}, where U_{deck} is the mean wind speed at deck level. In figure 2.5 the case U_{ref} =11.50 m/s is plotted, showing a good uniformity of the wind field. The U_{deck}/U_{ref} ratio was calculated to be 1.19. For all the other speeds considered the same U_{deck}/U_{ref}=1.19 was found, which was then used in the calculations. The speed-up effect between the end-plates is caused by the restriction of tunnel section (Venturi effect).

In smooth flow, a thin boundary layer (0 to 20 cm thick) was measured at the tunnel floor,

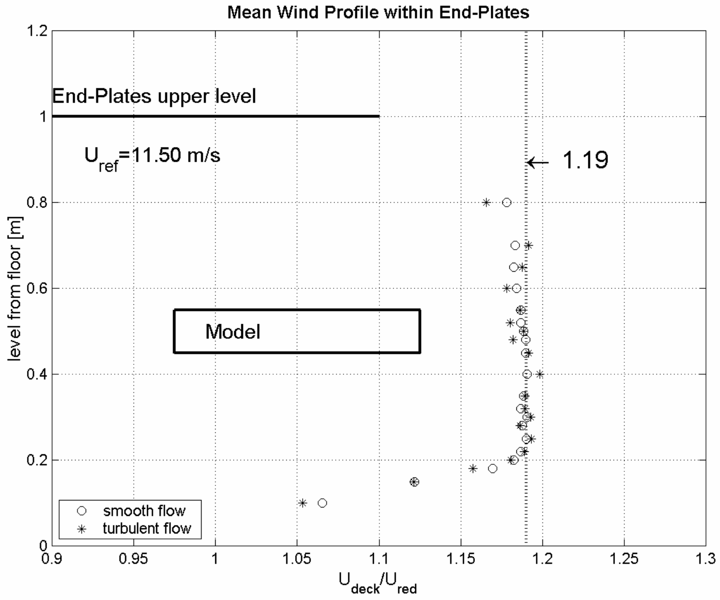

Figure 2.5 Mean wind velocity within the end-plates both in smooth and turbulent flow

Figure 2.6 Turbulence-generating grid

however in the area where the model is located (45 to 55 cm above the floor) the wind speed profile is almost constant, and the turbulence is negligible, simulating an excellent smooth flow condition (figure 2.5).

A turbulent flow was obtained by adding a coarse grid inside the tunnel (figure 2.6), placed 5.85 m downstream of the honeycomb grid and 4.05 m upstream of the model. An average intensity of turbulence of 0.17 was found in the region where the model was placed, while the longitudinal integral length scale was about 0.2 m. In figure 2.7 the spectrum of longitudinal turbulence is plotted.

2.3 STRUCTURE OF THE AERODYNAMIC AND AEROELASTIC FORCES ON LONG-SPAN BRIDGES

A study of the characteristics of the aerodynamic and aeroelastic forces on box girder long span bridge deck, was first performed, based on wind tunnel tests carried out at the Boundary

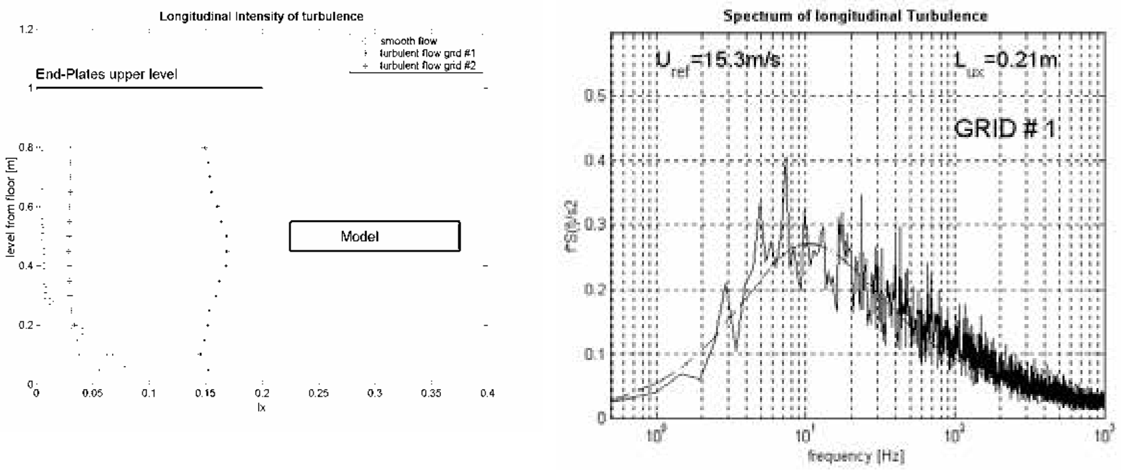

Figure 2.7 Left: Longitudinal Intensity of turbulence-vertical profile; Right: Spectrum of Longitudinal turbulence

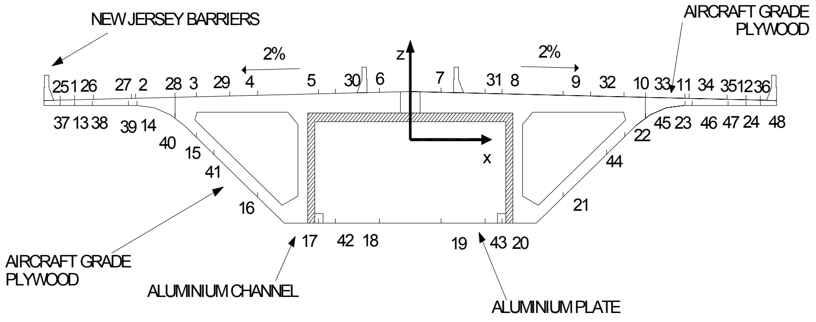

Figure 2.8 Cross section of the Sunshine Skyway Bridge with the 48 pressure taps distribution

Layer Wind Tunnel Laboratory of the University of Western Ontario, on the Sunshine Skyway bridge deck section model. The Sunshine Skyway Bridge (SSB) is a cable-stayed bridge with a main span of 364 m, a box girder deck, 29 m wide and 4.27 m deep. Due to the presence of a single plane of stays, aligned with the centreline of the deck, torsional stiffness is provided only by the girder, while the bending stiffness is the result of the combination of the girder and of the cables stiffness. As a result the first torsional and bending natural frequencies of the SSB are separated by a factor of 4, being 0.31 Hz the first bending frequency and 1.25 the first torsional frequency.

The 1:80 section model was provided with 48 pressure taps (figure 2.8) arranged in two sections around midspan, 2 cm apart. The tests were performed both on the stationary and on the vibrating model. In the first case in addition to the pressure system, four load cells were used, together with one hot wire anemometer placed in the wake of the model, for the measurement of the longitudinal and vertical components of the wind velocity. In the dynamic tests four loads cells on the supporting spring, four accelerometers and four laser displacement transducers were added to the pressure system. Moreover the vertical and longitudinal wind speed were measured at seven locations downstream and at one location upstream the model. More detailed information about the tests is given in [1].

2.3.1 Box girder aerodynamic forces and aeroelastic response

The streamlined geometry of the box sections of long span bridge decks is the main reason for their good performance in wind. At the same time, the streamlined shape increases the sensitivity to geometry variations (e.g. the addition of traffic barriers, vehicles, etc.). In figure 2.9 the drag coefficients of the SSB are plotted for the deck with and without traffic barriers. For a zero angle of attack the drag coefficient increases of 38% from bare deck to the traffic barriers configuration. Moreover, with the addition of the Jersey barriers, the Strouhal number changes from 0.93 to 0.73, referred to the deck width. The addition of the traffic barriers also proved to decrease the flutter critical speed.

The aeroelastic stability of the deck is the result of its combined across wind and torsional behaviours. When the aerodynamic coefficients are measured on the stationary model, their values do not take into account the motion-related forces. The vibration regimes of (a) buffeting or forced motion, (b) vortex shedding *lock-in* and (c) flutter are usually found for bridge decks. A fourth regime of galloping is also possible, though unusual.

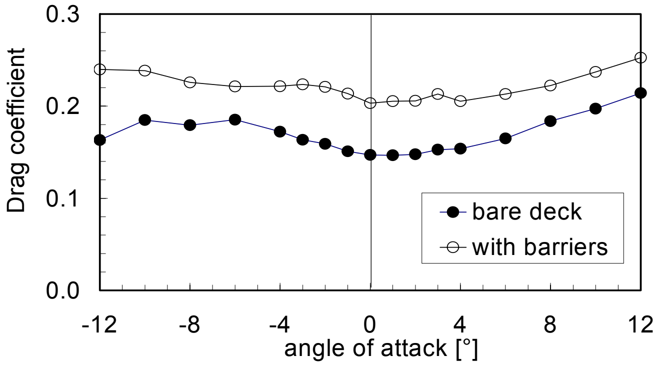

Figure 2.9 Drag coefficients of the SSB for different angle of attack with and without barriers

For the particular case of the SSB the three response regimes of torsional lock-in, of heave and torsion forced motion, and torsional flutter were observed, depending on the oncoming wind speed. In figure 2.10 the RMS rotation is plotted as a function of the reduced wind speed (with respect to the deck width). Four lines are plotted which are the outcome of two tests carried out with a low structural damping (0.2 %) and two tests carried out with a high structural damping (1 %), both in bending and in torsion.

For a reduced wind speed in the range of 1.1 to 1.7 a torsional lock-in was observed. For a reduced wind speed in excess of 3 the torsional flutter behaviour was observed. For a reduced wind speed in the range of 0.7 to 0.9 a vortex shedding resonance at a frequency half of the vibration frequency was also observed in some tests.

Comparing the results of each pair of tests for the two values of the structural damping, it is possible observe how for the lock-in and for the forced motion regimes the agreement is good. However, in the flutter vibration regime, tests no. 1 (in both cases of low and high structural damping), indicate a divergent behaviour while the tests no. 2 show an increase of the RMS response, not associated with a divergent behaviour. Flutter did not manifest itself in all the tests, but, as it will be shown, the characteristics of the excitation in this regime differ substantially from those of the other excitation regimes.

Comparison of the vibration and excitation frequencies provides insight to the mechanism of excitation in the three response regimes. In figure 2.11 the torsional vibration frequency and the

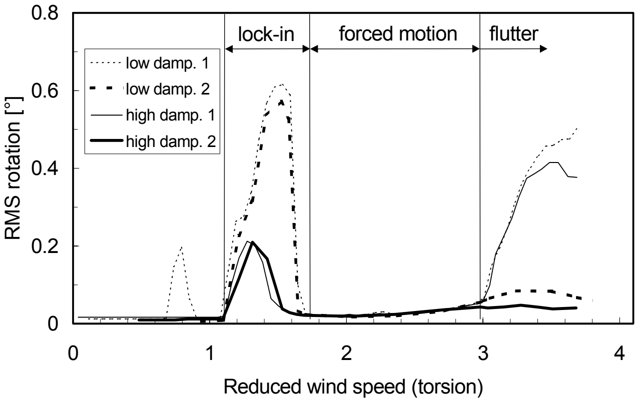

Figure 2.10 Torsional response plotted versus torsion reduced wind speed

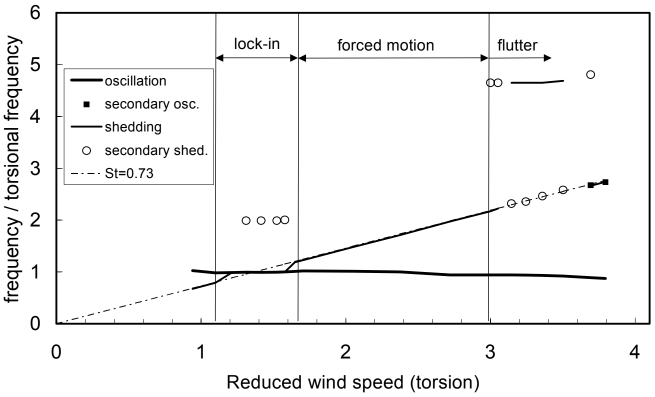

Figure 2.11 Shedding frequency and torsional vibration frequency vs. torsion reduced wind speed

torsional excitation frequency (both divided by the torsional natural frequency) are shown as a function of the torsional reduced wind speed for the low structural damping level. In the lock-in regime the torsional vibration frequency and the main excitation frequency coincide, in violation of the Strouhal law. In the forced vibration regime most of the excitation energy derives from shedding-induced forces at the Strouhal frequency. At flutter the vibration frequency reduces to 94% the value of the torsional natural frequency, suggesting that some negative stiffness is added to the system. Most of the excitation is concentrated at the constant frequency 4.6 times the torsional natural frequency, and a secondary peak exists at the Strouhal frequency. This suggests that two different mechanisms of excitation coexist, for these particular tests, one associated with the flutter behaviour and the other with vortex shedding.

From these tests the mean and RMS lift and torque coefficients were measured and compared to those obtained from the stationary tests. It was observed that only for forced motion vibration regime there is a reasonable agreement of the RMS pressure coefficient, while for the lock-in and for the flutter regimes the differences with the stationary value are quite significant.

Starting from the pressure coefficients it is possible to check the capacity of the measured aerodynamic coefficients to provide a reliable estimate of the mean deck response. In figure 2.12 the measured mean lift displacement and the mean rotation are plotted as a function of the reduced wind speed, and compared to the values calculated using the aerodynamic coefficients

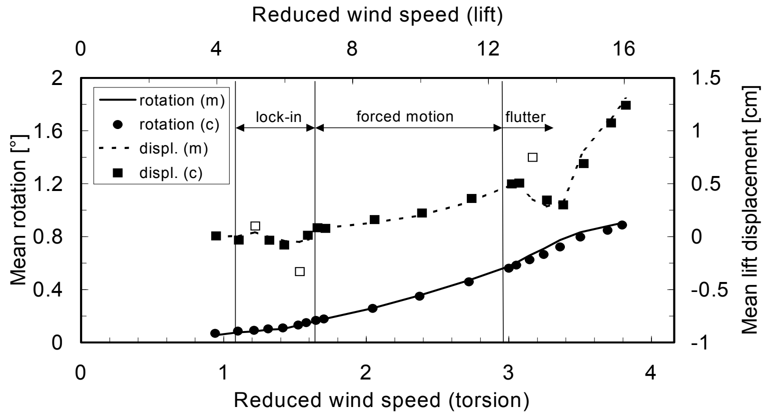

Figure 2.12 Measured response compared with calculated response

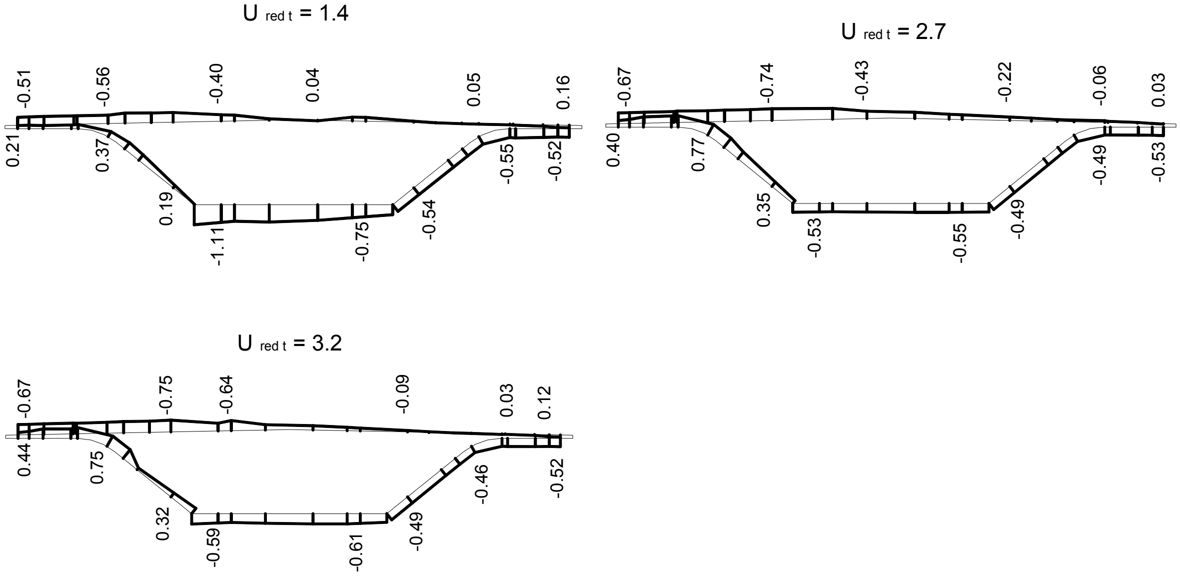

Figure 2.13 Mean pressure distributions for the three vibration regimes

measured on the vibrating deck. The agreement between the measured and the calculated response appears to be good, except for the lift displacement at the three reduced wind speed of 5.1, 6.4 and 13.7. These three points can be considered as affected by some measurement errors.

In spite of the variation of the torque coefficient with the wind speed the mean rotations in figure 2.12 can be accurately interpolated with a curve of the type cU^2, and the values of the mean torque coefficient inferred from the best fit of the measured response is 0.187, in excellent agreement with the values in the range of 0.187 to 0.189 measured on the stationary deck. However, the lift response points do not lend themselves to be interpolated with a parabola, and if one tries to predict the mean lift displacement using the lift coefficients of the stationary deck, an underestimation of the response takes place, which in the flutter regime can be as high as 2.7 times the measured values. This suggests that, as response is dominated by torsion, some degree of coupling exists between torsion and lift, which modifies the lift forces with respect to those measured on the stationary deck [2].

A procedure for the evaluation of bridge flutter derivatives was also applied to study the aeroelastic behaviour of SSB. The method used is based on the results of forced vibration wind tunnel tests on section models. Under the assumption that the total aerodynamic force is the sum of a narrow-banded self-excited component and a broad-banded buffeting component, the Least Squares Method is applied to find the values of the flutter derivatives that minimise the difference between the self-excited portion of the aerodynamic forces and the mechanical forces associated with the motion. Only two of the flutter derivatives could be identified, and more tests will be required to validate the procedure [3].

2.3.2 The use of pressure measurements for analysis of the aeroelastic behaviour of bridge decks

For a deeper understanding of the characteristics of the aerodynamic excitation, and of its dependency on the geometry and on the vibration regime, it is of use to analyse the deck pressure distribution.

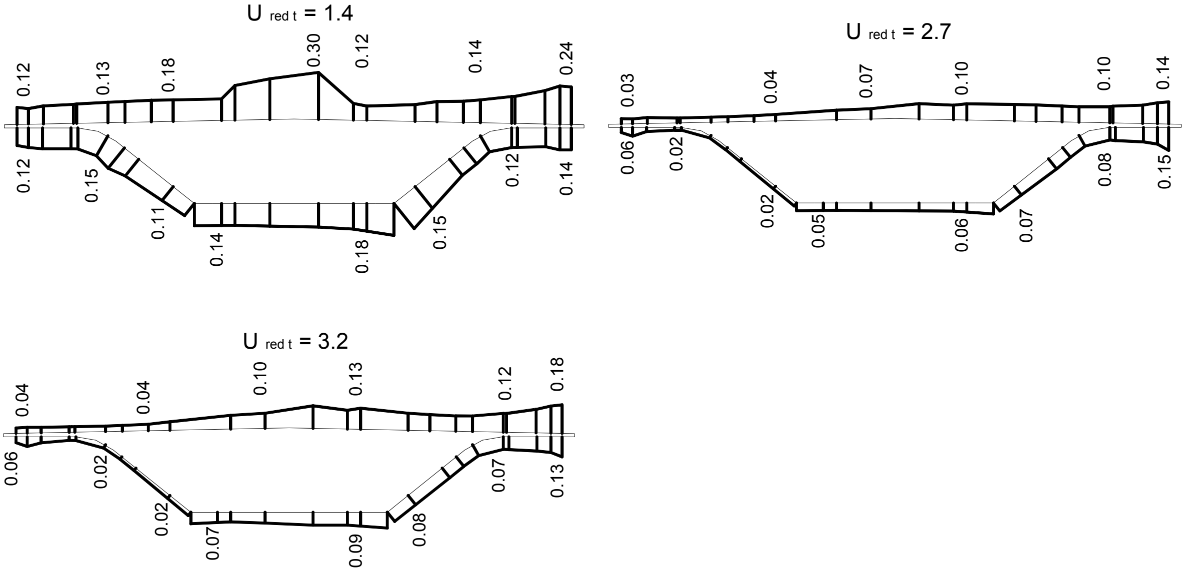

Figure 2.14 RMS pressure distributions for the three vibration regimes

The addition of the traffic barriers brings substantial modifications to both the mean and the RMS pressure distributions. In particular the addition of the traffic barriers brings to almost double the fluctuating pressure coefficients in the leeward portion of the deck, which explains the larger dynamic torsional response of the deck with barriers, with respect to the bare deck.

Even more relevant are the changes brought to both the mean and RMS pressure distributions by the deck motion. In figures 2.13 and 2.14 the mean and RMS pressure coefficients distributions on the deck provided with traffic barriers are shown, for the three reduced wind speeds of 1.4, 2.7 and 3.2, to characterise the lock-in, forced motion and flutter regimes. Both the mean and the fluctuating pressure distributions in the forced vibration regime well compare those pertaining to the stationary deck, which confirms that stationary aerodynamics can be applied in this case. However, both at lock-in and at flutter the mean and fluctuating pressure distributions are significantly different from those of the stationary deck.

At lock-in the fluctuating pressure coefficients at all locations are larger than for the stationary deck, and large pressure fluctuations are extended to the whole deck surface, as opposed to the case of the stationary deck, in which large pressure fluctuations are limited to the leeward portion of the section. In the latter case most of the torsional dynamic excitation was due to flow separation and reattachment, but at lock-in the fluctuating forces are associated with the motion, and therefore the whole deck surface contributes to the excitation. Under this circumstance the coherence between pressure fluctuations at different locations on the deck increases. But independently of the vibration regime, the coherence between pressure fluctuation and total aerodynamic torque at the vibration frequency is full. At higher frequencies the coherence is increased by the motion, but is never full. Lock-in brings also a variation of the mean pressure distribution, with values of the pressure coefficients up to 2.1 times higher than those of the stationary deck.

The effect of flutter on the pressure distributions could not be fully analysed, as pressure data for the case of the fully developed flutter are not available. However, from figures 2.13 and 2.14 it can be recognised that in the flutter wind speeds, even in the case in which flutter is not fully developed, these are differences in the mean and fluctuating pressure distributions with respect to the stationary case, with an increase of the fluctuating pressures.

The different fluctuating pressure distributions shown in figure 2.14 for the three vibration regimes are the result of different mechanisms of excitation of the deck. At lock-in most of the energy of the excitation is concentrated at the vibration frequency, and is directly associated with vortex shedding. Some other energy can be found at a frequency twice the vibration frequency, which is again associated with vortex shedding. In the forced vibration regime two different mechanisms of excitation coexist. The first is again associated with vortex shedding and is centred at the Strouhal frequency, the second is associated with the deck motion and is centred at the vibration frequency. At flutter three different excitation mechanisms can be singled out. The first is associated with vortex shedding and is centred at the Strouhal frequency, the second is associated with the deck motion and is centred at the vibration frequency, and the third is associated with the flutter mechanism and is centred at the flutter frequency [2].

2.3.3 The use of Proper Orthogonal Decomposition for the analysis of the aerodynamic and aeroelastic forces on box girder bridge decks

Understanding of the way in which the different mechanisms contribute to the excitation of the deck can be obtained through the use of Proper Orthogonal Decomposition (POD) techniques, applied to the deck pressure distributions. In particular, significant results can be obtained through the use of Covariance Proper Transformation (CPT) [c, d], [4] of the pressure fluctuations. In figure 2.15 contribution of the first six pressure covariance modes to the variance of the aerodynamic torque are shown, together with the first pressure covariance mode shapes for the vibrating deck at the reduced wind speeds of 1.4, 2.7 and 3.2. For all vibration regimes the first mode contributes with more than 60% to the total torque variance, with the other modes providing a larger or smaller contribution, depending on the vibration regime. It is significant that each mode can be associated with a particular mechanism of excitation, and that, in general, pairs of modes correspond to each mechanism, providing the in-phase and out-of-phase contribution to that particular mechanism.

At lock-in the first two modes are associated with the shedding induced excitation at the vibration frequency, and contribute with 71% to the total torque. Modes 3 and 6 are associated with the excitation at the first harmonic frequency, and contribute with 20% to the total torque. In the forced vibration regime the first two modes are associated with the shedding induced excitation at the Strouhal frequency, and contribute with 76% to the torque variance. At flutter modes 1 and 3 are associated with the flutter mechanism, and contribute with 67% to the torque variance. Modes 2 and 5 are associated with the shedding induced excitation at the Strouhal frequency, and contribute to the torque variance with 3%. Modes 4 and 6 are associated with the self-excited forces at the vibration frequency, and contribute to the total torque variance with 23%.

POD applied to the cross-spectral matrix was also used to investigate the mechanism of excitation of the bridge deck [5]. A correspondence between SPT and CPT modes is observed in some cases, if the phase shift between the components of the SPT complex modes is properly accounted for. It is also found that the frequency variation of the SPT eigenvalues is related to the characteristic frequencies of the different physical phenomena causing the pressure fluctuations.

2.4 VORTEX SHEDDING RESPONSE OF LONG-SPAN BRIDGE DECKS AND CABLES

The across-wind force due to vortex shedding from a fixed cylinder can be described as a more or less narrow band process, whose central frequency f_s is proportional to the wind U through the

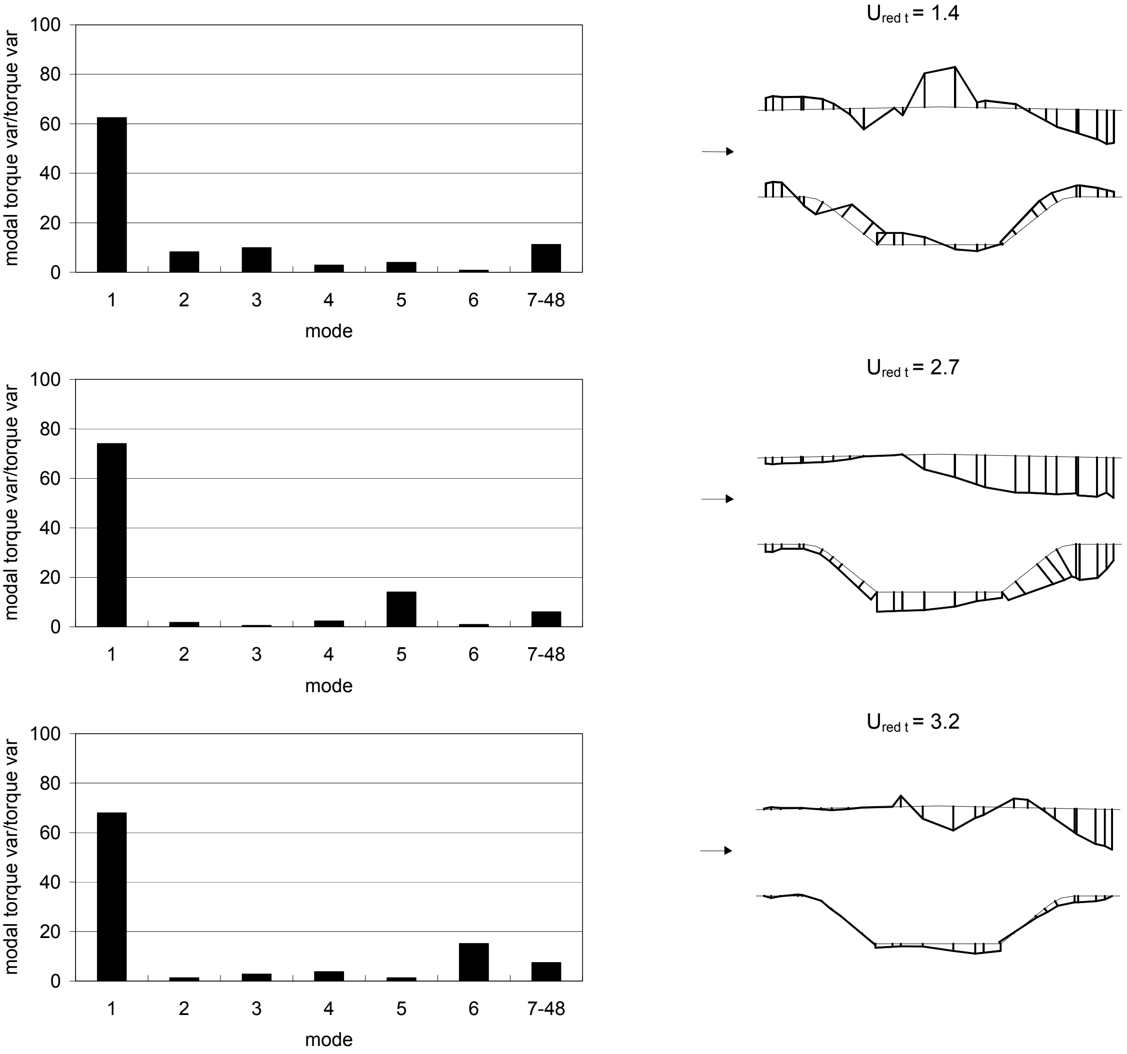

Figure 2.15 Contribution of the first six covariance modes and the first mode shape at the three vibration regime

Strouhal number *St*, which is a constant depending on the shape of the cross-section. The total force acting on a finite length of the cylinder depends on the longitudinal correlation of the sectional force, and is influenced by the turbulence of the oncoming wind. The same applies to an elastically suspended cylinder, as long as the shedding and vibration frequencies are well separated, and if the oscillation amplitude is sufficiently small.

When the shedding frequency is close to the vibration frequency, and if the structural damping is sufficiently small to allow large-amplitude oscillations (i.e., at least a few percents of the section crosswind dimension), an aeroelastic interaction between the shedding-induced forces and the structural response is observed, leading to synchronisation of the shedding to the oscillation frequency (*lock-in*). The magnitude of the across-wind forces and the amplitude of the *lock-in* wind velocity range are related to the structural response (oscillation amplitude and frequency) and, therefore, to the mechanical and aerodynamic properties of the deck.

The *lock-in* phenomenon shows a hysteretic and self-limiting behaviour, i.e., the oscillation amplitude never exceeds values in the order of the crosswind dimension of the section, also for very low values of the structural damping. A comprehensive fluid-dynamic model is not yet available in the literature, for application to a wide range of cases, although many models have been presented, which have been validated on a limited number of bluff sections [e, f, g, h,]. However, all these models require a preliminary evaluation of some characteristics of the response, among which the limiting amplitude of oscillation. Their ability to predict the maximum amplitude of the response is, therefore related to the accuracy of the parameters and the adequate description of the aeroelastic behaviour in the entire range of wind velocities. As a consequence, the structural response evalueted with the different theoretical models, may be very different, in particular for weakly damped systems.

The numerical simulations described below have been obtained through a model for the vortex-shedding induced loads, originally developed in [i] for circular cylinders and subsequently extended to other bluff bodies [*l*].

Implemented within the structural code described in Section 2.6, the proposed model is able to provide a reasonably accurate estimate of the response of slender structures to vortex shedding, including the steady-state oscillation amplitude (limit cycle). Applied to bridge decks, this procedure requires knowledge only of the aerodynamic parameters, usually available from wind-tunnel tests (Strouhal number *St*, drag coefficient C_D and vortex-shedding coefficient $C_{L\text{-}she}$), and an initial estimate of the Ω_L and Ω_U parameters, defining the lock-in frequency interval. It will be shown that, due to the intrinsic stability of the proposed loading model, even a rough estimate of these parameters (e.g. based upon results from the literature on similar sections) is enough to lead an accurate evaluation of the system response.

The model is based on the hypothesis that the vortex-induced response of an elastically suspended bluff cylinder can be dealt with as a non-linear oscillation phenomenon. A detailed description can be found in [i].

The model operates in the time domain. Its formulation schematically describes the loading of the structure through a time varying force per unit length, whose direction, frequency and phase, are functions of the relative wind velocity. The direction of the force is always perpendicular to the flow-structure relative velocity.

The lock-in phenomenon is simulated by setting the instantaneous correspondence of the excitation frequency with the oscillation frequency of the structure in a Ω_L to Ω_U range of frequencies. Outside this interval, the frequency of the force is calculated, according to the Strouhal law, as a function of the relative wind velocity. As the frequency varies, the continuity of the exciting force is ensured by a modification of its phase.

The forces acting on the cross section are shown in figure 2.16. The Δt term represents the integration time-step; the total force per unit length due to wind action at time *t* is:

$$F_w(t) = F_{she}(t) + F_{drag}(t) \tag{2.1}$$

The component due to vortex shedding at time *t* is the force $F_{she}(t)$, assumed perpendicular to the relative velocity $U_{w,rel}(t\text{-}\Delta t)$ at time $t\text{-}\Delta t$. The modulus of $F_{she}(t)$ is evaluated at time *t* as a function of the values at time $t-\Delta t$, according to the following expressions:

$$F_{she}(t) = \frac{1}{2}\rho D\ C_{L-she}\ U^2_{w,rel}(t)\sin\ (\omega_{she}(t)t\ +\ \varphi_{she}(t)) \tag{2.2}$$

$$U_{w,rel}(t) = \sqrt{U_w^2(t-\Delta t) + \dot{y}^2(t-\Delta t)} \tag{2.3}$$

$$\alpha(t) = \tan^{-1}\left(\dot{y}(t-\Delta t)\ /\ U_w(t-\Delta t)\right) \tag{2.4}$$

with:

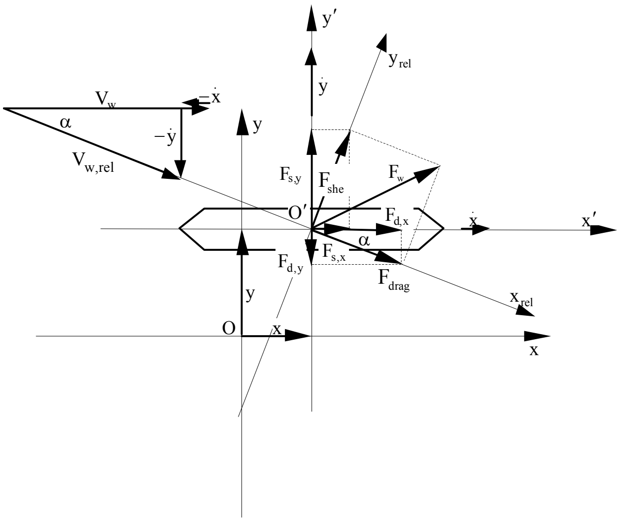

Figure 2.16 Forces acting on the cross section.

$$\omega_{St}(t) = 2\pi\, St\, \frac{U_{w,rel}(t)}{D} \tag{2.5}$$

$$\tilde{\omega}(t) = \frac{\pi}{\tau_{(y=\bar{y})_n} - \tau_{(y=\bar{y})_{n-1}}} \tag{2.6}$$

$$\begin{cases} \omega_{she}(t) = \omega_{St}(t) & \text{if} \quad \dfrac{\omega_{St}(t)}{\tilde{\omega}(t)} < \Omega_L \quad \text{or} \quad \dfrac{\omega_{St}(t)}{\tilde{\omega}(t)} > \Omega_U \\ \omega_{she}(t) = \tilde{\omega}(t) & \text{if} \quad \Omega_L \le \dfrac{\omega_{St}(t)}{\tilde{\omega}(t)} \le \Omega_U \end{cases} \tag{2.7}$$

$$\varphi_{she}(t) = [\omega_{she}(t-\Delta t) - \omega_{she}(t)]\ t + \varphi_{she}(t-\Delta t) \tag{2.8}$$

where U_w is the wind speed, y the acrosswind displacement, ρ the air density, and the dot indicates the time-derivative; $\tilde{\omega}(t)$ is the estimated value of the instantaneous circular frequency of the across-wind oscillation due to vortex shedding; $\bar{y}$ is the mean across-wind displacement of the section, while $\tau_{(y-\bar{y})n}$, $\tau_{(y-\bar{y})n-1}$ are the time instants corresponding to the last two zero-crossings of the function $(y-\bar{y})$.

The modulus of the F_{drag} component parallel to the relative wind velocity, is evaluated at time t as:

$$F_{drag}(t) = \frac{1}{2}\, \rho D\, C_D\, U^2_{w,rel}(t) \tag{2.9}$$

Figure 2.17 Great Belt Bridge (from [p])

The proposed model, when applied to the current design of the bridge on the Messina Strait Bridge [m], provided an estimate of the vertical acceleration of the deck very close to that obtained by Diana et al. [n] on the full-bridge aeroelastic model of the structure, in particular for wind speeds at deck level in the range of 10-20 m/s.

In [6] the model is applied to the Great Belt Bridge (figure 2.17). In particular, comparisons are shown with tests on a 1:80 section model reported in [o] and the full scale measurements performed by [p].

The tests on the 1:80 section model, reproducing the vertical frequency of the 8th natural mode (0.39 Hz), were carried out in the wind tunnel of the Danish Maritime Institute [o]. For a logarithmic damping δ=0.01 and for a wind speed U_w between 12 and 16 m/s, a maximum RMS value of acrosswind displacement $\eta_{max,rms} = 0.063D$ was measured, corresponding to $\eta_{max} = 0.09D$, assuming a lock-in peak factor of 1.41, D being the transverse dimension of the deck. For the same value of damping, for St=0.12 and assuming values Ω_L=1.0 and Ω_U=1.1 [i], the numerical model reproduces the measured displacement (broken line in figure 2.18) when a lift coefficient $C_{L\text{-}she}$=0.28 is used, consistent with literature values. In figure 2.18 U/U_{cr} (indicated as V/Vcr) is the ratio between the actual value of the wind speed and the value for which the Strouhal frequency coincides with the vibration frequency.

Simulations based on the value $C_{L\text{-}she}$=0.40 (closer to those suggested by Eurocode 1, part 2.4, for similar sections), are also reported in figure 2.18; in the same figure the results obtained for

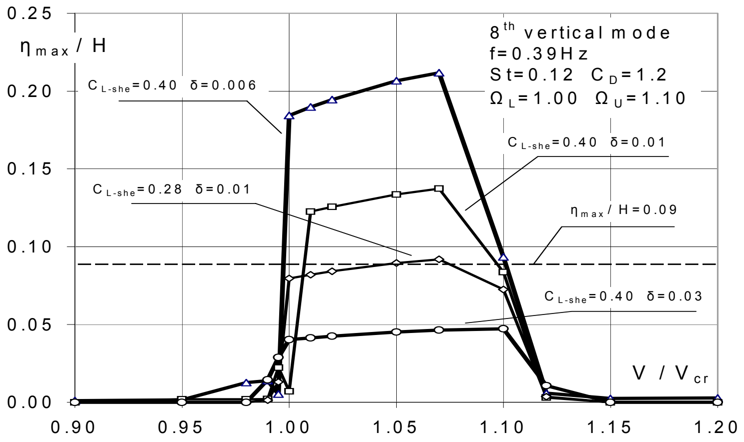

Figure 2.18 *Lock-in* curve for the 1:80 section model of the Great Belt Bridge

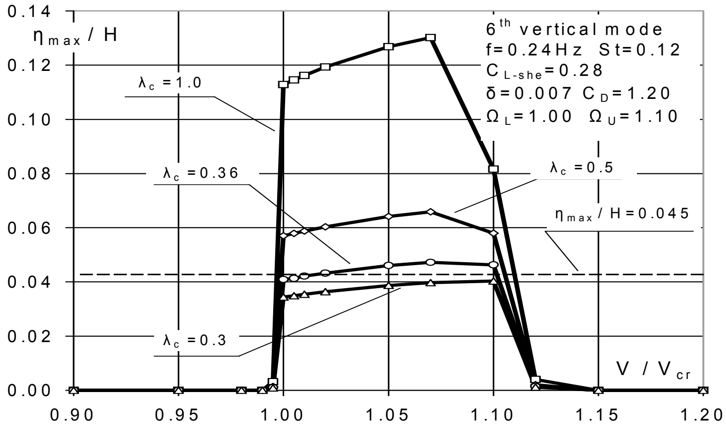

Figure 2.19 Lock-in curve for the Great Belt Bridge

different damping coefficients are plotted, for the purpose of comparison.

In consideration of the uncertainties related to the assessment of the aerodynamic parameters St, $C_{L\text{-}she}$, C_D, not reported in the quoted paper [o], the results obtained can be considered as quite satisfactory, in terms of both the maximum value of displacements and the overall shape of the lock-in curve.

The full-scale measurements reported in [p] gave maximum values of the across-wind displacements between 0.05 and 0.07 D for wind speed between 5 and 10 m/s, with longitudinal shapes corresponding to the 3th , 5th and 6th bending modes (natural frequencies of 0.13, 0.21 and 0.24 Hz).

Figure 2.19 shows the comparison between the maximum value of the measured displacement (broken line) in case of lock-in with the 6th mode and the curve, obtained for the same mode through the numerical model; a lift coefficient $C_{L\text{-}she}$=0.28, corresponding to the value identified from the section model analysis (figure 2.18), and a logarithmic damping δ=0.007 have been used. The curves refer to different values of the non-dimensional correlation length λ_c, defined as:

$$\lambda_C = \frac{l_c}{l} \tag{2.10}$$

where l is the distance between two adjacent nodes of the modal shape and l_c is the length of application of a fully correlated load ($\lambda_c \leq 1$).

Good correspondence between the numerical results and the experimental values is achieved for λ_c around 1/3, a reasonable value for this category of structures. The reliability of the proposed model is therefore confirmed.

2.5 FLUTTER MECHANISMS AND IDENTIFICATION OF THE AEROELASTIC PARAMETERS

2.5.1 Results for rectangular prisms

Several tests have been performed on rectangular sectional models, with slenderness ratios of B/D=12.5 and B/D=5, in order to evaluate the section behaviour in different flow conditions as illustrated in section 2.2. Tests were aimed at:

- evaluating flutter derivatives through free oscillations measurements of the bridge section under wind loading;
- comparing the results obtained through an eigenvalue analysis (to estimate the critical flutter speed), with those obtained from wind tunnel measurements;
- defining an aerodynamic stability performance index (ASPI), able to provide a first estimate of the behaviour of the section with respect to flutter.

In order to simultaneously measure all the flutter derivatives from section model tests, a system identification procedure CSIM [7, 8] has been developed, which estimates the values of the unsteady forces from two-DOF section model test results (coupled vertical-torsional free vibration test). The method consists in a combination of different procedures, like the ITD [q], MITD [r] and ULS [s] methods: the MITD method has been used to get initial conditions for the identification procedure, while aerodynamic derivatives have been identified by introducing an unified error function, whose minimisation allows to iteratively solve the governing set of non-linear equations. The unknowns of the problem are the system eigenvectors and eigenvalues, in a state-space representation.

Reliability, robustness, efficiency and performances of CSIM have been tested by several numerical simulations of mechanical systems in free oscillation, where to a mathematical system of known characteristic a random white Gaussian noise was added. The comparison between CSIM and ITD and MITD methods confirms that the proposed method is more efficient in retrieving the parameters; relative errors resulting from the use of CSIM are on average ten times and two times smaller than those resulting from the use of ITD and MITD, respectively.

Finally, CSIM method has been used to evaluate the flutter derivatives of the two mentioned sections; the reliability of the method have assessed through comparison with results by other authors [t, u, v].

The same identification procedure has been used in turbulent flow conditions. The effect of turbulence can be regarded as an added noise on the input signal to the system, so problems in identification are expected to occur when using any identification procedure. For this reason the output, in terms of critical wind speed using the extracted aeroelastic derivatives in the Scanlan flutter analysis theory are expected to be rather scattered (see figure 2.20 as an example of the results obtained).

The critical flutter speed U_c has then been obtained via both the classical eigenvalue analysis and directly from the model vibrations, that is by observing the wind speed at which divergent oscillations manifest themselves. In the study, three criteria to define the occurrence of U_c have been suggested:

- Coupling of Torsional and Heaving frequencies (direct measurement in the wind tunnel);
- Divergence of the free vibration in wind (direct measurement in the wind tunnel);
- Torsional RMS of 0.5° are exceeded in free vibration in wind (direct measurement in the wind tunnel).

Results have been used to define an index assessing the stability of the section, by comparing the results obtained with those arising from the flat plate theory. The theory of the Thin Airfoil or Flat Plate (FP) is an important tool in understanding the aeroelastic phenomena [x]; the comparison between the behaviour of a given section deck under wind action and the Equivalent Flat Plate (EFP), is a very useful tool in identifying whether a profile is prone to flutter or not. An Aerodynamic Stability Performance Index (ASPI) β, defined as the ratio between the critical flutter wind speed U_c of the particular section (to be estimated through wind tunnel tests) and the critical flutter wind speed for the EFP U_{fp} can then be introduced:

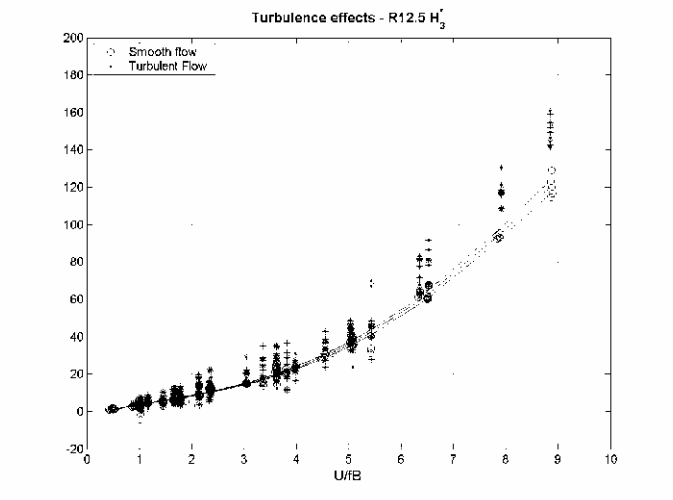

Figure 2.20 An example of flutter derivative in smooth and turbulent flow: H^*_3 values for B/D=12.5

$$\beta = \frac{U_c}{U_{fp}} \tag{2.11}$$

U_{fp} can be estimated either by the classical approach (i.e. by using Theodorsen functions) or by using one of the semi-empirical approximations available in literature (see [y]).

Knowledge of β is of use to provide a first approximation of the flutter critical speed, as a function of the geometry of the section only. The main advantages of this approach can be summarised as follow:

- the critical wind speed for the equivalent FP can be determined analytically, being its flutter derivatives expressed in an analytical form;
- the aerodynamic performance index β depends only on the geometric characteristics of the deck section, while it is independent of the other parameters characterising its dynamic response. In a preliminary design stage it is possible to estimate the critical wind speed of a given section without making provision for expensive wind tunnel tests, then looking for some refinements leading to a better performance of the bridge. Only in a later design stage, the real behaviour of the bridge can be assessed through specific wind tunnel tests, where the influence of the actual geometry can be better estimated.

At the end of the experimental campaign, a comparison has been performed between the values of the β index obtained by using the proposed criteria and that obtained through an eigenvalue analysis according to the Scanlan approach (using aeroelastic derivatives from experimental data).

Table 2.1 summarizes the main results obtained. The first two failure criteria directly applied

Cnfg	U_{div}/U_{fp}	*ASPI* -- β							
		smooth flow				turbulent flow			
		Coup.	*Div.*	*RMS*	*Eig.*	*Coup.*	*Div.*	*RMS*	*Eig.*
R12.5	1.38	0.83	0.90	0.69	0.80	N/R	N/R	0.69	N/R
R5	1.14	0.34	0.37	0.29	0.30	N/R	N/R	0.29	N/R
ratio		2.44	2.43	2.38	2.67	-	-	2.38	-

Table 2.1 Aerodynamic Stability Performance β (Coupling., Diverging oscillations, RMS: experimental values, Eig.: eigenvalue analysis)

to model oscillations subjected to smooth flow gave results which are in good agreement with those obtained through eigenvalue analysis. The criterion of observing when a given threshold in torsional amplitudes is exceeded brings conservative results, as it can be noticed from β value in smooth flow.

Moreover, in the range of reduced velocity investigated, divergent motion has never been observed in turbulent flow for the two sections analysed, even if large torsional vibrations have been detected. In the cases examined turbulence seems then to play a stabilising effect on the bridge deck.

2.6 NUMERICAL ANALYSIS OF THE WIND INDUCED RESPONSE

Time-domain methods have been addressed for the analysis of dynamic behaviour of long span bridges. In particular, the problem of aeroelastic stability has been considered in terms of numerical simulations and identification of flutter critical speed.

A linear unsteady load model has been adopted. Aeroelastic forces have been expressed with indicial functions. Wagner first [z] described the lift force arising on a wing profile due to a sudden change in the angle of attack with a special function that is referred to as indicial function. More in general, indicial theory asserts that the response of a system to an arbitrary input can be constructed by integrating a functional which involves the knowledge of the time-dependent input and a kernel response. This kernel response is a characteristic of the system. Once the kernel is known, the response of the system to an arbitrary input can always be calculated, by convolution of the kernel (the indicial function) and the input (the wind loading) to predict the output (the structural response).

The same approach can be applied, with some modifications, to bridges. Pioneering work on this subject is due to Scanlan and co-workers [aa] and to Lin and Li [ab].

The following self-excited forces (F_L represents the lift force while M_a corresponds to the aerodynamic moment) have been discussed and utilized in the model of a symmetrical cross-sectional two-dimensional system:

$$F_L(s) = \frac{\rho U^2 B}{2}\frac{dC_L(\alpha)}{d\alpha}\left[\int_{-\infty}^{s}\left(\Phi_{L\alpha}(s-\tau)\alpha'(\tau)+\Phi_{Ly}(s-\tau)\frac{y''(\tau)}{B/2}\right)d\tau\right] \tag{2.12}$$

$$M_a(s) = \frac{\rho U^2 B^2}{2}\frac{dC_M(\alpha)}{d\alpha}\left[\int_{-\infty}^{s}\left(\Phi_{M\alpha}(s-\tau)\alpha'(\tau)+\Phi_{My}(s-\tau)\frac{y''(\tau)}{B/2}\right)d\tau\right] \tag{2.13}$$

where ρ is to the air density, U the speed of the incoming wind, B the deck width, s the dimensionless time, defined as $2Ut/B$ and where the prime indicates differentiation with respect to s. The aerodynamic properties are represented by the coefficients C_L and C_M and by the four indicial functions Φ_{Ly}, $\Phi_{L\alpha}$, Φ_{My} and $\Phi_{M\alpha}$. The first subscript indicates the aeroelastic component, while the second indicates the degree of freedom (DOF) that experiences the sudden change.

A family of Wagner-like functions is accounted for:

$$\Phi(s) = a_0 - \sum_{j=1}^{n} a_j e^{-b_j s} \tag{2.14}$$

where n is the order of the Wagner-like function and specific numerical values need to be assigned to the coefficients a_0 and a_j. The a_0 coefficient is assumed equal to one in all functions and represents the quasi-steady component. All the other coefficients are obtained to match the aeroelastic derivatives, by minimising the error in the least-square sense. Both aerodynamic coefficients and indicial functions can be identified within the same procedure.

Rectangular sections have been selected, allowing comparison with available experimental results.

IF	a_1	b_1
Φ_{Ly}	0.186	0.1469
$\Phi_{L\alpha}$	1.5232	1.1933
Φ_{My}	0.0708	0.0089
$\Phi_{M\alpha}$	4.0419	14.571

Table 2.2 Indicial function coefficients for a rectangular section *B*/*D*=12.5

Different approximations of eq. (2.14) can be used. In this case the simplest form, including only one exponential group is adopted (table 2.2), and it seems to provide a good representation of experimental aeroelastic derivatives (figure 2.21).

Numerical tests have been performed, solving the dynamic problem with a fourth-order Runge-Kutta method. The experimental behaviour was well captured by time-domain simulations, in terms of amplitude and vibration frequency of the two DOFs. The flutter critical speed was slightly underestimated, but more complex indicial functions should better approximate the limit behaviour.

In general, it could be appropriate to account for the fading memory of the fluid enveloping the body, with an integration scheme that evaluates unsteady contributions only over a finite time interval, as studied in [9].

The analyses confirmed the validity of a time-domain formulation as an effective tool to capture the unsteady effects due to fluid circulation, and to estimate the time-history of the section response.

In addition, parametric analyses on a particular deck section have been performed, to analyse the influence of the indicial function coefficients [10].

Another relevant aspect of the numerical analyses is that of the evaluation of response of full (3-D) structures using Finite Elements (FE) codes. In the last ten years the TENSO code was developed [11, 12], which allows including non-linearities associated with both large displacements and mechanical behaviour. In particular the unilateral behaviour of hangers can be modelled. In addition the code allows for fluid-structure interaction, including vortex shedding.

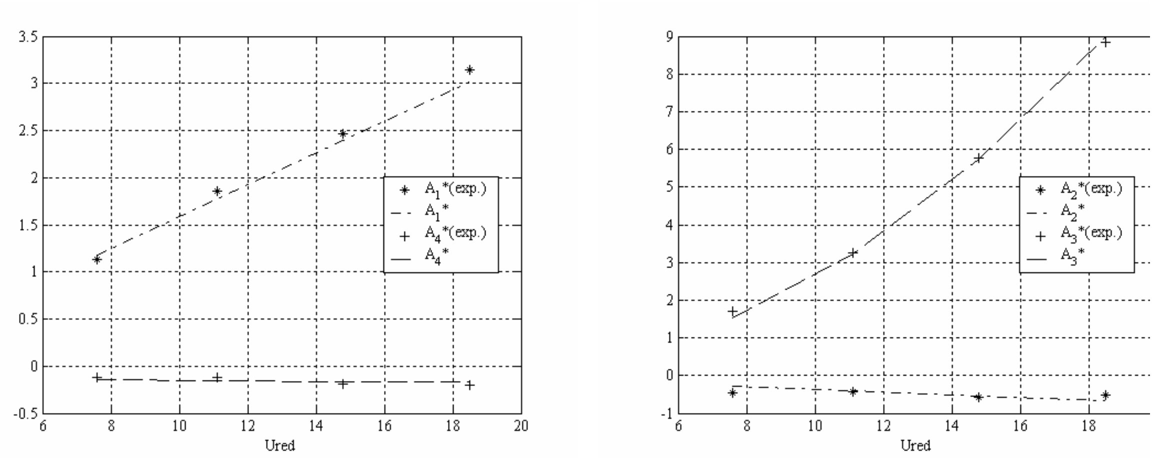

Figure 2.21 Approximation of experimental derivatives via indicial function. Left: Φ_{My}. Right: $\Phi_{M\alpha}$

The aerodynamic forces acting on the deck, towers and cables are evaluated through the static coefficients; the effective angle of attack is evaluated at each time instant by combining the effects of the wind speed, bridge deformation and motion, in accordance with the quasi-stationary approach.

Solution of the equations of motion is performed through a total Lagrangian approach by means of the Newmark step-by-step method; mechanical damping is described through the Rayleigh method, in terms of mass and stiffness matrices.

The TENSO code has been used to investigate the influence of the turbulence spectrum and coherence function on the structural response of long-span bridges. With the aim of aerodynamic and structural design, the most critical conditions, in terms of characteristics of the oncoming flow have been pointed out. The results confirm the crucial role of turbulence in the aeroelastic stability of bridge decks, and the sensitivity of the latter to the characteristics of turbulence.

A 2-DOF sectional model allows to evaluate the aeroelastic instability of long span suspension bridges taking into account the first pair of structural modes (in bending and torsion), assuming the critical wind speed as a time-averaged value, constant along the span. These assumptions are rather weak for very long spans, for which the wind field is strongly dependent on topography, and the structure dynamics is characterised by several modes with vertical, torsional and lateral components, whose frequencies are not always well separated.

In the latter case, it has been shown [ac, ad, ae] that a multimode approach to the aeroelastic instability allows to take into account all the relevant modal components with a computational effort that is only slightly larger with respect to that needed for the classical 2-DOF sectional model, whereas the evaluation of the critical wind speed and of the flutter mode is usually more accurate.

Through the multimode approach or through time domain investigations, in [11] the role of the atmospheric turbulence was investigated. Namely, while in the time domain several spectra and correlation functions have been considered, the analytical formulation based on the multimode approach assumes low-frequency wind speed fluctuations strongly correlated along the span, neglecting the beneficial effects due to a loss of coherence or to higher frequency components, and leads therefore to a safe evaluation of the flutter speed.

To describe the effects of the wind speed fluctuations on the aeroelastic stability a model has been used, that allows to distinguish between the random character of the time variation of such fluctuations at a given location on the structure and the corresponding fluctuations at the same time, at other locations; this model is appropriate for those low-frequency components (below 0.2 – 0.3 Hz) of wind speed fluctuations, that mainly affect the dynamic behaviour of the bridge deck. Such components are almost perfectly correlated even for large separations, due to the coherent structure of vorticity.

To this aim, the stochastic character of the wind speed fluctuations in a given point P of the bridge deck is described through a power spectral density $S_{uu}(\omega)$ and a random phase-lag $\vartheta(\omega)$between components at frequency ω.

Using the weighted amplitude wave superposition (WAWS), the i-th component is

$$u_i^P(t) = A_i \sin(\omega_i t + \theta_i) \tag{2.15}$$

where the amplitude A_i is related to the power spectral density around the frequency ω_i.

Given a target structure of turbulence, the spatial correlation is taken into account as follows: a deterministic phase-lag $\Omega_i\, x$ between the wind speed fluctuations in two different points with separation x is introduced for the i-th harmonic component of eq. (2.15), where Ω_i is assumed to be decreasing with decreasing frequency ω_i. In this way, the distance $\lambda_i=\pi/\Omega_i$ between two points with opposite phase-lags turns out to be increasing for decreasing ω_i, according to the physical interpretation of the low-frequency wind speed fluctuations generated by coherent vorticity.

Assuming x=0 in the reference point P, this leads to the expression

$$u_i\left(t,x\right)=A_i\sin\left(\omega_i t+\Omega_i\ x+\theta_i\right) \tag{2.16}$$

It has already been shown [af] that in such a way every point of the bridge deck has the same given power spectrum and that the wind fluctuations at any two points can be related through a chosen correlation function.

Let $\alpha(x,t)$, $h(x,t)$ be the rotation and the vertical displacement of the deck at time t and location x. In smooth flow, if the critical angular frequency ω_c, the critical wind speed U_c, the components $f_\alpha(x)$ $f_h(x)$ of the flutter mode together with their phase-lag φ are known from the classical analysis of aeroelastic instability, the structure oscillates with a given shape, behaving as a 1-DOF system, and the torsional and vertical displacements $A(t)$ and $H(t)$ are related to each other as:

$$\dot{H}\left(t\right)=\beta B\cos\varphi\,\dot{A}\left(t\right)-\beta B\omega_c\sin\varphi\,A\left(t\right) \tag{2.17}$$

where B is the deck width, and β a non-dimensional coefficient.

When the atmospheric turbulence is included in the model, the equations governing the motion can be obtained as a perturbation of the state of dynamic equilibrium, corresponding to the critical value U_c. Due to these fluctuations, the response of the system can have both an increasing or a decreasing amplitude, and the shape of the oscillation can also change with time. However, if the mean speed of the incident wind flow is slightly different from U_c, and also the fluctuation are very small, it is assumed that the shape response is close to the critical. For:

$$U(x,t)=U_c\left[1+\psi_0+\psi(x,t)\right],\qquad \psi_0<<1,\ \ \psi(x,t)<<1 \tag{2.18}$$

therefore, the motion is still described by a single scalar function, with a constant spatial shape, assumed coincident with the flutter mode. The aeroelastic torque and lift can be expressed as [12]:

$$M_{se}\left(\dot{h},\dot{\alpha},\alpha\right)=M_{se}^{(0)}+\Delta M_{se} \tag{2.19}$$

$$L_{se}\left(\dot{h},\dot{\alpha},\alpha\right)=L_{se}^{(0)}+\Delta L_{se} \tag{2.20}$$

where $M_{se}^{(0)}$, $L_{se}^{(0)}$, and $\Delta M_{se}^{(0)}$, $\Delta L_{se}^{(0)}$, are the aeroelastic actions corresponding to the critical speed U_c and to the difference U_c $[\psi_0+\psi(x,t)]$; in the formulation by Scanlan, the aeroelastic actions are expressed as a function of $\dot{h},\dot{\alpha},\alpha$ through the aeroelastic derivatives A_i^*,H_j^*.

For $\psi(x,t)$=0 each component $\alpha(x,t)$ and $h(x,t)$ satisfies the corresponding equation of motion:

$$I\ddot{A}+I\omega_c^2A=0 \tag{2.21}$$

$$m\ddot{H}+m\omega_c^2H=0 \tag{2.22}$$

with I and m generalised masses corresponding to the components $f_\alpha(x)$ and $f_h(x)$. Due to a variation of the wind speed with respect to the critical value U_c, and therefore of a variation ΔM_{se}, ΔL_{se} of the aeroelastic actions, the equations of motion become:

$$I\ddot{A}+I\omega_c^2A=\int_{span}\Delta M_{se}\left(x,t\right)f_\alpha\left(x\right)dx \tag{2.23}$$

$$m\ddot{H} + m\omega_c{}^2 H = \int\limits_{span} \Delta\, L_{se}\left(x,t\right) f_h\left(x\right) dx \tag{2.24}$$

which are dependent of each other (according to eq.(2.17)) only if a small perturbation of the wind speed is considered, as in eq. (2.18); this also allows to linearise the aeroelastic derivatives A_i^*, H_j^* around the critical value U_c.

Under this circumstance, the dynamics of the system can be described, either by eq. (2.23) or by eq. (2.24).

According to the hypotheses done on the spatial correlation of low-frequency components of turbulence, $\psi(x,t)$ in eq.(2.18) is expressed through the components:

$$\psi_i\left(x,t\right) = p_i \operatorname{sen}\left(\omega_i t + \Omega_i x + \theta_i\right) \tag{2.25}$$

It can be shown [12] that the motion is governed by a differential equation with a parametric excitation, having the coefficients of A and $\dot{A}$ depending on the wind speed. It can also be shown that the system is stable if:

$$p_i = A_i / U_c \tag{2.26}$$

The aeroelastic behaviour of the structure is influenced both by the shape of the flutter mode $f_\alpha(x)$ $f_h(x)$ and by the distance $\lambda_i = \pi / \Omega_i$ (“half-wavelength”) that is considered a known function of ω_i.

For a bridge with main span L, the flutter mode can be approximated by sinusoidal functions with n half-wavelength, here normalised as follows:

$$f_\alpha\left(x\right) = f_h\left(x\right) = \sqrt{\frac{2}{IL}} \operatorname{sen}\frac{n\pi x}{L} \qquad \Rightarrow \quad F_{\alpha\alpha} = F_{\alpha h} = 1/I \tag{2.27}$$

Eq. (2.27) describes a system with parametric excitation, with both coefficients of A and $\dot{A}$ depending on the wind speed and therefore, taking into account its time fluctuations.

The system governed by eq. (2.27) is stable if:

$$\Phi_{pp}\left(2\omega_c\right) < \frac{2I^2}{\pi^2 \rho U_c B^2} \frac{a_1^* \beta B \cos\varphi F_{\alpha h} + B a_2^* F_{\alpha\alpha}}{\left[a_1^* \beta B \cos\varphi\right]^2 + \left[B a_2^*\right]^2} \frac{\left(-\psi_0\right)}{c\left(\lambda_c\right)} \tag{2.28}$$

where a_i^* is the derivative of the aeroelastic coefficient A_i^* with respect to the reduced velocity ν, evaluated at its critical value ν_c. For a flutter mode as in eq. (2.27), $c(\lambda_c)$ in eq. (2.28) is the value corresponding to $2\omega_c$ of the function:

$$c\left(\lambda\right) = I^2\left[G_{\alpha\alpha}^2\left(\lambda,\theta\right) + H_{\alpha\alpha}^2\left(\lambda,\theta\right)\right] = I^2\left[G_{\alpha h}^2\left(\lambda,\theta\right) + H_{\alpha h}^2\left(\lambda,\theta\right)\right] \tag{2.29}$$

that turns out to have the following close form expression, independent of the phase-lag θ:

$$c\left(\lambda\right) = 32n^4 \frac{1 - \cos\dfrac{\pi L}{\lambda}}{\dfrac{\pi^2 L^2}{\lambda^2}\left(\dfrac{L^4}{\lambda^4} - 8\dfrac{L^2}{\lambda^2} n^2 + 16n^4\right)} \tag{2.30}$$

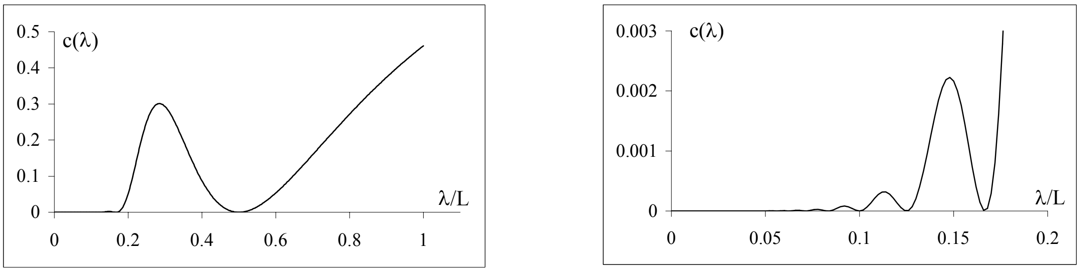

Figure 2.22 a) Coefficient $c(\lambda)$ for $n=2$; b) zoom in the range of high-frequency turbulence, where $c(\lambda)<<1$

The inequality (2.28) is satisfied only for $\Psi_0<0$. It is in fact evident that when the parametric excitation at frequency $2\omega_c$ has a non negligible energy content, i.e. $\Phi_{\eta\eta}(2\omega_c)>0$, the aeroelastic stability requires a positive damping and therefore a reduction of the mean wind speed with respect to the critical value. On the other hand, the intensity of the parametric excitation and therefore the reduction of the wind speed required to ensure stability, depends on coefficients $G_{\alpha h}$, $H_{\alpha h}$, $G_{\alpha\alpha}$ and $H_{\alpha\alpha}$, and therefore on $c(\lambda_c)$.

The maximum of $c(\lambda_c)$ amplifies the negative effect of the parametric excitation at frequency $2\omega_c$, and a reduction of wind speed required. Although not necessarily corresponding to a realistic range of wind speed fluctuations, it provides therefore an evaluation of the flutter speed that is certainly lower (and therefore on the safe side) with respect to any other possible situation. On the other hand, if the correlation length (and therefore λ) of the wind speed fluctuation at frequency $2\omega_c$ is much smaller than the bridge span, $c(\lambda)$ tends to zero; in this case, according to the proposed model of parametric excitation here, also $|\Psi_0|$ tends to zero (eq. 2.28), i.e. the aeroelastic stability is not significantly affected by the wind speed fluctuations.

However, this should also be considered as a safe result, that confirms the validity of (eq. 2.28) for preliminary design purposes. In fact when the mechanism of parametric excitation described so far can be excluded ($c(\lambda)\approx 0$), turbulence has often a stabilising effect on flutter.

As an example the Messina Strait Bridge project is considered, with a main span L=3300 metres and a multi-box deck optimised through wind tunnel tests.

The parameters that appear in the stability condition (eq. 2.28) are [12]:

$$B=60.4\,\text{m},\quad I=2.8\cdot 10^7\ \text{kgm}^2/\text{m},\quad U_c=94\,\text{m/s},\ \omega_c=0.418\ \text{rad/s}$$

$$n=2\ ,\ \beta=2.33\ ,\ \varphi=59.9^\circ\ ,\ a_1^*=1.38\ ,\quad a_2^*=1.16\ ,\ \rho=1.25\ \text{kg/m}^3$$

The coefficient $c(\lambda)$, that can be expressed in general in the closed form of eq. (2.30), is plotted in figure 2.22, for the value $n=2$ of the example.

Let denote by λ_c the distance between two zeroes of the component of the wind speed fluctuation with angular frequency around $2\omega_c$. Excluding on a physical basis the cases $\lambda_c/L>0.5$ (that for the value of L considered would imply $\lambda_c > 1500$ m), it can be observed from figure 2.22 that broad-band wind speed fluctuations, of the kind considered, can be relevant only in case that to the component with frequency close to $2\omega_c$ values of λ_c/L correspond, in the range of 0.2 to 0.4. In the example considered (ω_c=0.418 rad/s), L=3300 m), therefore, the only relevant components are those with λ_c larger than about 600 m, a value in agreement with the correlation curve of Saul.

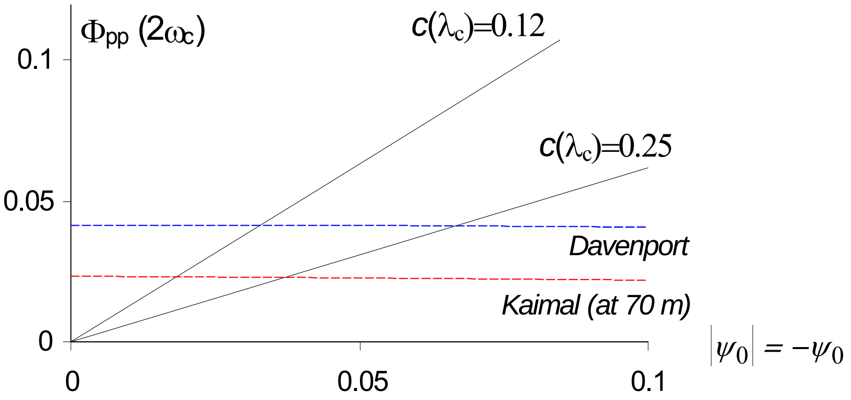

Figure 2.23 Upper limit of the stable behaviour in the $\Phi_{pp}(2\omega_c)$ vs. $|\Psi_0|$ plane for two different values of $c(\lambda_c)$ (Φ_{pp} in seconds).

Once the value of $c(\lambda_c)$ has been obtained, the stability condition of eq. (2.28) gives a linear relationship between the PSD of the non-dimensional wind speed fluctuation $\Phi_{pp}(2\omega_c)$ and the reduction Ψ_0 of the mean wind speed with respect to U_c; this relationship, providing an upper bound to the regions Φ_{pp} *vs.* Ψ_0 where the oscillations is asymptotically stable, is reported in figure 2.23 for two different values of $c(\lambda_c)$, corresponding to the worst and to the average situation in the interval of interest for λ (figure 2.22).

It is also clear from figure 2.22b that the wind speed fluctuation with higher frequency, characterised by $\lambda/L<0.2$, produces negligible effects on the aeroelastic stability ($c(\lambda)<<1$).

As a comparison with the closed form evaluation of the flutter wind speed, a numerical investigation in the time-domain has been performed by means of a FEM non-linear model of the Messina Strait bridge, with time histories generated through the weighted amplitude wave superposition (WAWS) and genetic algorithms [af].

The power spectral density of Davenport and that of Eurocode 1 have been considered, together with the correlation functions of Eurocode 1 and Saul. To underline the role of wind speed fluctuations with frequency around $2\omega_c$, that the closed form approach indicated as the most relevant on the aeroelastic behaviour, also time histories were generated taking into account only the power spectral density in the range 0.10 e 0.16 Hz (referred to as “partial spectrum”).

To separate the effects of the choice of the spectrum from those of the choice of the correlation function, the Davenport spectrum has been used not only in combination with the Davenport correlation (denoted with *Dd* and *Dd_p*, for the complete and partial spectrum, respectively) but also in combination with the Saul correlation function (denoted by *Ds* and *Ds_p*); similarly, the Eurocode 1 spectrum, either complete or partial, has been considered not only in combination with the Eurocode 1 correlation (*Ee* and *Ee_p*), but also in combination with the Saul correlation (*Es* and *Es_p*); in this way, eight combination were obtained, together with the smooth flow analysis (denoted by *lf*).

A reference mean wind speed of 94 m/s was assumed, corresponding to the instability limit for the numerical model, that diverges only after 1500 seconds or more.

Figure 2.24 shows a record of the time histories (corresponding to the beginning of the unstable behaviour) of the total energy for the nine cases described. The higher the total energy at a given time, the faster the trend to an unstable behaviour.

The effect of turbulence seems to be almost negligible, which confirms the excellent aerodynamic characteristics of the deck, accordingly with the analogous (and safe) evaluation already obtained in a closed form.

The numerical investigation performed, allow to draw some conclusions on the role of turbulence spectrum and of the coherence function. Depending on the correlation function, the Eurocode 1 spectrum can induce a worse behaviour, with respect to the aeroelastic instability, in comparison with the smooth flow case, while the Davenport spectrum usually implies a more stable behaviour. On the other hand, the role of correlation does not show a systematic trend, turning out to be relevant only for the time-histories based on the Eurocode 1 spectrum. The numerical results also show that using only a part of the spectrum (dashed lines in figure 2.24) produces smaller effects, either positive or negative, with respect to the complete spectrum; however, this is not in contrast with the other results, because in the closed form approach previously described the worst (although not realistic) possible correlation was assumed, and therefore on the safe side with respect to the (realistic) correlation functions used to generate the time-histories.

2.7 CONTROL OF THE WIND INDUCED RESPONSE

After the collapse of the Tacoma Narrows Bridge in 1940 it was recognized that wind stability is one of the most important design criteria for long-span bridges. The new Tacoma Bridge employed a deep truss girder, extremely rigid against wind instabilities. The deeper truss girder exhibits higher drag forces, if compared to box girders and so in the 1960s the concept of the shallow box-girder was introduces by Roberts in the construction of the Severn Bridge in England. The drawback of box-girder is the wind instability for spans longer than 2000 m. Among the several alternatives proposed in the next years, the multi-box cross section has been employed for the proposed 3300 m-span suspension bridge crossing the Messina Strait.

Two possibilities exist to control flutter instability of long span bridges. Via conventional design one can increase the torsional stiffness of the structure through modification in the cable stiffening system, or by modifying the aerodynamics. In the latter case, the common way to improve bridge behaviour is to change the section details (figure 2.25). For example, changing the solid parapet to a semi-porous parapet, or making venting slots on the bridge deck may

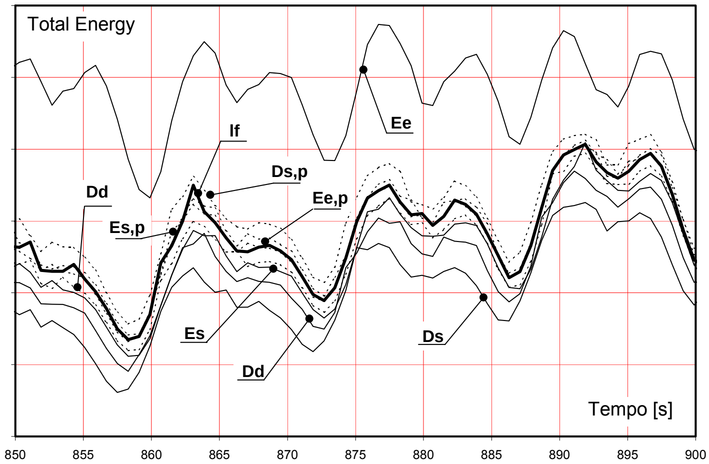

Figure 2.24 Time-histories of the total energy for different turbulence spectra and correlation functions

Figure 2.25 Typical aerodynamic modifications

significantly improve the aerodynamic behaviour. The other possibility is to employ structural control strategies, that allow the modification of wind loads acting on a bridge through auxiliary control devices. Among the different techniques employed is the addition of eccentric tuned mass dampers (TMDs) or of aerodynamic appendages. TMDs add damping to the structure as they modify structural properties of the bridge, conversely aerodynamic appendages modify the loads acting on the bridge through the modification of the aerodynamic behaviour of the deck.

To control flutter of long span bridges two eccentric tuned mass dampers can be used, placed at the two sides of the cross section of the deck, in order to passively control both vertical and torsional motion (figure 2.26). A formulation of the model accounting for the effect of TMDs and/or Active Tuned Mass Dampers (ATMDs) was proposed in [13]. An ATMD is a passive device to which a servo actuator is added. The basic principle of the ATMD control law is the feedback, as used in the modern control theory.

The drawbacks of this technique are an increase in the mass at mid span, and the need for a large space to accommodate the TMD stroke during strong winds.

The aerodynamic control of bridge flutter via aerodynamic appendages seems a better alternative to the use of mass dampers. The passive aerodynamic control was first proposed in [ag] by the addition of flaps eccentrically positioned to the deck section. The presence of these winglets modify the aeroelastic loads acting on the deck increasing the flutter critical velocity.

A schematic of the different layout of the passive aerodynamic appendages used on bridge decks are presented in figure 2.27. In case 3 the positioning of the winglet is modified by hand, while case 4 incorporates actively controlled movements of the winglets. In the latter case a number of sensors are placed inside the bridge girder to continuously measure the bridge response, the measurements are then processed by a control unit that regulate the motion of the flaps following the information obtained by a chosen control algorithm.

Usually, the flaps are positioned in several sections along the bridge span length and each of them can driven independently of the others.

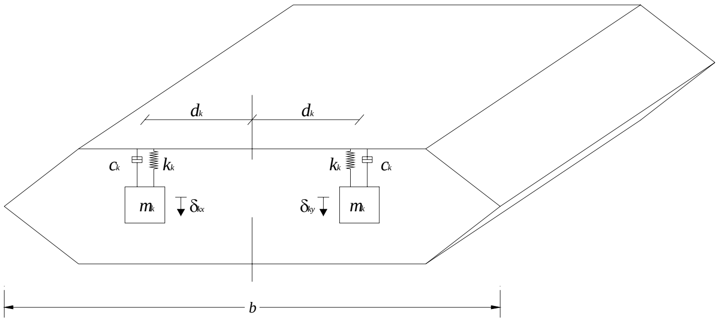

Figure 2.26 Schematic of a bridge section with two eccentric TMDs

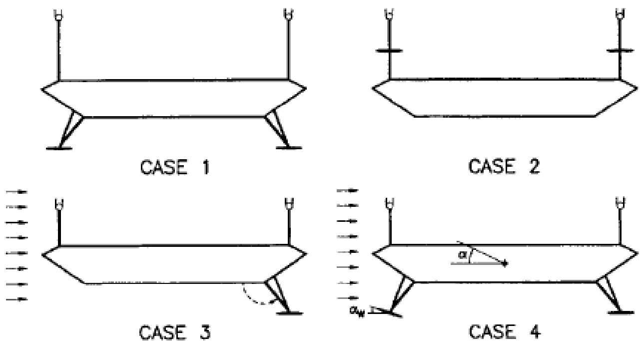

Figure 2.27 Schematic of different using of aerodynamic appendages (from [al])

Another proposed passive control system [ah] consists of auxiliary flaps attached directly to the bridge deck through a preloaded spring. When the deck undergoes pitching motion or relative horizontal motion with respect to the main cables, control flap rotation is governed by additional control cables taut between the control flaps and an auxiliary transverse beam supported by the main cables of the bridge. Since the control cables can only pull the flaps but not push them, additional preloaded springs are used to reverse the motion of the control surfaces (figure 2.28).

Ostenfeld and Larsen [ai] first proposed to ensure the aerodynamic stability of slender girder through actively controlled flaps, in both versions of figure 2.27, case 4 and as integrated parts of the bridge girder. Both proposals are sketched in figure 2.29.

When the flaps are exposed to the wind they exert forces on the bridge girder. Regulating the flaps can control the directions and sizes of the forces. By providing forces, which counteract the motion of the girder the oscillations are damped. The loads due to movement of a trailing flap are linear in the angle of the trailing flap and in the first and second derivatives. By assuming that the angle of a leading flap has no effect on the circulation it can be shown that the loads due to movement of a leading flap are also linear in the angle of the leading flap and the first and second derivatives. The motion-induced wind loads due to movement of the flaps can therefore be described accounting additional flutter derivatives for lift and pitching moment.

The conclusion that could be obtained are that the flap control system are very efficient to limit the vibrations, that long flaps are more efficient than short flaps, that trailing flaps are more

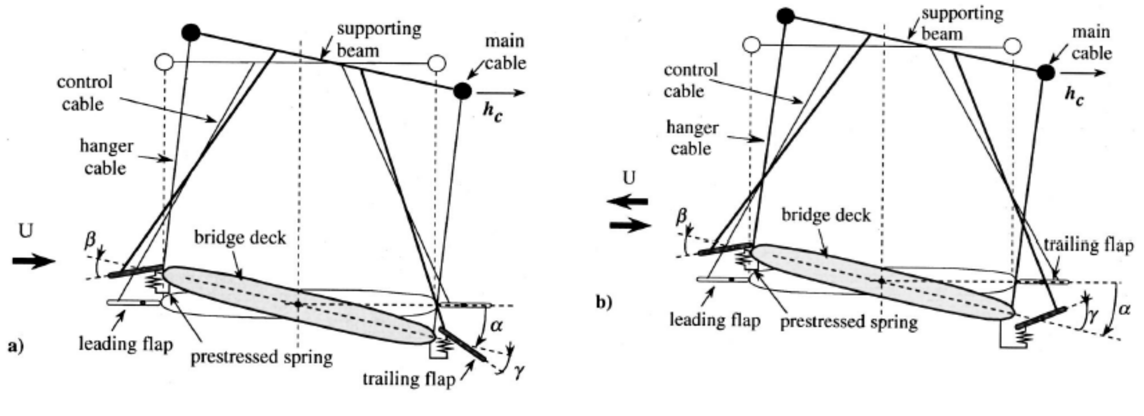

Figure 2.28 Passive aerodynamic control of bridge: a) asymmetric cable connection system; b) symmetric cable connection system (from [ah])

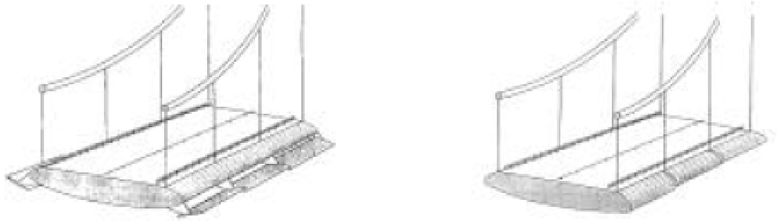

Figure 2.29 Sections with flaps on pylons and integrated in the section (from am])

efficient than leading flaps. A recommendation is to implement a robust control algorithm, a control technique that accounts for model errors and delay in control action. It is very important to ensure that flaps are regulated as specified in control law otherwise flutter wind velocity can be decreased by unfavourable flaps position.

2.8 BASIC REFERENCES

[a] Larsen A. 1992. *Aerodynamics of Large Bridge.,* A. Larsen (ed.), Balkema, Rotterdam

[b] Stansby P.K. 1975. The Effects of End-Plates on the Base Pressure Coefficient on a Circular Cylinder. *Aeronautical Journal*, January

[c] Solari G., Carassale L. 2000. Modal transformation tools in structural dynamics and wind engineering. *Wind and Structures,* **3**(4), 221-241

[d] Baker C. 2000. Aspect of the use of proper orthogonal decomposition of surface pressure fields. *Wind and Structures*, **3**(2), 97-115

[e] Simiu E., Scanlan R.H. 1986. *Wind effects on structures*. 2nd ed., Wiley Interscience

[f] Scanlan, R.H. 1998. Bridge flutter derivatives at vortex lock-in. *J. Struct. Eng. ASCE*, **124**(4), 450-458

[g] Goswami I., Scanlan R.H., Jones N.P. 1992. Vortex shedding from circular cylinders: experimental data and a new model. *J. Wind Eng. Ind. Aero.,* **41-44**, 763-774

[h] Ruscheweyh H., 1994. Vortex excited vibrations. in Sockel H. (ed.), *Wind excited vibrations of structures*, Springer-Verlag, New York, 51-87

[i] D'Asdia P., Noè S. 1998. Vortex induced vibration of reinforced concrete chimneys: in situ experimentation and numerical previsions. *J. Wind Eng. Ind. Aero.*, **74-76**, 765-776

[l] Caracoglia L. 2000. *Wind-structure oscillations on long-span suspension bridges*. Ph.D. Dissertation, University of Trieste, Italy

[m] Caracoglia L., Noè S., Sepe V. 2000. Aspetti non convenzionali della dinamica indotta dal vento nei ponti sospesi di grande luce. *IN-VENTO-2000*, 6th Italian Nat. Conf. Wind Eng., Genova, (in Italian)

[n] Diana G., Falco M., Bruni S., Cigada A., Larose G.L., Damsgaard A., Collina A. 1995. Comparisons between wind tunnel tests on a full aeroelastic model of the proposed bridge over Stretto di Messina and numerical results. *J. Wind Eng. Ind. Aero.*, **54-55**, 101-113

[o] Larsen A. 1993. Aerodynamic aspects of the final design of the 1624 m suspension bridge across the Great Belt. *J. Wind Eng. Ind. Aero.*, **48**, 261-285.

[p] Larsen A., Esdahl S., Andersen, J.E. & Vejrum, T. 2000. Storebalt suspension bridge - vortex shedding excitation and mitigation by guide vanes. *J. Wind Eng. Ind. Aero.*, **88**, 283-296

[q] Ibrahim S. R., Mikulcik E. C. 1977. A method for the direct identification vibration parameters from the free response. *The shock and Vibration Bull.*, **47** (Part. 4)

[r] Sarkar P., Jones N., Scanlan R.H. 1994. Identification of aeroelastic parameters of flexible bridges. *ASCE J. Engrg. Mech.*, **120**(8), 1718-1743

[s] Gu M., Zhang R.X., Xiang H.F. 2000. Identification of flutter derivatives of bridge decks. *J. Wind Eng. Ind. Aero.*, **84**, 151-162

[t] Matsumoto M. 1996. Aerodynamic damping of prisms. *J. Wind Eng. Ind. Aero..*, **59**, 159-175

[u] Matsumoto M., Kobayashi Y., Shirato H. 1996. The influence of aerodynamic derivatives on flutter. *J. Wind Eng. Ind. Aero.*, **60**, 227-239

[v] Matsumoto M., Daito Y., Yoshizumi F., Ichikawa Y., Yabutani T. 1997. Torsional flutter on bluff bodies. *J. Wind Eng. Ind. Aero.*, **69**, 871-882

[x] Frandsen A.G. 1966. Wind stability of suspension bridges Application of theory of ‘thin airfoils’. *Proc. Int. Symposium on Suspension Bridges*, Lisbon

[y] Gimsing N. J. 1996. *Cable Supported Bridges-Concept and Design*. 2nd edition, John Wiley and Sons, New York

[z] Wagner H. 1925. Über die Entstehung des dynamischen Auftriebes von Tagflügeln. *Z. Angew. Math. Mech.* Bd. 5-Helft 1.

[aa] Scanlan R.H., Béliveau J., Budlong K.S. 1974. Indicial aerodynamic functions for bridge decks. *ASCE J. Engrg. Mech.*, **100**(4), 657-670

[ab] Lin Y.K., Li Q.C. 1993. New stochastic theory for bridge stability in turbulent flow. *J. Engrg. Mech.,* **119**(1), 113-127.

[ac] Jain A.; Jones N.P. and Scanlan R.H., 1996. Coupled aeroelastic and aerodynamic response analysis of long-span bridges, *J. Wind Eng. Ind. Aero.*, **60**, 69-80

[ad] D'Asdia P. and V.Sepe, 1998. Aeroelastic instability of long span suspended bridges:a multi-mode approach. *J. Wind Eng. Ind. Aero.,* **74-76**, 849-857

[ae] Sepe V., Caracoglia L., D’Asdia P., 2000. Aeroelastic instability of long-span bridges: contributions to the analysis in frequency and time domains. *Wind and Structures*, **3**(1), 41-58

[af] Fathi S., Noè S., Viskovic A. 2000. Applicazione di algoritmi genetici alla generazione di storie di vento con il metodo dello sfasamento. *IN-VENTO-2000*, 6th Italian Nat. Conf. Wind Eng., Genova, (in Italian)

[ag] Ragget J.D. 1987. Stabilizing pair of winglets for slender bridge decks. Bridges and transmission line structures. *6th Struct. Congr. Of ASCE*, New York, 292-302

[ah] Omenzetter P., Wilde K., Fujino Y. 2002. Study of Passive Deck-Flaps Flutter Control System on Full Bridge Model. I: Theory. *J. Eng. Mech. ASCE*, **128**(1), 80-89

[ai] Ostenfeld, K.H., Larsen A. 1992. Bridge Engineering and Aerodynamics. In *Aerodynamics of Large Bridges* (A. Larsen ed.), First Int. Symp. Aerodynamics of Large Bridges, Copenhagen, Denmark

[al] Cobo Del Arco D., Aparicio A.C. 1999. Improving Suspension Bridge Stability with Aerodynamic Appendages. *J. Struct. Eng. ASCE.*, **125**(12), 1367-1375

[am] Thoft-Christensen P. 2001. Active Control of Suspension Bridges. Report *Aalborg University, Denmark*

2.9 LIST OF PUBLICATIONS

[1] Ricciardelli F., de Grenet E.T., Hangan H. 2002. Pressure distribution, aerodynamic forces and dynamic response of box bridge sections. *J. Wind Eng. Ind. Aero.,* **90**(10), 1135-1150

[2] Ricciardelli F. 2003. On the wind loading mechanism of long-span bridge deck box sections. *J. Wind Eng. Ind. Aero.*, **91**(12-15), 1411-1430

[3] Ricciardelli F., de Grenet E.T. 2002. A technique for the evaluation of bridge flutter derivatives from the wind excited vibration of section models. *Eurodyn 2002*, 5th European Conf. Struct. Dyn., Munchen

[4] Ricciardelli F., de Grenet E.T., Solari G. 2003. Analysis of the wind loading of a bridge deck box section using Proper Orthogonal Decomposition. *J. Fluid Mech. Res*., **29**(3-4), 312-322

[5] de Grenet E. T., Ricciardelli F. Spectral Proper Transformation of wind pressure fluctuations: application to a square cylinder and a bridge deck. to appear, *J. Wind Eng. Ind. Aero*.

[6] D'Asdia P, Sepe V., Caracoglia L, Noé S. 2003. A model for vortex-shedding induced oscillations of long-span bridges. *ISEC-02 - 2nd Int. Struct. Eng. and Construction Conf.*, **3**; 2029-2035;

[7] Righi M. 2003. Aeroelastic Stability of Long Span Suspended Bridges: Flutter Mechanism on Rectangular Cylinders in Smooth and Turbulent Flow. *PhD dissertation, University of Florence*, Florence, Italy

[8] Contri S. 2003. Il flutter negli impalcati da ponte: identificazione delle derivate aeroelastiche in galleria del vento. Master thesis dissertation, University of Florence, Italy (in Italian)

[9] Borri C., Costa C., Zahlten W. 2002. Nonstationary flow forces for the numerical simulation of aeroelastic instability of bridge decks. *Computers & Structures*, **80**, 1071-1079

[10] Borri C., Costa C. 2003. A parametric study of an indicial function model in bridge deck aeroelasticity. XVI Congresso Nazionale AIMeTA, University of Ferrara, **1**, 198

[11] D'Asdia P., Noé S., Sepe V., Viskovic A. 2002. Recent developments of the techniques to evaluate the aeroelastic stability of long span suspension bridges. IN-VENTO-2002, 7th Italian Nat. Conf. Wind Eng., Milano, (in Italian)

[12] Sepe V., D'Asdia P. 2003. Influence of low-frequency wind speed fluctuations on the aeroelastic stability of suspension bridges. *J. Wind Eng. Ind. Aero.*, **91** 1285-1297

[13] Mattei M. and Ricciardelli F. (2002). A Mathematical Model for the Design of Mass Dampers for Wind Excited Structures. *J. Eng. Mech. ASCE*; **128**(9), 979-988

WITH CONTRIBUTIONS FROM:

Gianni Bartoli, Università degli Studi di Firenze
Claudio Borri, Università degli Studi di Firenze
Carlotta Costa, Università degli Studi di Firenze
Piero D'Asdia, Università degli Studi "G. D'Annunzio" di Chieti-Pescara
Enrico T. de Grenet, Università degli Studi di Firenze
Salim Fathi, Università degli Studi di Trieste
A. David Pizzimenti, Università "Mediterranea" di Reggio Calabria
Michele Righi, Università degli Studi di Firenze
Vincenzo Sepe, Università degli Studi "G. D'Annunzio" di Chieti-Pescara
Alberto Viskovic, Università degli Studi "G. D'Annunzio" di Chieti-Pescara

3 Cooling towers

Gianni Bartoli
University of Firenze

3.1. INTRODUCTION

Natural draught cooling towers are high-rise structure mainly designed as thin hyperboloid reinforced-concrete shells with upper and lower stiffening rings, and hold up along the base circumference by a system of columns. Normally, the prevalent load is induced by the turbulent wind which produce quasi-static (background) and resonance responses. The proportion of resonance response depends on wind speed, determining the band width of exciting frequencies, and on the dimension and the natural frequencies of the towers. As for the increasing capacity of power plant it has been necessary to increase both the height and the diameter of cooling towers, so the aeolian risk of these structures, whose response to fluctuating wind has been previously taken into account by a gust response factor reproducing only the background peak responses, has been consequently amplified. The resonance response, in fact, assumed a significant role in defining design wind loads, increasing the computational efforts in the still complex design practices. The additional difficulties derived from the stochastic characterization of the resonance response, in time or frequency domain, necessary to well establish the dynamic behavior of the towers.

Since 40 years ago, the random process theory into wind loading ([b], [c] and [d]), has been an important key in the physical understanding of wind loading and its effects. The theory allows the estimation of expected peak values of wind-induced load effects and responses, whether or not significant resonant dynamic response is involved. However, such computations can be rather complex even when only a few load effects have to be evaluated. In fact, since its turbulence, the wind pressure field over structural surface should be understood like a multidimensional stochastic process, more or less correlated in time and space. So, the dynamic response is a stochastic process whose calculation depends on the complicated multiple random excitation of fluctuating wind. An alternative approach deals with the definition of wind loads in the form of the equivalent, or effective, static load distributions, which produce the peak load effects, rather than the local load effects themselves. Such an approach holds considerable attraction to structural engineering practices, since it lets to thin computational efforts in evaluating wind-induced load effects in quasi-static (background) or dynamic field.

The present report shows the main results obtained by several analyses performed during the last years on a RC cooling tower, one of the two towers located at the ENEL (Italian Agency for

Edited by Gianni Bartoli and Francesco Ricciardelli, WINDERFUL: Wind and INfrastructures: Dominating Eolian Risk
For Utilities and Lifelines, ISBN 88-8453-138-1, ©2004 Firenze University Press

Figure 3.1 Investigated tower, located at the ENEL power plant in Cavriglia (Arezzo, Italy)

Electricity Supply) power plant in Cavriglia (Arezzo, Italy), see Figure 3.1. Analyses have dealt with the assessment of design wind loads acting on cooling tower shells under turbulent wind; comparison among several methods ([g], [h], [i], [j], [k], [m], [n]) has been performed by using measurement data obtained from wind tunnel tests on an isolated cooling tower shell.

The tower under investigation has a height of 80.50 m, a throat diameter of 36.00 m and a basement diameter of 61.94 m, already studied in previous experimental campaigns ([1], [2], [4], [5], [7]).

3.2. DESIGN WIND LOADS MODELING

During the 60s, the GRF approach was introduced ([c], [r], [s]). This method involves the calculation of a Gust-Response-Factor (GRF) to be applied to the mean structural response, in order to get its peak value. The GRF is defined as the ratio between the peak response and the mean one. The equivalent static wind load, $\mathbf{P}_{eq}$, for the background response may be written as follows:

$$\mathbf{P}_{eq} = \mathrm{GRF} \cdot \overline{\mathbf{P}} \tag{3.1}$$

where $\overline{\mathbf{P}}$ is the mean load. The approach may include both background and resonant dynamic effects. The latter may be taken into account by means of a Resonance Factor (RF) defined as the ratio of the resonant peak response to the background one. So, for the total response the previous formulation may be rewritten as follows:

$$\mathbf{P}_{eq} = \mathrm{GRF} \cdot \mathrm{RF} \cdot \overline{\mathbf{P}} \tag{3.2}$$

The implication of this approach is that the effective static load distribution corresponding to the maximum response has the same shape as the mean wind load distribution.

This assumption may be acceptable for those type of structures for which the quasi-steady theory in aerodynamics is valid, and for simple cantilevered structures, often giving results which are adequate compared to code and standard recommendations. However, it can give quite confusing results for structures showing unusual influence lines, especially with sign reversal. The method is based on the hypothesis of coincident peak responses distributions, whose extreme value is involved in defining the gust-response-factor and then in the design wind load. The application of this load pattern may result in a non conservative design when the minima of the wind loads somewhere of the structures are more critical for a considered response.

Recently, a new approach called Load Response Correlation (LRC) has been introduced. It allows to quantify peak load distributions taking into account the components of the fluctuating wind which actually contribute to maximize or minimize a given structural response in quasi-static field ([j], [k]). The method is based on the definition of the correlation coefficient between the fluctuating wind pressures and the relevant load effect. Unlike the GRF method, the LRC approach gives results even for zero mean response. The main advantage of this method is the physical meaning of the load patterns to be understood as a really occurring distributions. Since the correlation analysis fades all components of the fluctuating load which do not contribute to maximize (or minimize) a certain response, a deeper understanding of load effects becomes possible. It enables the expected effective static load distributions for the background, or quasi-static, fluctuating wind loads to be formulated on a sound theoretical basis.

The expressions of the LRC method which maximize (or minimize) a given response S_i (an internal force, an internal stress, a displacement, and so on) are:

$$S_i = \sum_k \eta_{ik} \cdot [\overline{P}_k + g \cdot \rho_{S_i P_k} \cdot \sigma_{P_k}] \qquad \rho_{S_i P_k} = \frac{\sum_j \eta_{ij} \cdot \sigma^2_{P_k P_j}}{\sigma_{S_i} \cdot \sigma_{P_k}} \tag{3.3}$$

where η_{ik} are the influence coefficients, $\overline{P}_k$ and σ_{P_k} respectively the mean value and the standard deviation of the k-th load, g is the peak factor (usually assumed constant and equal to 4 [j], [k]), $\rho_{S_i P_k}$ is the correlation coefficient between P_k and S_i, and σ_{S_i} is the standard deviation of response S_i. The η_{ik} influence coefficient is defined as the contribution to the response S_i due to an unitary load P_k at location k. The quantity:

$$P_{ik,eq} = \overline{P}_k + g \cdot \rho_{S_i P_k} \cdot \sigma_{P_k} \tag{3.4}$$

is the k-th component of the equivalent static load associated to the extreme value of the concerned load effect, S_i.

This approach was later developed by Holmes [h] to incorporate proper orthogonal decomposition (POD) of fluctuating pressure fields, showing that the contribution to the total effective static load distribution of a POD mode, for background response, is also dependent on the similarity with the influence line. More precisely, using the expansion of the fluctuating pressures in terms of the eigenvectors of the covariance matrix it's possible to optimize the peak load distribution defined by the LRC method ([h]). Holmes showed that:

$$g \cdot \rho_{S_i P_k} \cdot \sigma_{P_k} = \sqrt{\sum_{n=1}^{N} \alpha_n^2 (\hat{\pi}_n - \overline{\pi}_n)^2} \cdot \left(\sum_{n=1}^{N} \alpha_n e_{k,n} \omega_n \right) \Big/ \left(\sum_{n=1}^{N} \alpha_n^2 \omega_n \right) \qquad \alpha_n = \sum_{i=1}^{N} e_{i,n} \eta_i \tag{3.5}$$

where $e_{i,n}$ is the eigenvector component at position i for mode n; η_i is an influence coefficient; ω_n is the eigenvalue associated with the n-th mode; and $\hat{\pi}_n, \overline{\pi}_n$ are respectively the peak and mean value of the n-th non-correlated component of the wind pressure field, $\Pi(t)$, defined as:

$$\mathbf{\Pi}(t) = \mathbf{E}^T \cdot \mathbf{P}(t) \tag{3.6}$$

where **E** is the matrix of eigenvectors of the covariance matrix. Substituting Eq. 3.5 in Eq. 3.4, a design wind load associated with N eigen-modes (POD modes) of the covariance matrix may be obtained.

A new and innovative approach is due to the work of Holmes [i] in which the mean and background responses are combined with resonant response from several modes of vibration. The combined effective static load pattern is as follows:

$$P_{ik,eq} = \overline{P_k} + \left(g_B \cdot \rho_{S_i P_k} \cdot \sigma_{P_k}\right) \cdot W_B + \sum_h^N \left(g_{R,h} \cdot m \cdot (2\pi n_h)^2 \cdot \sigma_{a,h} \cdot \mu_h\right) \cdot W_{R,h} \tag{3.7}$$

where $g_{R,h}$ is the peak factor for h-th resonant response; m is a mass per unit length; n_h is the h-th mode natural frequency, $\sigma_{a,h}$ is the r.m.s. modal coordinate (resonant contribution only), and μ_h is the mode shape for the h-th mode of vibration. Moreover:

$$W_B = \frac{g_B \cdot \sigma_{S_i,B}}{\left(g_B^2 \cdot \sigma_{S_i,B}^2 + \sum_{j=1}^N g_{R,j}^2 \cdot \sigma_{S_i,R,j}^2\right)^{1/2}} \qquad W_{R,h} = \frac{g_{R,h} \cdot (\alpha_h \omega_h^4 \sigma_{a,h}^2)^{1/2} \cdot}{\left(g_B^2 \cdot \sigma_{S_i,B}^2 + \sum_{j=1}^N g_{R,j}^2 \cdot \sigma_{S_i,R,j}^2\right)^{1/2}} \tag{3.8}$$

with

$$\alpha_h = \int_S m \cdot \mu_h \cdot I_r dS \tag{3.9}$$

where I_r is the influence surface. The subscripts B and R refer respectively to background and resonant components.

3.3. WIND TUNNEL SETUP AND MODEL CHARACTERISTICS

Wind tunnel tests have been performed in previous campaigns on a rigid model and have been carried out in the CRIACIV (Inter-University Research Center on Building Aerodynamics and Wind Engineering) BLWT (test section: 2.4 × 2.4 × 1.6 m). For a full description of the model and wind tunnel setup see [1], [2], [4], [5], [7].

The mean wind profile of the actual suburban area has been approximated through a power law with a profile exponent $\alpha=0.23$. The turbulence intensity was 20% at the full-scale reference height of 10 m. The frequency decomposition of the turbulent energy has been well approximated by the von Karmán spectrum (Figure 3.2).

Cooling tower test model, 1:300 scaled, was aluminum made and it was instrumented by means of 96 pressures taps placed at 8 different levels. At each level pressure taps were placed at a relative angle of 30° (Figure 3.3). The wind pressure field has been logged using a sampling frequency of about 1 KHz.

Reynolds' number mismatch between model and full-scale tower was avoided by putting additional surface roughness on the model (Figure 3.3): 24 meridian ribs 0.4 mm thick have been placed at relative angles of 15°.

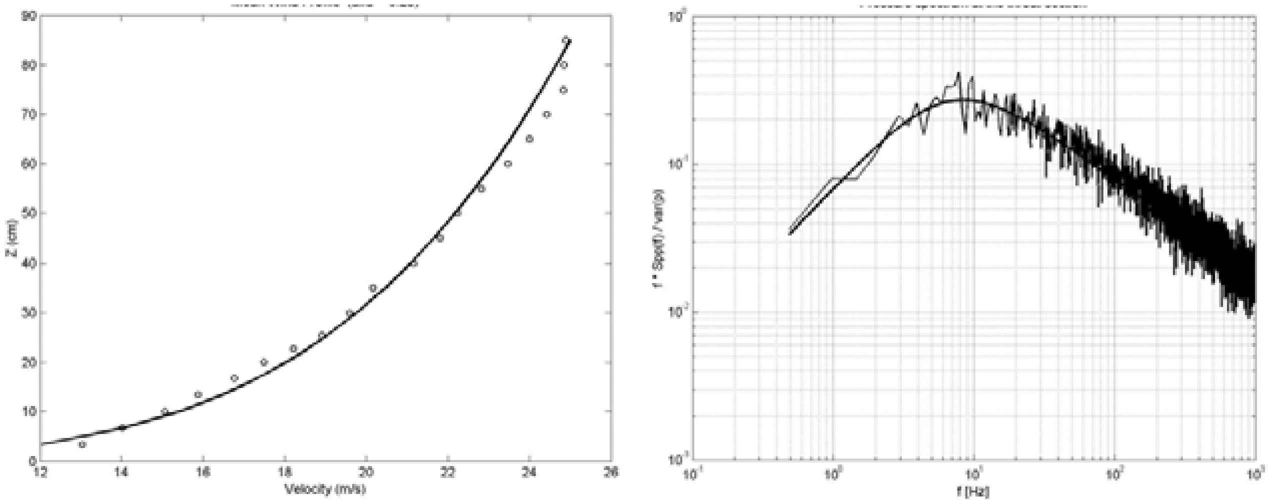

Figure 3.2 Mean wind profile (left); approximation of pressure spectrum at the upstream throat section with von-Karmán spectrum (right)

3.4. TOWER'S AERODYNAMIC AND PRESSURE DISTRIBUTION

Mean pressure at the height above ground z and angular coordinate θ is expressed by introducing the usual pressure coefficient $C_p(z,\theta)$:

$$C_p(z,\theta) = (\overline{P}(z,\theta) - P_0)/\overline{P}_D(z) \tag{3.10}$$

where $\overline{P}(z,\theta)$ is the mean pressure measured at the specific location, while

$$\overline{P}_D(z) = (1/2) \cdot \rho \cdot \overline{U}^2(z) \tag{3.11}$$

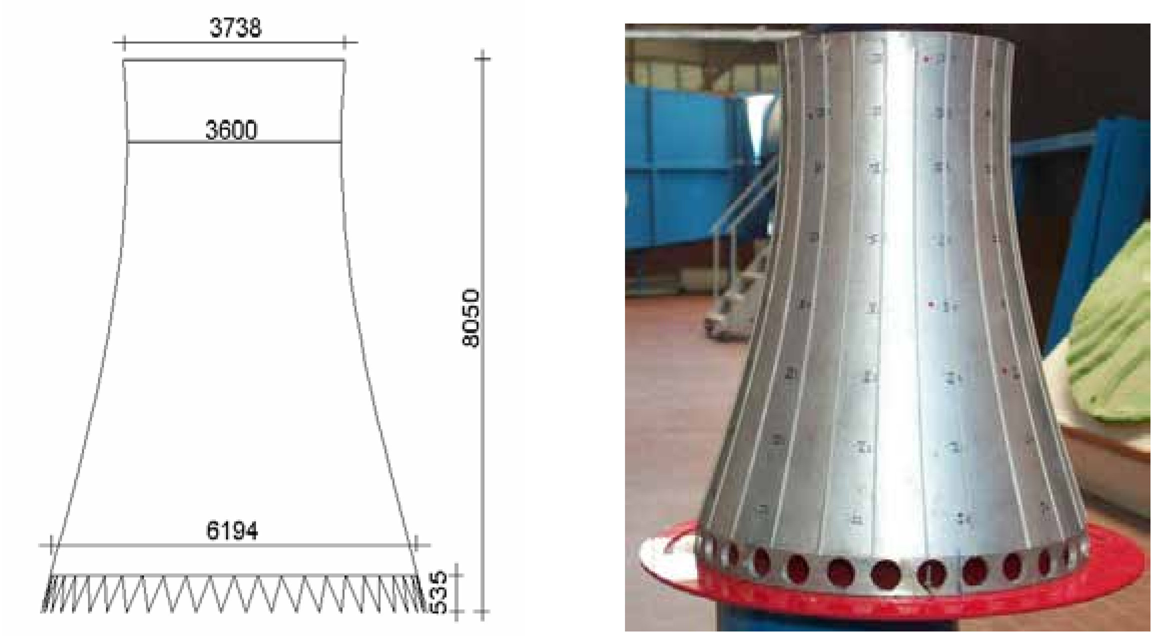

Figure 3.3 Full-scale tower and wind tunnel model.

is the reference dynamic pressure and P_0 represents the static pressure; both pressures are evaluated in undisturbed flow (that is without the presence of the tower) at the same height z.

The mean wind pressure acting on the external surface of the shell depends on the height above ground level and on the circumferential angle. In uniform flow apart from an area at the tower top, the variation of the pressure coefficients with height is small. Completely different result is obtained from measurements in turbulent flow.

Figure 3.4 shows that the mean pressure field around tower surface, in the simulated atmospheric boundary layer, can be divided in 3 regions: a windward (maximum pressure), a side (maximum suction), and a wake (constant pressure) region. Whereas at the stagnation point the maximum pressure is roughly equal to the dynamic pressure and it is constant with height z, like in uniform flow, the maximum suction (minimum pressure) increases from the top to the bottom level, and its position depends on the separation point of the flow, that is on the Reynolds number, *Re*, at a certain z, as it is typical for rotational shapes. Simultaneously, the base (wake) pressure coefficients decrease from the top to the bottom level.

In shear flow with different profiles, additional energy is transferred to the lower layers. Therefore, the maximum pressure, at the stagnation point, is sometimes larger than the dynamic pressure in the respective height. Moreover, even if the maximum suctions and the wake pressures varies with height, the pressure rise from the former to the latter is proportional to the velocity pressure at the respective height, so the pressure rise is again constant with height, similar to uniform flow.

Differences in the aerodynamic behavior between uniform and turbulent flow condition may be explained as follows: in turbulent flow, the wake vortices draw back along shell surface producing strong suctions in the side region; a the same time, because of the greater shear forces, typical of turbulent boundary layers, the wake narrows producing greater drag forces which correspond larger wake suctions.

The full-scale towers are in the transcritical regime, where the flow field is generally independent of Reynolds numbers. But, as pressure measurements at full-scale have shown the roughness of the external surface still has an influence on the pressure distribution. The suction peaks are particularly sensitive to surface roughness while maximum and base pressures are almost the same: the higher the roughness the lower the suction peaks. This leads to a magnification of the total resistance but nevertheless to a reduction of the maximum meridian stress resultant. Therefore, additional surface roughness, such as meridian ribs, are beneficial and used frequently, even to increase buckling safety related to the compressive stresses produced on the side region of the shell surface.

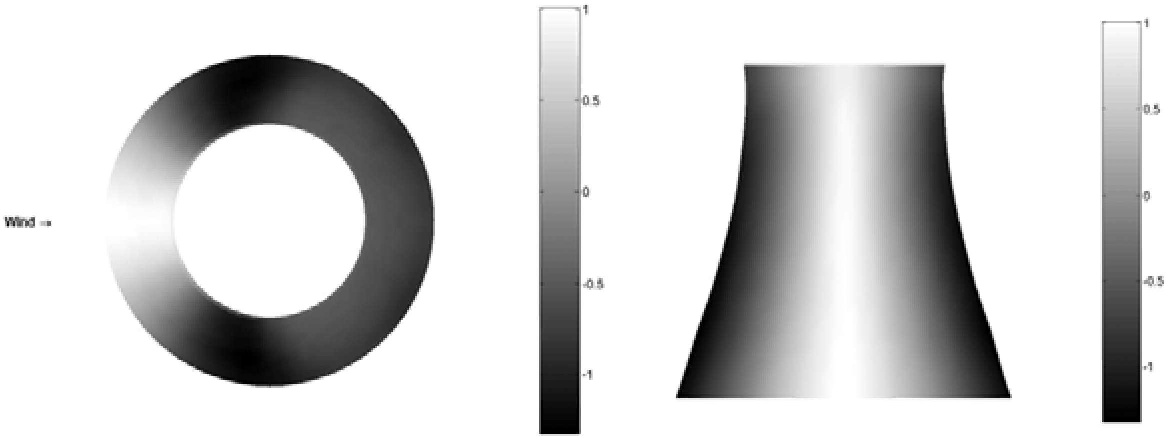

Figure 3.4 Mean pressure coefficient distribution: plan view (left); windward view (right)

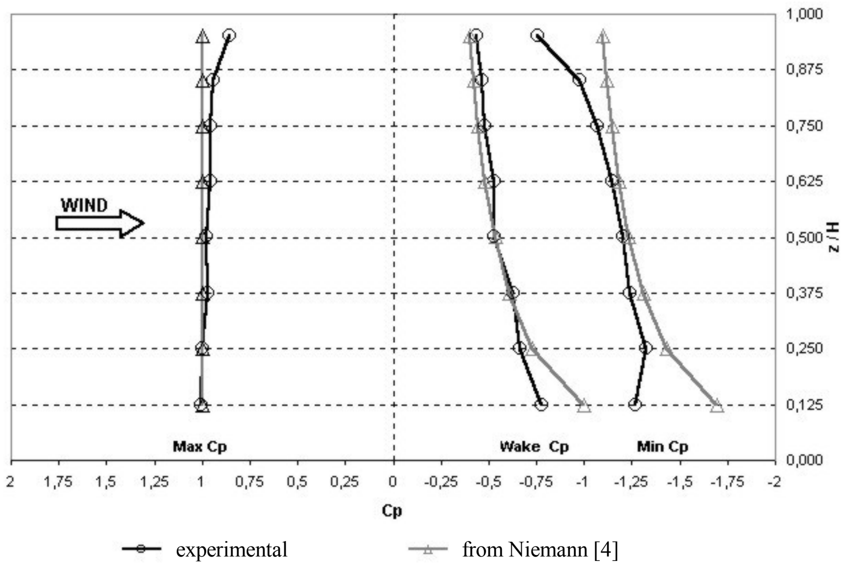

Figure 3.5 Cp distribution in the windward, side and wake region (comparison with reference values from Niemann, 1980)

Experimental mean pressure coefficients have been compared with theoretical curves as shown in Figure 3.5: experimental results are well approximated by those curves, although at the upper and bottom levels results were unreliable because of the three-dimensional behavior of the flow in those regions, and due to the disturbance induced by the floor roughness elements in the latter region.

Maximum and minimum pressures can be evaluated according to Davenport’s concept which holds true for stationary Gaussian processes ([c]). Expected extreme value can then be calculated by

$$[P(z,\theta)]_E = P(z,\theta) \pm g_P(z,\theta)\cdot\sigma_P(z,\theta) \tag{3.12}$$

where $g_P(z,\theta)$ is the peak factor defined as follows:

$$g_P(z,\theta) = \left[\sqrt{2\ln(\nu(z,\theta)\cdot T)} + \frac{0.5772}{\sqrt{2\ln(\nu(z,\theta)\cdot T)}}\right] \tag{3.13}$$

with T record’s length and ν number of “zero-crossing” per unit time

$$\nu(z,\theta) = \frac{1}{\sigma_p(z,\theta)}\sqrt{\int_0^\infty f^2\cdot S_P(z,\theta,f)\cdot df} \tag{3.14}$$

Maximum and minimum pressure coefficients can be computed once the extreme values at each tap are known. The peak factor is a local parameter, that is it depends on both z and θ; nevertheless a mean value of peak factor for each instrumented levels can been used, than introducing a peak factor as a function of the level height z only. Larger extreme values were observed at lower parallels because of larger turbulence intensity of the flow at the bottom side of boundary layer (Figure 3.6). On the whole, a peak factor in the range g=4.0÷4.2 can be used for design purposes over the whole tower surface, in a good agreement with results obtained by Orlando ([7] and [8]).

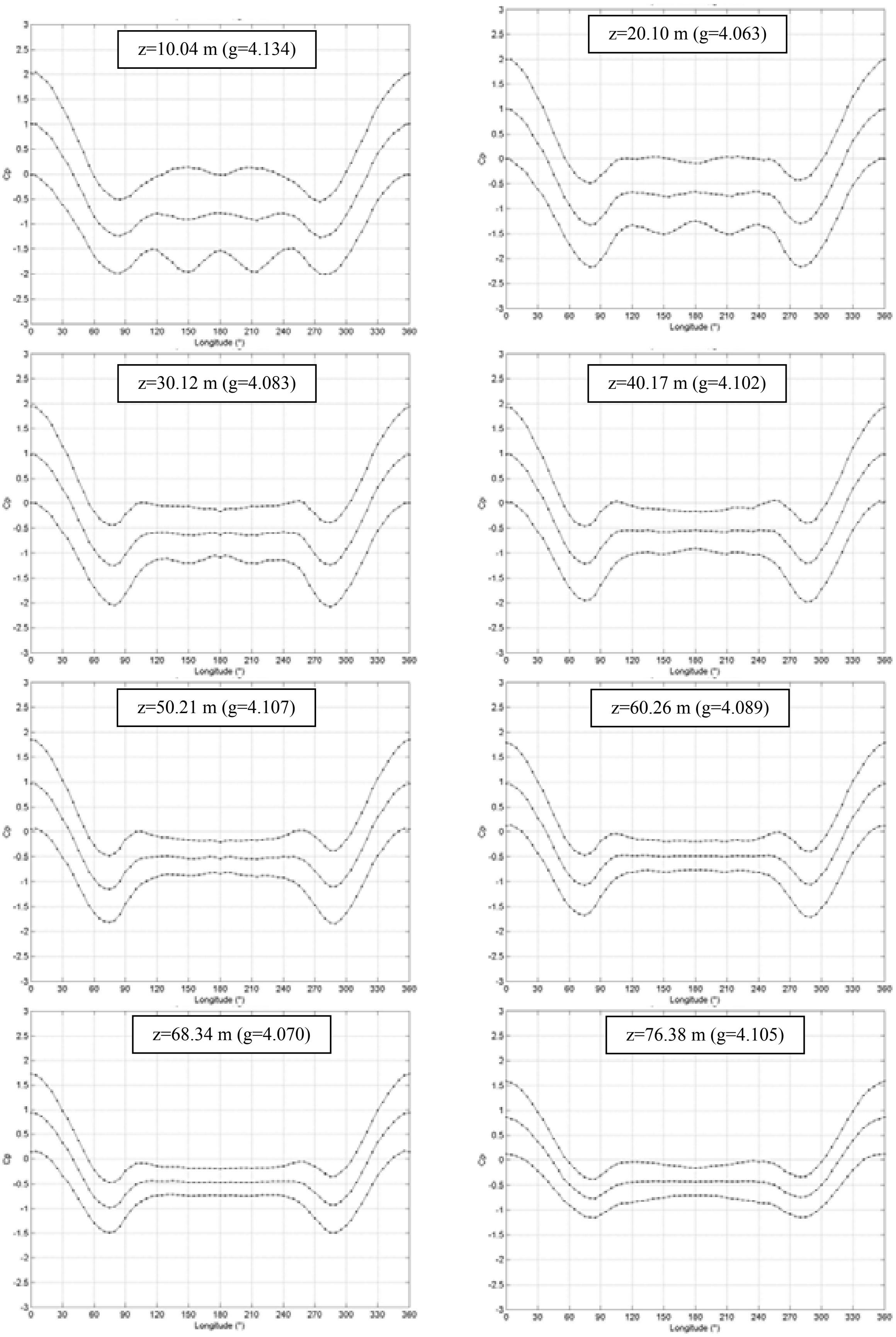

Figure 3.6 Mean, maximum and minimum C_p at instrumented levels

3.5. WIND PRESSURE FIELD MODELING

With the purpose of simulating the wind pressure field over the entire surface of the tower starting from measured data, pressures have been modeled with an autoregressive (AR) model starting from the power spectral density matrix of fluctuating wind pressures carried out in wind tunnel tests. The general formulation of AR model is expressed as follows ([1]):

$$\mathbf{P}(t) = \sum_{k=1}^{p} \mathbf{\Phi}_k \mathbf{P}(t - k\Delta t) + \mathbf{N}(t) \tag{3.15}$$

where $\mathbf{P}(t)$ is the multicorrelated random process; $\mathbf{N}(t)$ are random shocks; Δt is the time interval; p is the order of the AR filter; and $\mathbf{\Phi}_\mathbf{k}$ are the autoregressive coefficient matrices. The record length of time-histories was 10 min at full scale, and the scaled sampling frequency is about 8 Hz.

The real structure has been modeled by a FEM code, and the multicorrelated wind process, acting on the corresponding full scale points, has been extended around tower surface by means of a Radial Basis Function Artificial Neural Network (RBFANN) whose general expression writes ([6]):

$$\overline{\mathbf{P}}(\mathbf{x}) = \overline{a} + \sum_{k=1}^{D} \overline{b}_k x_k + \sum_{k=1}^{N} \lambda_k \varphi_k(\mathbf{x}) \tag{3.16}$$

for the mean pressure field, and

$$\widetilde{\mathbf{P}}(\mathbf{x},t) = \widetilde{a}(t) + \sum_{k=1}^{D} \widetilde{b}_k(t) x_k + \sum_{k=1}^{N} \gamma_k(t) \psi_k(\mathbf{x}) \tag{3.17}$$

for the fluctuating wind pressures. D is the dimension of the space of the co-ordinates; x_k are the components of the position $\mathbf{x}$ in the chosen reference system; $\overline{a}$, $\overline{b}_k$ and λ_k are constant coefficients, while $\widetilde{a}(t)$, $\widetilde{b}_k(t)$ and $\gamma_k(t)$ vary with time. The functions $\varphi(\mathbf{x})$ and $\psi(\mathbf{x})$ depend only on the position, $\mathbf{x}$. These functions are called *Radial Basis Function*, and each generic function depends on the distance of the position $\mathbf{x}$ from a point $\mathbf{c}^{(h)}$ which is called the center of the function. The dependence is such that the value of the generic k-th function decreases as the distance between $\mathbf{x}$ and $\mathbf{c}^{(h)}$ increases. These functions are assumed to be Gaussian ones; so, if the symbol $\|\bullet\|$ denotes the distance between two points, we can write that

$$\left.\begin{array}{l} \varphi_k(\mathbf{x}) \\ \psi_k(\mathbf{x}) \end{array}\right\} = \exp\left(-\frac{\left\| \mathbf{x} - \mathbf{c}^{(h)} \right\|^2}{\sigma^2} \right) \tag{3.18}$$

The only difference between functions $\varphi_k(\mathbf{x})$ and $\phi_k(\mathbf{x})$ is the decay parameter σ which has different values for each set.

A more detailed description and other application of the RBFANN procedure can be found in Ch. 7 of present volume.

3.6. QUASI-STATIC APPROACH

3.6.1. Quasi-static (Background) response

The effect $\overline{S}_i$ at a given location (z, θ), which originates from the mean forces $\overline{P}(z_h, \theta_h)$ acting at all the possible (z_h, θ_h) points on tower's surface, is given by:

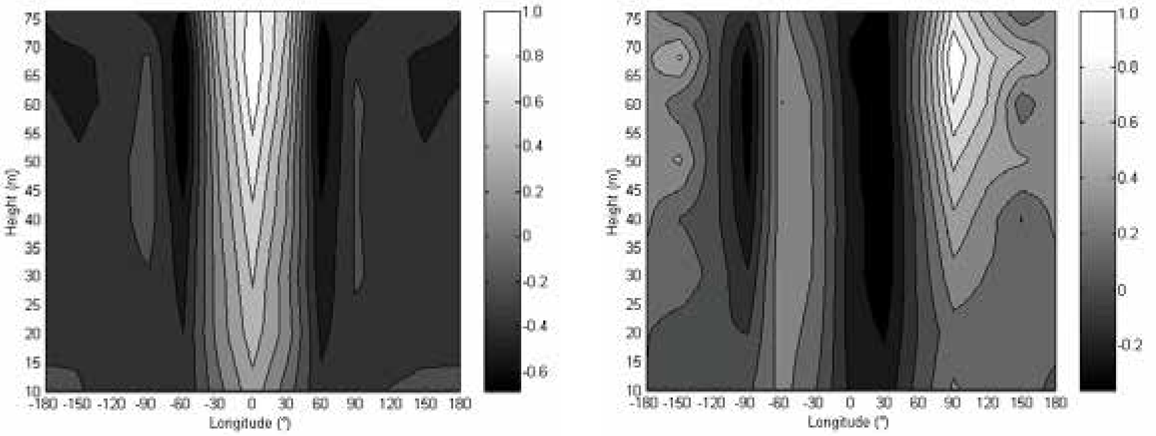

Figure 3.7 Correlation coefficient of external pressures: Left): cross-correlation coefficients between windward point (z=68.34 m, θ=0°) and the remaining points; Right) quasi-steady cross-correlation coefficients between side point (z=68.34 m, θ=90°) and the remaining points;

$$\overline{S}_i(z,\theta)=\sum_h \eta_i(z_h,\theta_h)\cdot\overline{P}(z_h,\theta_h)=\sum_h \eta_{ih}\cdot\overline{P}_h \tag{3.19}$$

where $\eta_i(z_h,\theta_h)=\eta_{ih}$ is the (i,h) term of the influence coefficient matrix, that is the response (in terms of the internal force of interest) at the location (z,θ) when an unit force orthogonal to the tower is acting at point (z_h,θ_h).

Mean forces at windward and side faces, act respectively inwardly and outwardly, then producing a larger mean stress in those regions. According to the analysis of correlation coefficients in quasi-steady field, between the windward point at the throat section (z=68.34 m, θ=0°) and the others points around tower's surface, it is possible to observe (see Figure 3.7) that the windward region is good correlated with the side region, but it is completely uncorrelated with the wake region, as just pointed out in [f]. It means that dynamic pressures, acting on the windward and side regions, cannot be treated separately, because their fluctuating effects produce a correlated magnification of mean stress in each of these regions. Nevertheless, wake dynamic pressures' effects may be considered apart, that is the correlation between windward and wake region may be neglected. Moreover the contour plot of the correlation coefficients between the side point (z=68.34 m, θ=90°) and remaining points around tower's surface, shows not only the obvious good correlation with the windward region, but also the good correlation with the opposite side region, this depending on the formation of the von-Karmán vortex street, that is on the vortex shedding phenomena: the flow separates alternatively from the opposite sides of cooling tower surface producing a fluctuating across-wind load.

The vortex shedding frequency was observed in pressure spectra ($f_S = 0.13$ Hz), but no peak at this frequency can be observed in the structural response, being this frequency far from the first eigen-frequency (around 1.45 Hz).

The quasi-static response of the structure under dynamic loading can be evaluated according to a similar approach to the one adopted for the determination of mean values. Neglecting the dynamic amplification due to the tower's characteristics, instantaneous internal forces can be evaluated according to the same formula reported above, that is

$$S_i(t)=\sum_h \eta_i(z_h,\theta_h)\cdot P(z_h,\theta_h,t)=\sum_h \eta_{ih}\cdot P_h(t) \tag{3.20}$$

The quasi-static approach was implemented and a stress field around the tower was found, representing a good approximation of previous results obtained in [7].

The tower response has been taken into account in terms of circumferential and meridian internal forces (namely N_{11}, M_{11}, N_{22} and M_{22}, where N and M respectively represent the axial force and the bending moment in the meridian direction, suffix 1, and in the circumferential direction, suffix 2) and normal stresses, respectively S_{11} and S_{22}. The most unfavorable stresses have been detected on the windward meridian (θ=0°) for each response, by means of the above quasi-static approach. The mean response plots show that cooling tower's behavior (as expected) is of membranal type because of small bending moments (see Figure 3.8). In the same figure, the dynamic response, which will be reported in following paragraphs, is also reported, in order to show that the response is mainly due to background component only.

3.6.2. GRF approach

The covariance matrix of internal forces is sufficient to estimate quasi-static response, when resonance response can be neglected. Recalling Eq. 3.22, the relationship between internal forces and influence coefficient is given by

$$S_i(t) = \sum_h \eta_{ih} \cdot P_h(t) \quad \Rightarrow \quad \mathbf{S}(t) = \boldsymbol{\eta} \cdot \mathbf{P}(t) \tag{3.21}$$

so that the quasi-static stress covariance matrix, $\mathbf{C_{SS}}$, can be written as:

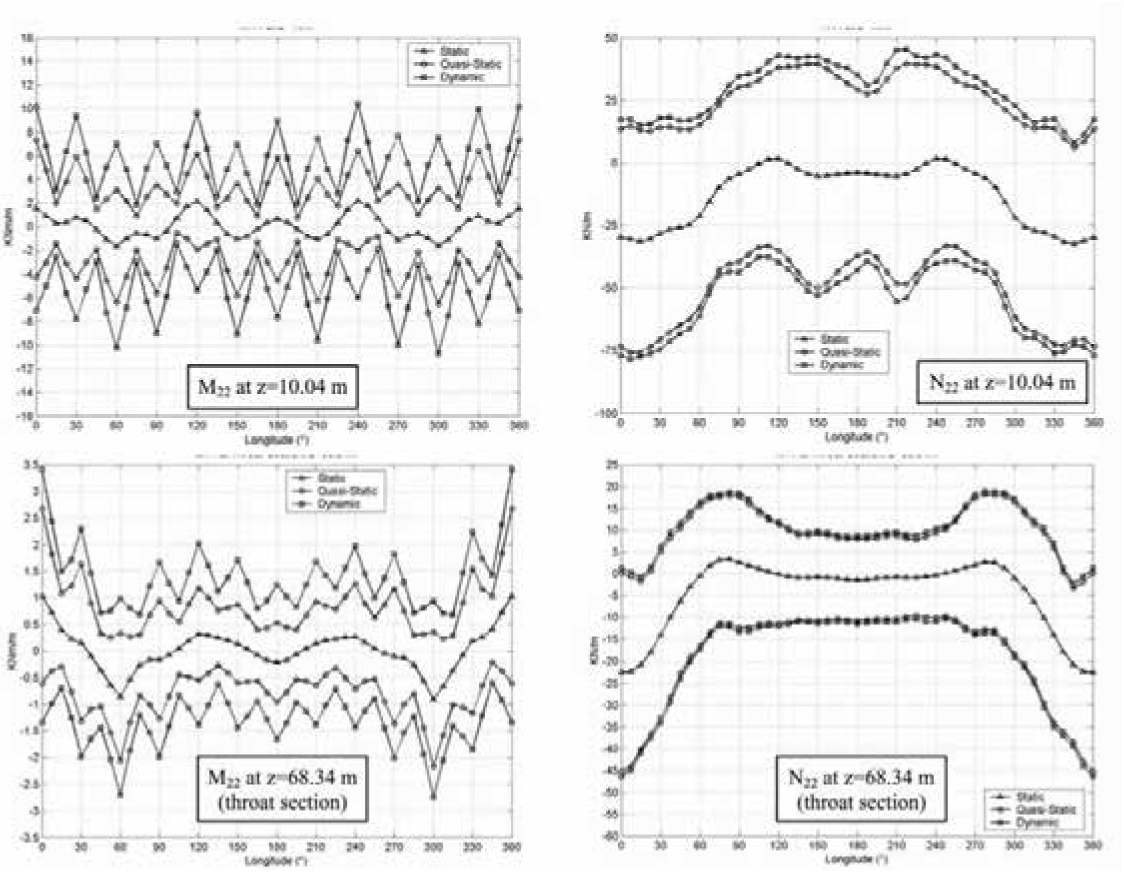

Figure 3.8 Static, quasi-static and dynamic stresses at two different levels, for two typical internal forces [left): meridian bending moment (M22) ; right) meridian axial force (N22)]

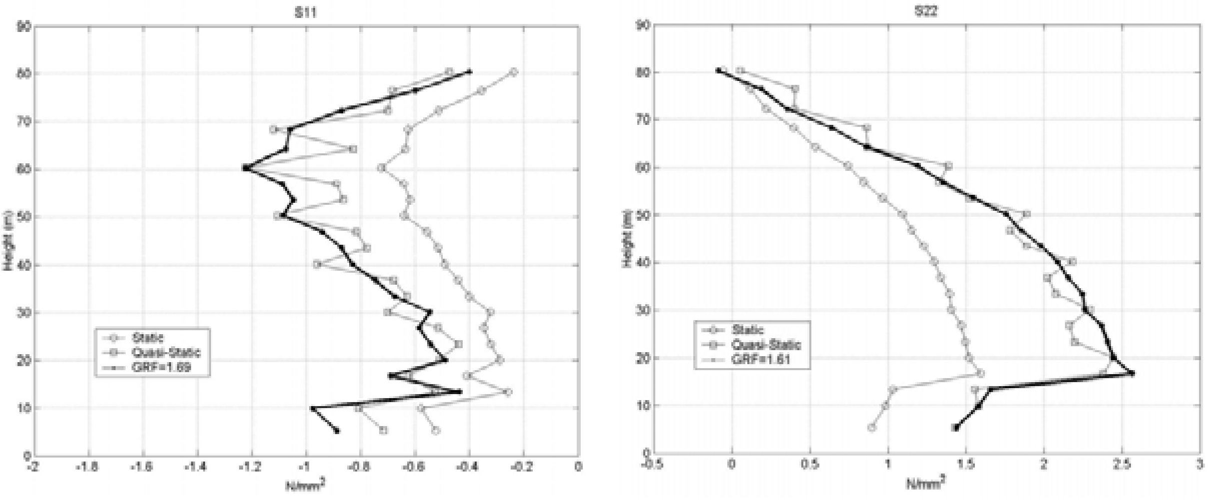

Figure 3.9 Circumferential compressive stresses (left), meridian tensile stresses (right), at windward meridian (θ=0°)

$$\mathbf{C}_{SS} = \boldsymbol{\eta} \cdot \mathbf{C}_{pp} \cdot \boldsymbol{\eta}^{T} \tag{3.22}$$

being $\mathbf{C}_{pp}$ the wind pressures covariance matrix. The i-th diagonal component of $\mathbf{C}_{SS}$ is the i-th total variance of quasi-static which can be used to define a suitable response factor. In fact, the maximum quasi-static response can be calculated by

$$S_i(z,\theta) = \overline{S}_i(z,\theta) \pm g_{S_i}(z,\theta) \cdot \sigma_{QS_i}(z,\theta) \tag{3.23}$$

where $S_i(z,\theta)$, g_{Si} and σ_{QSi} are, respectively, the generic quasi-static stress at height z and longitude θ, its peak factor and its standard deviation.

The amplification of the total response may be given in terms of Gust Response Factor, GRF defined as the ratio between the maximum response in quasi-static range and the mean response

$$GRF(z,\theta) = \frac{\overline{S}(z,\theta) \pm g_S(z,\theta) \cdot \sigma_{QS}(z,\theta)}{\overline{S}(z,\theta)} \tag{3.24}$$

The GRF method has given a good approximation not only of the extreme values of S11 (at a full-scale height z = 60.30 m) and S22 (at z = 20.10 m), but even of the entire meridian stresses. In particular, GRF=1.69 and GRF=1.61 have been obtained respectively for the circumferential compressive and meridian tensile stresses. Clearly, these results are limited to the hypothesis of coincident peak responses distributions (see Figure 3.9).

Obtained results are in a good agreement with those reported by other authors (see [n], [o], [p], [q]), as shown in Table 3.1. As it can be observed from the Table, the GRF values to be used in a design stage vary from 1.8 to 2.0, even if they have been evaluated for different cooling towers in different wind conditions.

It has to be noted that apparently values of GRFs seem not to be comparable among them, because some of them refer to the meridian axial force N22, while those reported in present research deal with the normal stress S_{22}. However the difference is not relevant, being the meridian stress mainly induced by axial force instead of bending moment; in the meridian direction, the ratio between the normal stress caused by bending moment with respect to the same stress induced by ax-

	Niemann & Ruhwedel, 1980	Niemann, 1980	Niemann, 1984	Niemann & Zerna, 1986	Investigated case
H (m)	122	200	125	125 / 165	80,5
H / d_g	2,43	2	2	2 / 1,6	2,24
α	0,27	0,16	0,24	0,16	0,23
I_U	31%	-	-	24% / 17%	20%
g	4	4	4	4	4
GRF_{N22}	1,8	1,8 - 2	2	2	-
GRF_{S22}	-	-	-	-	1,61
$S_{22}(M) / s_{22}(N)$	8%	-	-	-	8,6%
$S_{11}(M) / s_{11}(N)$	152%	-	-	-	160%

Table 3.1 Comparison among different results: H: tower's height; d: throat diameter; α: wind profile exponent; I_U: turbulence intensity at z =10 m; GRF: Gust Response Factor; g: peak factor; s(M): normal stresses due to bending moments; s(N): normal stresses due to axial force

ial force is about 8.6%, then negligible. The same cannot be stated for the circumferential direction (where stresses are mainly due to bending moments); in this direction the same ratio reaches values as high as 160%, in a good agreement with the result reported in [p].

3.6.3. LRC Method

The effective load patterns producing the extreme response for the circumferential and meridian stresses, has been obtained by the LRC method using a peak factor equal to 4. The LRC method has provided a good estimation of the extreme values of each responses, but in order to have the exact value of the quasi-static analysis, design peak factors for each responses have been calculated: g = 2.7 for S_{11} and g = 5.13 for S_{22} (see F).

In a previous paper ([2]), very similar values of GRF and design peak factors have been obtained, using the effective non-Gaussian pressure pattern obtained from wind tunnel tests. So, the differences with the values calculated herein, may be related to the influence of gaussianity in

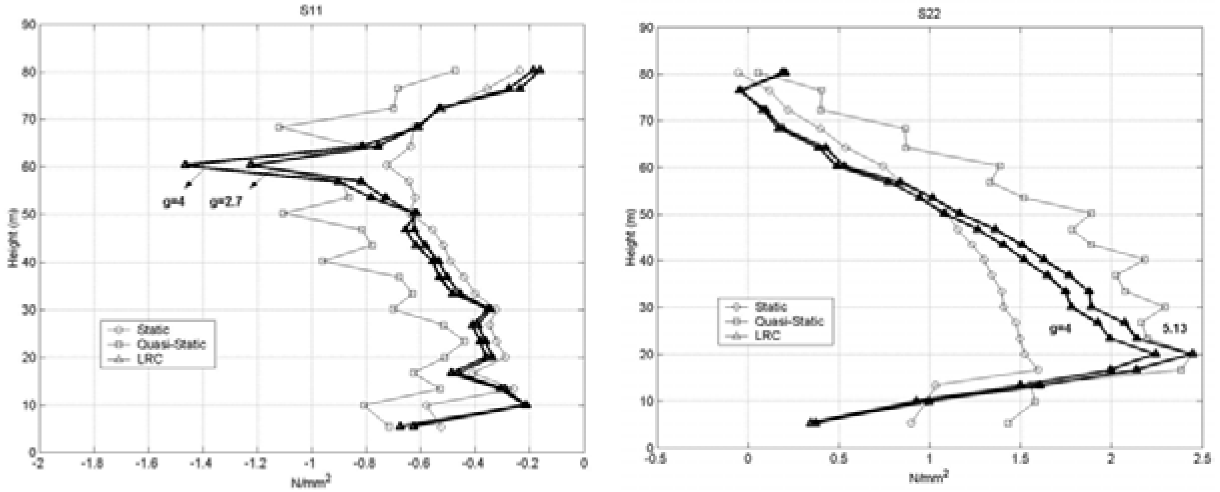

Figure 3.10 LRC method: design peak factor for circumferential compressive stresses (left, g = 2.7), and meridian tensile stresses (right, g = 5.13), at windward meridian (θ=0°)

modeling the wind pressure field.

3.6.4. Optimized Peak Load Distributions

Using the orthogonal expansion of wind pressures [h], the load distributions for S_{11} and S_{22} are in very good agreement with those obtained with LRC method with g=4. The number of modes involved in defining design wind load patterns and reproducing the 99% of the total response has been set to N=89 for circumferential compressive stresses and to N=81 for meridian tensile stresses (see Figure 3.11), while the total number of eigen-modes of the FEM model was 1056.

An approximation of the peak factor can be given by following expression [g]:

$$g = \sqrt{\sum_{n=1}^{N} \alpha_n^2 (\hat{\pi}_n - \overline{\pi}_n)^2} \Bigg/ \sqrt{\sum_{n=1}^{N} \alpha_n^2 \omega_n} \tag{3.25}$$

Therefore, an estimation of design wind loads may be written:

$$P_{ik,eq} = \overline{P}_k + g \cdot \left(\sum_{n=1}^{N} \alpha_n e_{k,n} \omega_n \right) \Bigg/ \sqrt{\sum_{n=1}^{N} \alpha_n^2 \omega_n} \tag{3.26}$$

Substituting the value of g with the background design peak factors, $g_D = 2.7$ for S_{11} and $g_D = 5.13$ for S_{22}, it is then possible to obtain the peak-load distributions for each responses, to be understood like a linear combinations of distributions associated with a small number of eigenvector of the covariance matrix ([5]). In Figure 3.12 and Figure 3.13 the results of the obtained design wind loads have been plotted.

3.7. RESONANT RESPONSE

In the dynamic domain, the tower response depends not only on the modification of the natural wind loads modified by the aerodynamic shape of the tower, but also because of its motion that can be divided in several mode shapes, differently excited by the wind loads according to its frequencies decomposition. The spectral density of the dynamic load fluctuations was similar to the wind load fluctuations with additional peaks at the eigen-frequencies of tower's natural modes.

In order to define a resonant design factor suitable for design purposes, the analysis was extended to dynamic response evaluation in frequency domain. When resonance cannot be neglected the dynamic response can be calculated as follows:

$$\mathbf{S}_{\mathbf{qq}}(f) = \mathbf{\Phi} \cdot \mathbf{H}^*(f) \cdot \mathbf{\Phi}^T \cdot \mathbf{S}_{\mathbf{pp}}(f) \cdot \mathbf{\Phi} \cdot \mathbf{H}(f) \cdot \mathbf{\Phi}^T \tag{3.27}$$

where $\mathbf{S}_{\mathbf{qq}}(f)$, $\mathbf{\Phi}$, $\mathbf{S}_{\mathbf{pp}}(f)$ and $\mathbf{H}(f)$ are respectively the cross-spectral densities response matrix, the modal shape matrix, the wind loads cross-spectral density matrix, and the mechanical admittance, whose complex conjugate matrix is $\mathbf{H}^*(f)$. Analysis' purpose is to evaluate the dynamic stress response cross-spectral density matrix:

$$\mathbf{C}_{\mathbf{S_d S_d}} = (\boldsymbol{\eta} \cdot \mathbf{K}) \cdot \mathbf{C}_{\mathbf{qq}} \cdot (\boldsymbol{\eta} \cdot \mathbf{K})^T \tag{3.28}$$

where $\mathbf{C}_{\mathbf{S_d S_d}}$ is the covariance matrix in the dynamic range, $\mathbf{K}$ is the tower's stiffness matrix and $\mathbf{C}_{\mathbf{qq}}$ is the dynamic displacement response covariance matrix.

The evaluation of the stiffness matrix could be performed by the usual relationship

$$\mathbf{K} = (\mathbf{\Phi} \cdot \mathbf{H}(0) \cdot \mathbf{\Phi}^T)^{-1} \tag{3.29}$$

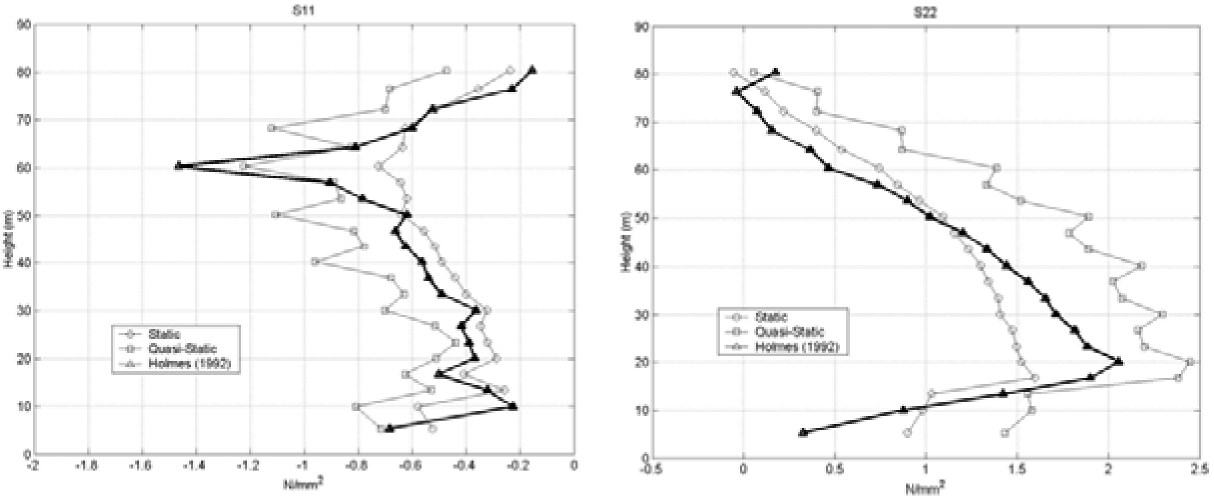

Figure 3.11 Circumferential compressive stresses (left, N=89), meridian tensile stresses (right, N=81), at windward meridian (θ=0°)

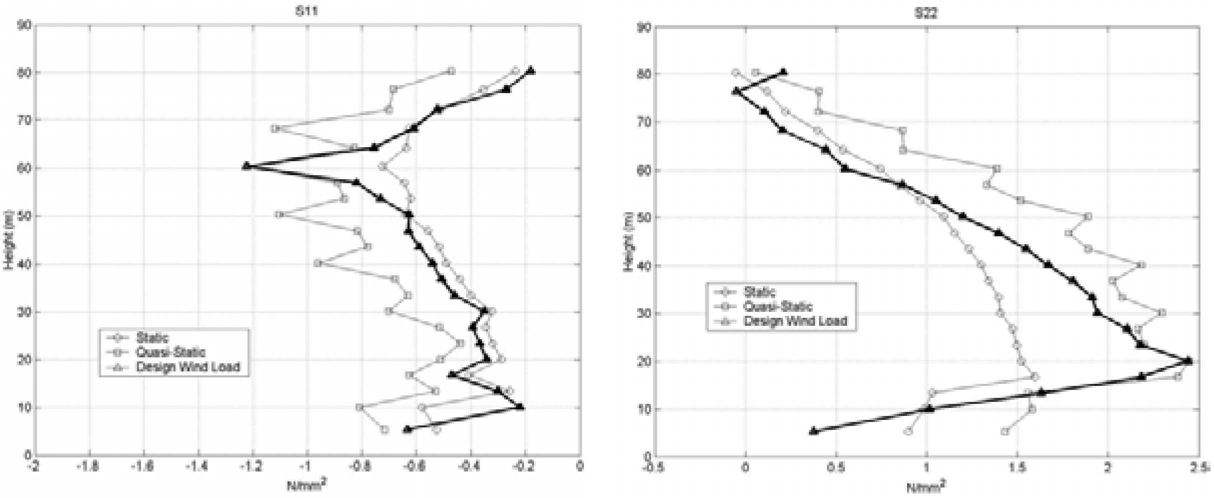

Figure 3.12 Circumferential compressive stresses (left, N=89, g=2.7), meridian tensile stresses (right, N=81, g=5.13), at windward meridian (θ=0°)

which implies the inversion of an (n×n) "sparse" matrix. By considering the contribution to the response given by the first m eigenvalues only, is more efficient from a computational point of view, to switch to following equivalent expression

$$\mathbf{K} = \mathbf{\Phi} \cdot \left(\mathbf{\Phi}^{\mathrm{T}} \cdot \mathbf{\Phi} \cdot \mathbf{H}(0) \cdot \mathbf{\Phi}^{\mathrm{T}} \cdot \mathbf{\Phi} \right)^{-1} \cdot \mathbf{\Phi}^{\mathrm{T}} \tag{3.30}$$

where only an (m×m) matrix has to be inverted.

3.7.1. Resonance factor (RF)

Since turbulent wind excitation was concentrated at low frequencies, response variance was mainly quasi-static, so that wind turbulence effects may be taken into account by an appropriate Response Factor, as it can be seen from Figure 3.14, where spectral densities of internal forces at two different points at the throat level are reported.

Resonant response is largely contained in the first four modes, but a significant part of peak response was observed in the higher modes because of their cross-coupling. This produces a magnification of response even for higher eigen-frequencies. However, no significant response was ob-

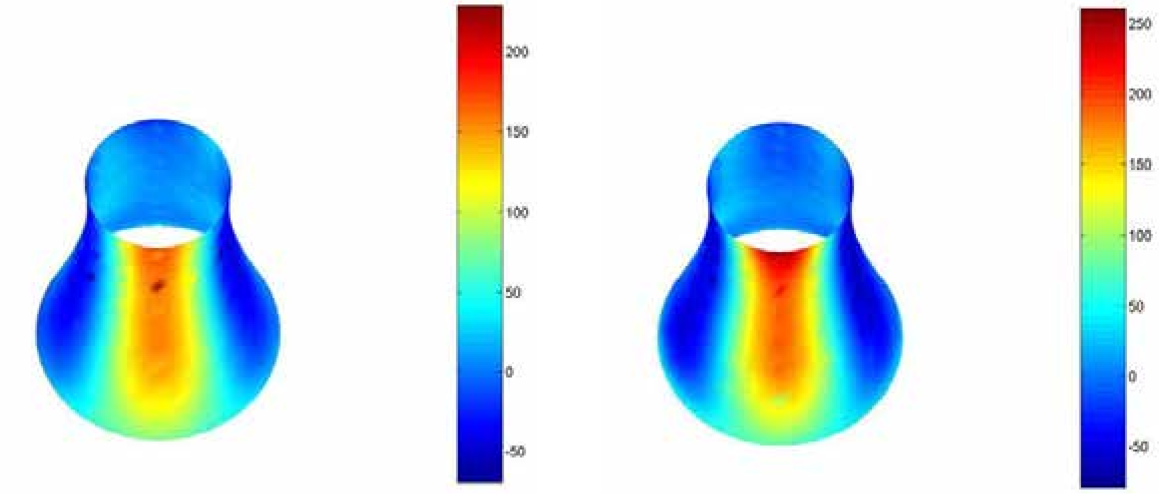

Figure 3.13 Design wind loads for the minimum compressive stress (left) and meridian tensile stress (right),

served after the 20th eigen-frequency. For a full description of the dynamic analysis and results see [1].

The i-th diagonal component of $\mathbf{C}_{\mathbf{S}_d\mathbf{S}_d}$ is the i-th total variance of dynamic stress which can be divided in a quasi-static and a resonant component:

$$\sigma_D^2(z,\theta) = \sigma_{QS}^2(z,\theta) + \sigma_R^2(z,\theta) \tag{3.31}$$

Finally, with usual symbols' meaning, the maximum response has been calculated as follows:

$$S_{max}(z,\theta) = \bar{S}(z,\theta) \pm g_S(z,\theta) \cdot \sqrt{\sigma_{QS}^2(z,\theta) + \sigma_R^2(z,\theta)} \tag{3.32}$$

The amplification of the total response may then be given in terms of Resonance Factor, RF, defined as the ratio between maximum dynamic and quasi-static response:

$$RF(z,\theta) = \frac{\bar{S}_i(z,\theta) \pm g_S(z,\theta) \cdot \sqrt{\sigma_{QS}^2(z,\theta) + \sigma_R^2(z,\theta)}}{\bar{S}_i(z,\theta) \pm g_S(z,\theta) \cdot \sigma_{QS}(z,\theta)} \tag{3.33}$$

From the obtained results, a suitable value for RF has been searched for: the choice of an unique value for RF equal to its maximum could be too conservative, especially if it is related to a small stress level, as in the bending stress case. Moreover, tower response to turbulence wind is mainly membranal, so a large design RF related to bending stress could be erroneous. Therefore, a more detailed analysis was performed, in order to establish a relationship between RF values and the stress level which this amount refers to.

By observing following Figure 3.15, it is possible to point out that larger resonance factors were related to smaller stress levels, whereas the total trend of resonance factors led to the asymptotic value 1.10 for compressive membrane stress and 1.15 for tensile membrane stress. In the latter case the asymptotic value of resonance factors is related to a lower level of membrane stress than in the first case, so the design value 1.10 can be proposed for RF, well in accordance with other results [a].

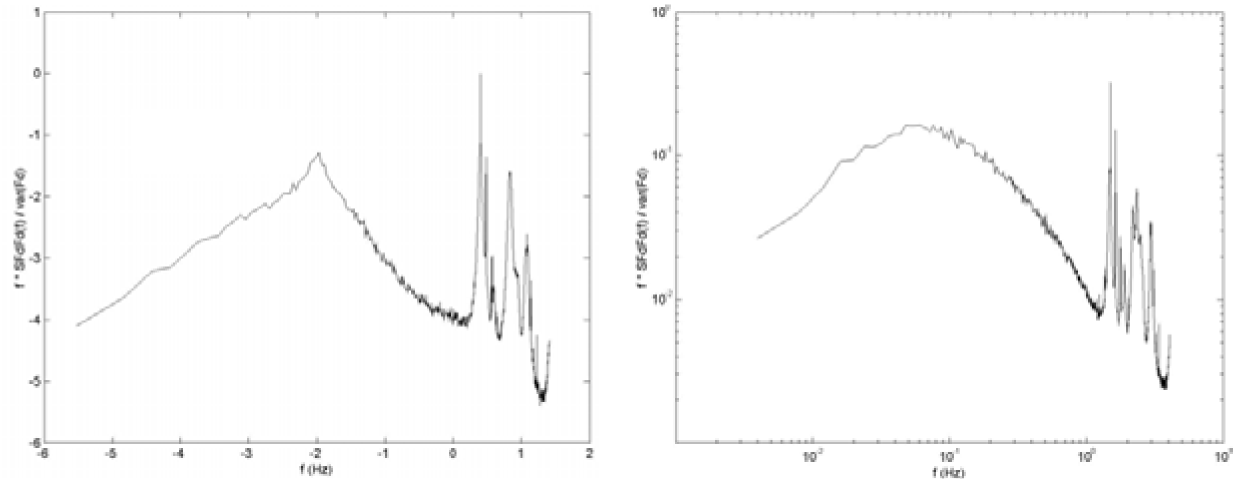

Figure 3.14 Amplified Dynamic Forces spectra at the throat section (z=68.34m): [left), θ=90°; right), θ=0°]

3.7.2. Design wind loads for the combination of mean, background and resonant response

In order to get the design wind loads for the combination of mean, background and resonant response, the procedure described in Section 2 has been implemented using, for the background components, the design peak factors previously considered. The results, in terms of circumferential and meridian stress, are plotted in Figure 3.16, while in Figure 3.17 the respective design wind loads have been mapped.

Calculating the ratio between the resonant peak response to the background one (Figures 6 and 8), it's possible to observe that this value is around 1.18 and 1.08 respectively for S_{11} and S_{22}.

These values are in good accordance with [a] indications, and with the results obtained in [1] where a design resonant factor equal to 1.1 was found on the base of the rigorous dynamic analysis in the frequency domain.

3.8. CONCLUSIONS

Since their aerodynamic behavior, wind effects on cooling tower shells may be argued in terms of almost correlated pressure patterns acting in the windward and side regions. The combinations of them leads to a response magnification in these regions rather than in the wake region whose effects may be taken into account in terms of static stresses and internal forces.

Results reflects the great capability of these structures in holding out against wind storms even in dynamic field. This strongly depends on their shape which confers them a remarkable geometrical stiffness in spite of their noteworthy height (up to 250 meters).

Tower's response to turbulent wind is mainly quasi-static, since the dynamic behavior accounts for about 10% more as regards quasi-static effects, whether for internal forces, mainly due to compressive actions, or for internal stresses for which bending regime became meaningful because of the small thickness of the shell.

Generally, it is worthwhile applying to design wind loads so as to thin computational efforts made much complicated by the stochastic feature of wind pressure pattern.

The design wind loads for the combination of mean, background and resonant responses have been detected for an isolated cooling tower shell under turbulent wind.. The results have been expressed in terms of circumferential (S_{11}) and meridian (S_{22}) stresses at windward meridian where the most unfavorable effects have been detected.

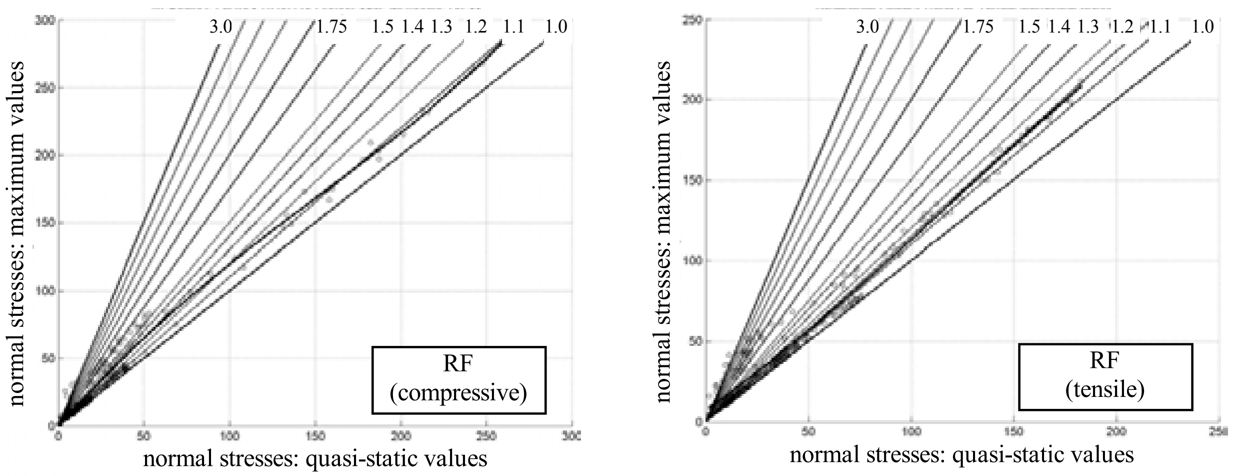

Figure 3.15 Ratio between quasi-static and dynamic stresses at throat section: Left) compressive membrane stress; Right) tensile membrane stress

Analyses has been performed in order to obtain both the quasi-static response and the resonant response; moreover, suitable response factors (in term of both Gust Response Factors, GRF, and Resonant Factors, RF) have been introduced to focus the attention on the maximum and minimum values of internal stresses.

The GRF method has provided good results for both S_{11} (GRF=1.69) and S_{22} (GRF=1.61) stresses, over the entire windward meridian. It's suited to point out the probabilistic density function of the wind pressure pattern which is in general discordant with Gaussian hypothesis. For instance, it has been drawn attention to the dynamic pressure at the windward meridian which is consistent with the square of the longitudinal component of wind velocity. It means that the dynamic pressure at the stagnation points follow a χ^2 distribution rather than a Gaussian density function. In the other regions of the tower the probabilistic characterization of the pressure field can't lie outside the aerodynamic admittance of the structure. Nevertheless, if the effective (in general non Gaussian) pressure pattern is considered, very similar values of GRF may be obtained.

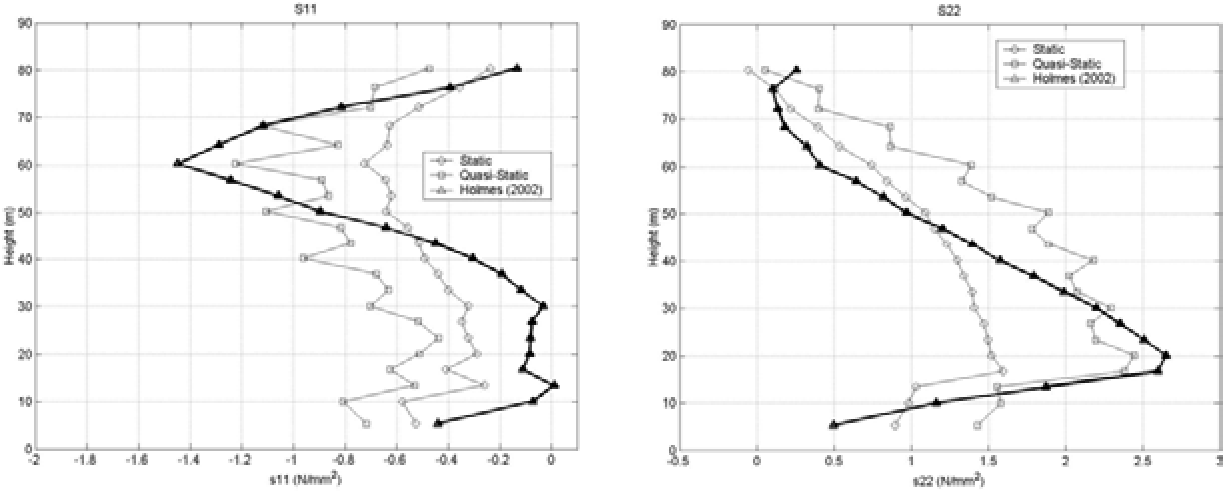

Figure 3.16 Circumferential compressive stresses (left), meridian tensile stresses (right), at windward meridian (θ=0°)

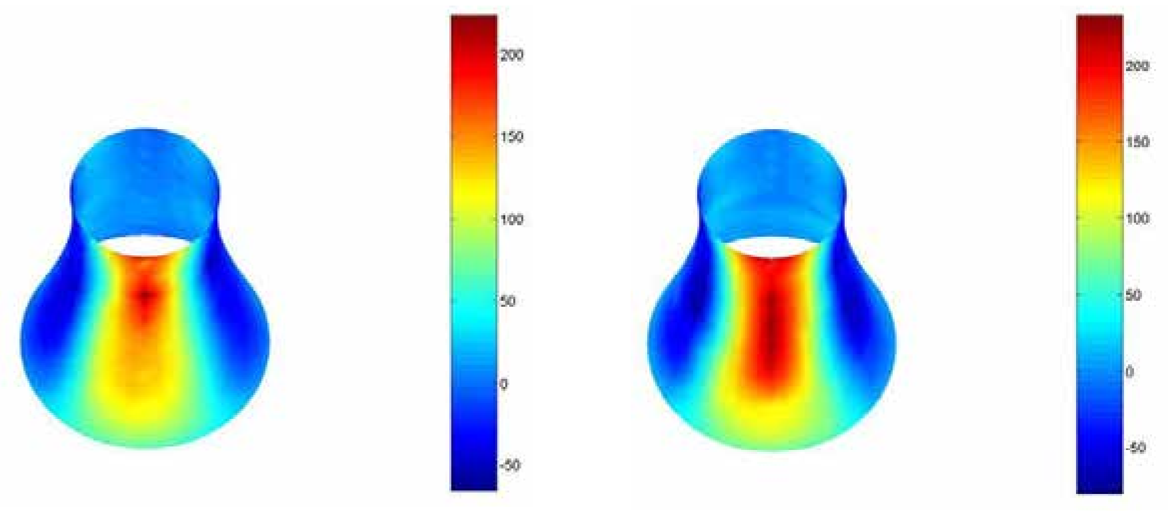

Figure 3.17 Design wind loads for the minimum compressive stress (left) and meridian tensile stress (right), for the combination of mean, background and resonant response

The GRF method provide wind loads pattern to be understood as an amplified mean load, since it neglects the correlation of the fluctuating pressure which actually contributes to maximize (or minimize) a certain response. In order to take into account the influence of the correlation of the fluctuating pressures over the whole structures, the LRC method has been implemented, obtaining a design peak factor, g, of 2.7 and 5.13 respectively for S_{11} and S_{22}. Inserting the design peak factors in the Optimized-Peak-Load-Distributions approach, equivalent static design wind loads composed of linear summation of the first 89 eigen-modes, for S_{11}, and of the first 81 eigen-modes, for S_{22}, have been then obtained.

Finally, design resonance factors have been provided: 1.18 for S_{11} and 1.08 for S_{22}.

3.9. BASIC REFERENCES

[a] BTR, Bautechnik Bei Kühltürmen 1990. VGB-Richtlinie, VGB-R 610 U, VGB Vertlag, Essen 1

[b] Davenport A.G. 1961. The application of statistical concepts to wind loading of structures. *Proceedings Institution of Civil Engineers (UK)*, **19**, 449-471

[c] Davenport A.G. 1964. Note on the distribution of the largest value of a random function with application to gust loading. *Proceedings Institution of Civil Engineers (UK)*, 187-196

[d] Davenport A.G. 1967. Gust load factors. *J. Struct. Division*, ASCE, **93,** 11-34

[e] Farell C. et al. 1976. Mean Wind Loading on Rough-Walled Cooling Towers. *J. Struct. Eng.*, ASCE, **102**(6), 1059-1081

[f] Hashish M.G., Abu-Sitta S.H. 1974. Response of Hyperbolic Cooling Towers to Turbulent Wind. *J. Struct. Division*, **ST5**, 1037-1047

[g] Holmes J.D. 1990. Analysis and synthesis of pressure fluctuations on bluff bodies using eigenvectors. *J. Wind Engrg. and Ind. Aerodyn.*, **33**, 219-230

[h] Holmes J.D. 1992. Optimised Peak Load Distributions. *J. Wind Engrg. and Ind. Aerodyn.*, **41-44**, 267-276

[i] Holmes J.D. 2002. Effective static load distributions in wind engineering. *J. Wind Engrg. and Ind. Aerodyn.*, **90**, 91-109

[j] Kasperski M. 1992. Extreme wind load distributions for linear and nonlinear design. *Engineering Structures*, **14**, 27-34

[k] Kasperski M., Niemann H.-J. 1992. The L.R.C. (load-response-correlation) – method. A general method for estimating unfavourable wind load distribution for linear and nonlinear structural behaviour. *J. Wind Engrg. and Ind. Aerodyn.*, **41-44**, 1753-1763

[l] Iwatani Y. 1982. Simulation of Multidimensional Wind Fluctuations having any arbitrary Power Spectra and Cross-Spectra. *J. of Wind Engrg. and Ind. Aerodyn.*, **11**, 5-18

[m] Niemann H.-J. 1980. The influence of realistic mean wind loads on the static response and the design of high cooling towers. *Engineering Structures*, **2**, 29-34

[n] Niemann H.-J. 1980. Wind Effects on Cooling-Towers Shell. *J. Struct. Eng.*, ASCE, **106**(3), 643-661

[o] Niemann H.-J. 1984. Modelling of wind loads with regard to gust effects. *Engineering Structures*, **6**, 29-34

[p] Niemann H.-J., Ruhwedel J. 1980. Full-scale and model tests on wind-induced, static and dynamic stresses in cooling tower shells. *Engineering Structures*, **2**, 81-89

[q] Niemann H-J., Zerna W. 1986. Impact of research on development of large cooling towers. *Engineering Structures*, **8**, 74-85

[r] Vellozzi J., Cohen E. 1968. Gust Response Factor. *J. Struct. Division*, ASCE, **94**, 1295-1313

[s] Vickery B.J. 1966. On the assessment of wind effects on elastic structures. *Aust. Civil Eng. Trans.*, **CE8**, 183-192

3.10. LIST OF PUBLICATIONS

[1] Bartoli G., Borri C., Pastò S. 2002. Frequency domain dynamic response of RC cooling tower shells under turbulent wind. *Int. J. of Fluid Mech. Research*, **29**

[2] Bartoli G., Borri C., Pastò S. 2002. Indagine sperimentale e numerica per la valutazione dei carichi di progetto agenti su una torre di raffreddamento soggetta alle azioni del vento (in Italian). *Proceedings, 7th National Conference on Wind Engineering IN-VENTO-2002*, Milano

[3] Bartoli G., Borri C., Pastò S. 2004. Equivalent Static Wind Loads for Background and Resonant Response of an Isolated RC Cooling Tower Shell. *Urban Wind Engineering & Building Aerodynamics COST Action C14*, Rhode-Saint-Genese, Belgium, May 2004

[4] Borri C., Orlando M., Spinelli P. 1999. Wind induced stresses on two neighbouring cooling towers. *Proceedings of 10th ICWE*, Copenhagen, Denmark, Balkema, Rotterdam, **1**, 401-408

[5] Borri C., Pastò S. 2004. Defining Design Wind Loads on RC Cooling Tower Shells. *Proceedings 5th International Symposium on Natural Draught Cooling Towers*, May 2004, Istanbul (in press)

[6] Facchini L., Bartoli G., Borri C. 2002. Simulation of non-Gaussian wind pressures on a 3-D bluff body and estimation of design loads. *Computer & Structures*, **80**, 1061-1070

[7] Orlando M. 1999. *Indagine Sperimentale e Analisi Numerica degli Effetti di Interferenza su Due Torri di Raffreddamento Adiacenti (in Italian).* PhD Thesis, Università degli Studi di Firenze, Dip.to di Ingegneria Civile

[8] Orlando M. 2001. Wind induced interference effects on two adjacent cooling towers. *Engineering Structures*, **23**, 979-992

WITH CONTRIBUTION FROM:

Claudio Borri, Università degli Studi di Firenze
Luca Facchini, Università degli Studi di Firenze
Maurizio Orlando, Università degli Studi di Firenze
Stefano Pastò, Università degli Studi di Firenze

4 Cables and cable supported systems

Nicola Cosentino
University of Bologna

4.1 INTRODUCTION

Different themes, often different in nature and from different Research Units, concern the cables and the cable supported structures. Common denominators, for such structures, are the high flexibility, with possible important geometrical non linear effects, and the very small inherent damping of the cable systems.

In this chapter, the following arguments are treated:

- Suspended large span roofs: the case of the New Braga Stadium;
- Cable-membrane structures: the case of the Montreal Stadium Roof;
- Removable guyed mast for mobile phone networks;
- Wind tunnel scale model testing of suspended cables;
- Rain-wind induced vibration of stay cables;
- Energy dissipation systems for stay cables.

4.2 SUSPENDED LARGE SPAN ROOFS: THE CASE OF THE NEW BRAGA STADIUM

Due to the geometric complexity, the flexibility which induce large displacement and the small inherent damping, several aspects have to be taken into account during the design stage of a suspended large span roof. The analysis of wind induced vibration requires, for instance, the evaluation of the pressure coefficients, the structural response analysis, the investigation of possible aeroelastic effects, etc, up to the design of additional energy dissipative system to reduce the vibrations themselves. A particularly interesting application of the techniques to study the cited problems has been made for the New Stadium built in Braga (Portugal) for the Euro 2004 Games. The main scope of the research was to review the design process from a unitary point of view. In fact, in the Authors experience, the different problems are usually studied by different specialists and the interference between the various aspects is often lost. Moreover, sometimes it happen that different analyses give contrasting results. Finally, in the present research, the most recent and advanced techniques to investigate some aspects of the problem have been applied. In Figure 4.1, an image of the aeroelastic model tested in the wind tunnel is shown.

Edited by Gianni Bartoli and Francesco Ricciardelli, WINDERFUL: Wind and INfrastructures: Dominating Eolian Risk For Utilities and Lifelines, ISBN 88-8453-138-1, ©2004 Firenze University Press

Figure 4.1 Aeroelastic model tested in the Politecnico di Milano boundary layer wind tunnel.

4.2.1 Wind induced response analysis from the rigid model wind tunnel data

Wind pressures are derived from a wind tunnel study, on a rigid scaled model, carried out by the RWDI [b,c]. Since the pressure time histories were simultaneously measured at different points, within the upper and the lower sides of the roof panels, the instantaneous pressure fields are available. As a matter of fact, due to the different spatial distribution of upper and lower pressure taps, preliminary interpolation is required to obtain the differential pressures, which represent the actual load on the structure.

The orthogonal decomposition techniques [a] have been adopted to simplify the pressure representation, and to reduce the computational effort. The structural response to wind actions has been determined by separately evaluating (1) the mean response, (2) the quasi-steady response and (3) the resonant response. The first term simply takes into account the mean pressure distributions. The second one is obtained by performing a classical covariance proper orthogonal decomposition (POD). The third one takes into account the dynamic amplification of a suitable number of structural vibration modes, each one of them being excited by the unsteady wind pressures.

The static responses and the modal parameters used in the above cited calculations have been evaluated by mean of a finite element model of the structure, implemented on the structural analysis program STRAND. Linear analyses have been performed, the geometric stiffness matrix corresponding to the equilibrium configuration under gravity loads.

An unsteady multivariate pressure field can be usefully simplified by projecting (POD) it on the space generated by the eigenvectors of the covariance matrix of the original field. Two main advantages can be achieved by this technique. Firstly, the new fields (pressure modes) are mutually uncorrelated, giving rise to advantages which will be explained below. Secondly, the energy content of the complete multivariate field is usually well represented by few components in the transformed space, allowing the representation of the effective pressure field by mean of few pressure modes. A possible third advantage, which is still debated by the scientific community, consists in the physical correlation between pressure modes and aerodynamic phenomena (such as incident wind turbulence, vortex shedding, etc.). As a matter of fact, since the covariance is fully representative of the correlation (for $\tau = 0$) only for Gaussian random processes, the pressure modes are mutually uncorrelated only for Gaussian multivariate pressure fields. It means that the POD method can usefully applied for global actions (were the non-Gaussianity becomes negligible) but not for the evaluation local loads.

The design wind speed has been conservatively assumed to be constant for all wind incidence, without taking into account for directionality effects. The value 46.5 m/s (referred to 600 m height), corresponding to the wind blowing approximately from the south has been adopted.

The experimental data show the pressure coefficients to be significantly lower – both in mean values and standard deviation – than those reported by standards (EC1) for similar geometry. Large values are essentially confined to the roof borders, corresponding to local vortex shedding. Hence, vortex induced pressures seem to not affect the global roof dynamics. Nevertheless, they can induce significant local stresses on the roof panels. Thus, it is recommended to study aerodynamic devices (as, for instance, rounding or introducing discontinuities on borders) able to reduce the peak pressures.

The proper orthogonal decomposition has been used to simply evaluate the quasi-steady effects. The derived quasi-steady responses result lower than those derived by the standard (EC1) approach. Hence, the spatial uncorrelation effects should be greater than those approximately taken into account by the EC1 simplified procedures.

Very important resonant effects have been found. They are dominant in determining the peak responses for most of the wind directions. It is important to observe that these effects are strictly related to the damping ratio (which has been assumed to be 1% for all considered vibration modes). On the other hand, the structural uncertainties – at the present state of the knowledge – do not allow to reliably assume larger values for ξ.

The large evaluated resonant effects suggest to study in depth the possibility to have exciting aeroelastic phenomena and to foresee, at the design stage, the possibility of introducing damping devices. At this purpose, an aeroelastic model of the roof has been tested in the BLWT of Dept. of Mechanics of Politecnico in Milano. In the first stage of the experiments, the aeroelastic stability of the roof (present design) is tested. In the second stage, the effect of a proposed damping system (stabilizing and damping stays located in correspondence of southern and northern roof inner vertices) is studied.

4.2.2 The aeroelastic model

The tests have been performed on a 1:70 aeroelastic model of the Braga stadium, under the following conditions:

- laminar flow, without surrounding topography, to check the presence of possible forms of aeroelastic instabilities;
- turbulent flow, with surrounding topography, in order to establish the response of the roof structure to the action of turbulent wind, in terms of roof acceleration and displacement and strain, and related mean drag forces.

In order to measure the response of the roof structure to the wind, accelerometers have been placed on the roof, also aiming at the definition of the modal shapes, to be compared with the theoretical one, for the full-scale structure. Moreover, the global drag forces acting on the roof are measured by means of properly designed load cell, and the stresses on critical points on the roof are as well monitored by means of strain gages. The following point have been treated in the tests:

- verification of the eigenfrequencies and related mode shapes of the aeroelastic model;
- response of the structure under laminar flow;
- response of the structure under turbulent flow, with surrounding topography;
- effects of damping devices applied to the corners of the roof, designed to reduce the vibration amplitude, in case their bend is not acceptable.

The activities of the present work have concerned the design, preparation and set-up of the aeroelastic model, that proved to be adequate for the purpose, in terms of frequencies, modal shapes and damping. The results from the wind tunnel test have shown that:

- The aeroelastic stability has been proved, up to 7m/s, corresponding to 58m/s in the full scale;
- The response to turbulent wind, with the effect of surrounding topography, showed, at the nominal design speed with 20% turbulence, amplitude levels that, at full scale, are of the order of 40÷50cm, with acceleration due to the first modes that reach peaks up to 1.5÷2m/s^2 and RMS values of 0.46m/s^2 A peak value of 2m/s^2 means that the overload due to dynamic motion is 20% of the dead load.
- The amplitudes of vibration generally found at the maximum speed are to be considered not acceptable, since there are uncertainties on the effective value of the turbulence on site and of the damping of the structure, which can cause a significant variation from the vealues found on the model. Therefore, in order to decrease such levels, and control their variation due to the parameters uncertainties (real damping and turbulence level), damping devices can be installed on the structure.
- In order to simulate their effect, proper dampers have been designed and implemented on the model, in order to increase the structural damping up to a maximum value of 7-8%. This allow to decrease the vibrations at 50% of the original global levels of vibration while the amplitude of the torsional frequency is reduced by a factor three, so showing the effectiveness of such devices. In the full scale, the required damping of each of the four dampers is in the range 100-l50kNs/m, i.e. as an ordinary ant-yaw dampers of train.

4.2.3 The sensibility analysis

Eighteen different wind directions were analyzed (i.e. wind directions from 0° to 340° spaced 20°). The following results are obtained: a) the sensibility of the failure probability of the roof to the spatial random distribution of wind loads, b) the wind direction that drive the structure to fail with most probability (considering all wind direction with a uniform distribution), c) the points of the roof that will fail with most probability, and d) the spatial distribution of wind loads that drive the structure to fail with most probability.

In order to identify the most dangerous wind direction, the minimum reliability index β for each direction was calculated. Therefore 300° resulted the wind direction that drives the structure to fail with most probability. The following results are related to that wind direction.

The zone with smallest values of β is related to the zone with maximum bending moment for the gravity load on the border where the wind load attack the roof.

The reliability analysis provides also the spatial distribution of wind loads that drive the structure to fail with most probability. A minimum Cp value near –3.0 is obtained concentrated near the border where the wind attack the roof. Note that most of the roof has small values of Cp showing the high concentration of wind pressure that is expected at failure. Note that this method provides the worst spatial wind load distribution associated to the wind variability and the weakness of the roof. Therefore this reliability-based method is better than the Proper Orthogonal Decomposition (POD), since in the POD method the obtained distribution depend only on the wind load variability itself.

The failure of the structure has considerable sensibility to the spatial distribution of wind loads. Note that the spatial distribution of wind loads that drive the structure to fail with most probability is considerably different to that assumed in codes for design. However, the values are acceptable for static wind analysis.

It is recommended the careful study of the dynamic response of the slab to control the possible amplification due to the roof flexibility. If the information is available, it should be useful to consider the frequency of high wind velocities at different directions to combine with the obtained sensibility of the roof at each direction.

4.2.4 Preliminary design of an additional damping system

The analysis of wind effects on the new Braga Stadium showed that the wind induced vibrations can reach very high amplitudes. Vibration amplitudes are very sensitive to the inherent structural damping ratio (approximately inversely proportional to $\xi^{0.5}$). In these analysis a damping ratio of 1% was assumed for each natural vibration mode, but strong uncertainties characterize this value. Whenever the actual inherent damping will be lower than 1%, the wind induced vibrations could reach even larger amplitudes than the estimated ones.

Hence, it seems important to monitor the actual structural damping (at this aim a monitoring system has been designed and is working on the real structure). If it results insufficient to adequately contain the vibration amplitudes, it will be necessary to add a damping system which guaranties an acceptable level of wind induced oscillations. In the following, the main properties of such a damping system have been preliminary evaluated.

The presence of a stiff beam at the inner borders of the roof (from points 1 to 3 and 4 to 6 in Figure 4.2a) induces the firsts natural modes, which are the most excited by the wind turbulence, to have the largest amplitudes at the ends of the beams themselves. Thus, the beam ends (points 1, 3, 4 and 6) are among the most quoted to locate external dampers. These are also among the few locations compatible with the architectural requirements.

Hence, the analyzed damping system consists of four linear viscous dampers located at the inner vertices of the roof; C represents the damping coefficient of such a dampers. As a matter of fact, the dampers will be located at the ground level and connected to the roof by mean of tensile strands. Thus, a mass or a spring will be necessary to avoid compression in the cables. Nevertheless, in the present preliminary analysis the only presence of a simple linear viscous damper has been considered, without taking into account the added mass or stiffness, the mean value of the cable tensile force, etc.

A deeper stage of the design should evaluate the specific problems as, for instance, the opportunity to realize a friction damping system rather than a viscous one, the devices to avoid the cable slackening, the support induced cable excitation, etc.

A preliminary estimation of the damping system efficiency has been carried out by mean of the eigenvalue analysis of the non-classical damped system. The eigenproblem is formulated by considering the firsts 10 modes of the undamped structure and the 4 added linear viscous dampers. The firsts 4 complex modes have been analyzed (the higher ones requiring a more refined model). Figure 4.2b shows the damping ratio associated to such modes, for different

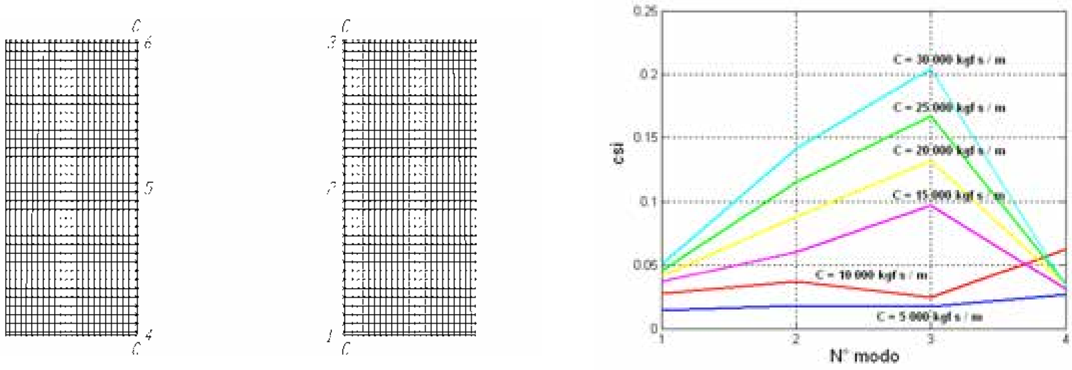

Figure 4.2 Dampers location and monitored points (left) and damping ratio of complex modes (right).

values of the damping coefficient.

In order to evaluate the realistic behavior of the damping system and the maximum force produced by the dampers, different time history analysis of the structure subjected to the pressure fields measured in the wind tunnel have been carried out. A significant reduction of the oscillation amplitudes can be obtained by using viscous dampers with a damping coefficient C=15000 kgf s/m. The subsequent damping force will reach an amplitude of about 6 tons, as order of magnitude.

4.3 CABLE-MEMBRANE STRUCTURES: THE CASE OF THE MONTREAL STADIUM ROOF

The drastic reduction in the ratio of permanent weight to variable load makes lightweight structures particularly sensitive to the effects of wind and snow. The dynamic nature of wind action can cause oscillations and deformations of such amplitude that they jeopardize the function of the roof and, in the worst cases, its structural stability. On the other hand, the static effect of snow represents an extremely heavy load for this type of structure, even reaching as high as 70-80% of the total load. Melchers demonstrated that one of the primary causes of collapse (corresponding to approximately 45% of the cases analyzed) lies in an erroneous evaluation of the loading conditions and of the structural response. With improvements in the methods for in-depth analysis in the design of lightweight wide-span roofing, theoretical studies can and must be used in combination with experimental tests performed in wind tunnels and in situ. From the observation of structures that have completely or partially collapsed:

- due to snow, e.g. the Hartford Coliseum (1978), the Pontiac Stadium (1982), the Milan Sports Hall (1985) and the Montreal Olympic Stadium (1992);
- due to wind, e.g. the Montreal Olympic Stadium (1988);
- due to the effects of water, e.g. the Minnesota Metrodome (1983) inflatable roof

The aim of the present study was to contribute, both in qualitative and in quantitative terms, towards explaining the failure phenomena that have occurred on several occasions in the roof of the Olympic Stadium in Montreal in apparently unexceptional conditions. See references [1,2,3] and [d] to [l] for theoretical and analysis details.

4.3.1 The static analysis

The "report" from the committee of experts suggested submitting the roofing to analyses in the non-linear field to test their assumptions and clarify certain aspects under debate. The present study, starting from data on the geometry, materials, and design details provided in said report, proposes a static analysis based on a new numerical model of the structure, comparing and discussing the results, and emphasizing the principal characteristics of the structural response.

The observers emphasize how the first collapse (the situation studied in this work) coincided with a wind of low intensity (approximately 19 m/s) coming to bear at an angle corresponding to approximately 60° between the direction of the wind and the main axis of the roof. Moreover, the structure was characterized prior to collapse by an antimetric dynamic movement with respect to its lesser dimension inducing an oscillation with an amplitude of around 5 meters.

The regime of major displacements that is dominant in this case is revealed by the non-linear relationship with the load. As we move towards the back of the roof, the cables become progressively more vertical and thus, unlike the situation with the load due to snow, they are only able to respond independently and adequately to lifting up to less than 50% of the final load. Under the effect of the total load, the prestressing applied in the 0 state is almost completely lost. As the load increases, the initially-linear displacement to load ratio demonstrates a radical non-

The deflection at the midline of the cables increases consistently, in a quasi-linear trend for the slanting cables and in a non-linear manner for the more vertical ones. The stress in the principal suspension cables diminishes to values of less than 100 N/mm^2 for the oblique cables and less than 50 N/mm^2 for the vertical cables, since the latter values are determined almost entirely by the self weight of the cables themselves.

The loss of tension on the suspension cables releases the membrane from the intermediate supports and the roof, as mentioned earlier, acquires a pressostatic behavior. In the connection cables, the midline deflections are recovered to some degree by the majority of the cables. Similarly, the stress increases in almost all the cables, but it is only in a couple of cases that this reaches values very different from the baseline, to the point of exceeding 450 N/mm^2. Here again, the course of the stresses proves to be non-linear.

Another main difference with respect to loading due to snow concerns the cable around the perimeter which continues to undergo no major displacements, but is subjected to maximum stresses in excess of 500 N/mm^2 along the majority of its perimeter, and not just at the front.It is evident that in both the static load conditions studied, the roof is incapable of opposing the load with sufficient stiffness and its global structural behavior changes to acquire a function capable of withstanding the exogenous action.

4.3.2 The dynamic analysis

Due to the flexibility of the Montreal Olympic Stadium roof, fluid acts on the directly exposed outer surface of the Montreal Olympic Stadium flexible roof as well as on its internal lining, depending on the latter's exposure to the same fluid's field.

The roof encloses a volume that can be classed as an appendage of external fluid, since connection is via exchange surfaces, such as stand access openings, etc. In case of large openings, the fluid field produces point-to-point variable internal pressures, acting on the internal side, which are rather small but not negligible when measured against external pressure level. Conversely, such pressures are not generated when the volume is closed.

The dynamic analysis covers structure high flexibility and its effects on structural response and applied loads, by introducing the following simplifications:

- structural deformation has no effect on the fluid motion field;
- wind speed is simulated with a classical Gaussian distribution and speed is transformed into pressure with a quasi-static formula;
- the constrained fluid volume effect modified by structural movements is introduced with a simplified model for which: (a) structural model speed are small when compared to fluid pressure wave propagation rate; (b) structural periods are high compared with time required for overcoming internal pressure propagation-induced transition.

Based on these hypotheses, internal pressure can be conceived as distributed quasi-homogeneously and structural dynamics can be described in a simplified form. The final fluid field structure-induced effect in the foregoing hypotheses is thus given by the algebraic sum of external and internal pressures, both of follower type, induced by the structural motion.

These hypotheses thus enable concentrating on the overall macroscopic variables of fluid volume and average internal pressure tied to the environmental conditions, i.e. temperature. Such variables are connected by a non-linear low implemented and solved in the time domain by the LOKI calculation code.

Dynamic analyses according to Borri and Zalthen [t], and Lazzari [1,2], are based on the sum of two transitory: one for average load balance and the other for the study the structural response due to pressure sample time series. Simulating speed fields and pressure coefficients obtained in Western Ontario, Canada wind tunnel generates load history.

The speed field was simulated at a 60° angle of incidence between average wind direction and main structure axis, this being the wind angle that had led to the roof breaking. Dynamic analyses on the structure numerical model were performed with three different boundary conditions and the wind applied was the same for all the following analyses:

- analysis I: exchange surface ∞, no fluid structure interaction effect;
- analysis II: 100 m^2 exchange surface, permeable structure;
- analysis III: 50 m^2 exchange surface, permeable structure.

The condition at which structural dynamics occur was postulated as being isothermal: since breakage occurred at $T > 20$ °C, $T = 298.15$ °K (25 °C) was assumed.

Analysis of the roof stress-load and displacement-load diagrams shows that structure behavior is distinctly non-linear. Major displacements under various load conditions lead to significant variations to roof structural stiffness and tensional state zeroing. The linearity study is consequently not significant and has little bearing on real roof behavior.

Simulating static and dynamic acting loads requires using follower forces to follow up significant displacements. Tensional state zeroing and local instability further complicate solving the problem and require using highly specialized rugged software. The roof features low structural stiffness and consequent excess deformability. Studies here carried out, enable identifying and better understanding its structural behavior, emphasizing the problems of the two cases considered and the potential solutions thereto.

4.4 REMOVABLE GUYED MAST FOR MOBILE PHONE NETWORKS

The fast development of mobile phones gave rise to a widespread diffusion of base stations to link mobile phones to the rest of the mobile and fixed phone network.

The radio links between mobile phones, base stations, and terminals connected to the main telephone network are operated through antennas with different sizes and shapes. These antennas are usually supported by slender structures that can be either free-standing and/or cable-stayed and thus the wind load represents the main design concern. Furthermore, the base stations are often removable (raw land sites) to accommodate for the required volume of users at any given area in the different times of the year. It follows that complex problems arise when designing, constructing, and maintaining such structures. Many of these problems have not found a final solution yet. First of all, the estimation of the appropriate wind loads, namely the pressure coefficients the aerodynamic and aeroelastic loads, is not trivial given the complex flow-structure interactions arising from the presence of several elements, such as the supporting structure, the cables, and the antennas. The different working condition make the aerodynamic loads uncertain and variable from case to case [m]. Useful information can be obtained by suitable experimental tests using wind tunnels and/or through on-site measurements.

Another important issue is the correct evaluation of the soil-foundation-structure interactions. In particular, given the need for fast and removable installations, the foundation structure is often made of an assembly of steel trusses and concrete slabs simply placed on the ground, providing a low-stiffness basement, which increases the overall displacements.

Moreover, the inherent dynamic nature of the wind load, and the lightweight of the supporting structures can make the evaluation of the mechanical damage due to stress fluctuations (fatigue) one of the main concerns in the design process, besides the estimation of the peak response. Indeed, fatigue failures of critical components of guyed masts exposed to turbulent wind have been reported in literature, with special reference to the connections between the cables and the structure [n].

Finally, it has to be recalled that severe requirements in terms of maximum displacements and rotations of the antennas have to be satisfied, for the radio signals to be successfully transmitted. This is a relevant issue when the stays are at a large angle with the ground, in order to limit the base dimensions of the mobile base station.

The described features have to be carefully considered when dealing with the system reliability and, in particular, with the safety to extreme winds and the serviceability.

Within this context, a research project was started by the Perugia Research Unit aiming at the following achievements:

- full-scale and model scale wind tunnel experimental tests;
- full-scale on-site measurements of both wind characteristics and structural response;
- estimation of the aerodynamic loads using on-site measurements and wind tunnel tests;
- structural identification using on-site measurements and wind tunnel tests;
- numerical modeling, assessment, and optimization of the supporting structure;
- mechanical damage and service life estimation.

The results of the first stage of the research on a typical cable-stayed mast used for mobile base stations, aimed to characterizing the aerodynamic coefficients to be used for its design, are reported in [4,5,6].

4.4.1 The raw land site

The mobile base station studied in the research project of the previous section is often referred to as raw land site. Three are the main components of these base stations (Fig. 4.3): the supporting structure (cable stayed mast with steel pipe cross section and 6 orders of three stays linked to the precast reinforced concrete foundation slab), the antennas and/or dishes for signal transmission (two order of two dishes at height 28 and 29 m, one order of 3/6 prismatic antennas over 30.5 m), the technological devices used for controlling the correct working operation of the transmission systems (placed into an aluminum shelter).

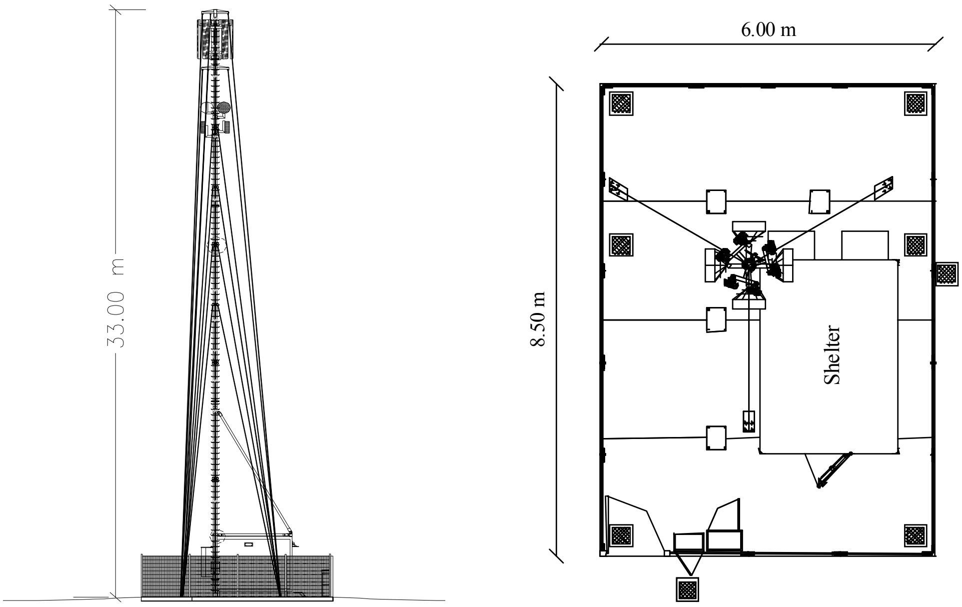

Figure 4.3 Raw land site with a cable-stayed supporting mast: (left) elevation, (right) plan view.

4.4.2 Experimental tests

Several models of structural portions of the system in Fig. 4.3 were tested at prototype scale (1:1) using a wind tunnel facility. Three of these models are reported in [4] and are referred to as setup A, setup B, and setup C. Setup A (Fig. 4.4 – left) was assembled with part of the supporting mast with pipe section (170 cm), safety ladder (181 cm), rack for the antennas cabling, supports to secure the stays, adjustable dish with 60 cm diameter. In order to estimate the aerodynamic coefficients, tests were repeated for partial configurations obtained removing the single elements described above. Some of these configurations can be considered as representative of portions of the structure at different heights.

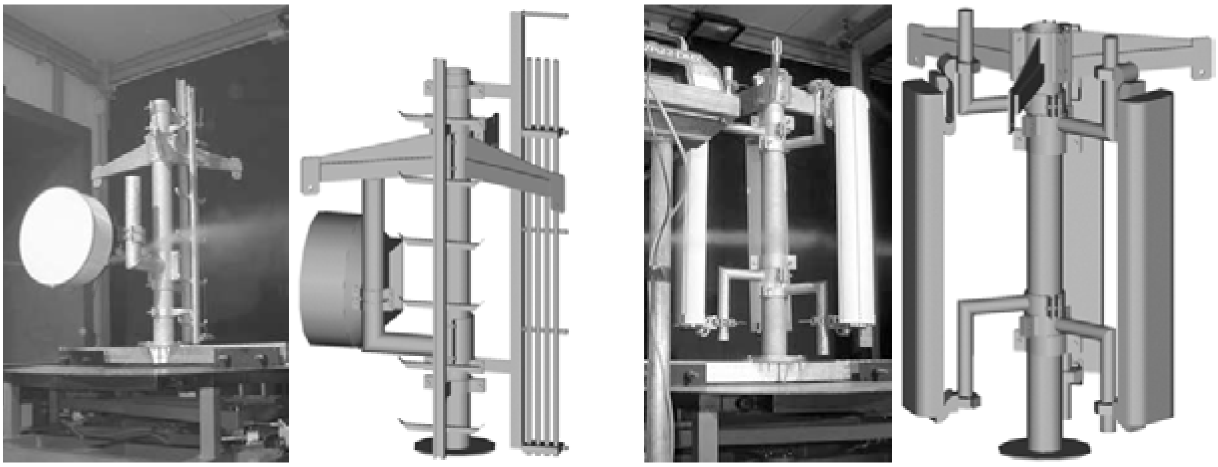

Figure 4.4 Picture and CAD model of the experimental setup A (left) and experimental setup B (right)

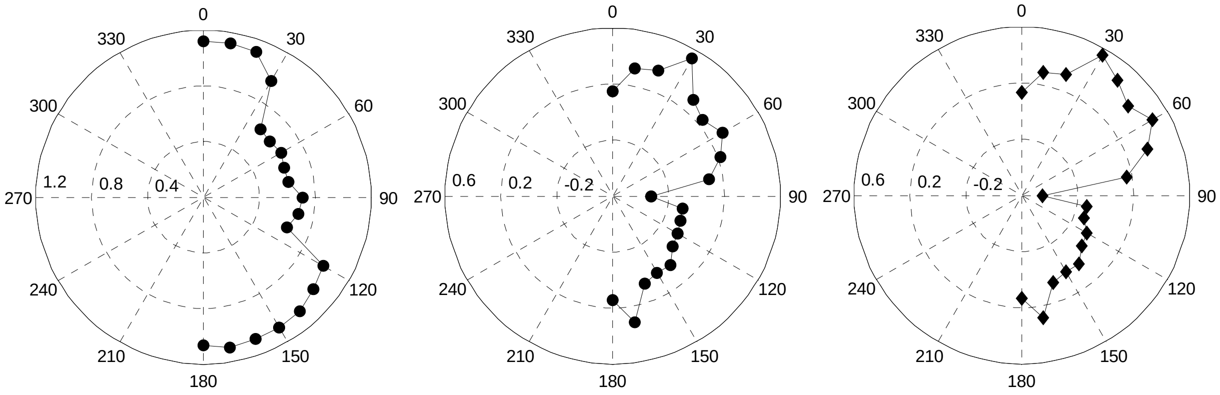

Figure 4.5 Experimental setup A: drag coefficient (left), lift coefficient (middle), CL/CD ratio (right)

Setup B (Fig. 4.4 – right) was assembled with part of the supporting mast with pipe section, supports to secure the stays, three antennas placed at a 120 degree angle with each other. Setup C is obtained from setup A removing the adjustable dish [4].

The influence of the oncoming wind direction on the aerodynamic coefficients was also considered in each of the configurations, by varying the impinging wind direction with 10 degree steps. The relevant forces were measured for each oncoming wind direction, and normalized to obtain the aerodynamic force coefficients (drag CD, lift CL, moment CM)[5]. Some of the results obtained with the experimental setup A are shown in Fig. 4.5.

The structural response associated with different load models based on these coefficients was then evaluated and compared to that obtained using the EUROCODE-1 standard provisions for wind loads [5]. Finally, different directions of the oncoming wind were used to perform a sensitivity analysis that identifies the peak response of the structure, and points out the role of the (usually neglected) lift forces [6].

4.5 WIND TUNNEL SCALE MODEL TESTING OF SUSPENDED CABLES

One of the main interesting problems in the performance of cables under dynamic loading is the fatigue life evaluation. This aspect is mainly studied in the maintenance and retrofitting of suspended bridge where vehicular and wind loads induce stress variations in the primary cables that could result in component fatigue.

This requires considering the following topics:

- adequate characterization of the wind velocity field (mean speed and turbulence stochastic processes),
- analytical and/or numerical modeling to describe the mechanical behavior of the cable,
- full-scale and model scale wind tunnel experimental tests,
- assessment of the random vibration under stochastic loading,
- mechanical damage and service life estimation.

The results of the first stage of the research aimed to characterize the dynamic response of cables under wind loading and to check numerical model are reported here. In particular, several experimental tests have been carried out on a cable model using a wind tunnel facility.

4.5.1 The wind tunnel tests

The experimental tests were carried out at the at the wind tunnel of the CRIACIV in Prato (Italy), which is a boundary-layer wind tunnel.

The tunnel is of the open type and the target wind speed (in the range 0-35 m/s) is obtained by means of both the regulation of the pitch of the 10 blades constituting the fan and the rotating speed. The tunnel has an overall length of 22.09 m and the test section has dimensions of 2.40x1.60 m.

The model of the cable was build with 48 segments, each one consisting in a cylinder of cherry-wood 40 mm in diameter and 40 mm in length (the weight is 36 g). The diameter of the segments was chosen in reference to the weight of the whole cable and to the initial axial load at the supports. The sag of the cable after it was suspended across the gallery was 1/10 of the length, which is typical of cables used in suspension bridges. In this configuration, the axial load was about 22.5 N and the relation between the geometric and mechanical quantities [p] was

$$\sinh\left(\frac{Wl}{2HL_0}-\frac{W}{2EA_0}\right)=\frac{W}{2H} \tag{4.1}$$

where W is the weight of the cable, H is the horizontal component of cable tension, L_0 is the unstrained length, l is the distance between supports, A_0 is the uniform cross-sectional area, E is the Young’s modulus. The cable was suspended so that it lay in the middle band of the tunnel where the flow was more uniform (see Fig. 4.6a).

Furthermore, the diameter of the segments was chosen to furnish a sufficiently wide area to the action of the wind during the tests. The segments were connected by a 0.7 mm-diameter steel strand (with a Young’s modulus equals to 165000 MPa), which was chosen to model the axial

Figure 4.6 The experimental model of the cable (left), the cable-end supports (right top) and the laser transducer (right bottom).

rigidity of the cable, without giving a significant flexural stiffness. The wire passes across holes coaxial to the axis of the cylinder, and joined to it with a polyurethane foam. Particular attention was devoted to place the segments at a sufficiently large distance to avoid contact during the motion of the cable (the distance between the segments was about 8 mm). The overall length of the cable was about 2480 mm.

The cable was supported at its ends by means of two identical devices, each one having a pulley and a ball bearing to avoid, as much as possible, friction and torsion in the cable, which may corrupt the measure of the axial load (see Fig. 4.6b).

The axial load was measured by means of two load cells, with a measurement range of 0-120 N. The displacements of the middle point of the cable were measured by mean of a laser system: two laser transducer were used to follow the movement of the selected point (see Fig. 4.6c). The

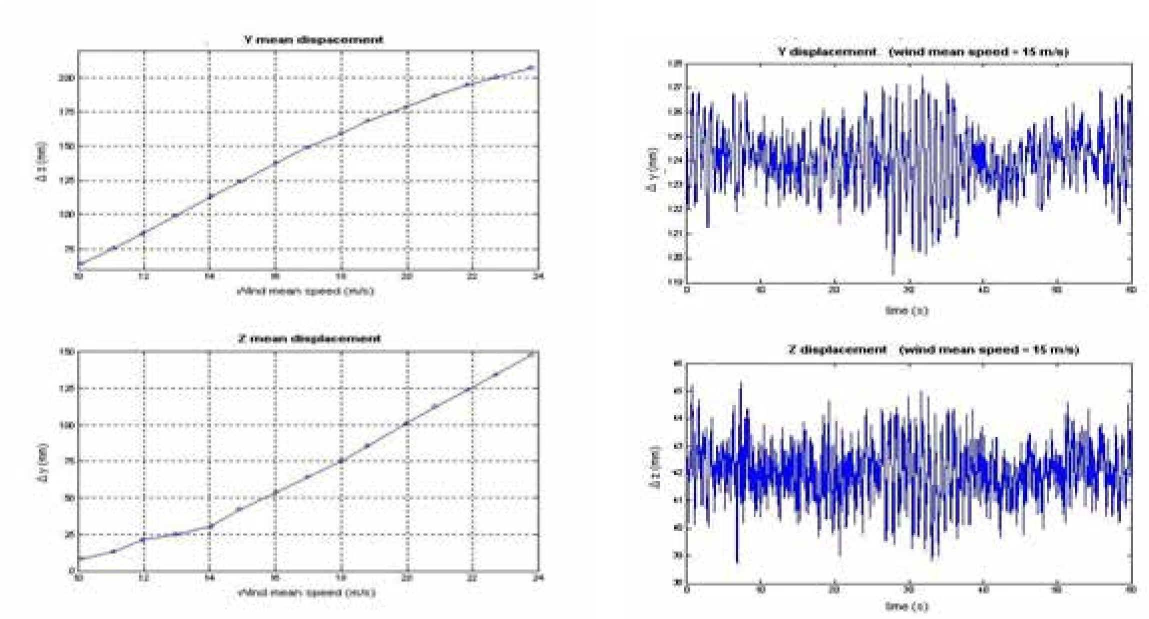

Figure 4.7 Mid-point mean displacements (left) and mid-point displacement history (wind speed of 15 m/s) (right).

measured values were corrected to consider the transducers overall displacement before and after the wind flow started.

The tests were carried out at different wind velocity, both with laminar flow and with turbulence flow. In laminar flow, two sets of data were acquired: in the first, attention was devoted to measuring the displacement of the middle point of the cable, in the second the drag force was measured. The turbulence flow was obtained with the insertion of a grid in the wind tunnel. Each test had duration of 60 seconds, and data were acquired at 1000 Hz. The wind speed range was from 10 m/s to 24 m/s, by increments of 1 m/s each test.

During a first set of experimental tests with laminar flow, the measured values were the horizontal axial loads at the supports, the wind velocity, the displacement of middle point of the cable. In a successive set of experimental tests with laminar flow and with turbulence flow the drag forces were recorded too. Two load cells, with an equal range of 0-120 N, were used. Some results, in terms of variation of horizontal axial force, mid-point mean displacement and mid-point displacement history, recorded during the first set of tests, are reported in Figures 4.7 and 4.8a.

4.5.2 Numerical modelling

The cable was modeled numerically assuming a non-linear behavior: the non-linearity is geometrical, whereas the mechanical behavior is linear. A Finite Element Method, adopting a two joint truss element, was used. At t + Δt time instant, the equation that rule the problem is:

$$M\,{}^{t+\Delta t}\ddot{U} + C\,{}^{t+\Delta t}\dot{U} + ({}^{t}_{0}K_L + {}^{t}_{o}K_{NL})U = {}^{t+\Delta t}_{0}R - {}^{t}_{0}F \tag{4.2}$$

where M and C are the mass and damping matrices, U is displacement vector, F and R are the applied and unbalanced forces. The K_L elastic and K_{NL} geometric stiffness matrixes were determined assuming large displacements, large rotations and small deformations, simplifying in this way the model. The elastic stiffness matrix and the geometric stiffness matrix [q] assumed respectively the following expressions:

$${}^{t}K_L = \frac{E^0A}{L}\begin{bmatrix} 1 & 0 & 0 & -1 & 0 & 0 \\ 0 & 0 & 0 & 0 & 0 & 0 \\ 0 & 0 & 0 & 0 & 0 & 0 \\ -1 & 0 & 0 & 1 & 0 & 0 \\ 0 & 0 & 0 & 0 & 0 & 0 \\ 0 & 0 & 0 & 0 & 0 & 0 \end{bmatrix}, \quad {}^{t}K_{NL} = \frac{E^0A}{L}\begin{bmatrix} 1 & 0 & 0 & -1 & 0 & 0 \\ 0 & 1 & 0 & 0 & -1 & 0 \\ 0 & 0 & 1 & 0 & 0 & -1 \\ -1 & 0 & 0 & 1 & 0 & 0 \\ 0 & -1 & 0 & 0 & 1 & 0 \\ 0 & 0 & -1 & 0 & 0 & 1 \end{bmatrix}. \tag{4.3}$$

The problem was solved by an incremental and iterative procedure. This consisted of a modified Newton-Raphson algorithm, while the analysis in time domain was carried on by mean of α-H.H.T. (Hilbert-Hughes-Taylor) method, which is a generalization of Newmark method.

The numerical model of the cable was made of 20 two joints truss elements (see Fig. 4.8b), assuming for the axial stiffness EA the value 63.50 kN and for the mass density the value 0.75 kg/m. The overall length of the cable was 2.48 m, the same of the experimental one, and the initial sag was 1/10 of the length.

The analysis was carried out of plane, by means of forces acting in Y direction modeling wind drag forces [o], estimated assuming a drag coefficient of 0.8. The comparison between the numerical and experimental results are showed in Fig. 4.8c, in terms of mid-point mean displacement for different oncoming mean wind speed.

This work concerns the first results of a ongoing research about evaluation of wind effects on cable structures. Experimental tests were made on wind tunnel to evaluate the variation of axial

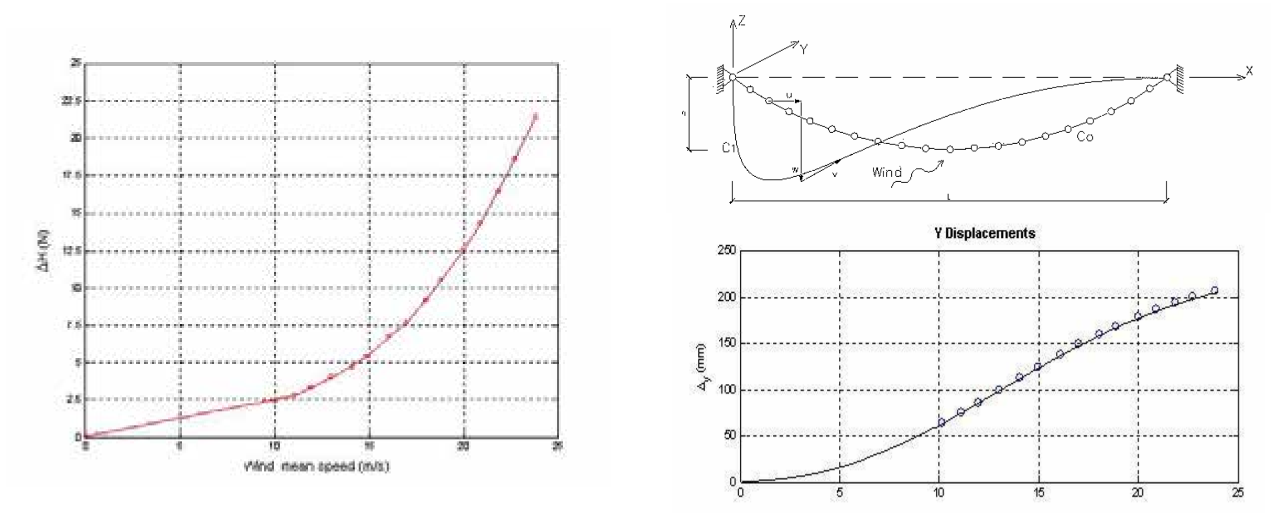

Figure 4.8 Horizontal axial force versus wind velocity (left); FEM model of the cable (top) and comparison between numerical model and experimental tests - mid point horizontal mean displacements (bottom).

loads in the cable, by means of measures of the horizontal reaction at the support. Moreover the displacement of the mid-point was recorded.

Varying the mean wind speed, the experimental tests were performed in laminar and turbulent flow. Eventually a comparison between the experimental results and the numerical ones, obtained by a finite element model with non linear geometrical behavior, was performed.

4.6 RAIN-WIND INDUCED VIBRATION OF STAY CABLES

Strong vibration of inclined stay cables (up to 2 m amplitude) in moderately windy and rainy days was firstly reported by Hikami in 1986 and subsequently named as Rain-Wind Induced Vibration (RWIV). Several full-scale observations of RWIV, as well as stay cable vibration induced by wind in dry conditions (even if of smaller amplitude), have been reported since 70's and especially during last decade.

An extensive experimental campaign was carried out at the Jules Verne climatic wind tunnel of CSTB in Nantes and reported in [7]. Following the experimental results, a physical interpretation of RWIVs was given. It was based on a periodic alternation of flow regimes (and subsequent periodic aerodynamic forces) induced by an oscillating rivulet produced by the rain on the upper part of the cable. A mechanical model was also proposed in [8] to simulate the RWIV of an inclined stay cable.

In the present work, the two main aspects, still open in the cited papers, are treated. The first one concerns the aerodynamics of inclined cables (without rain) and its degree of correlation with RWIVs. The second one involves the calibration of some parameters used in the mechanical model.

At this purpose, a wind tunnel experimental program has been arranged and experiments are running in the CRIACIV wind tunnel in Prato (Fig. 4.9a). The cable model consists of a 160 mm diameter iron tube, 2 to 4 m variable length, equipped by a tap crown at the middle section to measure the unsteady pressures. The cable diameter is the same as the model tested at CSTB and it corresponds to a commonly RWIV sensitive diameter value. The 1:1 cross section has been adopted to avoid any scale reduction effect.

The cable supports allow to test different geometries and, in particular, a wide range of yaw and inclination angles. The wind speed covers the range of practical interest for wind and rain-wind induced vibrations. A particular attention is focused on the flow regimes close to the critical Reynolds number, where RWIVs occur and where aerodynamic phenomena are particularly complex.

Two main cable surfaces are tested. The smooth one reproduces the actual cable surface (usually covered by HDPE sheath) in dry conditions. The other one supports an artificial strip which simulates the water rivulet (Fig. 4.9b). As a matter of fact, a solid strip cannot accurately reproduce the water rivulet. In fact, the rivulet shape, dimensions and mobility have to carefully reflect the actual water film responsible of RWIV. Nevertheless, if the actual rivulet shape and dimensions are reproduced, some interesting aspects can be suitably investigated by a quasi-steady approach.

Tests on the smooth tube allow to characterise the vortex shedding around cylinders (and cables) inclined to the flow (yawed) and the subsequent cable excitation. The effects of vortex unsteadiness (axial flow and 3D vortex shedding as reported in literature) on the low frequency cable excitation are also examined. On the other hand, the tube with the attached strip is used to confirm the reliability of the RWIV mechanism and to calibrate some mechanical parameters involved in the model [8,9].

4.7 DISTRIBUTED ENERGY DISSIPATION SYSTEMS FOR STAY CABLES

Guyed structures are widely used for bridges and large span roofs. Nevertheless, one of their main problems is the susceptibility to be dynamically excited. This is due to the wide range of external load frequencies and to the very small inherent damping in highly tensioned cables (usually lower than 1‰). The induced vibrations, if they are not suppressed or strongly mitigated, can give rise to fatigue problems and damages in cables and/or anchorage systems. In the present research, it has been demonstrated that the use of distributed dissipative systems is more efficient than the use of lumped dampers. In fact, if a terminal part of the cable is immersed in a dissipative material, a wide range of frequencies can be efficiently damped. The mathematical problem is treated in a continuous sense; nevertheless the results can be extended to a discrete series of lumped dampers placed along the terminal part of the cable. See [10] for the analysis details.

4.7.1 The dynamic equations

The existence of an optimal value of the damping was demonstrated in [r]. In fact, increasing damping over a certain threshold can induce a fictitious stiffness in the cable which vanishes the

Figure 4.9 The cable model tested in the BLWT of CRIACIV in Prato.

energy dissipation role of the damper. Pacheco et al. [s] demonstrated the existence of a universal damping curve which relates the cable/damper parameters to the effective damping ratio produced by the damping system. In the present work, the existence of the optimal damping value and the universal curves are extended to the case of distributed dissipative systems.

Following the procedure introduced in [s], for lumped damping systems (Fig. 4.10a) it results:

$$T\frac{\partial^2 v}{\partial x^2}=m\frac{\partial^2 v}{\partial t^2}+c\frac{\partial v}{\partial t}\delta(x-x_c)\ , \tag{4.4}$$

T being the tension in the cable, m the mass per unit length, c the damping coefficient, δ the delta Dirac function, x the along cable coordinate, x_c the damper location, t the time, v the lateral displacement. Expanding v in series of sine functions, corresponding to the undamped cable vibration modal shapes:

$$v(x,t)=\sum_1^n b_i(t)\phi_{oi}(x)\ ,\ \phi_{oi}(x)=\sin\frac{\pi i x}{L}\ , \tag{4.5}$$

n being the generalized considered dofs, $b_i(t)$ the magnitude of the i^{th} dof, L the cable length. In order to write the equations in a dimensionless way, we assume (ω_{oi} is the i^{th} cable frequency):

$$\omega_{oi}=\frac{\pi i}{L}\sqrt{\frac{T}{m}},\quad \mathbf{b}=\frac{[b_1(t),b_2(t),\ldots b_n(t)]^T}{L},\quad \tau=\omega_{o1}t\,,\quad (\bullet)'=\frac{\partial(\bullet)'}{\partial\tau}\,. \tag{4.6}$$

By using a classic Galerkin method [q], and taking into account the orthogonality property

$$\int_0^L \phi_{0i}(x)\phi_{0j}(x)dx=\frac{1}{2}L\delta_{ij}$$

the dynamic equation becomes:

$$\mathbf{Mb}''+\mathbf{Cb}'+\mathbf{Kb}=\{\mathbf{0}\}\ , \tag{4.7}$$

where,

$$\mathbf{M}_{ij}=\delta_{ij}\,,\ \mathbf{C}_{ij}=2\left(\frac{c}{mL\omega_{o1}}\right)\sin\frac{\pi i x_c}{L}\sin\frac{\pi j x_c}{L}\,,\ \mathbf{K}_{ij}=i^2\delta_{ij}\,, \tag{4.8}$$

It can be noted that the cable and dampers parameters are grouped in dimensionless factors.

It is now assumed that the dissipative system is uniformly distributed along x = [0, x_c], as schematized in Figure 4.10b. We assume $c_s(x)=c_s(x_c)$, $y = x/x_c$ and $\int_0^{x_c} c_s(x)dx=c$. The procedure above described for lumped systems, in this case gives rise to:

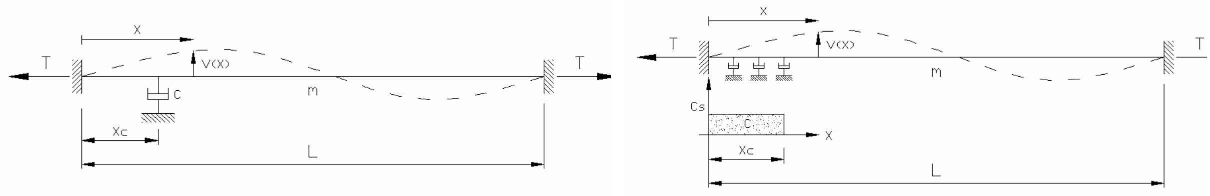

Figure 4.10 Cable with lumped viscous damper (left) and uniformly distributed damping (right).

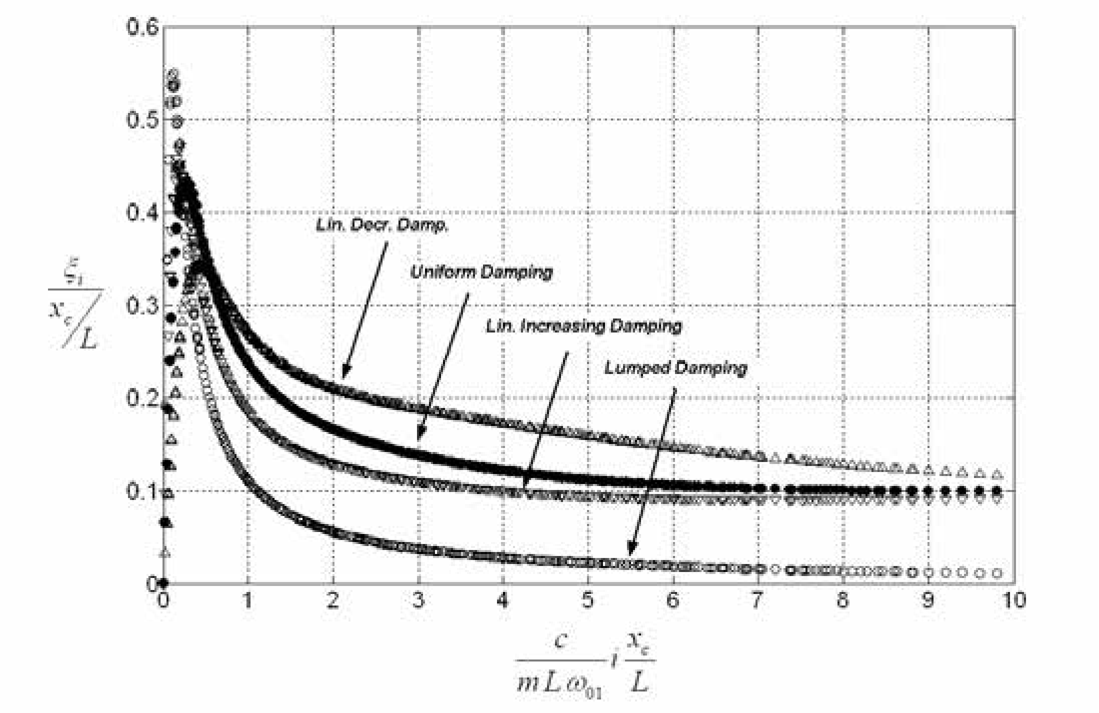

Figure 4.11 Modal damping ratio (ξi) vs cable and damping parameters.

$$\mathbf{C}_{ij} = 2\left(\frac{c}{m L \omega_{o1}}\right)\int_0^1 \sin\frac{\pi i x_c y}{L}\sin\frac{\pi j x_c y}{L} dy \ , \tag{4.9}$$

The cases of linearly increasing damping ($c_S(x)=c_S(x_c)x/x_c$) and linearly decreasing damping ($c_S(x)=c_S(0)(x_c-x)/x_c$), have also been treated.

4.7.2 The damping curves

The eigenvalue analysis has been applied to the dynamic equations above derived. Since the damping matrix is not diagonal, the eigenvalues and the eigenvectors are complex. Such analysis allow to determine the equivalent damping ratio for the non-classical damped system.

If the dimensionless parameters above cited are used, the damping ratio can be expressed as in Fig. 4.11. The main result of this analysis is to have proved a better efficiency of distributed systems (with respect to lumped ones) in damping the natural modes higher than the optimization reference one. For instance, if the optimal damping is calibrated on the 1st mode, the uniformly distributed system shows a loss of efficiency on the 1st mode with respect to the lumped damper; a substantial equivalence for the 2nd, 3rd and 4th modes but a significantly increasing performance for the 5th mode and higher.

Thus, the distributed systems are more efficient to suppress the vibration induced by wide frequency range loads (as, for instance, some environment actions). Furthermore, they reduce the problem of the bending moment induced at the damper location. Finally, they can be suitably integrated into the so-called anti-vandalism tube.

In order to test the effectiveness of some real materials in mitigate the cable vibrations, several experimental tests have been carried out at the LaPS (Laboratorio Prove Strutture) Laboratory of the DISTART Dept. - University of Bologna. Different materials (sand, oil, clay) have been used. Oil and clay (with different water percentage and, hence, viscosity coefficients) have shown a

Figure 4.12 Experimental setup at the LaPS Laboratory.

behavior very close to the theoretical one above derived. Figure 4.12 shows the experimental setup, the cable tender system and the tube filled with the dissipative material.

4.8 BASIC REFERENCES

[a] Vickery, B.J., 1993. Wind loads on the Olympic Stadium: Orthogonal Decomposition and Dynamic (Resonant) Effects, *Report BLWT*-SS28A

[b] RWDI, 2001. Wind tunnel study of roof wind pressures, Braga Stadium, *Report 01-327*, October 2001

[c] Ove Arup, 2001. Wind climate analysis report, Braga Stadium, *Report 66161*, September 2001.

[d] Rossi R., Lazzari M., Vitaliani R. Wind Field Simulation For Structural Engineering Purposes, *accepted for the publication in the International Journal for Numerical Methods in Engineering*

[e] Melchers R.E. 1987. *Structural reliability* Elley Horwood ltd.

[f] Majowiecki M., 1998. Snow and wind experimental analysis in the design of long-span sub-horizontal structures, *Journal of Wind Engineering and Industrial Aerodynamics*, **74 - 76**, 795-807

[g] Lazzari M., Saetta A., Vitaliani R., 2001. Non-linear dynamic analysis of cable-suspended structures subjected to wind actions, *Journal of Computers and Structures*, **79** (9), 953-969

[h] Lazzari M., Majowiecki M., Saetta A., Vitaliani R., 1998. Analisi dinamica non lineare di sistemi strutturali leggeri sub - orizzontali soggetti all'azione del vento: Lo stadio di La Plata, *Proc. of the 5th National Congress of Wind Engineering*, Perugia, Italy.

[i] Boyd R.A., Ishii K., Majowiecki M., Muhlberger H. 1992. *Final Report, Montreal Canada*

[j] Kato S., Yoshino T., Minami H., 1999. Formulation of constitutive equations for fabric membranes based on the concept of fabric lattice model", *Engineering Structures*, **21**, 691–708

[k] Schweizerhof K., Ramm E., 1984. Displacement dependent pressure loads in nonlinear finite element analyses, *Computer & Structures*, **18** (6), 1099–1114

[l] Schweizerhof K., Ramm E., 1987. Follower force effects on stability of shells under hydrostatic loads, *J. Engng. Mech. ASCE*, **113** (1), 72–88

[m] Savitskii G.A., 1982. *Calculations for Antenna Installations – Physical Principles*. National Science Foundation, Washington, D.C.

[n] Fischer O., 1992. Wind Actions on Slender Structures *Proc. 2nd Italian Conference on Wind Engineering*. Capri, Italy, 15-25.

[o] Simiu, E., Scanlan, R. H. 1977. Wind effects on structure: an introduction to Wind Engineering. J.Wiley & Sons, New York

[p] Irvine, M. 1981 Cable Structures. Dover Publications, Inc., New York

[q] Bathe, K.J. 1996. *Finite Elements Procedures*. NJ: Prentice-Hall

[r] Kovacs I. 1982. Zur frage de seilschwinggungen und der seildampfung. *Die Bautechnik* **10**, 325-332 (in Tedesco)

[s] Pacheco M., Fujino Y. and Sulekh A. 1993, Estimation curve for modal damping in stay cables with viscous damper. *Journal of Structural Engineering* **119**:(6), 1961-1979

[t] Borri, C., Zahlten, W. 1991.Fully simulated nonlinear analysis. of large structures subjected to turbulent, artificial wind, (*Int. Journ. of) Mechanics Of Structures And Machines*, **19**(2), 213-250

4.9 LIST OF PUBLICATIONS

[1] Lazzari M., Majowiecki M., Saetta A., Vitaliani R. 2002 Comportamento non lineare per geometria dello Stadio Olimpico di Montreal *Proc. of the 7th National Congress of Wind Engineering, Milano, Italy*

[2] Lazzari M., Majowiecki M., Saetta A., Vitaliani R. F.E. 2002. Analysis of Montreal Stadium Roof Under Variable Loading Conditions, *IABSE Symposium "Towards a better built environment – innovation, sustainability, information technology"*, Melbourne

[3] Lazzari M., Majowiecki M., Saetta A., Vitaliani R. "Large cable roof: Montreal Stadium and La Plata Stadium", *C.T.A. Collegio dei Tecnici dell'acciaio* – Venezia, 26-28 Settembre 2001.

[4] Gioffrè M., Gusella V., Materazzi A. L., 2002. Problemi di progettazione di antenne per telefonia mobile, *Proc. 7th Italian Conference on Wind Engineering,* Milano, Italy

[5] Gioffrè M., Gusella V., Materazzi A. L., Venanzi I., 2003. Optimal design of raw land sites for mobile phone networks. *Proc. 11th Int. Conf. Wind Eng,* Lubbock, Texas, USA

[6] Gioffrè M., Gusella V., Materazzi A. L., Venanzi I., 2004. Removable guyed mast for mobile phone networks: wind load modelling and structural response. *J. of Wind Engineering & Industrial Aerodynamics*, **92**(6), 463-475

[7] Cosentino N., Flamand O., Ceccoli C. 2003^{i}. Rain-Wind Induced Vibration of Inclined Stay Cables. Part I: Experimental Investigation and Physical Explanation". *Wind and Structures,* **6**(6). 471-484

[8] Cosentino N., Flamand O., Ceccoli C. 2003^{ii}. Rain-Wind Induced Vibration of Inclined Stay Cables. Part II: Mechanical Modelling and Parameter Characterisation". *Wind and Structures,* **6**(6). 485-498

[9] N. Cosentino. 2002. Rain-Wind induced vibrations of stay cables, *Ph.D. Thesis,* Bologna

[10] Cosentino N., Benedetti A. 2003. Mitigazione delle vibrazioni di stralli con sistemi a smorzamento distribuito, *C.T.A. Collegio dei Tecnici dell'acciaio* – Genova, Italy

WITH CONTRIBUTION FROM:

Gianni Bartoli, Università degli Studi di Firenze
Federico Cluni, Università degli Studi di Perugia
Massimiliano Gioffrè, Università degli Studi di Perugia
Vittorio Gusella, Università degli Studi di Perugia
Massimiliano Lazzari, Università di Padova
Massimo Majowiecki, IUAV Venezia
Annibale Luigi Materazzi, Università degli Studi di Perugia
Ilaria Venanzi, Università degli Studi di Perugia

5 Wind flow in the urban environment and its effects

Vincenzo Sepe
University “G. D’Annunzio” of Chieti-Pescara

5.1 INTRODUCTION

Researchers of the Winderful project have been dealing with the effects of wind flow in urban environment for several years. The research has been initially motivated by studies on Street Architecture items (i.e. bill-boards, traffic signs and traffic lights, lighting poles, news-stands, bus stop shelters, as well as scaffoldings and other temporary structures) [a].

The damage caused by wind to Street Architecture (SA) items, in fact, not only produces economic losses, but can also cause injuries. On the other hand, proper design of such items can give a significant contribution to improve the quality of urban life from both viewpoints of functionality and aesthetics, while minimizing the erection costs and failure losses. The performance of street architecture in wind is thus not only an economic question, but is also relevant to comfort and safety of the urban environment.

To date, however, wind engineers have paid very little attention to street architecture items, probably because these were considered minor structures, not deserving much design effort. The effects of recent heavy windstorms on European cities showed that this is not quite true, and that a proper design is indeed necessary. Many failures have in fact occurred mostly as a consequence of the underestimation of wind-induced loads and of poor design. This is also related to the increasing slenderness and reduced weight often requested by architects and city planners to improve aesthetics. The safety and functionality of street architecture under strong winds need therefore to be carefully evaluated. The locations of SA items should be chosen taking account of the configuration of the surrounding buildings, and the design carried out accounting for realistic wind loads. On the contrary, current structural design standards and codes of practice do not include special provisions for the specific problems of wind loading on SA (3-dimensional flow, bluff-body aerodynamics, interference between buildings and with moving vehicles, “street canyon" effects, neighbouring interference, corner effects, etc.).

For these reasons, a part of the Winderful project was devoted to investigate, above all from the experimental point of view, the characteristics of the wind flow in the urban environment. The

Edited by Gianni Bartoli and Francesco Ricciardelli, WINDERFUL: Wind and INfrastructures: Dominating Eolian Risk
For Utilities and Lifelines, ISBN 88-8453-138-1,

main results are summarised below, while reference is made to the published papers (see list of publications) for further details.

5.2 STATE OF THE ART ON THE WIND FLOW IN THE URBAN ENVIRONMENT

In the transition between a rural area and an urban area the characteristics of the wind flow are modified and, accordingly, the wind loads on the structures located in the lower layers of the Urban Boundary Layer (UBL) cannot be accurately evaluated using the wind model appropriate for structures either located outside the city (Rural Boundary Layer: RLB), or in the higher layers of the UBL.

As discussed in Sect.5.2.1 and Sect.5.2.2 below, inside an urban area two different flow regimes can be found, whose separation is located at a height roughly corresponding with the average height of the buildings [b]. The layer located below this height is termed canopy layer, and the characterisation of the wind field in this layer is essential to evaluate the wind-induced loads on SA and similar object. Referring to [b] for further details, it can be observed that the flow in the canopy layer is driven by the energy transfer between the upper layers of the Urban Boundary Layer; moreover, the characteristics of the flow inside the canopy layer are marginally dependent on the characteristics of the incident flow, while mainly depend on the geometry of the built area.

The experimental tests performed during the Winderful project in the Boundary Layer Wind Tunnel (BLWT) of CRIACIV in Prato (Sect.5.3 below) confirm that the characteristics of the wind flow in the UBL are significantly different from those in the RBL, and require therefore an *ad hoc* approach.

5.2.1 Structure of the wind flow in the Urban Boundary Layer

The structure of the Atmospheric Boundary Layer (ABL) in the urban environment is rather different from that occurring over smoother surfaces in the free field. As discussed by Rotach et al. [b], the Surface Layer can be subdivided (Fig.5.1) into an Inertial Sublayer (IS) and a Roughness Sublayer (RS). In the IS the wind statistics at any particular location are close to the spatially averaged values.

The characteristics of the flow in the RS, i.e. the lower portion of the UBL, is strongly dependent on the building arrangement, and relevant parameters are the uniformity of the building height and the building aspect ratio (ratio of the average building height to the average street width, H/W). Depending on the latter parameter, three different types of behaviour can be found, of isolated roughness flow ($H/W<0.3$), for which the aerodynamics of the isolated building dominates, of wake interference flow ($0.3<H/W<0.65$), for which aerodynamic interference between the buildings takes place, and of skimming flow ($H/W>0.65$), which is the case of densely distributed, medium- to high-rise buildings. In the latter case, that of densely built city centres, a well defined average canopy height can be found, which separates the SL into an upper part and a lower part, termed Canopy Layer (CL).

The flow in the CL is almost completely governed by the local roughness, i.e. the street geometry and building height distribution, and little affected by the characteristics of the flow in the upper layers. The energy transfer between the upper layers of the UBL and the CL, occurring at the canopy height governs the air motion in the street canyons, but the characteristics of the flow inside the canopy layer appear to be marginally dependent on the characteristics of the incident flow. Within the RS (whose thickness z* has been estimated to be for European-style cities in the order of 2 times the average building height have) it is not possible to accept the

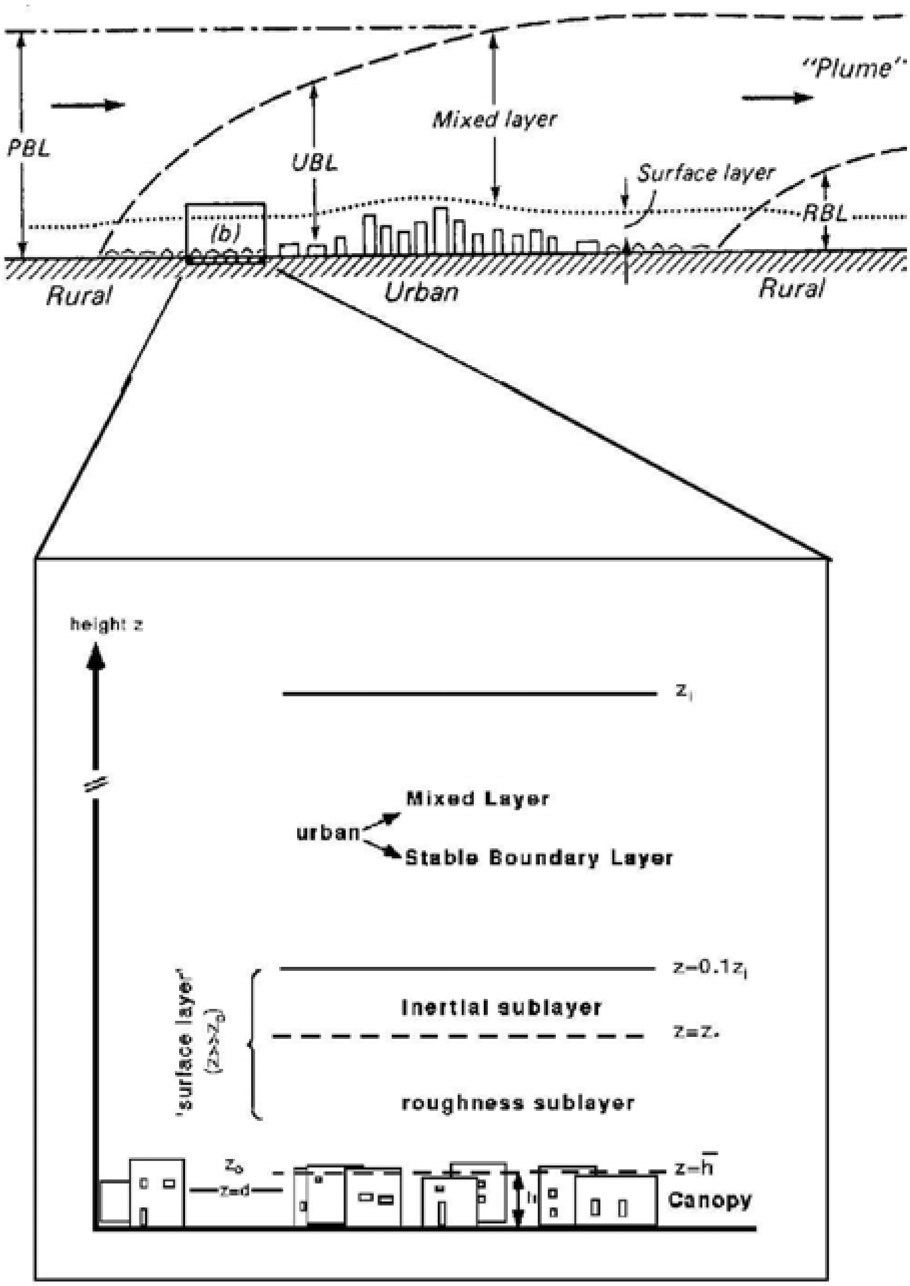

Figura 5.1 Structure of the Urban Boundary Layer (after Rotach et al. [b])

hypothesis of constant turbulence statistics, and therefore of constant Reynolds stresses, with the elevation above ground.

This is proved e.g. by the results of wind tunnel measurements by Kastner-Kline and Rotach [c] reported in Fig.5.2, that show the vertical distribution of the mean wind speed and of the shear stresses in a number of location in the city of Nantes. Because of these strong variations, a different procedure from that based on the similarity law must be applied to evaluate mean wind speed distribution in the UBL. A specific procedure has been suggested by Rotach [d], based on a local scaling velocity, which accounts for the vertical variability of the Reynolds stresses. The resulting mean wind profile turns out to be shifted upwards by a quantity denoted

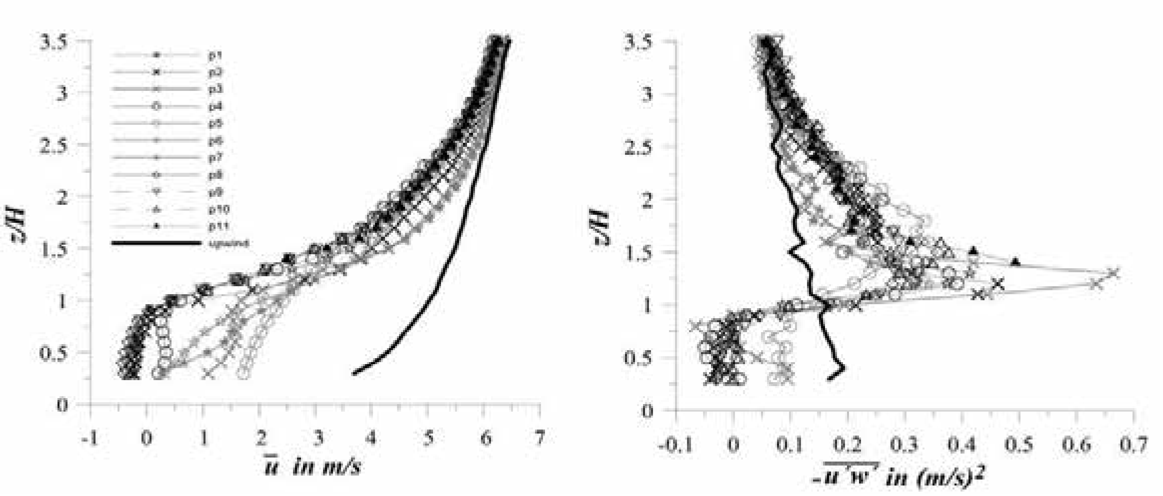

Figure 5.2 Mean velocity and Reynolds stress profile for the city of Nantes (after Kastner-Kline and Rotach [c])

“displacement height”, h_{dis} , that depends on the geometry and density of the surrounding buildings (a value h_{dis}= 0.7 h_{ave} is on the average reasonable). This upward shift is related to the fact that, for densely built areas, the rough surface over which the boundary layer develops is the canopy rather than the ground. The concept of displacement height had been introduced in a draft of the revised Eurocode on Wind Actions [e], with prescribed h_{dis} values in the range from 0 to 0.8 h_{ave} (Fig.5.3).

5.2.2 Wind flow in the Canopy Layer

Quite opposite is the case in which a few buildings are much taller that the average. In this case [f][g] the flow is diverted vertically by the taller buildings, which leads to higher mean wind speeds in the CL. The ratio between the wind speed at a given location in the CL to the speed at the same elevation in the RBL is in this case in the range of 0.22 to 2.0, but can get as high as 5 at particular locations.

The approach by Stathopoulos and Wu [f] relates directly the wind speed in the CL to that in the RBL, without considering the transition between the RBL and the UBL. A different approach

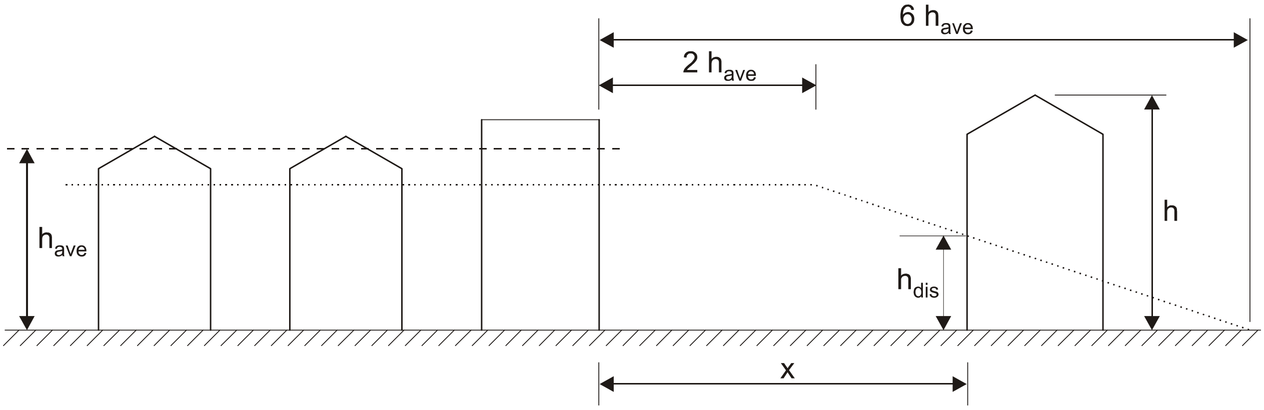

Figure 5.3 Obstruction height and upwind spacing (from prEN1991-1-4, Draft July 2000, [e])

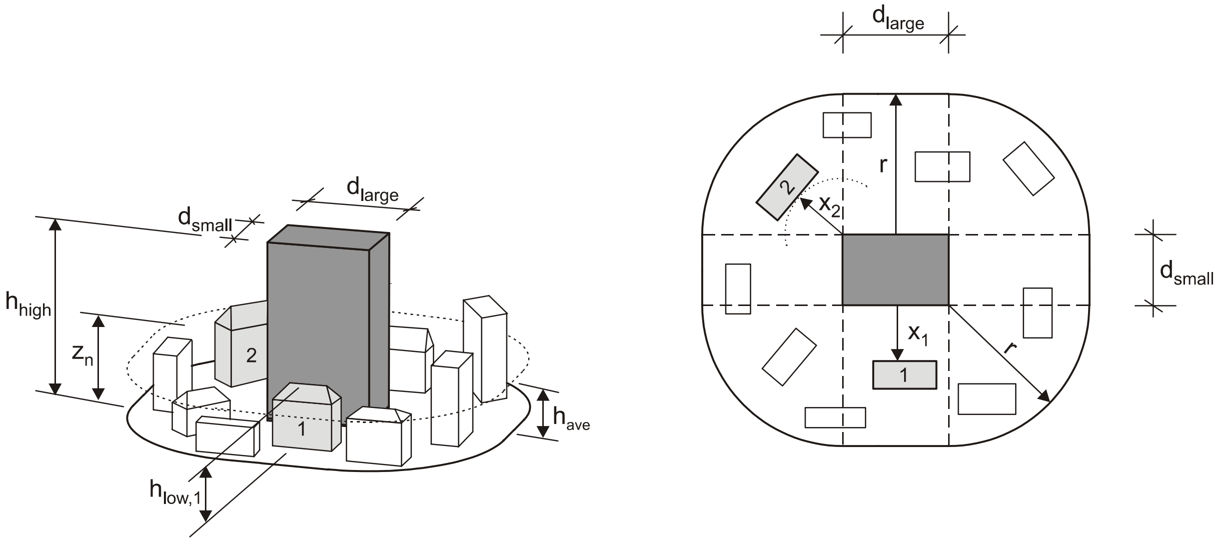

Figure 5.4 Influence of a high rise building on the design of two different nearby structures (1 and 2) (from prEN1991-1-4, Draft July 2000, [e])

can be to calculate first the mean wind profile in the UBL (e.g. following the procedure by Rotach, [d]), and then relate the mean speed in the CL to the speed in the UBL. In Kastner-Klein et al. [h] it is shown that the maximum mean wind speed in the CL is roughly equal to the mean wind speed at the average roof level h_{ave}. The latter quantity, however, cannot be accurately determined, and therefore it is usually preferred to relate the wind speed in the CL to a speed at a higher elevation in the UBL. The maximum mean wind speed in the CL proves to be of about 20% of the mean wind speed at an elevation of 4 h_{ave}.

Also this effect had been taken into account in the already quoted draft of the revised Eurocode on Wind Actions [e] which suggested, at least as a first approximation, to base the design of structures located near a building more than twice as high as the average height h_{ave}, on the undisturbed wind speed at an elevation z_n above ground depending on a few geometrical parameters, namely the structural height h_{low}, the radius r, the distance x and the dimensions d_{small} and d_{large}, all defined in Fig.5.4.

The CL flow is characterised by very high levels of turbulence. In Kastner-Kline et al. [h] it is shown that the intensity of turbulence (both longitudinal and lateral) in the CL can be as high as 0.80, if evaluated with reference to the mean wind speed at the average roof level.

Not only the intensity of turbulence is higher in the CL, but also the shape of the Probability Density Function of the wind speed fluctuations is quite different [g] from that in a RBL, that is usually assumed to be Gaussian. This results in a change in the peak factor: peak factors of more than 7 are not unrealistic. Large peak factors, however, are usually associated to low values of the mean speed, while large values of the mean speed are associated to moderate values of the peak factor.

Street canyon flow also changes the frequency content of the turbulence. The characteristics of the wind turbulence in the CL, in fact, are related to the local turbulence generation rather than to the characteristics of the turbulence of the oncoming flow. Thus a shift of the energy towards the higher frequencies, a reduction of the spectral peak, and eventually a modification of the spectral shape result [g].

Figure 5.5 Experimental setup with prism in the CRIACIV wind tunnel

5.3 WIND TUNNEL TESTS ON THE WIND FLOW IN THE URBAN ENVIRONMENT

With the aim of a deeper understanding of the characteristics of the wind flow in the lower layers of an urban environment, two sets of wind tunnel tests were carried out in the CRIACIV boundary layer wind tunnel in Prato by Ricciardelli and Polimeno; the main results are summarised below (Sect.5.3.1 and 5.3.2), while details of the second test are reported in [1][2]. The first test was aimed at assessing the caracteristics of the wind flow downstream a prism (Fig. 5.5), and their relation to those of the oncoming flow. In the second test a model of a very simple urban area was considered, shown in figure 5.6, on which flow measurements were carried out, in order to assess the changes brought to the flow by the city environment, and their relation to the incident flow.

Wind tunnel tests were also performed by Paulotto, Ciampoli and Augusti (Sect.5.3.3).

5.3.1 Characteristics of the wind flow behind a prism

In the first test by Ricciardelli and Polimeno (Fig.5.5), measurements were carried out with an X probe hot wire anemometer, which allowed calculation of mean wind speed profiles, integral scales of turbulence, intensities of turbulence, spectra of the wind speed and Reynolds stresses, for different locations near the prism.

The experimental results confirmed the findings of Isyumov and Davenport ([g], see. Sect.5.2.2). In Fig. 5.7 some results are shown; Fig. 5.7a and 5.7b show the spectra of the longitudinal component of turbulence at two locations, upstream and downstream the block, respectively. The central frequency of the velocity fluctuations is increased by a factor of 2 due to the presence of the block. In figure 5.7c the vertical profiles of the intensity of the longitudinal component of turbulence at two locations are plotted, upstream and downstream the block. The plot shows how the two profiles are quite coincident in the upper layers, but totally different in

Figure 5.6 Model of urban area in the CRIACIV wind tunnel

the lower layer, with intensities of turbulence that can be as high as 0.55 downstream the block. In figure 5.7d, where the horizontal broken line corresponds to the height of blocks, the vertical profiles of the Reynolds stresses at two locations are plotted, upstream and downstream the block. In the upper layers the Reynolds stresses are much larger downstream the block than upstream, but inside the canopy layer they become rather low; this can be explained through the totally different nature of the flow in that region.

5.3.2 Characteristics of the wind flow in a typical urban street arrangement

In Ricciardelli and Polimeno [1][2], the results of wind tunnel tests carried out in the CRIACIV boundary layer wind tunnel are presented and discussed, mainly aimed at a characterisation of the mean and fluctuating component of the wind speed, with future goal of a more realistic definition of the wind loads acting on structures in the CL.

The main results are summarised below, while details can be found in [1][2].

Wind velocity measurements were carried out in the street canyons of a regular orthogonal street pattern, using a x-probe hot wire anemometer. The model, shown in figures 5.6 and 5.8, is made of 20 wooden prisms, 20x16 cm in plan and 15 cm high (*H*), with a 12 cm spacing. Two conditions of smooth and turbulent oncoming flow were examined. In smooth flow the wind speed was set to about 10 m/s, and a thin boundary layer was detected at the location of the model, 10 cm thick. The turbulent flow was generated using spires and roughness elements, and was characterised by a mean speed power law profile with $\alpha = 0.28$, and an undisturbed mean speed of about 10 m/s. At 15 cm of elevation i.e. at the roof level, the mean wind speed and intensity of turbulence in the tunnel without model were measured to be 7.5 m/s and 0.13, respectively, and the integral scale of the oncoming turbulence was 0.29 m. Measurements were taken at 12 elevations along 9 verticals as shown in figure 5.8. Sampling took place at 2000 Hz for 90 s.

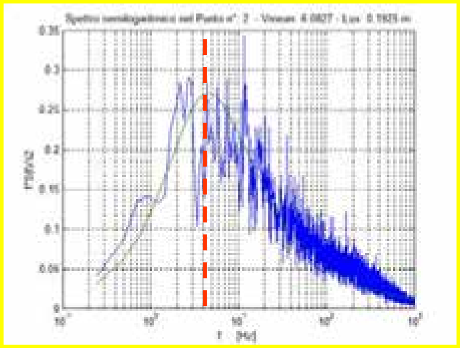

Figure 5.7a Spectrum of the upstream wind speed

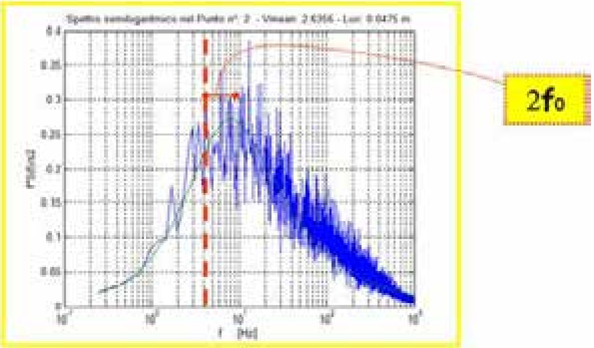

Figure 5.7b Spectrum of the downstream wind speed

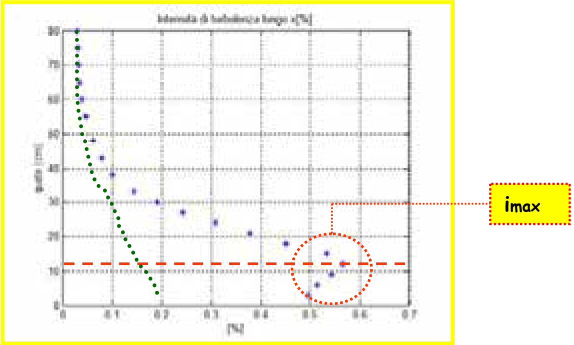

Figure 5.7c Profiles of the intensity of turbulence upstream (circles ·) and downstream (stars*) the prism

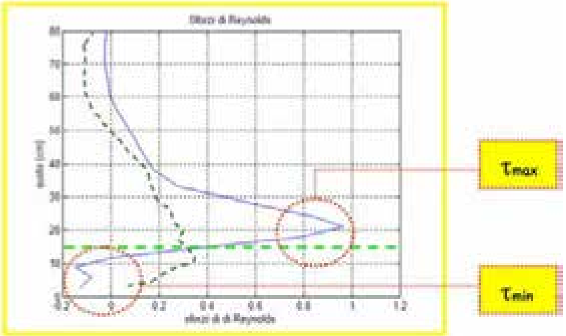

Figure 5.7d Profiles of the Reynolds stresses upstream (broken line) and downstream (continuous line) the prism

In figure 5.9 the mean wind velocity profiles are shown, for verticals B, C, G, H, M, O and Q of Fig.5.8. In particular, in figure 5.9.a and 5.9.b the smooth flow profiles for verticals G, H, M, O and Q in a longitudinal canyon, and for verticals B and C in a transversal canyon, are shown, respectively. As expected, the flow patterns in the longitudinal and transversal canyons are rather different from each other, but also rather similar within the same canyon. For the longitudinal canyon a negligible speed-up effect is observed for z>2H, probably the effect of tunnel blockage, while below that height a almost linear decrease of the mean wind speed is found. This linearity tends to be in some cases violated at very low elevations, where the channelling flow effect seems to dominate, bringing mean wind speeds slightly higher then those consistent with a linear variation. In the transversal canyon a linear variation of the mean wind speed also starts at z=2H, which, however stops at z=H. Below that, a much lower mean speed was measured, weakly varying with the elevation. The horizontal variation of the mean wind speed is in all cases quite large. As an example, at an elevation of 0.2H, the mean wind speed varies in the range of 2 to 4.3 m/s in the longitudinal canyon, and of 2.5 to 3.9 m/s in the transversal canyon.

The same features were found for the turbulent flow condition (figures 5.9.c and 5.9.d), in which a linear variation of the mean speed is found, for z<1.7H in the longitudinal canyon, and almost constant values in the transversal canyon. In figures 5.9.e and 5.9.f the mean wind speed profiles for the smooth and turbulent flow conditions are compared for verticals O (longitudinal canyon) and C (transversal canyon). In the longitudinal canyon a difference always lower than 15% is observed between the mean wind speed in the case of smooth and turbulent oncoming flows, whereas much large differences would be found at the same location in the tunnel without

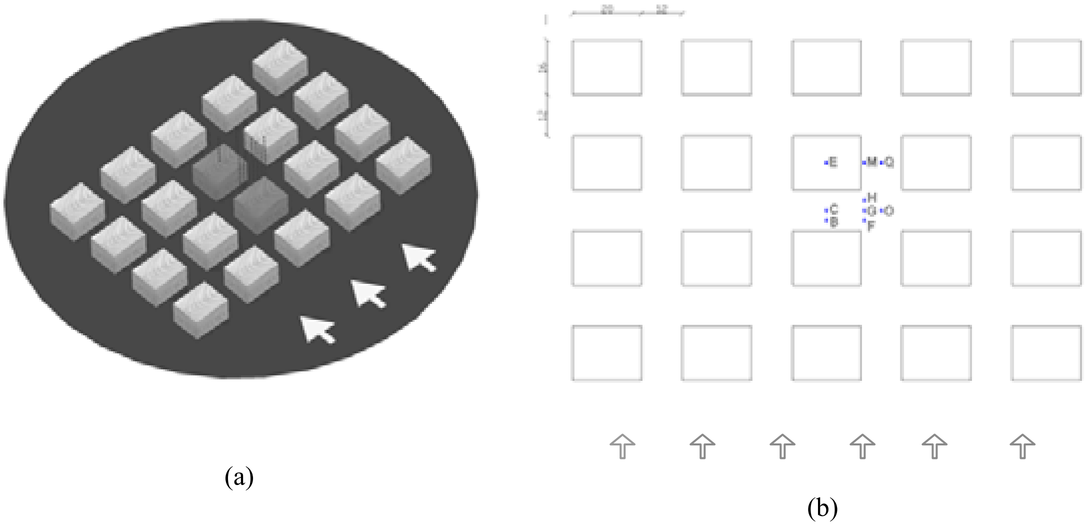

(a)

(b)

Figure 5.8: Sketch of the wind tunnel model (a) and measurement points (b)

model. This can be explained as the result of the channelling effect dominating on the characteristics of the oncoming flow. For the transversal canyon the differences between the smooth and turbulent flow conditions are larger, as if the presence of turbulence in the RS were responsible for a modification of the mean flow pattern in the CL.

A relevant experimental result is that the oncoming turbulence very little affects the intensity of the turbulence in the longitudinal street canyon, even though the presence of a channelling flow would make one expect the oncoming turbulence somehow penetrate in the canyon. From figure 5.10.a, reporting the longitudinal intensity of turbulence in the vertical O, it appears in fact that the differences when the intensity of turbulence is measured at the same location in smooth and turbulent flow are always lower than 20%.

Comparison of the turbulence intensity profiles at vertical C (figure 5.10.b) in smooth and turbulent flow shows that for the transversal canyon the influence of the oncoming turbulence on the CL intensity of turbulence is larger than for the longitudinal canyon.

Some profiles of the integral scale of the longitudinal component of turbulence are reported in Fig. 5.11.a (longitudinal canyon) and in Fig. 5.11.b (transversal canyon); other details can be found in [1][2]. In particular, figure 5.11.b shows that in transversal canyon highly different values of the scale of turbulence in the RS for the case of smooth and turbulent oncoming flow correspond to the same values in the CL. This can again be explained as the result of the fact that, especially for transversal canyons, the characteristics of turbulence in the CL are weakly affected by the characteristics of the oncoming turbulence. As far as the longitudinal canyon is concerned, a significant difference is observed; namely, from figure 5.11.a it seems that a superposition of the oncoming large scale turbulence with the locally generated, small scale turbulence takes place, and that this makes the turbulence in the longitudinal canyon of a smaller scale than that of the undisturbed flow, but of a larger scale than that in the transversal canyon, where there is almost only locally generated turbulence.

Referring to [1][2] for further details, globally the tests confirmed that the mean and fluctuating characteristics of the flow in the CL are more dependent on the local geometry, than on the characteristics on the oncoming flow. It was also observed that different types of behaviour take place in canyons parallel and orthogonal to the mean flow.

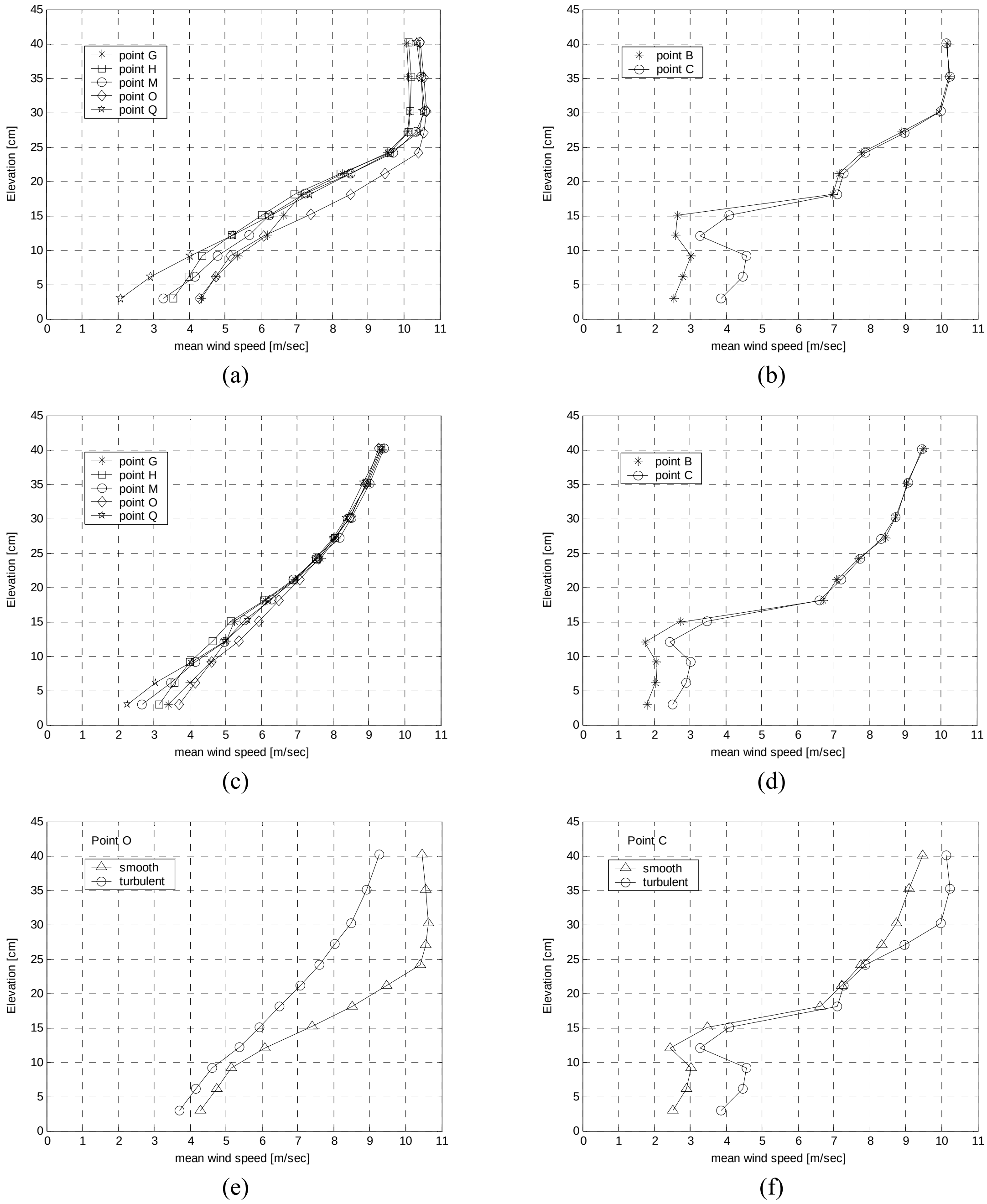

(a) (b)

(c) (d)

(e) (f)

Figure 5.9: Mean wind speed profiles: (a) positions G, H, M, O and Q, smooth flow, (b) positions B and C, smooth flow (c) positions G, H, M, O and Q, turbulent flow, (d) positions B and C, turbulent flow, (e) position O, smooth and turbulent flow, (f) position C, smooth flow and turbulent flow

In the longitudinal canyon the channelling flow behaviour dominates, with mean speeds (almost linearly) decreasing with height, and almost constant velocity fluctuations. There results that the turbulence intensity profile is almost linearly decreasing with height. The characteristics of turbulence in the longitudinal canyon is dependent on the characteristics of the oncoming turbulence in the sense that they seem to be those of a superposition of the oncoming large scale turbulence and of the locally generated small scale turbulence.

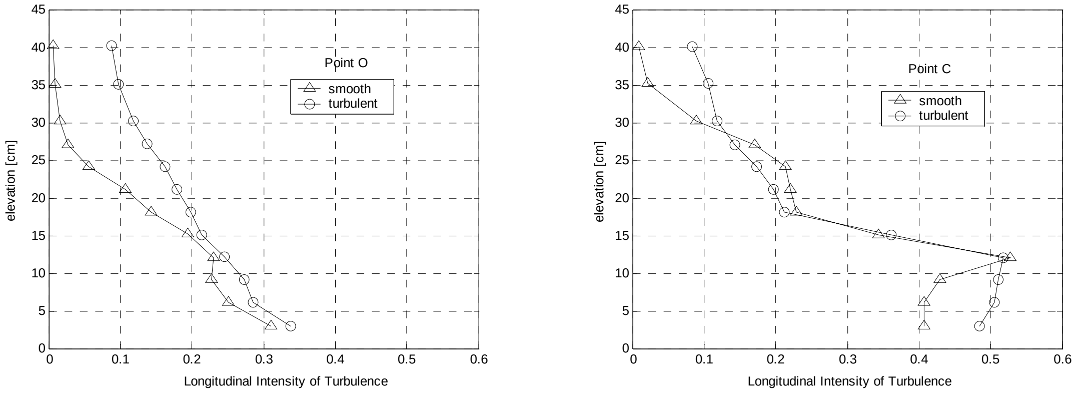

(a) (b)

Figure 5.10: Longitudinal turbulence intensity profiles: (a) position O, smooth and turbulent flow, (b) position C, smooth flow and turbulent flow

In the transversal canyon the turbulence seems to be only that which is generated locally, as its scale is totally unaffected by the turbulence of the oncoming flow. The mean and RMS wind speeds, however, are different in smooth and turbulent flow. This suggests that the turbulence of the oncoming flow is unable to penetrate in the transversal canyon, but somehow influences the energy transfer between the upper RS and the CL.

The strong, and to certain extent unpredictable space variability of the statistics of the wind speed suggests that when these have to be used as input data for a wind loading model, and when no wind tunnel measurements are available for the particular urban configuration under examination, large values be taken, for the final result to be on the safe side.

5.3.3 Influence of different arrays of buildings

The tests performed by Paulotto, Ciampoli and Augusti [3] in the CRIACIV wind tunnel were aimed at evaluating the influence of different arrays of buildings and to discuss the possibility of extending the usual representation of the wind mean profile to urban areas. In fact the roughness coefficient z_0 of the classical logarithmic law is a surface property only for fully developed flow, where an *inertial sublayer* exists, in which the turbulence statistics are approximately constant

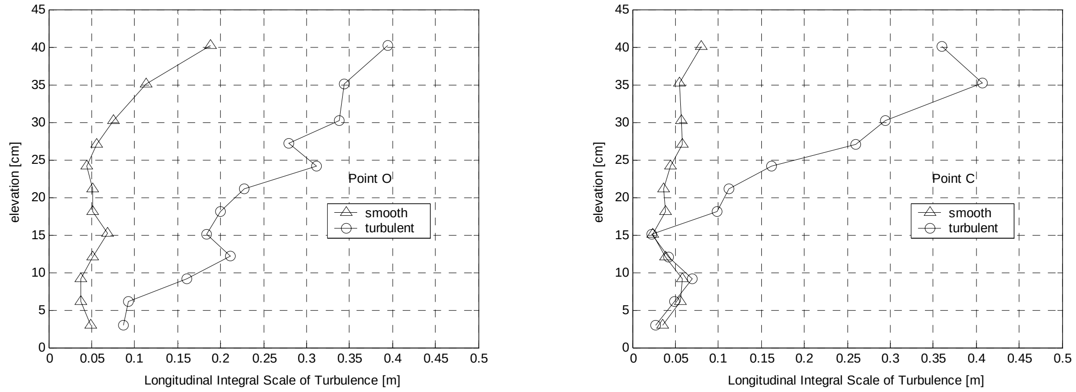

(a) (b)

Figure 5.11: Longitudinal integral scale of turbulence profiles: (a) position C, smooth and turbulent flow, (b) position C, smooth flow and turbulent flow

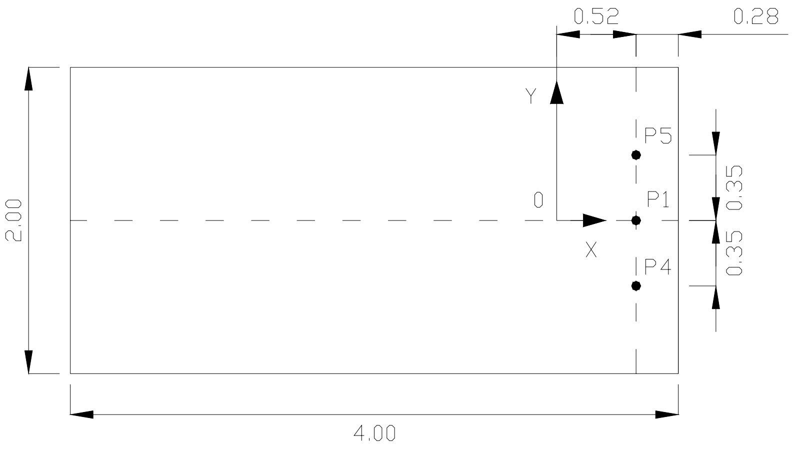

Figure 5.12. Plan locations of the vertical lines where measurements have been taken (dimensions in m); *x* denotes the wind-tunnel axis.

with height. In urban areas, instead, where roughness frequently changes, it is possible that a significant inertial sublayer cannot develop at all.

The roughness elements used for these tests were sharp-edged wood cubes with a side dimension of 90 mm. They were glued onto a plywood baseboard (4 m long and 2 m wide) in staggered patterns: each pattern was characterized by a constant value of the parameter λ, the ratio between the frontal area of the obstacles and the lot area of the obstacles.

Experiments were carried out considering three values of λ (that is, λ = 9%, 14% and 18%), corresponding to three different roughnesses, denoted as R1, R2 and R3, respectively.

Wind tunnel tests were carried out at a nominal free stream velocity U_∞ of 24 m/s, and measurements were taken along the three vertical lines P1, P4, P5 shown in Fig. 5.12.

Hot wire anemometer was the main instrumentation adopted in the experiments. A sampling frequency of 2 kHz and 65,536 samples were used at each measurement location. As described in

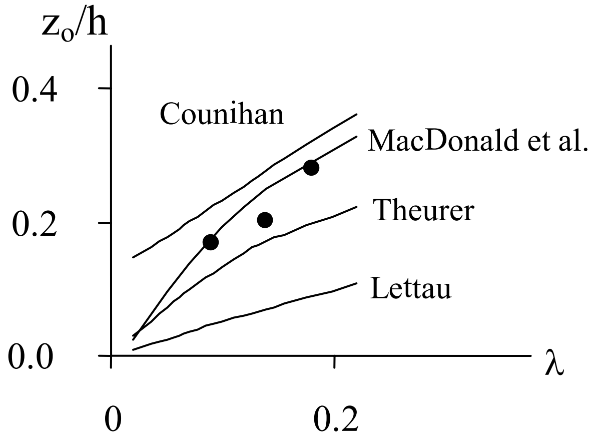

Figure 5.14. Variation of the ratio z_0 to the roughness height, *h*, as a function of the frontal area density, λ. Experimental results (Paulotto et al. [3]), compared to different empirical expressions (reported and discussed in [3])

detail in [3], it was noted that the mean velocity *U* (non-dimensionalised with respect to the free stream velocity U_∞) and the turbulence intensity in the streamwise (*x*) direction do not change significantly in the direction orthogonal to the mean flow (Fig.5.13) over the whole investigated range of heights *z* for the three roughness values (R1, R2, R3). On the contrary, Reynolds shear stresses τ_R exhibit significant variations.

As already said, the question arises if and how a significant value of z_0 could be obtained from point measurements of wind velocity, in order to use also for the urban environment the format of the logarithmic law. To this aim, and following the suggestions of (Macdonald et al.[i][*l*]), lateral averages of the mean velocity profiles have been considered in [3]: the roughness length z_0 has been estimated by means of a least square fitting of the lateral averages (at different heights) of the three vertical mean velocity profiles, assuming that the roughness sublayer and the inertial sublayer could be described together by a single logarithmic law.

The resulting values of z_0 have then been compared with previous experimental results (see. [3] for details), and with the values obtained by empirical equations. In particular, as shown in Fig.5.14, experimental results are in good agreement with the relation proposed by Macdonald et al. [m] for sharp edges obstacles

However, it must be noted that all relations proposed in the scientific literature between roughness length and obstacle aspect ratio fail when λ > 20-25 %, due to the aerodynamic interaction between the obstacles and the development of a finite displacement height in the velocity profile. This limitation is a problem in many practical applications, and especially in urban situations, where λ can very easily exceed 20% (cf. [3]).

5.4 WIND LOADS ON STREET ARCHITECTURE

5.4.1 Wind loads in the codes of practice

As shown in the previous sections, the availability of experimental data would allow to relate the characteristics of the air flow in the CL to the oncoming wind. The wind loading on Street Architecture items and the structural response could therefore be evaluated on the basis of a realistic description of wind in urban environment. This should be taken into account in the Codes of Practice, which instead do not specifically address this issue.

In fact, the design mean wind speed below a certain "minimum" elevation in the urban

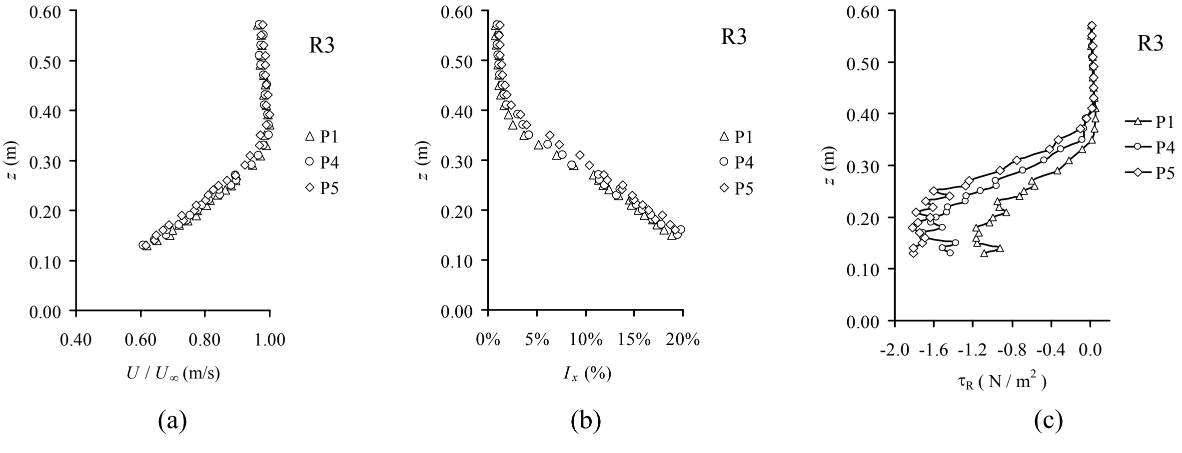

(a) (b) (c)

Figure 5.13. a) Mean velocity profiles along the verticals P1, P4 and P5 for the three investigated roughness values (R1, R2, R3); b) Turbulence intensity profiles c); Reynolds shear stress profiles.

environment is usually taken in the Codes as a constant value, equal to that corresponding to the mean wind profile (either a power law or a logarithmic profile) at that elevation.

Most of the Codes account for the effect of turbulence through a gust factor. This is given as a number, for simple design procedures, and as an expression, for detailed procedures. In the latter cases it is possible to account for the period and damping of the considered structure. However, the turbulence spectra are those specific of the atmospheric boundary layer, and no provision in made for the characteristics of the turbulence in the urban environment.

Finally, for very few shapes the aerodynamic force coefficients are available in the Codes, as for billboards in the shape of a flat plate and for some usual structural cross-sections. However, it is not considered that the “aerodynamic admittance”, i.e. the reduction of expected wind pressure with invested area, is strongly affected by interference with larger structures and with other SA items.

5.4.2 A numerical example

As an example, the effects of the above issues on the design wind load were calculated by Augusti, Ricciardelli and Sepe [a] for a particular case, namely a rectangular signboard, 6 m wide and 3 m high, with its centre 3 m above ground.

The natural frequency and damping ratio of the signboard were set to 3 Hz and 0.05 respectively. The wind load was first calculated following the specifications of Annex A.10 of Eurocode 1-2-4 [n], for an exposure category IV, a terrain roughness class A and a reference wind speed U_{ref} = 27 m/s, that corresponds to a local wind speed U_{10} = 14.9 m/s at 10 m of elevation above ground: the total force on the signboard resulted to be 20.7 KN.

The calculations were repeated, again following the procedure of Eurocode 1 [n], but including the largest reasonable variations in the mean wind speed, peak factor g and PSDF of the turbulence (see. Sect. 5.2.2). Three cases were considered: (1) buildings of the same height ($U/U\text{o} = 0.75$, $g = 7.2$); (2a) few buildings higher than average ($U/U\text{o} = 2.0$, $g = 3.2$); (2b) few buildings higher than average, extreme case ($U/U\text{o} = 5.0$, $g = 3.2$), where g is the peak factor, U the mean wind speed in a given location of UBL, including local effects of buildings, and Uo the undisturbed speed. In all cases a shift of the turbulence PSDF of one order of magnitude towards the higher frequencies was considered, as derived from results presented by Isyumov and Davenport [g].

The results, summarised in Table 5.1, show for case (1) a total force of 17.4 KN, quite close to the value obtained following Eurocode 1 (20.7 KN). However for case (2a), a force of 55.2 KN was obtained, 2.7 times larger than the value given by the Eurocode. Moreover, if the extreme value of $U/U\text{o} = 5.0$ is used, a force of 195 KN was calculated, almost 10 times larger than the Eurocode value.

	Case 1 [KN]	Case 2a [KN]	Case 2b [KN]
$\overline{F}$: average value	1.93	13.7	48.3
$\widetilde{F}$: standard deviation	2.15	13.0	45.7
g: peak factor	7.2	3.2	3.2
$\hat{F} = \overline{F} + \mathrm{g}\widetilde{F}$	17.4	55.2	195.0

Table 5.1 – Example: wind load on a signboard (after Augusti et al., [a])

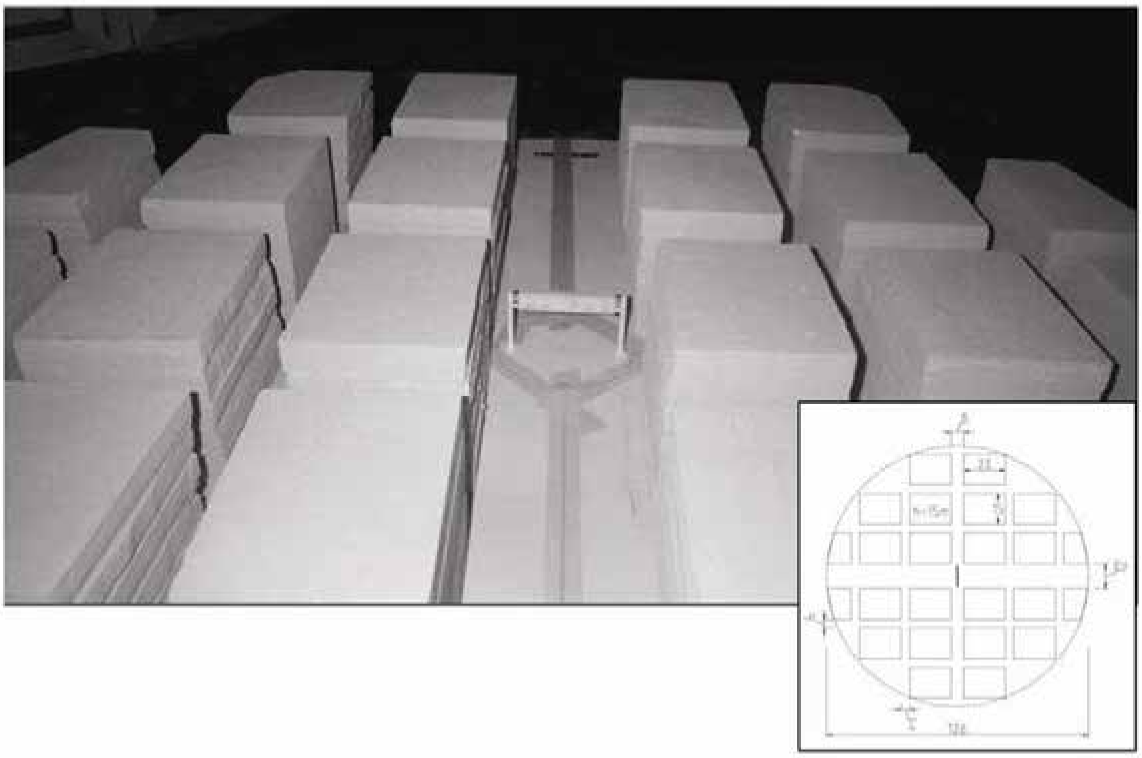

Figure 5.15. Model of a traffic-sign, surrounded by a regular path of buildings.

5.4.3 Wind tunnel tests

As a first example of wind effects on SA in urban environment, experimental tests have been performed in the boundary layer wind tunnel of CRIACIV by Ciampoli, Sepe and Marini (see [4] for details); tests have been carried out on a 1:100 model of a regular path of buildings with almost the same height and streets orthogonal to each other (Fig.5.15), including a model of a traffic-sign (sides: 100×20×9 mm, Fig.5.16) equipped with 18 pressure taps.

Wind tunnel tests have been performed for different wind speeds and for a varying angle of attack of the flow (0°, 45°, 90°, 135°, 180° with respect to the wind tunnel axis, obtained by turning the circular base of the test chamber). For each one of the five different directions and for each pressure tap, the pressure field has been recorded at 540.75 Hz for a 40 seconds interval. Data so obtained have then been averaged and tranformed in the pressure coefficients reported in Fig. 5.17, whose values are referred to the kinetic pressure at the same height and in absence of the model (buildings and traffic-sign).

For these tests also, a significant increment of turbulence is observed in the frequency range 0.1 – 10 Hz, according to results of Davenport and co-workers [g] and with experimental results of other participants to the WINDERFUL project [1][2].

On the base of the measured pressure fields, the dynamic response has been numerically evaluated for structural models with the same geometry and mass of the traffic-sign tested in the wind tunnel, but with different values of the stiffness, and therefore with different natural frequencies (between 0.1 Hz e 10 Hz, including values for several realistic cases).

This numerical investigation showed that the maximum equivalent static pressure can be between 2 and 8 times larger than the kinetic pressure, depending on the damping coefficient, and

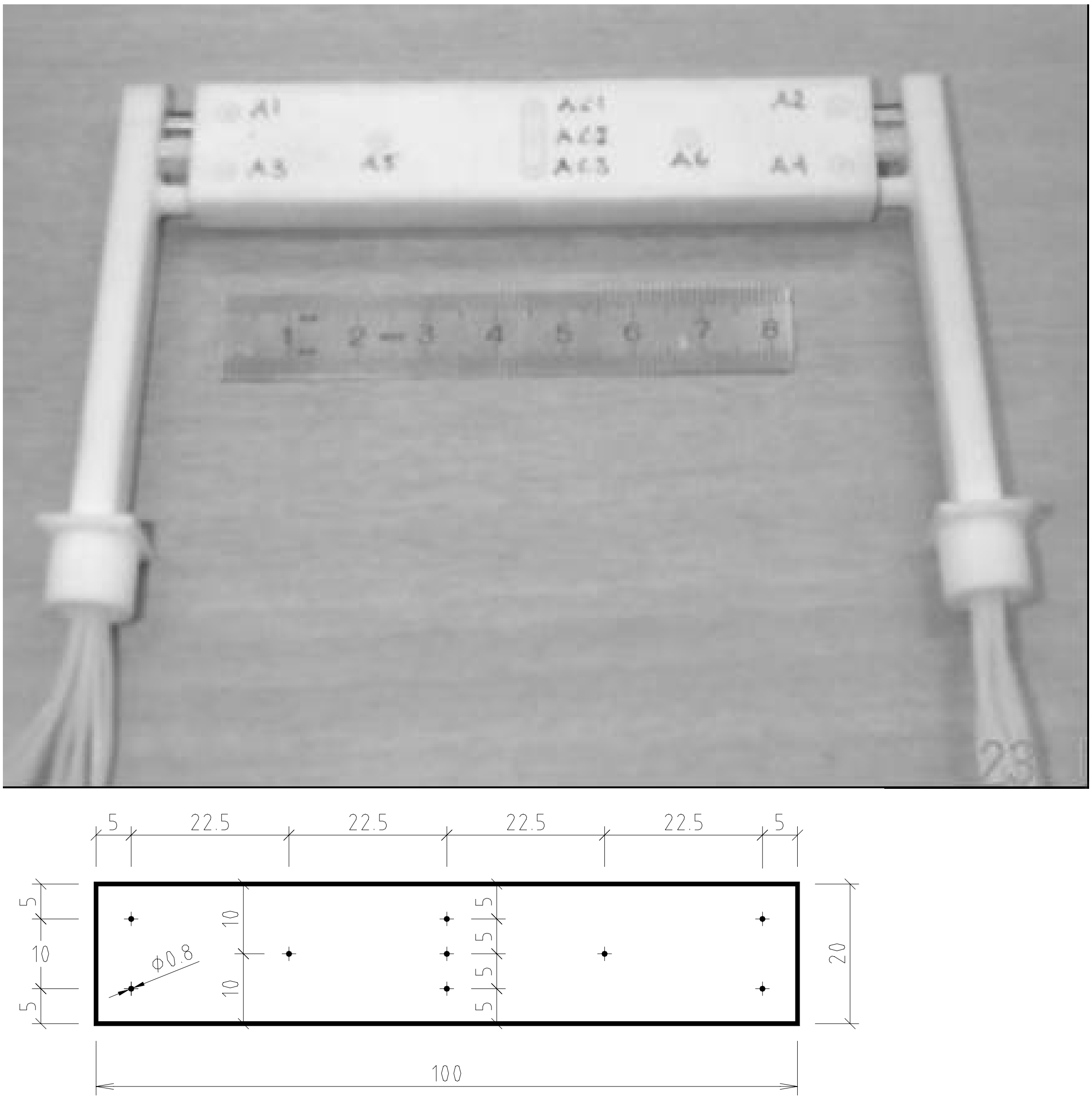

Figure 5.16. Detail of the model of a traffic-sign and position of pressure taps (from A1 to A9 on the front side, from D1 to D9 on the rear side).

therefore it can be much larger than for more traditional structures as buildings. This should warn designers to pay more attention to SA items, deserving to them appropriate calculation and design effort, as for other structures.

5.5 BASIC REFERENCES

[a] Augusti G., Ricciardelli F., Sepe V., 2001. Wind-Resistant Street Architecture, *3rd European & African Conference on Wind Engineering,* Eindhoven, The Netherlands.

[b] Rotach M.W., Batchvarova E., Berkowicz R., Brechler J., Janour Z., Kastner-Klein P., Middleton D., Prior V., Sacrè C., and Soriano C.. 2000. Wind input data for urban dispersion modelling. *COST 715 WG4 Meeting,* Prague.

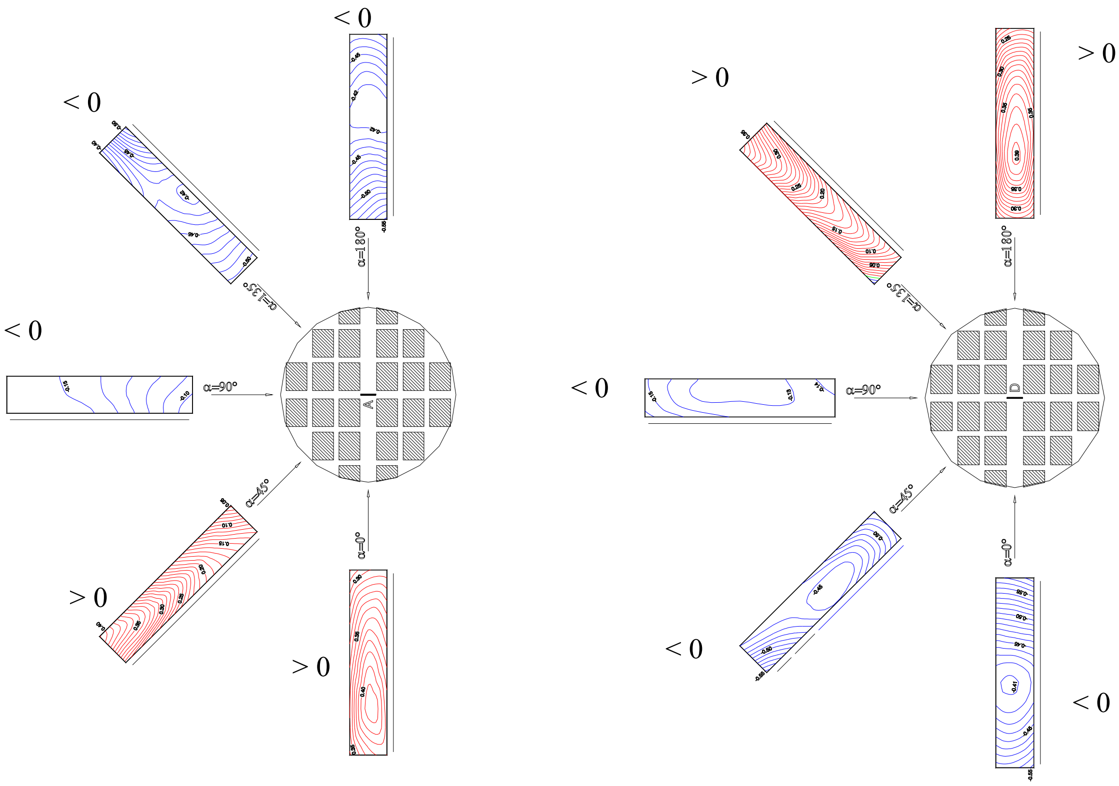

on the front side A

on the rear side D

Figure 5.17. Distribution of the average pressure coefficients cp on the "front side" A and on the "rear side" D of the traffic-sign for different angle of attack of the flow (< 0: suction).

[c] Kastner-Klein P. and M.W. Rotach, 2001. Parametrization of the wind and turbulent shear stress profiles in the urban roughness sublayer. *Third Int. Conf. on Urban Air Quality,* Loutraki, Greece

[d] Rotach M.W, 2000. Estimation of the wind speed at an "urban reference height" from an observation at some other height. *COST 715 WG1 Working Platform*

[e] Eurocode 1 "Action on Structures", CEN/TC250/SC1, 2000; Part 1-4 Wind Actions; *prEN1991-1-4*; Draft, July 2000

[f] Stathopoulos T. and H. Wu. 1995. Generic models for pedestrian-level winds in built up regions. *J. Wind Eng. Ind. Aero.*,**54/55**,515-525

[g] Isyumov N. and A.G. Davenport, 1975. The ground level wind environment in built-up areas. *4th Int Conf. On Wind Effects on Tall Buildings and Structures*, Heathrow.

[h] Kastner-Klein P.; E. Fedorivitch and M.W. Rotach, 1999. Organised and turbulent air motions in a wind tunnel model of a street canyon with and without moving vehicles. *Sixth Int. Conf. on Harmonisation within Atmosph. Disp. Modelling.* Rouen, France

[i] Macdonald, R.W., Carter, S. & Slawson, P.R. 2000. Measurements of mean velocity and turbulence statistics in simple obstacle arrays at 1:200 scale. *Thermal Fluid Report 2000*-1. Canada: University of Waterloo

[l] Macdonald, R.W. 2000. Modelling the mean velocity profile in the urban canopy layer. *Boundary-layer Meteorology* **97**: 25-45

[m] Macdonald, R.W., Griffiths, R.F.& Hall, D.J. 1998. An improved method for the estimation of surface roughness of obstacle arrays. *Atmospheric Environment* **11**: 1857-1864

[n] CEN 1994 *Eurocode 1* Basis of Design and Actions on Structures, Part 2, Chap.2-4: Wind Actions; ENV1991-2-4

5.6 LIST OF PUBLICATIONS

[1] Ricciardelli, F., Polimeno, S., 2004. Some experimental results concerning the characteristics of the wind flow in the canopy layer, *Urban Wind Engineering & Building Aerodynamics COST Action C14*, Rhode-Saint-Genese, Belgium

[2] Ricciardelli F., Polimeno S. 2004. Analisi delle caratteristiche dei campi di vento a bassa quota in ambiente urbano (in Italian), *Proceedings 8th National Conference on Wind Engineering IN-VENTO-2004*, Reggio Calabria, Italy

[3] Paulotto, C., Ciampoli, M., Augusti, G., 2003. Some experimental results on wind field in a built environment, *System-Based Vision for Strategic and Creative Design*, edited by F. Bontempi, Balkema, 3, 2309-2315

[4] Ciampoli, M., Marini, A., Sepe, V., 2002. Sperimentazione in galleria del vento di elementi strutturali per l'arredo urbano (in Italian), *Proceedings 7th National Conference on Wind Engineering,* Milan, Italy

[5] Polimeno S., 2002 Effetti del vento sulle strutture a bassa quota in ambiente urbano (in Italian), *Degree Thesis in Civil Engineering*, Università Mediterranea di Reggio Calabria

WITH CONTRIBUTION FROM:

Giuliano Augusti, Università di Roma "La Sapienza"
Marcello Ciampoli, Università di Roma "La Sapienza"
Carlo Paulotto, Università di Roma "La Sapienza"
Santo Polimeno, Università "Mediterranea" di Reggio Calabria
Francesco Ricciardelli, Università "Mediterranea" di Reggio Calabria

6 Vortex shedding

Salvatore Noè
University of Trieste

6.1 INTRODUCTION

The effects of the vortex shedding load, with particular reference to the lock-in condition, must be taken into account in a number of design situations, in which a slender cylinder immersed in a fluid stream is considered, thus comprising a vast number of fields of engineering. Mechanical, naval, ocean and civil engineering are some examples.

Concerning civil engineering and with reference to the wind effects on constructions, the most dangerous situations regard for example chimneys and particularly those in steel, usually very low damped, antenna steel stacks and all slender parts of cable stayed and suspended bridges, thus including decks, towers and cables.

The effects of the vortex shedding load which are to be considered in the design stage can be either the total collapse of the structure (due to the attainment of maximum bending resistance of the oscillating stack or else due to fatigue fracture) or the excessive oscillation amplitude (causing service difficulties, as in the case of bridge decks, or simply alarm in the bystanders).

It is not always possible to avoid the lock-in using aerodynamic devices, or to increase the structural stiffness (in order to reach critical wind speed values sufficiently high so as to exclude synchronization) or the structural damping (using hydraulic dampers or tuned mass dampers, to avoid excessive oscillation amplitude). On the contrary the critical velocity often corresponds to wind speed values which are frequent at the building site. Consequently the availability of reliable methods for the assessment of the maximum expected amplitude of the structural oscillations in lock-in condition is of the utmost importance. It would be even better to dispose of methods able to assess the maximum structural response for a wider range of wind speed or possibly describe the response to a predetermined wind speed history.

Although in the last forty years there have been carried out several theoretical and experimental studies (see review in [a]), up to date the phenomenon has not been completely understood and there is no complete analytical formulation able to furnish an exact description of the aeroelastic interaction between the wake and the oscillating structure [b].

Edited by Gianni Bartoli and Francesco Ricciardelli, WINDERFUL: Wind and INfrastructures: Dominating Eolian Risk
For Utilities and Lifelines, ISBN 88-8453-138-1,

From the normative point of view, the lack of an adequate solution creates maximum expected amplitude previsions evaluated from different Codes being sometimes very different, in particular in case of very low damped structures [c].

For these reasons a part of the Winderful project has been dedicated to the research on this phenomenon, with reference to chimneys and suspended bridges.

6.2 VORTEX SHEDDING AND LOCK-IN

When a cylindrical bluff body is immersed in air flow, boundary layer detaches alternatively from the surface of the cylinder and a wake of vortices is formed. If the body is fixed, the main shedding frequency n_{St} is proportional to wind velocity u by the Strouhal relation:

$$n_{St} = St\frac{u}{d} \tag{6.1}$$

where St is the Strouhal number (mainly depending on the shape of the cross section and the Reynolds number) and d is the characteristic dimension (the diameter in case of a circular cylinder). The alternate shedding and the associated oscillating pressure field on the surface of the cylinder, which causes an oscillating lift force on the body, are in general strongly three-dimensional phenomena.

If the body is flexible or elastically mounted in the across-wind direction, the alternate lift force associated with the vortex shedding causes the cylinder to oscillate in cross-wind direction.

If the mechanical system is sufficiently low damped and the Strouhal frequency close to one of its natural frequencies (condition of critical wind velocity) the oscillation amplitude can be sufficiently large to influence the vortex shedding and consequently the associated pressure field and the whole phenomenon becomes strongly aeroelastic.

The response is non symmetrical with respect to the natural frequency and hysteretic (Figure 6.1). As wind velocity gradually increases, going past the upper limit of the lock-in range, the shedding frequency abruptly returns to the values predicted by the Strouhal relation. Due to the hysteresys the fluid-structure interaction and consequently the response, are different whether the air velocity is increasing or decreasing when crossing the lock-in range.

The aeroelastic interaction at lock-in governs not only the shedding frequency but all main aspects of the wind load: intensity and regularity of lift fluctuation, its spatial correlation and the phase relation between motion and force.

A similar influence on the vortex shedding and on the associated surface pressure load on the cylinder can be caused in forced oscillation conditions, i.e. forcing the body to oscillate with a sufficiently large amplitude and with a frequency close to the Strouhal one.

Theoretical models developed so far can be divided into two main categories [a]: single-degree-of-freedom (SDOF) models and coupled wake-oscillator models. Models of the former group are more widely used for design purposes and often allow only an assessment of the oscillation peak amplitude, while models of the latter group offer a tentative description of the interaction between vortex shedding and oscillating body. Moreover SDOF models can be subdivided into models based on the negative damping concept [b, d] and models based on force-coefficient data [e,f].

6.3 RESEARCH WITHIN THE WINDERFUL PROJECT

Within the Winderful project both theoretical and experimental studies have been carried out.

Experiments have been conducted on real structures and on wind tunnel models.

6.3.1 Analytical model of the vortex shedding load

A new numerical formulation of the aeroelastic vortex shedding load, both for wind speed included in or out of the lock in range, has been proposed. The formulation has been obtained as a consequence of a number of successive improvements of the numerical model developed in the past years [h]. The improvements were introduced on the basis of the experimental results obtained from first of the wind tunnel tests [3,4]. In the formulation both the amplitude of the lock in range and the lift coefficient value depend on the oscillation amplitude.

Starting from the experimental results, two different synchronization conditions are recognized, for wind speed lower or higher than the value corresponding to the maximum amplitude of the response (lower and upper synchronization). The whole synchronization domain is therefore divided into sub- domains (Figure 6.1).

The availability of first hand experimental data has been extremely useful. The experience obtained from the development of the model has proved to be very important for the definition of the tests programmed on the second aeroelastic model carried out at the CRIACIV wind tunnel.

Within the two synchronization sub-domains different relations between the oscillation amplitude and the lift coefficient are valid and different conditions on the phase between force and displacement are imposed.

The total lift force at time t on a cylinder oscillating with frequency n_c is:

$$F_L = \frac{1}{2}\rho\, u^2 C_{L,tot}\, d \quad L \sin\,(2\pi n_L t + \phi_L) \tag{6.2}$$

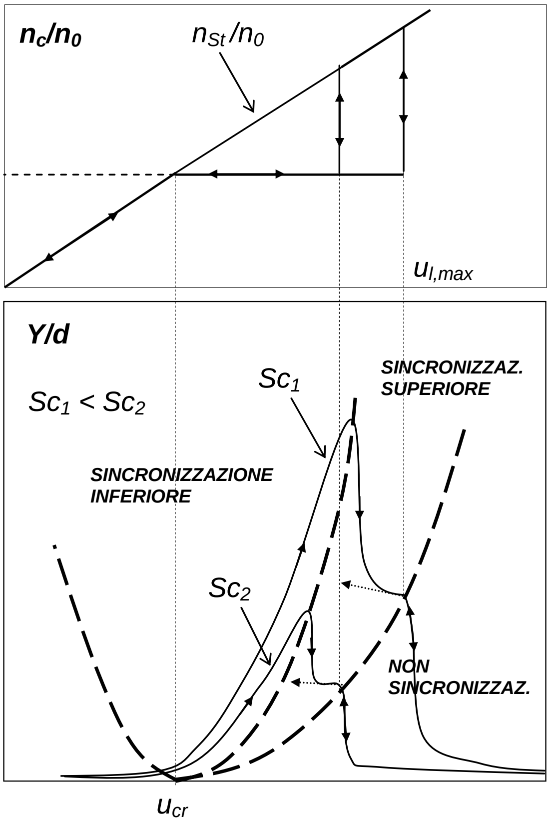

Figure 6.1 Synchronization sub-domains

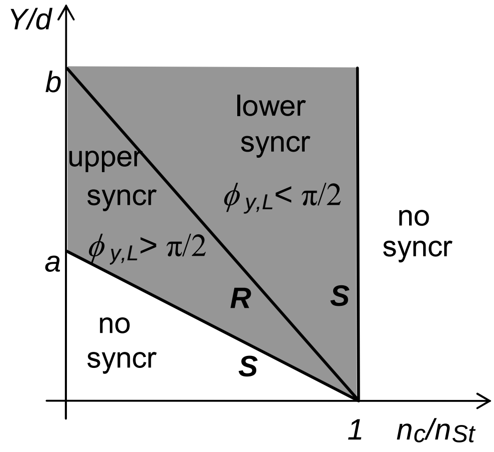

Figure 6.2 Synchronization sub-domains

where L is the loaded length. The load frequency n_L depends on the frequency ratio n_c/n_{St} on the relative amplitude Y/d and on the phase $\phi_{y,L}$ between force and motion as in Figure 6.2.

Inside the synchronization sub-domains the condition $n_L = n_c$ is imposed; outside the condition is $n_L = n_{St}$. The domain shown in Figure 6.2 is a drastic simplification of the synchronization domain experimentally obtained from forced oscillations tests as the one shown in Figure 6.3 [g].

For functions R and S which describe the sub-domain boundaries the following simple equations are proposed**:**

$$S = a\left(1 - \frac{n_c}{n_{St}}\right) \quad \text{for } n_c/n_{St} \le 1 \qquad (6.3)$$

$$S = \infty \quad \text{for } n_c/n_{St} > 1 \qquad (6.4)$$

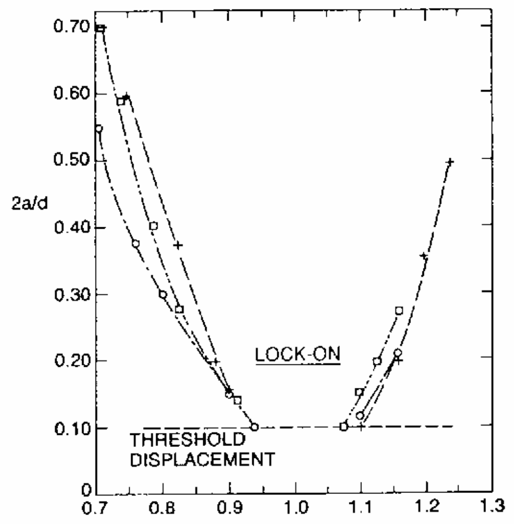

Figure 6.3 Syncronization range with forced oscillations [g]

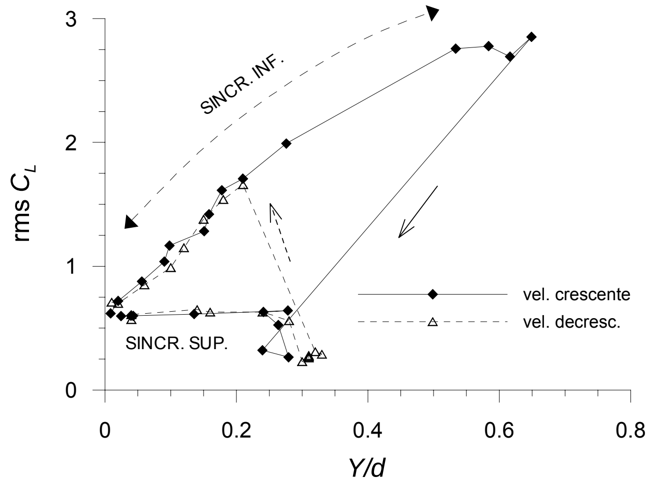

Figure 6.4 Local lift coefficient (r.m.s.) vs reduced amplitude [4]

$$R = b \left(1 - \frac{n_c}{n_{St}}\right) \tag{6.5}$$

The parameters *a* and *b* are determined on the basis of experimental results. The relationships between the lift coefficient $\boldsymbol{C_{L,tot}}$ and the reduced oscillation amplitude for the two sub-domains are the following:

$$C_{L,tot,low} = C_{L,tot,0} \left(1 + k_{low} \frac{Y}{d}\right) \tag{6.6}$$

$$C_{L,tot,upp} = C_{L,tot,0} \left(1 + k_{upp} \frac{Y}{d}\right) \tag{6.7}$$

where $C_{L,tot,0}$ is the value valid for fixed cylinder. Even the values of the parameters $C_{L,tot,0}$ e k_{low} e k_{upp} have to be experimentally calibrated. The experimental results described in [4] indicate that $k_{low} > k_{upp}$ (Figure 6.4).

Outside of the synchronization domain a value $C_{L,tot} = C_{L,tot,0}$ is adopted. The previsions of the numerical model have been compared with the experimental ones, obtaining the results shown in Figure 6.5, referring to the first of the wind tunnel model [5]. The test as shown in the figure has been conducted with increasing wind speed.

The two responses show a good correspondence. It can be particularly noticed the ability of the model to reproduce minimal variations of the frequency load n_L within the lock in range. The slight raise of the load frequency with the increasing of the wind speed is correctly reproduced.

This continuous adjustment (Eq. 6.3 – 6.5) is critical for the correct reproduction of the amplitude response within the lock in range while the load frequency is close to the natural frequency of the system.

6.3.2 In situ experimentation

Within the Winderful project the experimental campaign, begun in the past years [h], on the concrete chimney of the new municipal waste disposal incinerator in Trieste, has been continued.

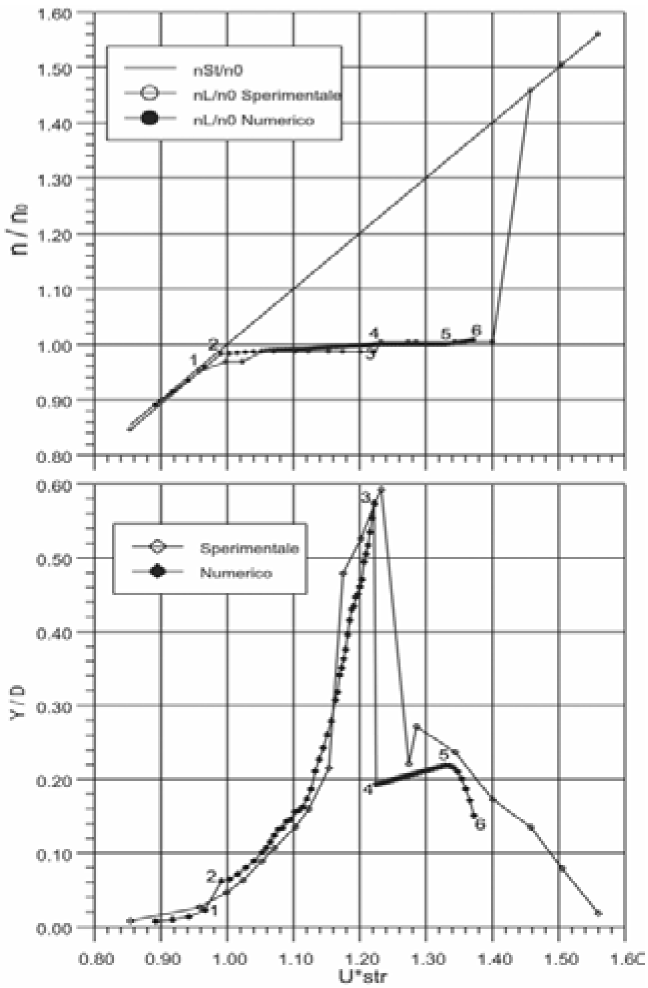

Figure 6.5 Comparison between experimental data and numerical simulations [5]

The chimney (Figure 6.6) is perfectly cylindrical. The stack is 100.0 m high with a diameter of 6.3 m. A biaxial accelerometer, an anemometer ,a wind-vane and a GPS antenna are presently installed. A number of time series of the dynamic response of the structure under wind action and of the wind velocity and direction have been obtained.

6.3.3 Wind tunnel tests

The tests on aerolastic models have been performed in the boundary layer wind tunnels at the University of Western Ontario and at CRIACIV [3,4,6].

In both the cases a light, but very strong, carbon-fibre cylinder, about 2.2 m long with a 0.16 m diameter was used, as shown in Figure 6.7.

Structural loads were measured directly with load cells. In the first model surface pressures were measured at 225 locations in order to obtain loading correlations along the cylinder for a large range of freestream velocities and detailed velocity field information has been obtained at lock-in with laser Doppler anemometry.

In both the experiments displacements were measured with laser transducers.

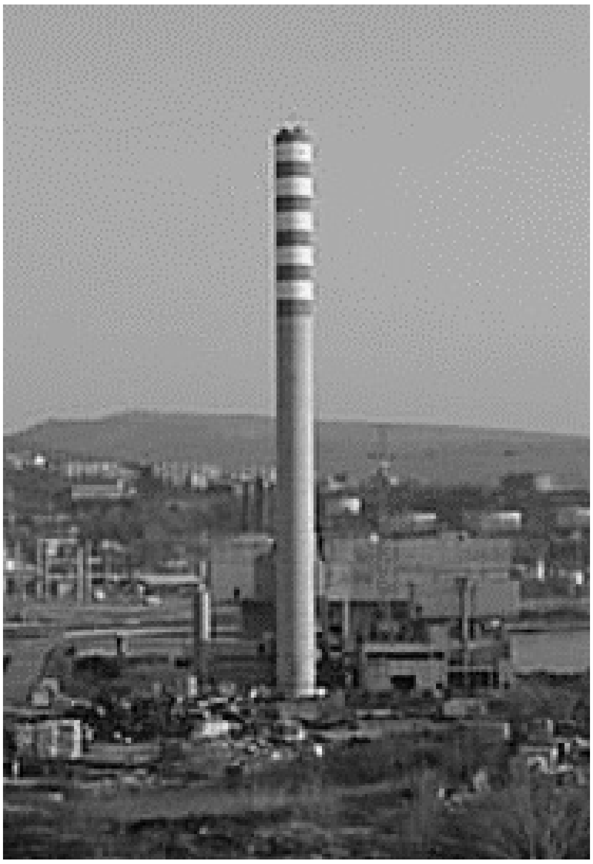

Figure 6.6 Concrete chimney used for in situ experimentation

The tests on the second model in the CRIACIV wind tunnel were taken out with different values of turbulence intensity.

Particular attention has been dedicated in order to determine the relations between the main variables which characterize the lock in phenomenon (frequency and amplitude of the cylinder oscillation, Strouhal frequency, local lift coefficient and its' correlation along the cylinder length, phase angle between load and motion).

Some examples of the results which, as mentioned before, have been used also for the calibration of the numerical model are shown in the following Figure 6.8 up to 6.11

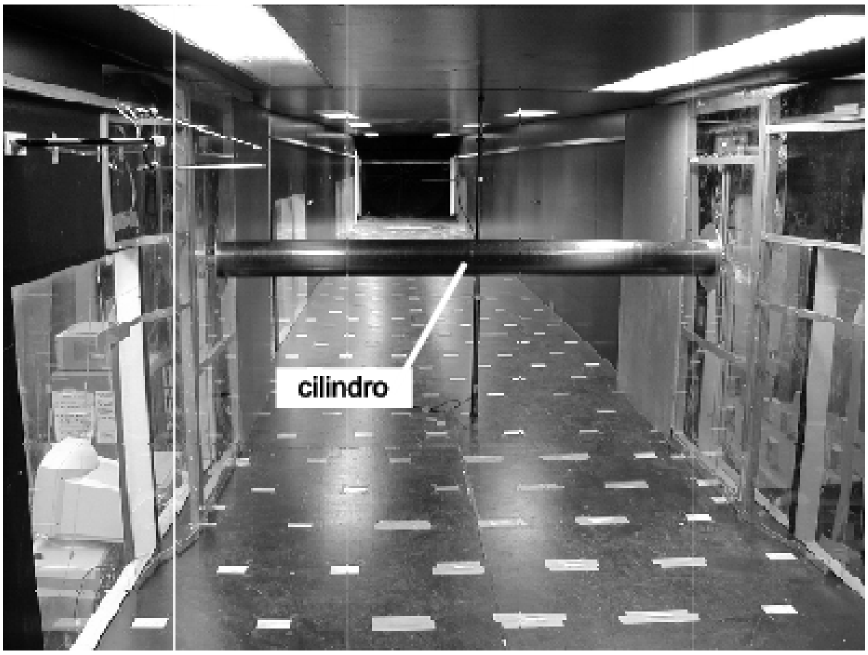

Figure 6.7 Aerolastic model [4].

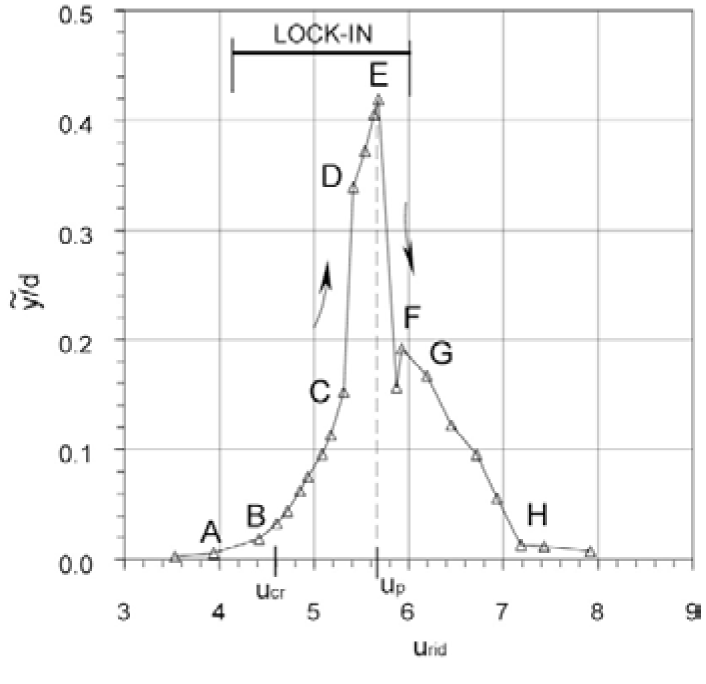

Figure 6.8 Oscillation amplitude vs. reduced velocity for increasing wind speed [4].

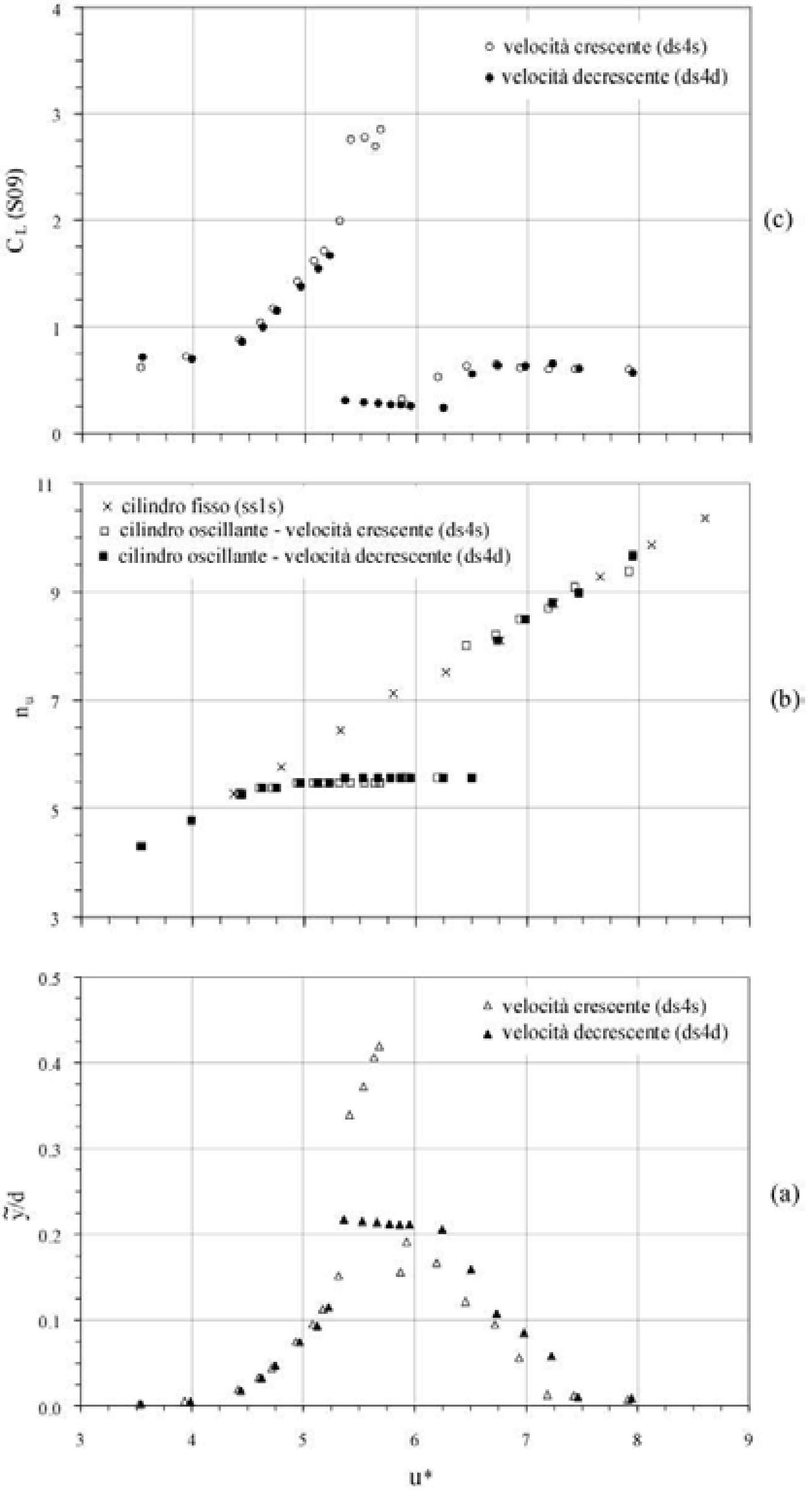

Figure 6.9 (a) amplitude oscillation (r.m.s.), (b) shedding frequency and (c) lift coefficient C_L (r.m.s.) at mid section vs reduced wind velocity [4].

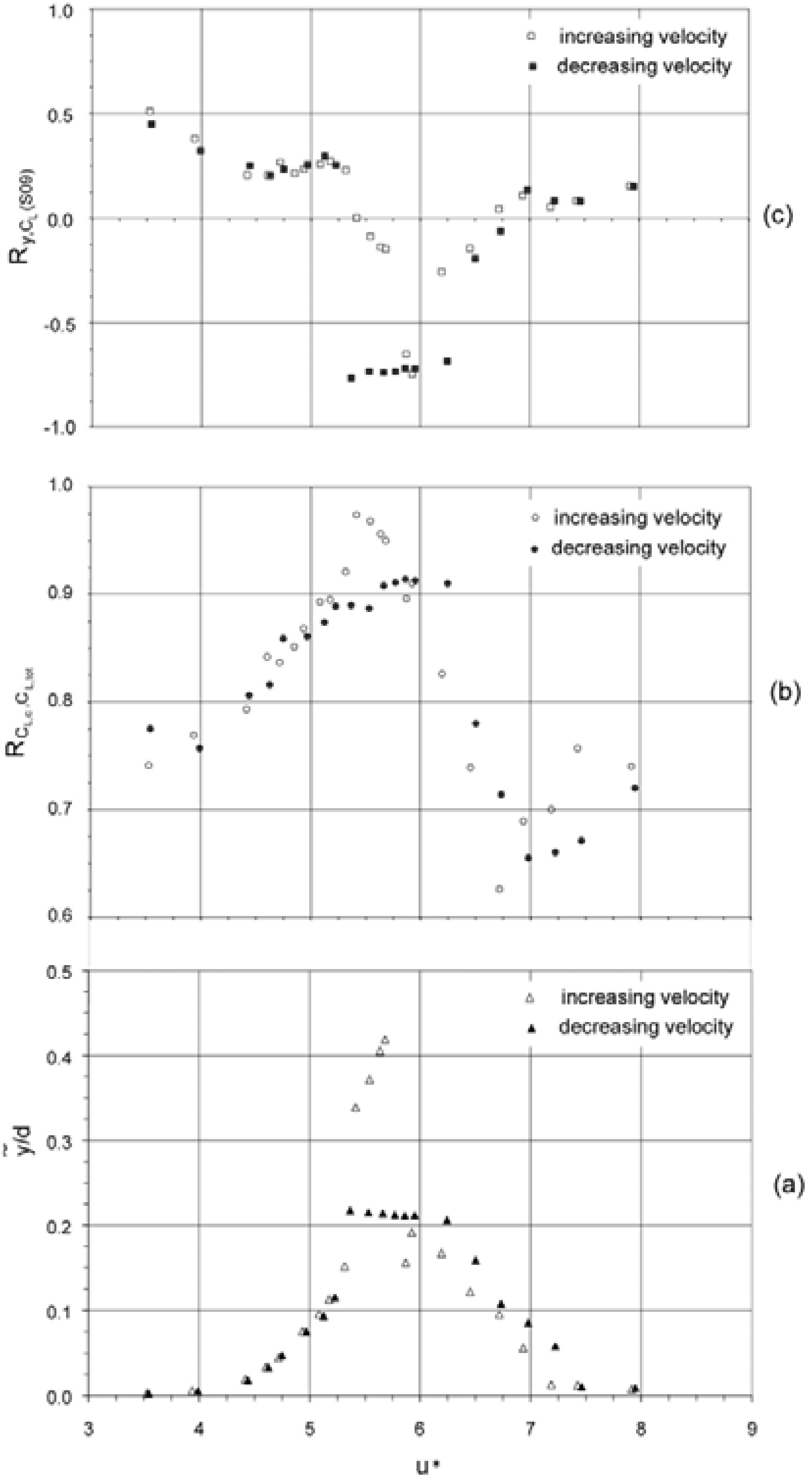

Figure 6.10 (a) amplitude oscillation (r.m.s.); (b) correlation between lift at mid section and global lift and (c) correlation between lift at mid section and displacement vs reduced wind velocity [4].

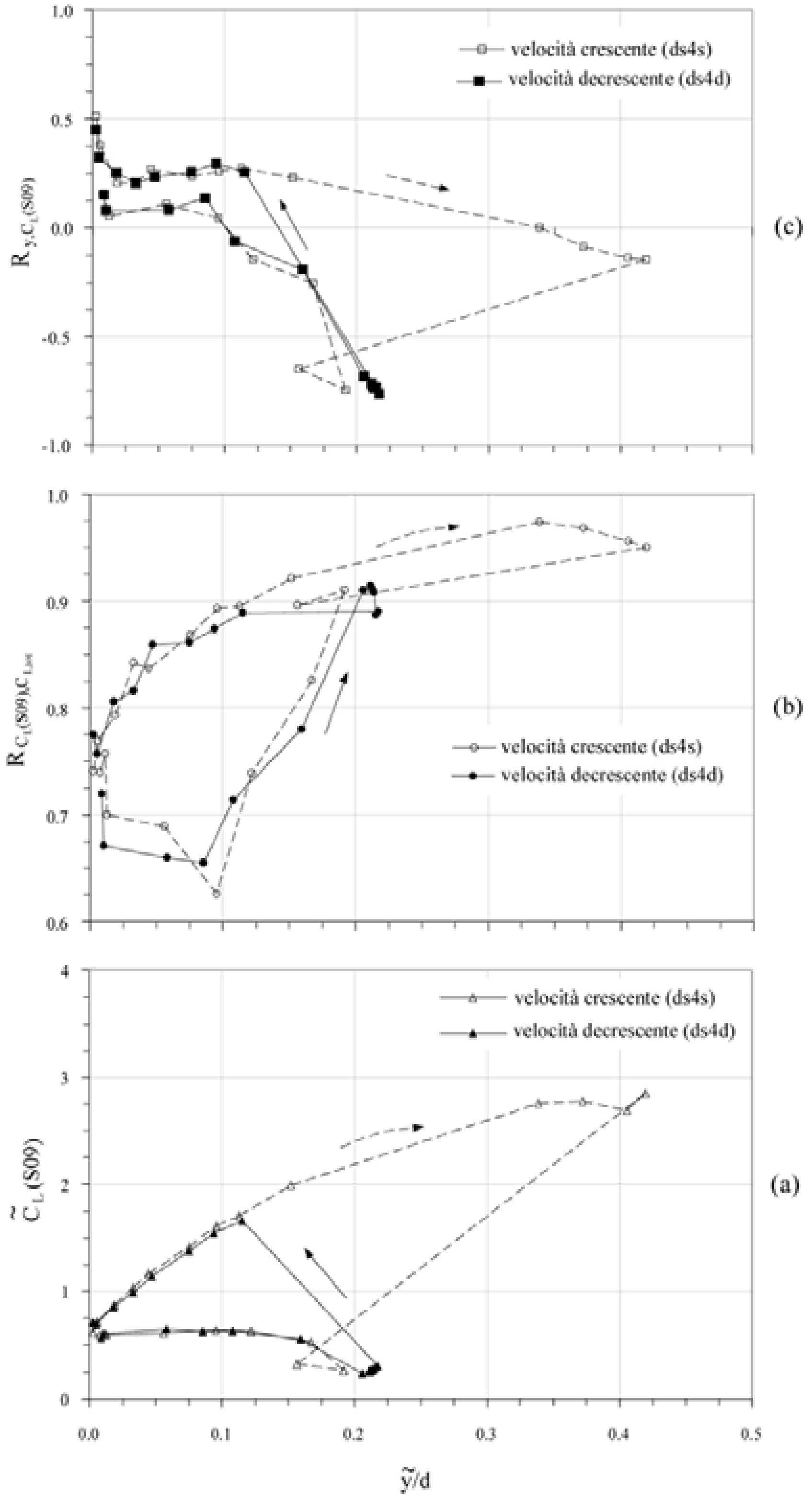

Figure 6.11 (a) lift coefficient at mid section (r.m.s); (b) correlation between lift at mid section and global lift and (c) correlation between lift at mid section and displacement vs reduced amplitude (r.m.s) [4].

Figure 6.12 Great Belt Bridge [n]

6.3.4 Vortex shedding load on suspended bridges

Recent studies have highlighted the relevance of vortex shedding from the bridge deck for wind speed in the lock-in interval, during or after the erection of the structure [i,j,k,l,m]. An example from the past is also represented by the Menai Strait Suspension Bridge in England (1826), corresponding to the first recorded event of vortex-induced vibration observed during the construction stages of the structure. Vortex induced steady-state vibrations have been observed on different categories of bridges, all characterized by extreme slenderness of the deck.

The key aspect of all the examples is the fact that, as a consequence of the extremely low values of the inherent mechanical damping, significant vertical oscillation of the deck can be noticed at relatively low wind speed (15-25 m/s), considerably lower than the flutter instability threshold, and likely to occur very often in the lifetime of the structure. Consequences associated with this kind of cyclically wind-induced oscillations might potentially include fatigue problems on the structural elements (e.g., hangers, in particular at the anchorages) and the reduction of travel safety and/or comfort levels for both road and railroad users.

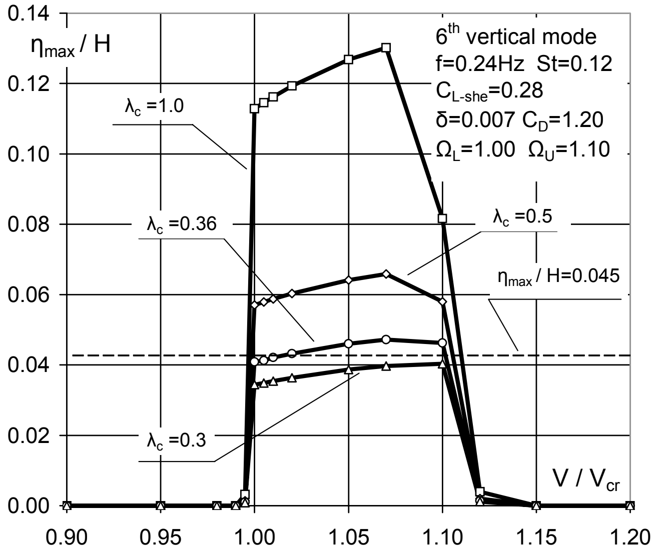

Figure 6.13 Lock-in curve for the Great Belt Bridge [7]

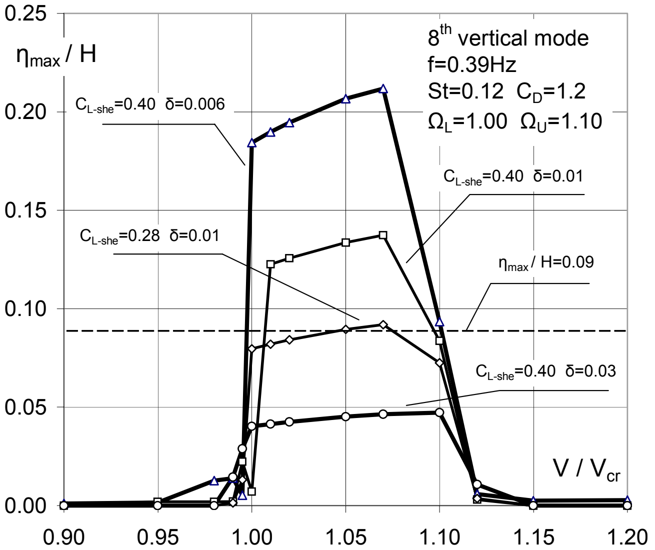

Figure 6.13 Lock-in curve for the 1:80 section model of the Great Belt Bridge [7]

To examine this kind of problem the vortex shedding load model described in [h] has been implemented in the f.e. code TENSO. The code, which has been progressively improved in the last ten years, is now able to model different kinds of geometrical and mechanical non-linearities, including the monolateral behaviour of the hangers, together with the most important kinds of wind effects on slender structures (static, dynamic or aeroelastic forces). The vortex shedding load model has been applied to the Great Belt Bridge (main span L=1624 m, Figure 6.12). In particular, comparisons have been shown with tests on a 1:80 section model reported in [n] and the full scale measurements performed by Larsen [o].

For the same damping measured on the section model, the proposed model is capable of reproducing the experimentally derived displacement (broken line in Figure 6.13) when a lift coefficient $C_{L\text{-}she}$=0.28 is considered, compatible with values currently reported in the technical literature. In Figure 6.13 V/V_{cr} denotes the ratio between the actual value of the wind speed and the value for which the Strouhal's shedding frequency coincides with the structural eigenfrequency. Simulations based upon the value $C_{L\text{-}she}$=0.40 (closer to values suggested by the Eurocode 1, part 2.4, for similar sections), are also reported in Figure 6.13; in the same figure the results obtained for different damping coefficients are plotted, for the sake of comparison.

In consideration of the uncertainties related to the assessment of the aerodynamic parameters St, $C_{L\text{-}she}$, C_D, not reported in the quoted paper, the results obtained can be considered as quite satisfactory, in terms of both the maximum value of displacements and the overall shape of the lock-in curve.

Figure 6.14 shows the comparison between the maximum value of the measured displacement (broken line) in case of lock-in with the 6th mode and the curve, obtained for the same mode by the proposed model; a lift coefficient $C_{L\text{-}she}$=0.28, corresponding to the value identified from the section model analysis, and a logarithmic damping δ=0.007 have been adopted. The curves refer to different values of the non-dimensional correlation length λ_c, defined as:

$$\lambda_C = \frac{l_c}{l} \tag{6.8}$$

where l is the distance between two consecutive nodes of the modal shape and l_c is the length of application of a perfectly correlated load ($\lambda_c \leq 1$).

Good correspondence between the numerical results and the experimental values is achieved for λ_c around 1/3. In consideration of the fact that such a correlation length is reasonable for this category of structures, the reliability of the proposed model is confirmed.

6.4 BASIC REFERENCES

[a] Goswami I. 1991. *Vortex-induced vibrations of circular cylinders*. PhD dissertation, The John Hopkins University, Baltimore, Md

[b] Simiu E., Scanlan R.H. 1996. *Wind Effects on Structures*. Fundamentals and Applications to Design. 3rd Edition, Wiley, New York

[c] Hansen S.O. 1998. Vortex-induced vibrations of line-like structures, *Cicind Report*, **15**.(1)

[d] Basu R.I., Vickery B.J. 1983. Across-wind vibrations of structures of circular cross-section. Part II. Development of a mathematical model for full-scale applications. *Journal of Wind Engineering and Industrial Aerodynamics*, **12**, 75-97.

[e] Sarpkaya T. 1978. Fluid forces on oscillating cylinders. *J. Wtrwy., Port, Coast. and Oc. Div.*, **104**(1), 19-24.

[f] Ruscheweyh H. 1994. Vortex excited vibrations, in Sockel H. (ed), *Wind excited vibrations of structures*, Springer-Verlag, New York, 51-87

[g] Koopmann G.H. 1967. The vortex wakes of vibrating cylinders at low Reynolds numbers. *Journal of Fluid Mechanics*, **28**, 501

[h] D'Asdia P., Noè S. 1998. Vortex induced vibration of reinforced concrete chimneys: in situ experimentation and numerical previsions. *Journal of Wind Engineering and Industrial Aerodynamics,* **74-76**, 765-776

[i] Larsen A.., Jacobsen S. 1992. Aerodynamic Design of the Great Belt East Bridge. In Larsen A. (ed), *Aerodynamics of Large Bridges*, Balkema, Rotterdam, 269-283.

[j] Lee S., Lee J.S., Kim J.D. 1997. Prediction of vortex-induced wind loading on long-span bridges. *Journal of Wind Engineering and Industrial Aerodynamics*, **67-68**, 267-278

[k] Scanlan R.H. 1998. Bridge flutter derivatives at vortex lock-in. *ASCE Journal of Structural Engineering*, **124**(4), 450-458

[l] Kawatani M., Toda N., Sato M., Kobayashi H. 1999. Vortex-induced torsional oscillations of bridge girders with basic sections in turbulent flows. *Journal of Wind Engineering and Industrial Aerodynamics*, **83**, 327-336

[m] Frandsen J. B. 2001. Simultaneous pressures and accelerations measured full-scale on the Great Belt East suspension bridge. *Journal of Wind Engineering and Industrial Aerodynamics*, **89**, 95–129

[n] Larsen A. 1993. Aerodynamic aspects of the final design of the 1624 m suspension bridge across the Great Belt. *Journal of Wind Engineering and Industrial Aerodynamics*, **48**, 261-285.

[o] Larsen A., Esdahl S., Andersen J.E., Vejrum T. 2000. Storebelt suspension bridge - vortex shedding excitation and mitigation by guide vanes. *Journal of Wind Engineering and Industrial Aerodynamics,* **88**, 283-296

6.5 LIST OF PUBLICATIONS

[1] D'Asdia P., Noè S. 2001. Distacco dei vortici su strutture verticali snelle. *Ingegneria del vento. Introduzione alla progettazione strutturale alla luce della nuova normativa*, Augusti G., Materazzi A.L., Sepe V., Eds, CISM, Udine, Italy

[2] Fathi S., Noè S. 2001. Numerical and analytical assessment of lock-in response. *Int. J. Aerodynamics and Wind Tech.*, **2**, 1-17

[3] D'Asdia P., Fathi S., Noè S., Kopp G.A., Galsworthy J. 2001. Vibrazioni indotte dal distacco dei vortici. indagini sperimentali. *Proc. Nat. Workshop on "Problemi di vibrazioni nelle strutture civili e nelle costruzioni meccaniche"*, Perugia, Italy

[4] Fathi S., Noè S., Kopp G.A., Galsworthy J. 2002. Vibrazioni across-wind per distacco di vortici: prove sperimentali. *IN-VENTO-2002 – 7th National Conf. on Wind Engineering*, Milano, Italy

[5] Fathi S., Noè S., D'Asdia P., Comisso S., Visintin A. 2002. Il carico aeroelastico nelle vibrazioni across-wind per distacco di vortici. *IN-VENTO-2002 – 7th National Conf. on Wind Engineering*, Milano, Italy

[6] Kopp G.A., Galsworthy J., Martinuzzi R.J., Kamprath M., Fathi S., Noè S. 2002. Velocity and surface pressure measurements from a circular cylinder at lock-in. *Proc. 2002 ASME Fluids Engineering Summer Conference*, Montreal, Quebec

[7] D'Asdia P., Sepe V., Caracoglia L., Noè S. 2003. A model for vortex-shedding induced oscillations of long-span bridges. *Proc. ISEC-02 - 2nd Int. Struct. Eng. and Construction Conf.*, Roma, Italy.

WITH CONTRIBUTION FROM:

Luca Caracoglia, University of Illinois, Urbana, Illinois, USA
Piero D'Asdia, Università "G. D'Annunzio" di Chieti-Pescara
Salim Fathi, Università "G. D'Annunzio" di Chieti-Pescara
Vincenzo Sepe, Università "G. D'Annunzio" di Chieti-Pescara

7 Wind pressure distribution analysis

Massimiliano Gioffrè** & **Vittorio Gusella
University of Perugia

2.1 INTRODUCTION

Accurate estimates of the global wind action can be obtained for line-like structures using the quasi-static theory, i.e. calculation of forces and moments using the wind speed and the drag, lift, and moment coefficients. Within this theory it is possible to neglect the turbulence quadratic terms and to obtain a Gaussian probabilistic model for the response assuming Gaussian wind speed and linear structural behavior. It follows that well known advantages arise when evaluating the structural safety using the response peak values and/or the fatigue damage associated to repeated fluctuations.

The described methodology does not give accurate results when structural shape and dimensions induce flow-structure interactions and/or the wind local effects are of interest. In these cases focus has to be shifted to the point characteristics evaluating pressure and pressure coefficients fluctuations.

This second approach is definitely more complete and accurate than the quasi-static method for describing both aerodynamic and aeroelastic features. On the other hand the correct evaluation of the aerodynamic load is a very difficult task because many of the research topics associated to this approach didn't find a definitive solution yet. Some of these can be summarized as follows:

- wind pressure fields experimental assessment both on site and using wind tunnel models;
- wind pressure fields theoretical modeling;
- wind pressure fields numerical simulation;
- estimation of the structural response to wind loads.

One of the main aspects arising from the analysis of wind pressure time series is their non-Gaussian nature, that has to be carefully considered for the complete understanding of the complex flow-structure interaction phenomena. Furthermore, the non-Gaussian features of the local pressure fluctuations directly influence also the global forces on the construction envelope and the internal forces on the structural system. Depending on the correlation structure of the pressure field, the central limit theorem might fail when integrating pressure time histories to obtain aggregate forces on the cladding surfaces or when filtering the pressure field to estimate the structural response.

Within this context a new research theme was faced in the last five years based on the concept

Edited by Gianni Bartoli and Francesco Ricciardelli, WINDERFUL: Wind and INfrastructures: Dominating Eolian Risk
For Utilities and Lifelines, ISBN 88-8453-138-1, ©2004 Firenze University Press

of Database Assisted Design (DAD), where the design wind load and load effects are estimated directly from wind tunnel experimental tests. The obtained results are compared to those suggested by the current standard provisions to verify the possibility to use the DAD approach as a reliable alternative to the codes prescriptions.

The topics described above were studied mostly by the Firenze and Perugia Research Units and the main results obtained will be described in the following with reference to the specific structural typologies under investigation and highlighting the four central themes: experimental data, wind pressure field modeling, numerical simulation, wind load effects.

2.2 LOW-RISE BUILDINGS

Mitigation of the damage caused by windstorms to low-rise buildings is one of the top priorities of the wind engineering community today. The main topics studied in the research project by the Perugia Research Unit are summarized in the following:

- wind pressure field modeling from statistics on sets of pressure coefficient fluctuations obtained from wind tunnel experimental tests;
- wind pressure field numerical simulation;
- estimation of aggregate forces on the building cladding and internal forces in the structural system;
- estimation of design loads from experimental data and comparison with current standard provisions [ASCE-7 98, EUROCODE 1 (EC1), and DM 96 (Italian)];

2.2.1 Wind pressure field modeling

The wind pressure field on a typical low-rise building can be modeled using the information given by the statistical characterization of experimental data obtained from wind tunnel tests.

The pressure coefficient time series were recorded at University of Western Ontario (UWO), Canada [a] on gable roof building models with roof pitch of 1 on 24. All the buildings have the same full-scale plan dimensions of 61 m by 30.5 m and two different eave heights: 6.1 m and 9.75 m. The boundary layer wind tunnel was configured to simulate open country and suburban terrain changing the roughness elements. The six model configurations used in the study are summarized in Tab. 7.1.

The pressure coefficient time histories were simultaneously recorded for 60 seconds at 500 locations (Fig. 7.1) with sampling frequency 400 Hz. Different directions of the incoming wind were considered varying from 0° to 180° with 5° steps. The velocity scale was fixed at 1:2.5, which gives the time scales of 1:80 and 1:40 in the 1:200 and 1:100 building models, respectively.

Setting	Length scale	Roughness	Eave height	v_H	v_H / v_{10}
			m	m/s	
S11	1:200	Open country	6.10	10.15	0.926
S12	1:200	Open country	9.75	10.95	0.996
S21	1:200	Suburban terrain	6.10	8.30	0.897
S22	1:200	Suburban terrain	9.75	8.95	0.994
S31	1:100	Suburban terrain	6.10	9.35	0.897
S32	1:100	Suburban terrain	9.75	10.05	0.994

Table 7.1 Test model settings used in [a]

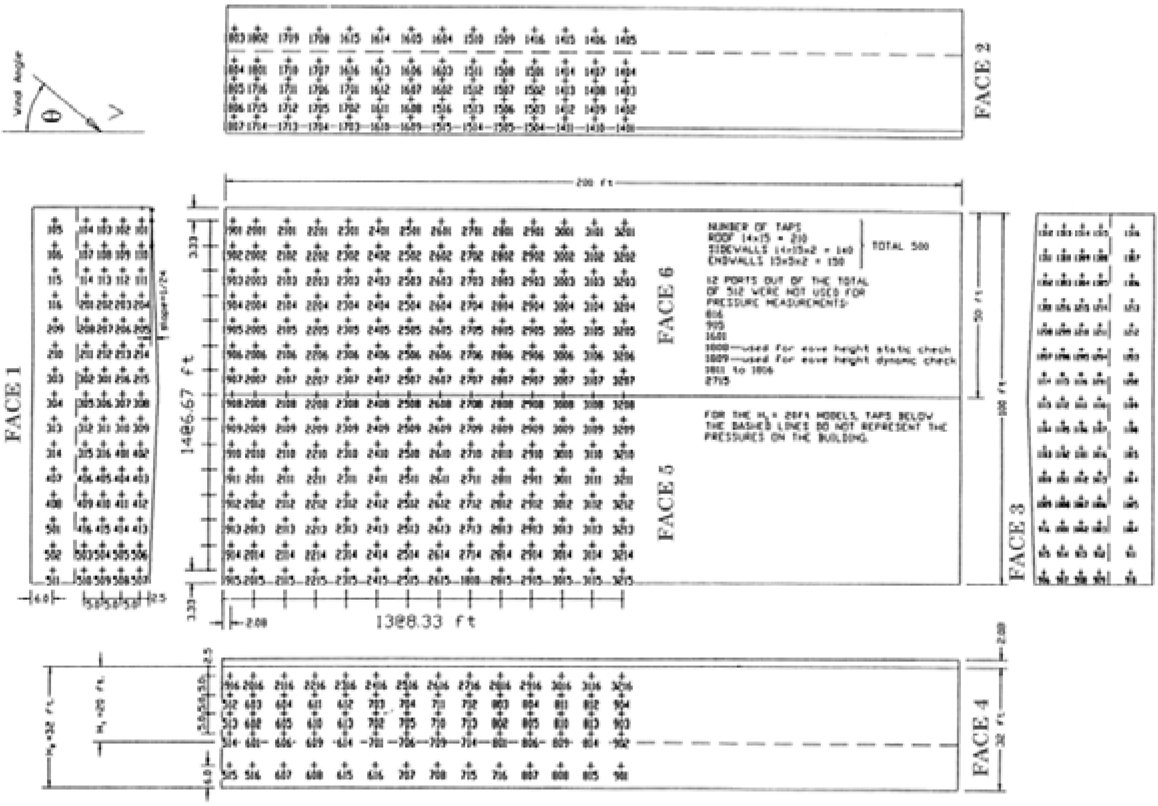

Figure 7.1 Pressure tap locations

Given the large amount of data, a set of interactive numerical procedures is developed to summarize the main statistical properties into 3D maps. In particular, these procedures give the opportunity to obtain plots of the pressure coefficient time histories, histograms, auto- and cross-correlation functions, auto- and cross-spectral functions at each desired tap or couples of taps, for each of the available configurations. Moreover it is possible to have maps of the first four statistical moments (mean, rms, skewness and kurtosis coefficient) at all the faces of the building monitored by pressure taps. Figs. 7.2-7.5 show an example relative to model S22 when the wind is blowing from 45° (cornering wind).

It can be noted that this kind of representation is very effective to establish were the wind pressures deviate from the Gaussian model, which is characterized by the skewness coefficient and kurtosis coefficient. Figs. 7.4 and 7.5 confirm that the separated flow regions are characterized by a strong non-Gaussian behavior (e.g the suction delta-wings on the windward roof). The analysis of the other model configurations demonstrated that the influence of the roughness, the model scale, and the eave height on the non-Gaussian localization in space and magnitude changes significantly from case to case [1,2]. This demonstrates that DAD can be very useful especially when dealing with extreme values and reliability analysis.

2.2.2 Wind pressure field numerical simulation and estimation of aggregate forces

Numerical simulation procedures are developed to reproduce the pressure coefficient fluctuations recorded in the boundary layer wind tunnel at the Wind Load Test Facility at Clemson University. Details on the data sets and the wind tunnel configuration can be found in [b,c].

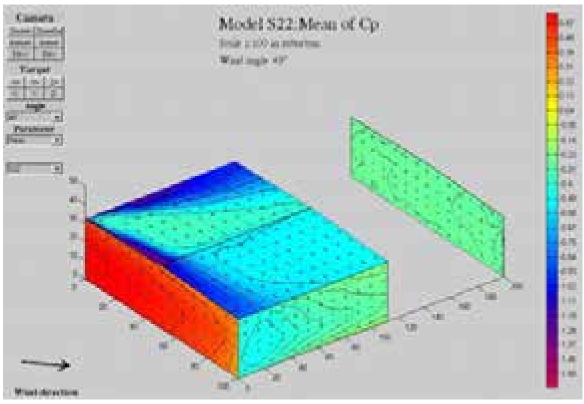

Figure 7.2 Maps of the pressure coefficient mean

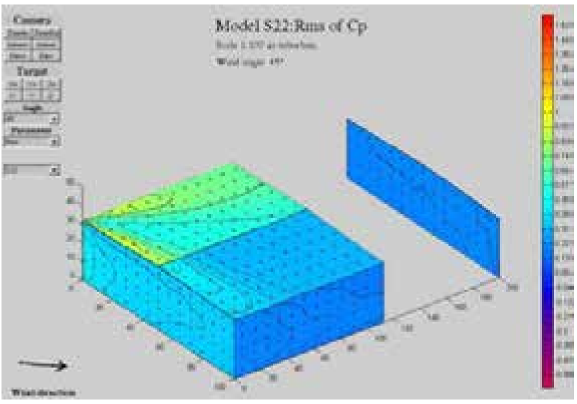

Figure 7.3 Maps of the pressure coefficient rms

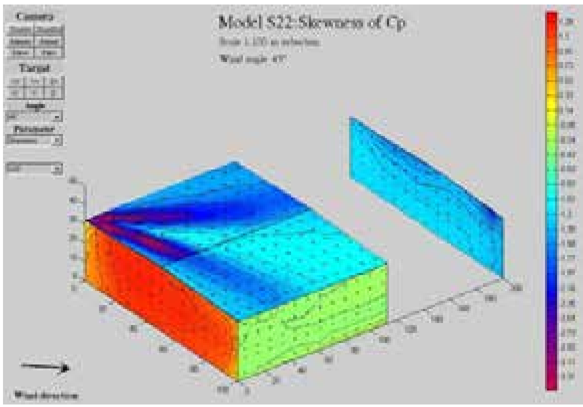

Figure 7.4. Maps of the pressure coefficient skewness

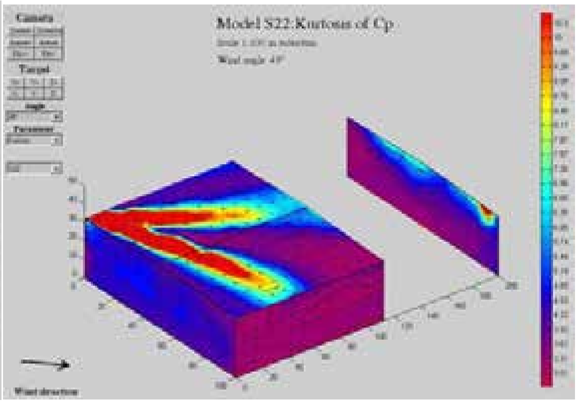

Figure 7.5 Maps of the pressure coefficient kurtosis

In particular, a small area on the roof is considered, representing a panel of roof sheathing near the ridge line for the building model with roof pitch of 5 on 12 in open country terrain. Two rows of seven roof taps are used to obtain the pressure time series used in the study. Two wind directions are used: the 90 and 180 degree angles of incidence, producing cases of strongly non-Gaussian and Gaussian pressure, respectively [d]. Fig. 7.6 shows the location of the taps and the angles of incidence, where the corner of the building containing the pressure taps is shaded.

The physical limitations on the number of taps that could be sampled at the same time did not permit simultaneous measurement of more than one row of taps, preventing the evaluation of correlation between taps in neighboring rows. Three correlation structures between the pressure time series among taps in neighboring rows were thus assumed: case a) full correlation between rows; b) no correlation between rows; c) no correlation between any of the 14 taps.

Among the number of methods available to generate non-Gaussian time histories (e.g. [e, f, g, h]) the study reported here uses the correlation distortion-based method presented by Grigoriu [g] and applied to wind pressure fluctuations by Gioffrè et al. [i] due to its easy adaptation to multi-variate simulation and the efficiency of computation. Using this simulation methodology sets of 14 taps are simulated based on the correlation and probability functions measured from the wind tunnel data, and presented in [d]. Both the chosen directions result in a high degree of correlation between taps in a single row, suggesting a large aggregate load effect on the sheathing panel. Results are presented here for the 90 degree case only due to space limitations.

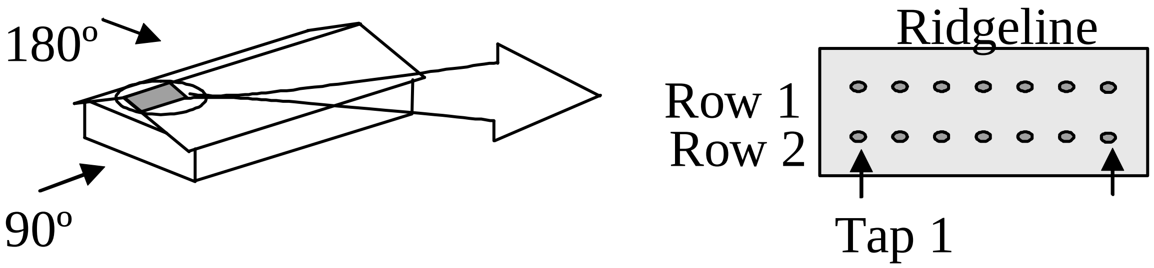

Figure 7.6 Angles of incidence and tap locations

The overall aggregate pressure coefficient is determined for the total panel and in the separate ASCE zone 2 and zone 3 regions on the panel using 100 simulations consisting of 6000 time steps per simulation [3]. The mean value is independent of the assumed correlation case, while standard deviation, skewness and kurtosis of aggregate load changes significantly from strong correlation among taps of neighboring rows to no correlation. Fig. 7.7 displays the difference in the higher moment information for cases a), b) and c) over 100 simulations. The legend refers to high correlation, low correlation and no correlation, corresponding to case a), b) and c) respectively.

Figure 7.7 shows a much higher standard deviation and more severe skewness and kurtosis in aggregate load for the case of high correlation. The effect is a much higher probability of larger overall pressure for the strongly correlated case. This is demonstrated in Fig. 7.8 by comparing the histograms from 100 simulations of the aggregate pressure coefficients in the edge and corner zones (ASCE zone 2 and zone 3 regions on the panel) in ratio with the ASCE 7-98 assigned pressure coefficients for these zones. For the case of no correlation, the individual highly skewed taps sum to an essentially Gaussian distribution of load due to the central limit theorem. The

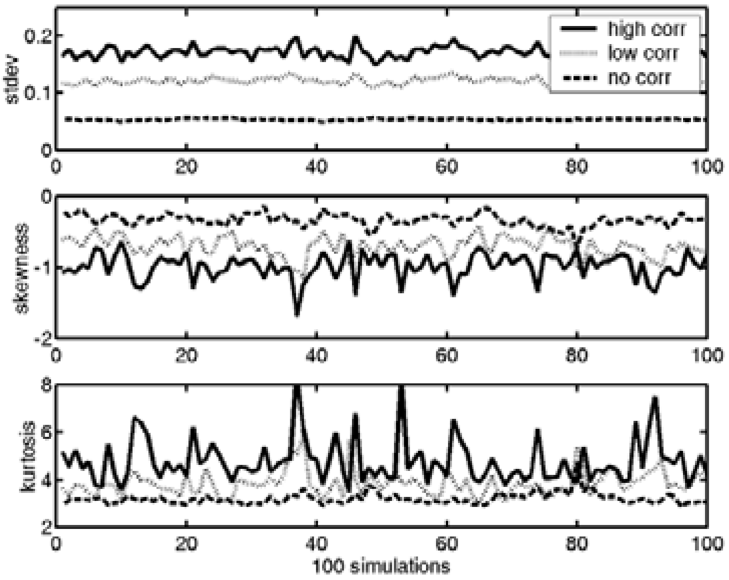

Figure 7.7 Standard deviation, skewness and kurtosis of aggregate pressure coefficient over panel for the three assumed correlation cases (100 simulations)

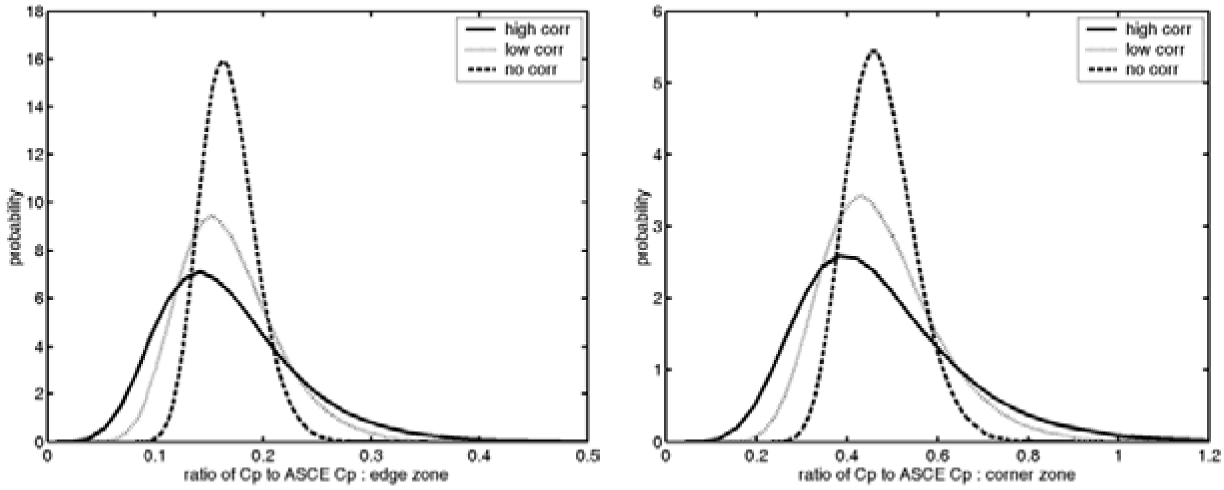

Figure 7.8 Histograms for edge (left) and corner (right) zone aggregate pressure coefficients in a ratio with the ASCE 7-98 pressure coefficients

highly correlated tap case results in a higher standard deviation and strong deviation from Gaussian since the central limit theorem does not apply to the addition of correlated variables. This leads to a significant probability of exceedence of the ASCE pressure coefficients for the corner zones.

The simulated aggregate loads are compared with the uplift capacity of 4 x 8 sheathing as determined experimentally by Cunningham [*l*]. Results are presented for a Douglas fir panel with 6d nails in a 6/12 nail pattern. The aggregate loading over the panel is calculated for the three correlation cases, and time histories are produced for the ratio of load over capacity. Calculations are done using the 150 m.p.h. wind zone in ASCE 7-98, corresponding to Miami and other hurricane prone south Florida cities. Fig. 7.9 shows the histograms for this ratio for the three correlation cases, and a sample time history of the ratio for a single simulation of the full correlation case. The high correlation and skewed probability of the 14 individual taps results in a highly skewed time history of aggregate load to capacity, such that numerous peaks exceed unity. The histogram of the fully correlated aggregate load clearly shows a significant likelihood of panel failure. The assumption of no correlation between rows reduces the likelihood of failure to an insignificant probability.

2.2.3 Estimation of internal forces in the structural system

The measurements described in Section 7.2.1 are also used to seek the spatial stochastic characteristics of wind effects in the main resisting structure of low-rise gable roof buildings made of steel truss frames connected by a bracing system [4].

The pressure coefficient time histories are used in the basic DAD framework to obtain the response time series at any cross-section of any member of the wind load resisting system of low-rise gable roof buildings. Calculation are carried out using a modified version of the numerical procedure WiLDE-LRS developed at N.I.S.T. [m]. This application program is a pilot project aimed to overcome the oversimplification inherent in conventional standards that reduces the highly complex nature of wind-structure interactions into simplified tables and plots both for the lack of comprehensive information and the need of simplified design procedures. The growing availability of wind tunnel facilities, wind tunnel data, and new communication technologies

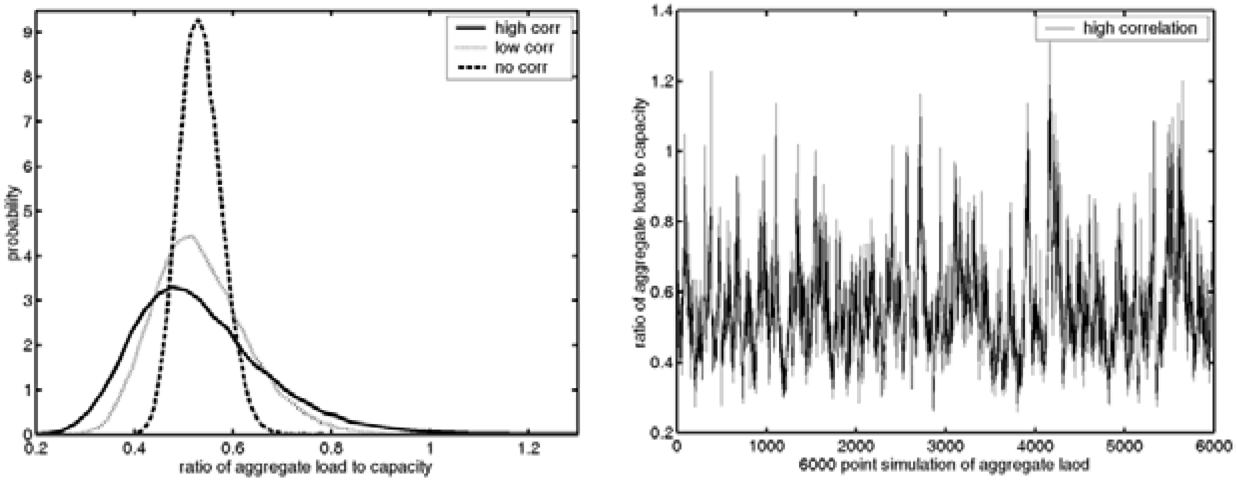

Figure 7.9 Ratio of aggregate pressure to maximum uplift capacity. Left: PDF for three levels of correlation among taps. Right: time history ratio for high correlation

validate the effort in this direction that is promising to give more risk-consistent, safer, and economical designs.

The WiLDE-LRS procedure is based on four main stages. In the first stage the influence coefficients for the building structural system constituted by rigid portal frames hinged at the column bases are calculated from the geometric frame properties. In the second stage the wind pressure time series are computed from the aerodynamic databases containing pressure coefficients as functions of wind directions and from information on extreme wind speeds. The wind load transferred to the frames by the girts and purlins is determined in the third stage. Finally, in the fourth stage the internal forces time histories are computed by adding up the effects of the wind loads transmitted by the girts and purlins at each time instant weighting with the respective influence coefficients.

The basic assumptions that are used in the program at the present stage are the linear elastic behavior of the structure, and that effects arising from cross-bracing between the frames and wind-induced dynamic effects are negligible. This last assumption is warranted for low-rise buildings with natural frequencies of vibration not less than about 2 Hz. Work is in progress on the extension of WiLDE-LRS to other types of structural systems with linear and nonlinear behavior, and that experience wind-induced dynamic effects.

A slightly different structural system made of nine steel truss frames fixed at the column bases and connected by bracing systems is used in the study reported here (Fig.7.10). The new influence coefficients are computed using the finite element approach and are used as input in the WiLDE-LRS numerical procedure to obtain the response time histories in each truss element of the nine frames. Fig.7.11 shows a detailed view of the i-th truss frame constituting the structure with the element numbering.

The obtained internal forces time histories in the truss are used to estimate the response probabilistic features by statistical analysis. Histograms of the axial force fluctuations are plotted together with the associated Gaussian distribution calibrated from the mean and the standard deviation (continuous line). Furthermore, the skewness and kurtosis coefficients are estimated to quantify the degree of deviation from the Gaussian model.

Fig.7.12 shows the axial force time series at six elements of the most upwind frame (frame F1) when wind is perpendicular to the gable end ($\beta = 0$). It is sudden evident that the force

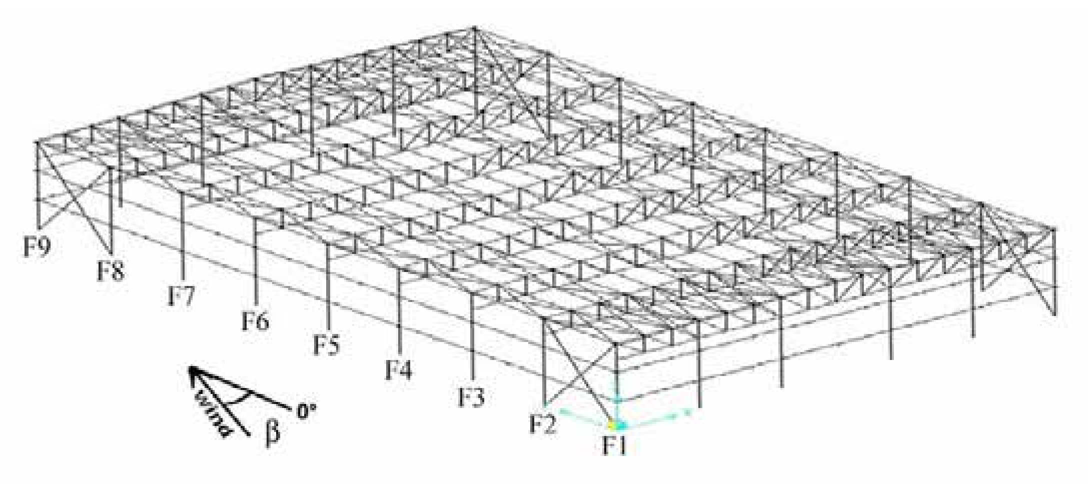

Figure 7.10 View of the main wind load resisting system

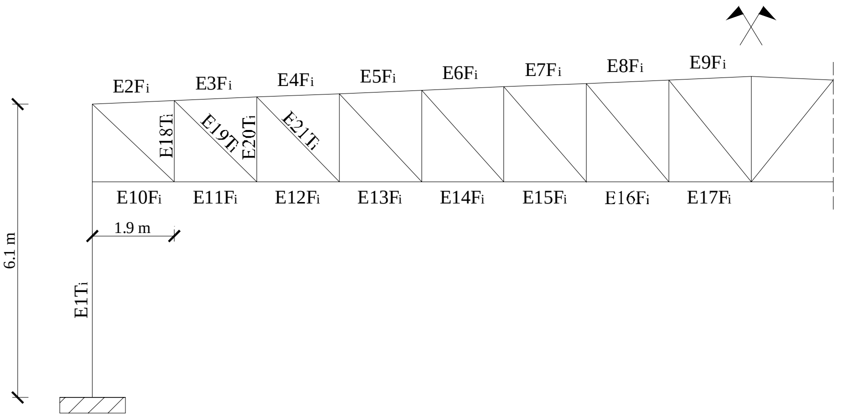

Figure 7.11 Detail of the i-th truss frame with the element numbering

fluctuations are asymmetric about positive mean values and have variability increasing from the eave (E2) to the ridge (E9). The negative pressures arising from flow separation at the gable end induce positive axial forces in the truss upper elements while the lower elements experience compression. This force inversion has to be carefully considered in order to avoid instability phenomena.

The probabilistic features of the axial forces of Fig. 7.12 are reported in Fig. 7.13. The non-Gaussian properties that characterize the wind pressure fluctuations in the separated flow area at the gable end are still reflected in the response time series that experience high values of the skewness coefficients. This result confirm that it is not possible to claim the central limit theorem when adding up strongly non-Gaussian and correlated pressure fluctuations. All the elements considered in frame F1 have similar stochastic features given the symmetry of the structure about the wind flow direction.

The results presented here and those reported in [4] demonstrate the variability in space and time of wind load effects and confirm the need to update conventional codes and standards using the growing availability of wind tunnel facilities, shared databases, powerful computational systems, and fast internet connections. This update would lead to improve the risk-consistency, safety, and economy of the structural design. The limited information capacity of the current standard provisions can be easily enlarged using the DAD approach. The internal forces time

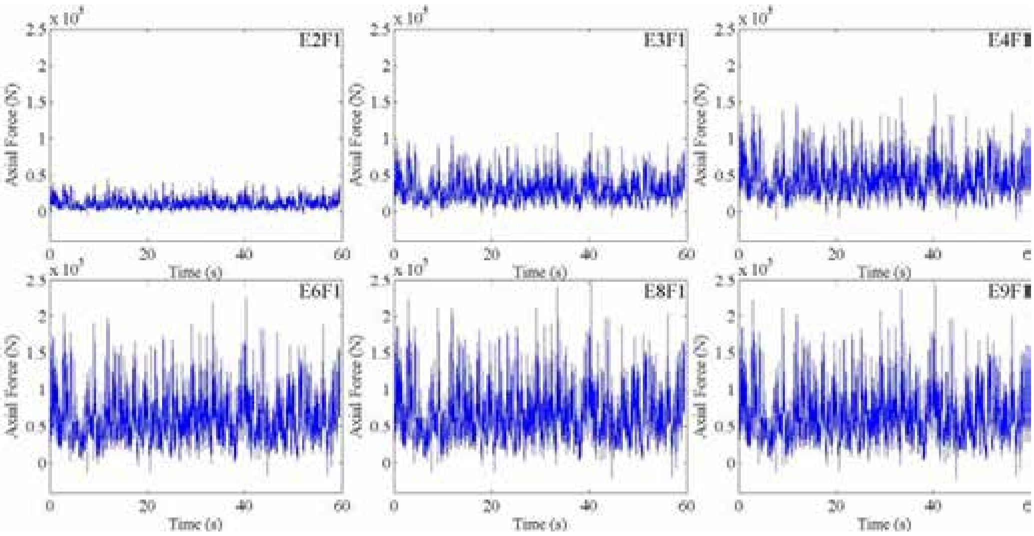

Figure 7.12 Axial force time histories at six elements of frame F1 for β = 0

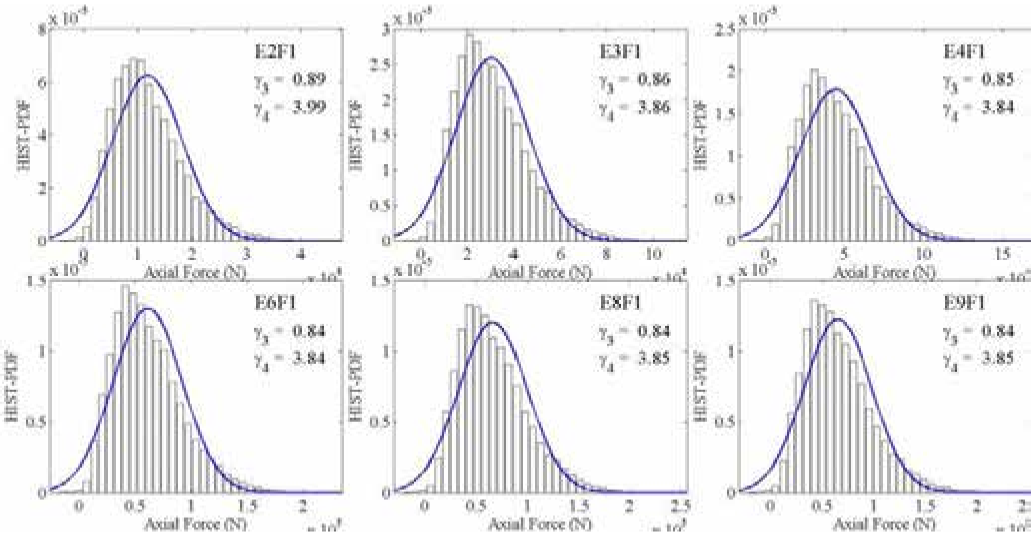

Figure 7.13 Axial force histograms, skewness and kurtosis coefficients estimated at six elements of frame F1 for β = 0.

series can be used both for design purposes and for reliability analysis based on the probability information associated to the structural response. In particular, peaks of internal forces with specified mean recurrence intervals can be accurately estimated using basic theory of stochastic processes that account both for Gaussian and non-Gaussian

behavior of the time histories of interest [n,o]. Furthermore, new modules for the WiLDE-LRSsoftware are currently under development to add simulation capabilities. It will be possible to calibrate suitable stochastic models on the available data and to generate artificial response time histories to be used to enlarge the information needed for reliability analysis.

2.3 BASIC REFERENCES

[a] Lin J., Surry, D. 1997. Simultaneous time series of pressures on the envelope of two large low-rise buildings. *BLWT-SS7-1997*, Boundary-Layer Wind Tunnel Laboratory, The University of Western Ontario. London, Ontario.Canada

[b] Monroe J. 1996. Wind Tunnel Modeling of Low Rise Structures in a Validated Open Country Simulation, *Master's Thesis*, Clemson University Department of Civil Engineering, Clemson, South Carolina

[c] Cope A. 1997. Load Duration Effects on Peak Minimum Pressure Coefficients, *Master's Thesis*, Clemson University Department of Civil Engineering, Clemson, South Carolina

[d] Cope A., Gurley K. 2001. Spatial Characteristics of Pressure Coefficients on Low Rise Gable Roof Structures, *1st Americas Conference on Wind Engineering*, Clemson University, Clemson, South Carolina

[e] Yamazaki, F., Shinozuka M. 1988. Digital Generation of Non-Gaussian Stochastic Fields, *Journal of Engineering Mechanics, ASCE,* **114** (7), 1183-1197

[f] Gurley K., Kareem A. 1997. Analysis, interpretation, modeling and simulation of unsteady wind and pressure data, *J. of Wind Eng. and Industrial Aerodynamics,* **69-71**, 657-669

[g] Grigoriu M. 1998. Simulation of Stationary Non-Gaussian Translation Processes, *Journal of Engineering Mechanics, ASCE*, **124** (2), 121-126

[h] Deodatis G., Micaletti R. 2001. Simulation of Highly Skewed Non-Guassian Stochastic Processes, *Journal of Engineering Mechanics, ASCE*, **127** (12), 1284-1295.

[i] Gioffre M., Gusella V., Grigoriu, M. 2000. Simulation of non-Gaussian field applied to wind pressure fluctuations, *Probabilistic Engineering Mechanics*, **15** (4), 339-345

[l] Cunningham T.P. 1993. Roof Sheathing Fastening Schedules for Wind Uplift, *APA Report T92-28,* American Plywood Association, Tacoma, Washington

[m] Whalen T. M., Shah V., Yang J. S. 2000. A Pilot Project for Computer-Based Design of Low-Rise Buildings for Wind Loads - The WiLDE-LRS User's Manual, National Institute of Standards and Technology, Gaithersburg, Maryland

[n] Gioffrè M., Grigoriu M., Kasperski M., Simiu E. 2000. Wind-induced peak bending moments in low-rise building frames, *Journal of Engineering Mechanics, ASCE,* **126**(8), 879-881

[o] Sadek F., Simiu E. 2002. Peak Non-Gaussian Wind Effects for Database-Assisted Low-Rise Building Design, *Journal of Engineering Mechanics, ASCE,* **128**(5), 530-539

7.4 LIST OF PUBLICATIONS

[1] Gioffrè M., Gusella V., Materazzi A. L. 2002. Problemi di progettazione di antenne per telefonia mobile, *Proc. 7th National. Conf. Wind Eng*, IN-VENTO -2002, Milano, Italy

[2] Gioffrè M., Grazini A., Gusella V. 2002. Reliability of Low-Rise Buildings: Experimental Wind Load Modeling vs. Building Codes, Reliability and Optimization of Structural Systems, *Proceedings of the 10th IFIP WG 7.5 Working Conference on Reliability and Optimization of Structural Systems*, Osaka, Japan

[3] Gioffrè M., Gurley K., Cope A. 2002. Stochastic simulation of correlated wind pressure fields on low-rise gable roof structures, *Proceedings, 15th ASCE Engineering Mechanics Conference (EMD 2002)*, Columbia University in New York City, New York

[4] Gioffrè M. 2003. Stochastic characterization of wind effects from experimental data, System-based *Vision for Strategic and Creative Design, Proc. of the second international conference on structural and construction engineering*, Rome, Italy

8. Reliability and vulnerability

Giuliano Augusti & Marcello Ciampoli
University of Roma “La Sapienza”

8.1 INTRODUCTION

In the last decades, there has been a steep increase in the number of natural disasters and the losses they generate.

This is also the case of windstorms that, in recent years, have produced enormous human and economic losses. Therefore, the risk due to windstorms cannot be neglected in comparison with other environmental risks, and stringent countermeasures against wind risk are imperative.

The main causes of such a dramatic increase of losses are the migration of population (and goods) into wind-hazardous areas and the changes in environmental conditions. Moreover, the structures are becoming more vulnerable to wind action as their weight decreases: for lightweight structures the wind action becomes a leading, dominant effect.

Windstorms that can damage buildings and other facilities can be classified in ascending damage potential (i.e. according to the contribution to wind *hazard*), as: (i) synoptic storms (or winter storms) of the mid-latitudes, (ii) tropical cyclones, and (iii) tornadoes (in some regions, thunderstorms may prevail). The wind speeds are typically of the order of 45 m/s, 70 m/s, and 120 m/s. respectively. Synoptic storms build up within a few hours and reach their climax in a series of extreme gusts. Cyclones may sustain their high level for many hours, whereas tornadoes last at each site just a number of seconds.

But not only the storms of highest intensity are relevant for the risk of damages to building constructions: for instance, smaller but more frequently occurring wind intensities may give rise to *fatigue* damage leading to collapse.

Another risk not depending on extreme loads only, and specifically connected with wind actions, has to do with the interaction of the displacements induced by the wind forces, and the forces themselves: due to this interaction, the motion of the structure inputs energy from the air flow into the structural system. This input may become larger than the structure’s ability to dissipate energy and lead to aeroelastic instability and collapse.

Finally, it can be expected that small storms, even if not causing any significant structural damages, may damage non-structural components and thus give rise to the necessity of extensive and costly repair interventions: hence, they can be very relevant with respect to long-term economic risk.

Edited by Gianni Bartoli and Francesco Ricciardelli, WINDERFUL: Wind and INfrastructures: Dominating Eolian Risk
For Utilities and Lifelines, ISBN 88-8453-138-1, ©2004 Firenze University Press

In what follows, the techniques that can be used to formulate and solve the problem of the *optimal resource allocation* in a campaign for environmental (and especially wind) risk reduction of constructed facilities and lifelines, taking account of several objective functions, are illustrated. This type of optimisation can be a decisive help in the formulation of a rational strategy for wind risk reduction.

8.2 THE OPTIMAL ALLOCATION PROBLEM AND ITS FORMULATION

Let us start by defining *risk* as the product (better, the convolution integral) of three factors, namely

- *hazard* = probability of occurrence of a dangerous event (the *action*): to each *risk*, a different *hazard* corresponds;
- *exposure* (or *exposition*) = probability that the *action* finds something that can be damaged;
- *vulnerability* = (conditional) probability that the object or facility is damaged when hit by the dangerous *action*.

All above definitions can refer to single buildings or facilities, to systems (e.g. lifelines), and to whole inhabited communities.

According to the defined terms, *risk* is the *absolute* probability of *failure* (or the integral of the probabilities of exceeding each degree of *damage*), while *vulnerability* is defined by the corresponding *conditional* probabilities.

The site *hazard* (sometimes improperly indicated also as *risk*) is the probability of occurrence of the dangerous event in the relevant site. If an *intensity* of the event is defined, the hazard is a curve (or a set of curves) relating each intensity to the probability of occurrence in given time span(s).

The *exposure* (or *exposition*) is related to the presence of vulnerable facilities in the site. It has already been noted that population and wealth tend to increase in areas with significant wind hazard; the consequent increase of the *exposure* is thus thought to be the main cause of the increase of wind damages in recent decades.

The *vulnerability* is the sensitivity of the facility to the event in terms of damage.

To reduce risk, one must consider and should act on each of the three factors (*hazard, exposure, vulnerability*). However, with reference to existing built facilities, it is difficult, if not impossible, to modify *hazard* and *exposure*: hence, *risk reduction* is usually identified with preventive interventions aimed at reducing the *vulnerability*.

In planning a risk-reduction campaign, the most common approach is to fix a quantitative target for the considered objective (e.g. that the probability of failure P_f must be below a certain threshold) and then to calculate the amount of resources necessary to attain that target.

It appears more rational to formulate an optimization problem, that in turn can be put in at least three alternative ways. Namely, indicating by C_{tot} the total cost of interventions, deterministic once they have been chosen, and by G_{tot} the *gain* or reduction of *expected losses*, always uncertain in whatever way it is defined and calculated:

I. just minimize the expected losses ($C_{tot} – G_{tot}$);

II. maximize the ratio between total gain and total expenditure (G_{tot}/C_{tot});

III. reverse the problem, and assume that the economic resources available for maintenance and interventions are limited (as indeed they usually are): therefore, to optimize will mean to maximize the total gain for a given maximum total expenditure ($G_{tot} \mid C_{tot}$).

The approach that has been followed (and is illustrated here) is the third one, as it appeared the more realistic: a problem of optimal allocation of resources was thus set up. In simple words, it is searched *how one can make the most out of the limited resources available*, without a pre-

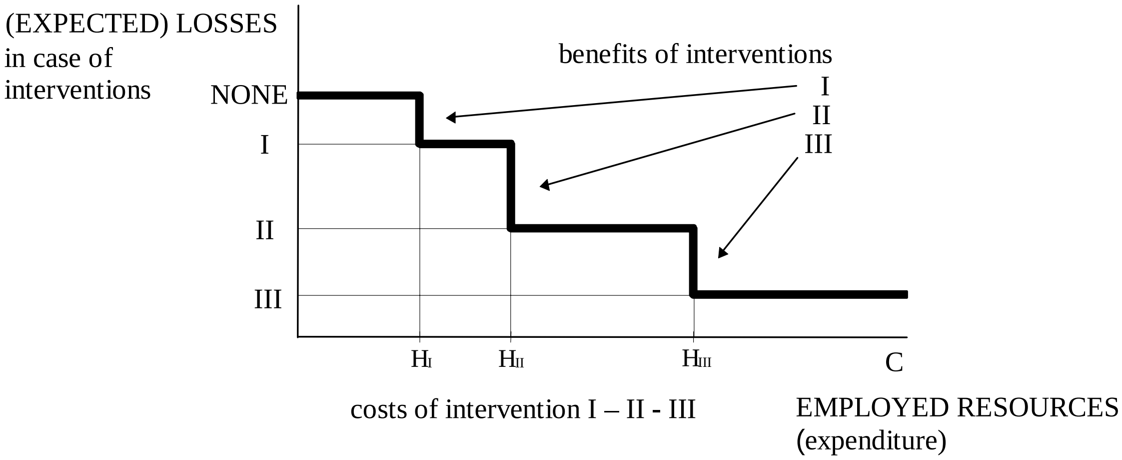

Figure 8.1 Effects of interventions on expected losses for each facility.

determined quantitative target.

As a prerequisite for implementing such an *optimal allocation of resources*, the possible interventions on each facility must be designed, and their costs and expected *gains* (or *loss reduction*) evaluated. Since any intervention requires a finite amount of resources, the relation between the resources employed and the expected losses is a discontinuous (step wise) relation, as qualitatively shown in Fig.8.1.

Provided that such relations were available, the procedures that have been developed allow to estimate and optimize the benefit to be expected from any amount C_{ava} of resources employed in upgrading. However, this requires that all data are available or can be estimated: but this is often the greatest challenge for the actual implementation of the procedures. Indeed, while seismic risk was the subject of many studies in recent years, other environmental risks (like wind risk) has received a comparatively lower attention, and there is a lack of data on damages to built facilities due to these risks.

Three points must be underlined in particular:

- Apart from the difficulties in collecting data and calculating the relevant quantities, these are all uncertain: therefore, the treatment is inherently *probabilistic*, and all quantities must be seen as *expected* and not *deterministic*.
- The actual total loss is seldom just the sum of the losses on each building or facility, especially if the losses are widespread, as in the case of a severe windstorm, because of the general disruption of economy and/or social life in a region. Moreover, some facilities, like lifelines, act as *systems*, and this has a direct effect on the losses. Usually in fact, the losses on *buildings* can be considered simply additive, while *system effects* will play an essential role in the study of *lifeline networks*.
- Several types of losses (and benefits) must be taken into account, and they are often incommensurable (e.g. economic losses, casualties, damage to the cultural heritage, ...): the optimization can be performed separately for each objective, but also "multiple-objective" optimization techniques are needed.

8.3 THE ASSESSMENT OF THE ENVIRONMENTAL VULNERABILITY OF BUILT FACILITIES

8.3.1 Generalities

The last century has been characterized by numerous and remarkable civil engineering achievements, such as large structures, tall buildings, long-span bridges, wide-span enclosures, etc. All these follow a common logic, having as primary rule and criterion to carry the external loads (static and/or dynamic) while ensuring a certain level of safety, minimising the amount and cost of construction material to be employed and optimising the overall construction process.

The use of ever lighter, higher-resistance construction materials, the intense research (analytical, computational as well as experimental) on analysis and prediction of the structural response, and new design methods, all contribute to the increase of the performances and challenges of the engineering facilities. All this has not been accompanied by a generalized increasing attention on a suitable modeling of the wind action and effects, so that research results have been not always been converted into (actual) building practice. As a consequence, the vulnerability of built facilities has increased.

Less spectacular, but much more frequent, damages depend on the turbulent nature of wind. Even if the wind-induced stresses remain considerably below the ultimate and fatigue stress, the large amplitude oscillations may make the structure unable to function as planned. For instance, strong accelerations may make tall buildings uncomfortable; transmission towers may undergo displacements and rotations incompatible with the emitting functions of the antennas; road and rail traffic on bridges may be hindered by large oscillations; …

It is therefore evident that the more the technology of buildings and constructions will proceed towards new frontiers, and ever larger and lighter facilities are realised, the more their *vulnerability* to wind excitation will increase.

Non structural components of modern buildings and infrastructures, and street architecture items (*urban fittings*) have also become elements that increase substantially the total risk of stormy winds.

To formulate a rational strategy for reduction of losses, the first problem that must be faced is the assessment of the *environmental vulnerability* of the existing built facilities, that is, the buildings or the critical elements of a lifeline network.

Apart from the still open problems concerning the elaboration of significant statistics from the survey data in case, for example, of strong windstorms, two evident difficulties now face the exploitation of the collected information, namely: the limited amount of resources that may be available for any preventive upgrading programme, and the multiplicity of quantities whose reduction should be pursued in any such programme, like direct and indirect economic losses, casualties and deaths, damage to artistic and cultural heritage, environmental damages, deterioration of the *quality of life*.

8.3.2 Environmental vulnerability and upgrading

The prerequisite for the optimal allocation of the available resources in a risk-reduction programme is of course the availability of sufficient statistical data on environmental vulnerability and hazard. Limited work has indeed be made on both these aspects in recent years: in particular, no significant statistics have been and are being collected on the *wind vulnerability* of buildings and constructed facilities.

Several alternative ways of describing such *vulnerability* exist, which can be divided into three categories.

In general, the vulnerability of a structure is fully described by a set of *fragility curves*, that relate the probability of reaching a certain *degree* (or *level*) *of damage* (or a well defined *limit state*) with the *intensity* (i.e. the local dangerousness) of the environmental action (e.g. the windstorm).

Alternatively, vulnerability can be measured in an approximate way by a number (the *vulnerability index*) or - even more simply - by including the structure in a *vulnerability class*.

Each description has its appropriate field of application and can be associated to a different way of describing quantitatively the degree of *upgrading* which is necessary, and of evaluating the effectiveness of preventive retrofitting measures.

These methodologies have been fully developed for seismic action, but in principle could be extrapolated to other environmental actions.

Fragility curves require the definition of (i) the relevant *limit state(s)* or quantitative measures of the damage, and (ii) the intensity of the action. A set of *fragility curves* refers to a specific construction, and can be obtained by statistics on similar constructions or by numerical calculations. They are therefore used for important structures: to evaluate the effectiveness of an *upgrading* intervention in this case, a new set of fragility curves must be evaluated for the retrofitted structure, and compared with the initial one.

As cited before, this set of fragility curves can be replaced, although in an approximate way, by a number: the *vulnerability index* V, which characterizes a built facility without explicit reference to the intensity of the environmental action, like wind, and to the level of damage.

The vulnerability index can be obtained by summing up the values associated to the condition of different items, multiplied by the proper weights: the higher values of V correspond to the most vulnerable facilities. An *upgrading* intervention can be defined as affecting one or more items of the form, and be assumed to bring the concerned item(s) into the best condition, i.e. to reduce to zero the contribution of that item to the vulnerability index V, thus decreasing its value.

Of course, to be of significance for prevision of damages and evaluation of the effectiveness of risk-reduction campaigns, the values of the vulnerability index must be calibrated versus actual damages. Such a calibration requires the definition of a measure of the intensity of the environmental action and of the *degree* of damage.

Another definition of vulnerability assumes that all relevant facilities can be subdivided into a limited number of *vulnerability classes*, and that each class X can be associated with a damage probability matrix (DPM). By definition, each element $P_{ji}(X)$ of the DPM pertaining to the vulnerability class X, is the probability that a facility of that class undergoes a damage of level j, if subjected to a wind storm of intensity i. The damage of the facilities and the intensity of the environmental action must therefore be described according to discrete scales.

DPMs can be obtained from statistical analyses of the damages due, e.g., to one or more windstorms, when many buildings of a similar nature are affected in areas of different intensities. All significant modifications to the vulnerability of a facility due to a repair or upgrading intervention can be indicated by its initial and final class.

8.3.3 Objectives of optimization

As already hinted, any structural design and any programme of environmental risk reduction should take many aspects into account, like economic losses, casualties and deaths, damages to the artistic and cultural heritage, environmental damages, deterioration of the quality of life.

Many of these quantities are incommensurable with each other, and cannot be combined into a single *objective function*, not even by means of weighting factors: optimizations with respect to different objectives should therefore be pursued separately from each other.[1] Fortunately, the objectives of the optimizations usually do not conflict with each other (a preventive intervention aimed at reducing the expected economic losses would also reduce the expected number of victims); however, the respective optimal solutions - in general - could not coincide.

As discussed above, much research and statistical investigations are in progress on the environmental *vulnerability* of existing built facilities, so that the expected damage after, e.g., a

---

[1] The rigorous approach to a rational strategy for wind risk reduction would thus be to formulate and solve a problem of *multi-objective optimal resource allocation*. Such a formulation will be exemplified in the final Section of this text, but it will be seen to lead to rather cumbersome numerical procedures and therefore is not always practicable.

windstorm can be estimated. Also, many retrofitting techniques, aimed at *upgrading* the built facilities (i.e. at reducing their expected damage after, e.g., a windstorm), are being developed.

However, comparatively little attention has been paid - at least to the authors' knowledge - to the several possible consequences of the damages, other than the *direct economic costs*: therefore, cost-benefit analyses of a campaign of preventive interventions seem possible only with reference to this aspect, and the question remains very open on how to account for the other, non-monetary aspects (often denoted *intangibles*) that have been quoted above.

A possibility would be to correlate directly the intensity of the environmental action and each of the consequences, e.g. casualties. This approach, in principle the most correct, would require specific and independent statistics for each type of consequences: and, for instance, damage statistics, elaborated with reference to economic costs only, would be useless with regard to *intangibles*. Not much significant work is available along these lines, but some is being in progress.

On the contrary, the possibility of using the vulnerability statistics in all cases requires that *damage* be defined and measured independently from the specific consequence. Other statistical relationships should relate the damage to each relevant consequence: however, this approach could be applied only if reliable damage-consequence relationships of this type were available.

In a ideal world of perfect mathematics and complete knowledge the two approaches would not differ one from the other: in the real world, they do.

The great asset of the *vulnerability* approach lies in the unified treatment of the damage and its statistics, and in the possibility of studying the results of preventive interventions as a decrease of vulnerability, independent of the specific consequences. Its greatest liability might appear the necessity of formulating other and separate relationships between damages and consequences, thus introducing an extra step in the calculations.

But if one considers that in any case a reliable relationship between action and consequences is necessary but in many instances not (or not yet) available, it should be clear that such an approach allows to obtain at least approximate results through extrapolations of known relationships. If the relationship between damage and consequence is deterministic and immediate (as it is implicitly assumed when no distinction is made between damage and its, say, economic cost), then the introduction of the extra relationship does not pose any problem whatsoever.

Thus, the great liability of this approach remains in the unified quantitative definition of damage, be it made in linguistic terms (e.g. slight, significant, heavy, etc.) or in fractions or percentages (usually, 0 corresponds to no damage, and 100% to complete collapse; but also intermediate values, e.g. 50% or 70%, must be defined in an unequivocal way) or, perhaps better, according to a small number of *damage levels*.

However, the vulnerability approach appears essential in an optimal allocation procedure, which looks for the *best* distribution of the upgrading interventions, whose costs are assumed to be known, under a constraint on the total expenditure. In fact, it allows to calculate and introduce unified relationships between the costs of the interventions and the reduction of the vulnerability, to evaluate the reduction of the expected damage for each distribution of interventions, and to make use of the relationships between damages and the consequence chosen as the objective of the optimization in order to choose the *most efficient* one.

In the following, it will be seen that such alternative optimizations are possible by simplified procedures or by sophisticated mathematical instruments.

8.3.4 Optimal allocation of resources among built facilities

In this Section 8.3.4, for the sake of simplicity, the total losses will be considered simply as the sum of the losses on each building.

8.3.4.1 Allocation to vulnerability classes

The first example that is considered deals with a procedure in which no formal optimization procedure is necessary. The scope is to plan the preventive interventions to reduce environmental risk: it is assumed that the vulnerability of the built facilities can be described through DPMs.

Realistic costs have to be estimated (as percentages of the construction cost), both for restoring a facility of each class to its original condition after a level j damage, and for each type of upgrading intervention. In general these percentages (and the construction cost per unit volume) depends on the volumes of the built facilities actually involved in the operations.

The restoration costs after a windstorm of any relevant intensity can be forecast - for each class - by multiplying the probabilities of damage by the unit restoration costs estimated for each damage level, and summing up the columns.

The intervention are here assumed to correspond to a change of the class of the facility, and therefore of the forecast cost of damage: thus, the *unit gains* δr_i due to each type of intervention, forecast for each given intensity i, that is, the differences between the forecast restoration costs without and with the interventions, must be derived.

Multiplying these forecast gains by the probabilities of occurrence π_i of the relevant windstorm during the design life of the building, and summing up, the *expected unit gains* δr_p can be calculated.[2]

Finally, on the basis of the assumed (deterministic) costs C_l of each intervention (once more, estimated as percentages of the construction cost), the *expected efficiency* G_c of each type of intervention can be assessed.

It can be noted that, if the values of G_c are smaller than one, no economic advantage should be expected from preventive interventions: under this limited view point, it would then appear logical not to perform any intervention. However, the danger to human lives and to the environment, and a number of other considerations invalidate such a conclusion: in general, it has therefore to be assumed that preventive interventions are actually performed and only their optimal choice is sought.

No formal mathematical procedure is necessary to optimize the allocation of resources in this example. It is sufficient to remark that the larger or smaller efficiency of an intervention depends on the relative values of the ratio G_c.

Noting that, once the facilities have been assigned to a class, the procedure does not distinguish between individual facilities but can only refer to fractions of the volume of each class, the choice of the interventions to be performed in this specific case for any amount of available resources does not present any difficulty.

This optimization can be referred to direct economic gains and losses, but also to alternative optimization objectives, like the decrease of the number of persons endangered by a wind storm. The final choice of the solution should take into account the results of calculations carried out with reference to different objectives.

8.3.4.2. Allocation to individual built facilities by dynamic programming

Assume that the environmental vulnerability of each facility is measured by a number V (the *vulnerability index*) that is related to the degree of damage D and to the intensity of the environmental action, like the windstorm, by known (or assumed) relationships; define different possible types of interventions, and estimate their costs, together with the cost of construction of the facility.

---

[2] Note that the term *forecast* is intended as a value *conditional* on a given windstorm intensity, while *expected* includes the probability of occurrence of each windstorm intensity.

In order to formalize the optimization problem, define *gain* or *return* $g_i^k(C_l)_m$ of an intervention of cost C_l performed on the m-th facility, the decrease in the expected damages when an environmental action of intensity i occurs (the index k denote the considered objective). In other words, the return is equal to the difference between the damages that would occur without any intervention and after having performed the intervention of cost C_l. For discrete types of interventions, the return functions are multiple step functions (see Fig.8.1).

Then, with reference to the *forecast* return under an environmental action of given intensity i, the optimization problem can be formulated as follows:
maximize the total return $F_{k|i}$ (for a given intensity i of the environmental action):

$$F_{k|i}\{(C_l)_1, (C_l)_2, ..., (C_l)_m\} = \sum_m g_i^k(C_l)_m \tag{8.1}$$

subject to:

$$\sum_1^N {}_m (C_l)_m \le C_{ava} \tag{8.2}$$

where the index m = 1, 2, ..., N indicates the built facility, the index i = 1, 2, 3, 4 the relevant interval of windstorm intensities, and C_{ava} the maximum amount that can be spent in preventive interventions (the available resources).

The maximum can also be sought of the *expected* total return[3]:

$$F_k = \sum_i \sum_m \pi_{im} g_i^k(C_l)_m \tag{8.3}$$

where π_{im} is the probability of occurrence of a windstorm in the intensity interval i at the site of the facility m.

Under the assumptions made, the objective functions $F_{k|i}$ or F_k are the sum of as many quantities as the built facilities, each in turn a function of the resources assigned to the m-th facility only. But, as already noted, the nonlinearity and discontinuity of the relevant relationships do not allow the use of differential maximization procedures.

However, an optimization problem in which all relevant quantities are discrete-value variables can be tackled via a *multi-stage decisional process*, in which each stage of decision is independent of the previous ones: as stated by the *optimality principle*, such a process is optimal if, whatever the decisions taken at stage x, further decisions correspond to an optimal solution compatible with the state of the system after the decisions taken up to stage x.

The optimization algorithm is then furnished by *dynamic programming*, which involves a comparatively small number of operations [a].

8.4 OPTIMAL ALLOCATION OF RESOURCES IN THE CASE OF A LIFELINE NETWORK

8.4.1 General considerations: connectivity of a network

At a first sight, no significant difference appears whether the optimal allocation problems presented in Section 8.4 refer to buildings or to other facilities.

But in the case of single facilities dealt with so far, the initial vulnerability, the consequences of failures and the benefits derived from an intervention on any element of the ensemble can be assumed - at least as a first approximation - to be independent from each other and then summable, which simplifies very much the problem.

---

[3] Remember the definitions of *forecast* and *expected* (Note 2).

On the contrary, if the facilities are the elements of a *system*, this is no more possible: the consequences of failure of each facility, hence the effectiveness of any preventive measure, depend not only on the vulnerabilities of the single facility, but also, in an essential way, on the logical diagram of the system, the critical condition considered and the collocation *(role)* of each element; therefore the vulnerability of the *system* must be evaluated on its own account.

On the other hand, it is now a well recognized fact that the disruption of *lifeline* systems are among the most damaging effects of environmental actions. Indeed, as recent examples have confirmed, damages of this type can not only have immediate and dramatic effects in the aftermath of, e.g., a windstorm, but also consequences lasting for months on the economy, as well as on the conditions of life, of the whole area affected by the windstorm. And the increasing relevance of communications and services in modern life makes these effects all the more important.

It becomes thus essential to develop the optimal allocation methodology, not only with regard to single facilities, but also to *systems*, and in particular to *lifeline networks*.

A lifeline can be in general modelled as a redundant network, comprising a number of vulnerable (or *critical*) elements, that may themselves be complex redundant structural or mechanical systems. The network topology depends on the connections between the elements and on the assumed functionality condition, and is usually described by the minimal cut set or the minimal path set representations; then, from the network topology and the element vulnerabilities, it is possible to derive the reliability of the network as a whole.

To elaborate a strategy for improving the reliability of the network, it is also necessary to estimate the costs and benefits of possible preventive measures in terms of their effects on the vulnerability of the critical elements and of the whole system.

In what follows, specific reference will be made to a lifeline network. The main aim of such network is to ensure a connection between a *source* node S and a *destination* node D (*connectivity*): hence, it is assumed that the network fails when this connection is severed. Therefore, the *probability of failure* P_f of the network is defined throughout the following as the probability of *loss of connectivity*.

In this Section, optimization of networks with respect to the *probability of failure* P_f (i.e. to *connectivity*) will be dealt with: this objective has obvious limitations, because many factors are not taken into account (e.g. the capacity of the network) but it is certainly the one to start with. Alternative objectives will be introduced in Section 8.5.

It is assumed that the environmental vulnerability of the critical elements of the network is described by *fragility curves*, known before and after some well defined *upgrading intervention.*

For these items, the costs of construction and intervention might be estimated, and the failure condition identified, for example with the attainment of an appropriate threshold value of a damage indicator. The fragility curves of each facility (in its actual or upgraded condition) could be evaluated by a Monte Carlo procedure.

8.4.2 Upgrading the critical elements of a network

As an example, consider the five networks diagrammatically represented in Fig.8.2. Each critical element is labelled by a serial number (1-5 or 1-10) and a letter indicating the structural typology.

The first network, denoted SE, is an elementary chain of elements in series, and may correspond to elements located along a single lifeline stretch. It fails if any one of the elements fails: therefore, assuming that element failures under a given windstorm are stochastically independent on each other, the (conditional) probability of network survival ($1 - P_{SE}$) is equal to the product of the probabilities of survival of all elements, whence:

Network SE

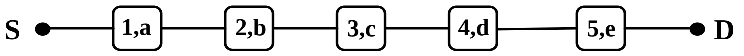

Network PA

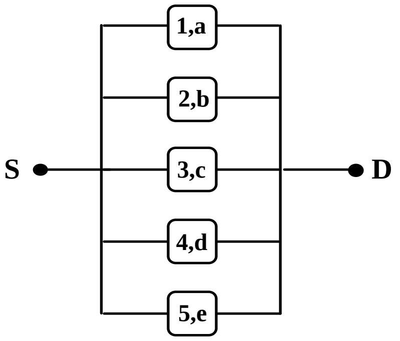

Network SP1

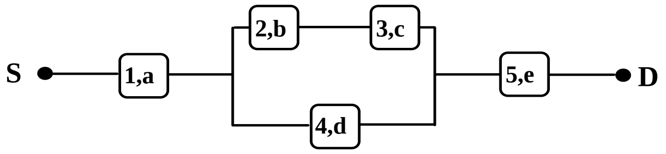

Network SP2

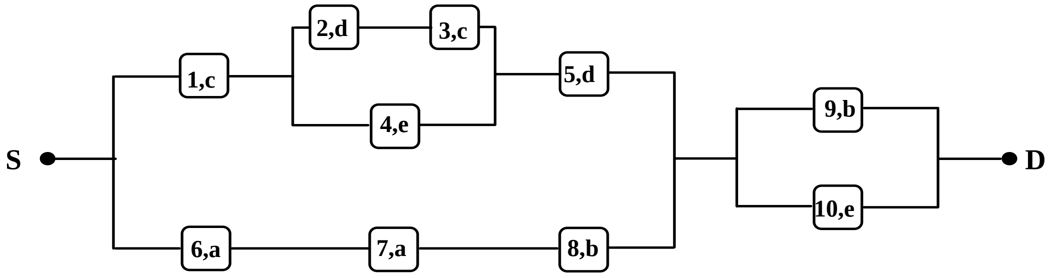

Network CO

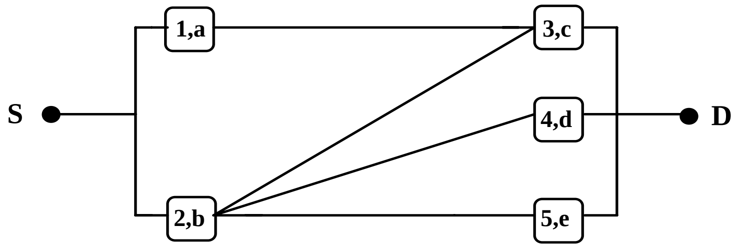

Figure 8.2 Diagrams of five example networks; locations and identification of critical elements.

$$P_{SE} = 1 - \Pi_i \{1 - P_i\} \tag{8.4}$$

where P_i is the probability of failure of element i subjected to a given wind storm.

The second network, denoted PA, is an elementary bundle of elements in parallel. The connection between the source and destination nodes fails if all bridges fail, whence:

$$P_{PA} = \Pi_i P_i \tag{8.5}$$

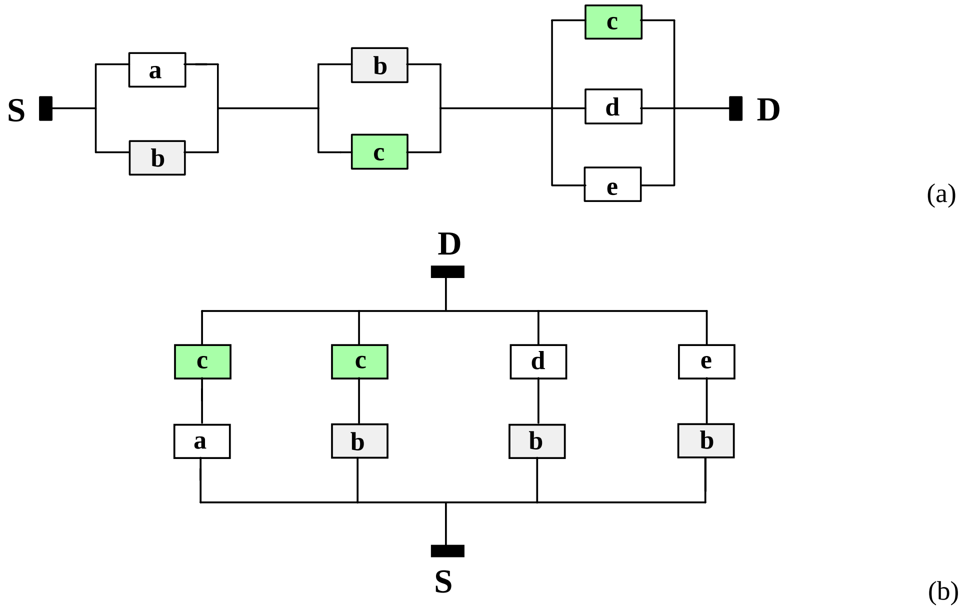

Figure 8.3 Minimal cut set (a) and minimal path set (b) representations of network CO (Fig.8.2).

The laws yielding the (conditional) probability of failure of the networks SP1 and SP2, that can be represented as a combination of independent subsystems in series and/or in parallel, are appropriate combinations of these rules.

With regard to network CO, note that its functional logic cannot be represented by a combination of independent subsystems in series and/or in parallel. This is made evident by the minimal path set and minimal cut set representations in which some elements must be repeated in different subsystems (Fig.8.3): that's why this network, according to a widely accepted definition [b], although appearing structurally simple, is *complex* from the reliability viewpoint.

Instead of distributing uniformly the upgrading intervention on all critical elements, it is possible, by applying dynamic programming (see Section 8.3.4.2), to distribute the interventions among the elements in such a way that, for a given total amount of employed resources, the probability of network failure P_f (loss of connectivity) after a windstorm of given intensity is minimized.

The whole range of significant values of the available resources C_{ava} can be investigated, from zero up to the value that would allow the most efficient intervention on all elements.

The failure probabilities of the networks, after interventions optimized in this way, can thus be evaluated versus the amount of resources C_{ava} (in *resource units*, r.u.).

The optimal distributions of interventions between the element of the network for each given amount of resources, as well as the minimum amount of resources that is needed to modify the probability of network failure are thus evaluated, obtaining the beneficial effect of a set of interventions, as well as the amount of resources that is needed to limit the probability of failure to a threshold value.

8.5 THE GENERAL CASE: OPTIMAL ALLOCATION OF RESOURCES IN COMPLEX SYSTEMS

Still within the definition of *network reliability* given in Section 8.4 (referred to *connectivity* only), let us now present a more systematic treatment.

To solve any optimization problem it is first necessary to identify the structure of the network. If serialty prevails over redundancy, the best representation is given by the minimal path sets: then, the functionality of a path can be defined by a *state function* S_i which is 0 if the path has failed, 1 if the path has not failed. Since the vulnerable elements are in series along each path i,

$$S_i = \prod_{j=1}^{n_{Pi}} S_{ij} \tag{8.6}$$

where S_{ij} is the analogous state function of the j-th among the n_{pi} vulnerable elements (bridges) encountered on the i-th path.

The algorithm which finds all the minimal paths connecting one source node S with one destination node D can be described by the following recursive procedure. The input data are the connections between the nodes of the graph, that are defined so that for each node n_i (*father*) all the nodes n_j (*children*) that are serviced by n_i are explicitly put in evidence.

Initially, let NODE be the source node S (which, by definition, has no *father*).

1. If any of the two following conditions is met, then interrupt the procedure, and go back to the current father:
   (i) NODE has been already marked.
   (ii) Any of the fathers of NODE, excluding the current one, has been already marked.
2. Mark NODE.
3. If NODE is the destination node, then generate a minimal path by collecting all the currently marked nodes and unmark all nodes of that path.
4. For each of the nodes serviced by NODE, grouped in the vector CHILD(i), apply the same procedure [the current NODE becomes the father for CHILD(i), and CHILD(i) becomes NODE]: steps 1 to 3.

The above procedure generates all and only the minimal paths from the source to the destination, even for complex structural topology, including the case of undirected and cyclic networks: as an example, the minimal paths of network CO are shown in Fig.8.3b.

While the presented examples deal only with networks with one source node and one destination node, let us briefly note that if the network has more than one source (as it may be the case when it is only a part of a larger network, and a number of peripheral source nodes simulate the effects of the excluded parts) it is possible to transform the network under study into one with a single source by introducing a fictitious node connected to each of the actual sources: the minimal paths do not change. On the other hand, if more than one destination node is present, that is, if many sites are to be connected to the source node, the minimal path for each destination node are found first, then the combination of the minimal paths (one per destination node) is a minimal path for the multiple destination node case. The elimination (by means of adsorption) of the redundant paths yield all and only the minimal paths for the multiple destination node network.

Once the minimal paths have been determined, the structure of the network is expressed by the overall state function *S*:

$$S = 1 - \prod_{i=1}^{n_P} \left[1 - S_i\right] \tag{8.7}$$

where n_P is the number of minimal paths in parallel, each composed by n_{Pi} element in series.

The reliability of the network is the expected value of *S*, which, provided that the failure of different vulnerable elements are independent events, can be evaluated as:

$$R = \sum_{i=1}^{n_p} E\left[S_i\right] - \sum_{i=1}^{n_p-1} \sum_{j=i+1}^{n_p} E\left[S_i S_j\right] + \sum_{i=1}^{n_p-2} \sum_{j=i+1}^{n_p-1} \sum_{k=j+1}^{n_p} E\left[S_i S_j S_k\right] - \ldots \tag{8.8}$$

where the first two addenda are given by:

$$E\left[S_i\right] = E\left[\prod_{j=1}^{n_{pi}} S_{ij}\right] = \prod_{j=1}^{n_{pi}} E\left[S_{ij}\right] \tag{8.9}$$

$$E\left[S_i S_j\right] = E\left[\prod_{h=1}^{n_{pi}} S_{ih} \prod_{k=1}^{n_{pi}} S_{jk}\right] = \prod E\left[S_{ir}\right] \tag{8.10}$$

with the last product extending to all different elements of the paths i and j. The other terms of the sum can be derived accordingly.

The preceding expression can be explicitly evaluated if the number n_P of paths in parallel is limited: the formulae presented in Section 8.4.2 are particular cases.

In the case of network CO (whose minimal paths are in Fig.8.3b), the reliability is given by the relation:

$$R = 1 - P_f = 1 - \left(P_a \cdot P_b + P_b \cdot P_c - P_a \cdot P_b \cdot P_c + P_c \cdot P_d \cdot P_e - P_b \cdot P_c \cdot P_d \cdot P_e\right) \tag{8.11}$$

P_f being the probability of failure of the network and P_i the probability of failure of the facility i (= a - e), all conditional upon the assumed value of a_g.

The solution of this optimization problem is a set of upgrading interventions distributed among the vulnerable elements such as to maximize the objective function R (or, equivalently, to minimize P_f), which is a discontinuous function (refer to Fig.8.1).

Therefore, as repeatedly stated, the usual differential techniques cannot be employed to find the optimal solution, which would instead require an exhaustive search and the comparison between all possible sets of interventions. However, such search and comparison rapidly become impossible, as the number of vulnerable components and alternative paths grows.

For non-complex systems, an optimization problem in which all relevant quantities are discrete-value variables can be tackled via a multi-stage decisional process, in which each stage of decision is independent of the previous ones, i.e. by *dynamic programming*, which involves a comparatively small number of operations.

With regard to network CO, that, although appearing structurally simple, is *complex* from the reliability viewpoint, the optimal distribution of the interventions should be obtained through an *exhaustive search*.

To perform a direct exhaustive search, the diagram of the network must be *exploded* by splitting each node in order to represent each vulnerable element in one of its n possible conditions (in the example: 4, namely the actual condition and three conditions resulting from repair or upgrading interventions) and each S-D possible path examined.

The number of nodes - hence the complexity of the problem - increases very rapidly with the number of the alternative conditions (i.e. the number of intervention types), depending on the number of vulnerable elements and of the links: the 5-node network CO of Fig.8.2 *explodes* into a 58-node graph (Fig.8.4).

For the 5-node network, the exhaustive search is still possible with a reasonable computational effort, but it is evident that for larger networks exhaustive search can easily become intractable. (It is however possible to simplify the graph, by eliminating the paths associated to vulnerable elements characterized by a reliability below an acceptable threshold.)

However, in some example numerical calculations, dynamic programming have been applied

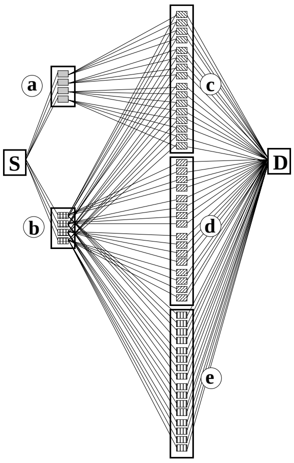

Figure 8.4 5-node network CO transformed into an exploded graph (each node: 4 alternative conditions).

also to such complex systems.

As a matter of fact, for a complex network the results of the two procedures might not coincide, because in dynamic programming the problem is analyzed by successive steps that, in this case, cannot correspond to independent minimal cut sets.

However, the solutions obtained by dynamic programming and by exhaustive search for network CO have been found identical for all practical purposes, being different only in some limited range of C_{ava}: this result seems to indicate the possibility of applying the procedure based on dynamic programming also to complex networks.

By applying the optimal allocation procedure, it has been noted how the distribution of the optimized interventions sometimes changes drastically when the amount of economic resources varies. The convenience of an optimal versus a uniform distribution of resources has also been put in evidence.

It is also important to note that, under the set assumptions, the optimization procedure only suggests the most convenient interventions in order to increase the reliability of the connection between S and D, but does not imply an explicit control of the actual safety level of each critical element. This limit should be taken into account in applying such a strategy.

Finally, it is of interest to note that a number of researches have tackled the choice of the facilities on which to perform preventive upgrading interventions as a *prioritization* problem. However, the priority can change with the amount of available resources (and also the objective considered): therefore, it appears that taking account of the whole network at the same time can lead to more significant results.

8.6 ALTERNATIVE OBJECTIVES OF THE OPTIMIZATION

8.6.1 General remarks

To ensure *connectivity* can be not the only aim of a risk-reduction programme of a lifeline network: several other objectives can be envisaged. Thus, different objectives can be considered, namely:

- the *network reliability* R, defined as the probability of maintaining the *connectivity* (i.e. the connection between the source node S and the destination node D) when a windstorm hits the area; equivalently, reference can be made to the complementary *probability of network failure* $P_f = 1 - R$): this objective has been extensively dealt with in previous Sections;

- the expected *capacity* of the network, i.e. the maximum flow (e.g. of electric power) that can be expected to run between the source and destination nodes after a windstorm of given intensity;
- the *out-of-service time* of the network, that is, the expected duration which the whole network remains out of service after a windstorm of given intensity;
- the *time-efficiency* of the interventions, defined as the ratio between the increase of the network reliability due to a specified set of upgrading interventions and the time necessary for their execution (the minimization of this quantity appears a key point also for the optimal planning of the repair interventions on a damaged network).

As a prerequisite for trying and employing the resources in an optimal way, the possible interventions on each facility must be designed, and their costs and gains evaluated for each objective function: relations like Fig.8.1 are thus obtained, and one is able to estimate the benefits to be expected from the amount C of resources employed in upgrading.

Starting from assumed relations of this type, the available resources can be allocated in an optimal way with respect to each of the four above stated objectives, and also in a multi-objective allocation (with assumed weights for the different objectives).

It is to be remembered that, because of the uncertainties in the physical conditions of the items and in their future loading history (occurrence and characteristics of the wind storms), the treatment is inherently probabilistic: all values and results must be regarded as *expected values* and not as deterministic quantities.

Optimization for objectives other than *connectivity* will thus be illustrated in the following.

8.6.2 Expected capacity of the network

Remembering that, by assumption, only the nodes of the network are vulnerable, the expected *capacity* c_{ij} of each link ($n_i \rightarrow n_j$) is defined as an *estimated capacity* of the link multiplied by the reliability of its end node in its actual (original or upgraded) condition. The estimated capacity of the link is identified with an assumed (or measured) value.

The *capacity of the network* can be identified with the *maximum flow* between the source node S and the destination node D that satisfies the link capacities and the mass balance constraints at all nodes.

The search of the maximum flow is carried out by means of an *augmenting path algorithm*, a class of algorithms that can be applied to a network if the following three assumptions are satisfied:

- the network is directed (note that any undirected network can always be transformed into a directed network);
- the capacity associated with each link ($n_i \rightarrow n_j$) is a nonnegative integer;
- the network does not contain either parallel links between the same two nodes, nor an S -D path composed only by links of infinite capacity.

An augmenting path algorithm is based on the *max-flow min-cut theorem*, whose formulation requires the definition of *residual network, S-D cut*, and *augmenting path*.

The *residual network* with respect to a certain global flow F sent through the network is the network consisting of links ($n_i \rightarrow n_j$) with positive residual capacity r_{ij}, this latter being defined as the maximum additional flow that could be sent from node n_i to node n_j.

An *S-D cut* is a partition of the whole node set in two complementary subsets V and V^c that have no common elements, and are such that $S \in V$ and $D \in V^c$; equivalently, it can be identified with a set of links whose elimination severs the connection between S and D.

The *capacity of an S-D cut* is the sum of the capacities of the cut links; a *minimum S-D cut* is the cut whose capacity is the smallest among all S-D cuts.

An *augmenting path* is a directed path from S to D in the residual network.

The *max-flow min-cut theorem* can be expressed in three equivalent formulations [c] and [d]

- the value of any flow F in the network is not larger than the capacity of any S-D cut in the network;
- the value of the maximum flow F_{max} from the source node S to the destination node D equals the capacity of the minimum S-D cut;
- the flow in the network is maximum if (and only if) no augmenting path exists in the residual network: indeed, whenever the network contains an augmenting path, it is possible to send additional flow from S to D.

In the present research, the maximum flow F_{max} in the network is evaluated by means of the basic Ford-Fulkerson algorithm, as modified by Edmond and Karps to limit the computational burden and to eliminate the need of taking integer values for the link capacities. The steps of the procedure can be summarized as follows:

1) put initially $F_{max} = 0$;
2) using one of the available algorithms evaluate the minimum path between S and D on the residual network (that in the first iteration coincides with the original network);
3) along this path recognize the link(s) ($n_i \rightarrow n_j$) of smallest capacity c_{min};
4) subtract the capacity c_{min} from the capacities of all links in the network;
5) eliminate the link(s) with capacity equal to 0; thus, the residual network with respect to the actual maximum flow $F_{max} + c_{min}$ is defined;
6) put $F_{max} = F_{max} + c_{min}$;
7) go back to step 2;
8) iterate as long as an augmenting path can be found.

When no further augmenting path can be found, the set of links with nil capacity identifies the minimum S-D cut (if more than one zero-capacity links are found on a path, the nearest to S is considered); the actual value of F_{max} is the sought maximum flow.

In order to maximize the *expected capacity* after a windstorm, the resources are optimally allocated by the following procedure:

A) fix the amount of available resources C_{ava};
B) identify in the existing network the minimum S-D cut (steps 1-8 of the above procedure);
C) by applying a dynamic programming procedure (or an exhaustive search, if the number of critical elements that must be examined is sufficiently low), find the distribution of upgrading interventions among the end nodes of the links forming the cut, such as to maximize the increase of flow in the cut;
D) verify that this increment coincides with the increment of the maximum flow in the upgraded network; otherwise, identify the new minimum cut in the upgraded network, and go back to step C) operating alternatively on the two cuts;
E) iterate until the optimal solution is derived.

The steps B) and C) of the procedure can be simplified by finding for each node n_i of the cut the minimum ratio of the expected capacities of all links that end in n_i and the expected capacities of the links that emanate from n_i, and considering at first the nodes characterized by the lowest values of this ratio.

8.6.3 Out-of-service time of the network

Another quantity of great significance in planning the interventions appears to be the *out-of-service time*, defined as the expected time necessary to restore the functionality of the network when it fails as a consequence of a windstorm.

The times required by the different types of interventions on each item of the network must be estimated. Also, the expected *out-of-service times* (i.e. the expected time required to restore an item hit by a windstorm) must be evaluated.

Given the assumed out-of-service times of each item, the *out-of-service time* of the network can be evaluated in several alternative ways, and in particular as the sum of the time intervals necessary to perform either (i) all the interventions, or (ii) the interventions on the vulnerable elements of only one path connecting S with D.

To perform this optimization, a *weight* must be associated to each link, corresponding to the time necessary to restore the functionality of the vulnerable element at the end of that link.

Given the amount of available resources, the minimal among the admissible S-D paths (that is, those paths that corresponds to a total expenditure less than or equal to the fixed amount of available economic resources) in the exploded network can be recognized by means of the Floyd-Warshall algorithm (refer to Section 8.6.2).

8.6.4 Time-efficiency of the interventions

It can also be assumed that the most efficient set of interventions is the set that yields the largest increase of the reliability in the shortest time (this is very significant in the case of repair interventions, when, because of emergency, time limits prevail); the optimization can then be referred to an objective function denoted as *time-efficiency* and assumed equal to the ratio:

$$\eta=\frac{\Delta R}{T^*} \tag{8.12}$$

between the increase ΔR of the network reliability and the time T^* necessary to implement a set of interventions.

To find the optimal allocation of resources from this viewpoint, the distribution of interventions that maximizes the reliability of the S-D connection in the shortest time is found for each S-D path, and then, the path corresponding to the largest time-efficiency is selected.

To this aim, an algorithm can been used that searches in a graph the path yielding the largest rate of the attained level of efficiency versus the time needed to attain it, that is the path that corresponds to a global optimum [e] and [f].

The time T^* can be evaluated as the sum of the times needed to implement each intervention or assumed equal to the longest time needed for one intervention, as if all interventions were implemented at the same time.

Once having defined the path that corresponds to the global optimum, the additional interventions can be planned either on the most time-efficient path among the alternative ones, or in a way such to maximize the further increase in the system reliability: however, very few differences result in many considered example cases.

8.6.5 Comparison of results

Depending on the objective function and other data, different paths can be more significant. Therefore, it may be important to take account at the same time of several possible objectives of the prevention strategy: this is attempted by the multi-objective allocation procedure proposed in the following Section 8.7.

8.7 MULTI-OBJECTIVE OPTIMIZATION

Let g_h denote the h-th objective function (h = 1, ..., k), d_n the n-th path of the weighted graph (Fig. 8.3) connecting the source node S to the destination node D, and $g_h(d_n)$ the value of the h-th objective function after the set of interventions corresponding to that path.

If the h-th objective function is summable, it is given by

$$g_h(d_n) = \sum_{(n_i \to n_j) \in d_n} f_h(n_i, n_j) \tag{8.13}$$

where f_h (n_i, n_j) is the value of the h-th objective function relative to that link, assumed as the weight (or length) of that link.

If the h-th objective function is not summable (for example, the reliability of the network or its expected maximum traffic capacity), a different formulation must be applied, as the value of the objective function must be referred to the whole network.

The multi-objective optimal allocation of resources consists in finding the distribution of interventions among the vulnerable elements of an S-D path (under the constraint of a fixed total amount of available resources) in such a way that all the k objective functions are taken into account. This search procedure is composed by two steps:

- determination of alternative distribution of interventions optimal in the Pareto sense under the constraint of a given maximum expenditure;
- choice of an “absolute” optimum according to a well defined decision strategy.

8.7.1 Search of the Pareto optimal paths

A path d^P is Pareto optimal if for every other path d_n, and for any h:

$$g_h(d_n) \subseteq g_h(d^P) \tag{8.14}$$

with

$$g_h(d_n) \subset g_h(d^P) \tag{8.15}$$

for at least one objective function. The sign $\subset$ indicates that the path d^P is "better" than the path d_n with respect to the h-th objective function, while the sign $\subseteq$ includes the case of equivalence between the two paths.

Usually, a set of Pareto optimal paths can be found among the admissible solutions (i.e. all the paths that require an expenditure less than or equal to the available total amount of economic resources).

For moderate-size networks, all the paths of the exploded graph (Fig.8.3) can be examined, and the whole set of Pareto optimal paths individuated. For larger networks, the problem is computationally intractable, and a more efficient method of solution must be used.

To this aim, an algorithm [g] has been implemented that allows to take into account also not summable objective functions. The algorithm consists in first seeking the optimal path for an arbitrarily chosen objective function, and then in the ordered examinations of the varied paths in the exploded graph with the aim of seeking an *a priori* fixed number of Pareto optimal solutions. Selecting different objective functions for the choice of the starting path, it is possible to investigate the whole range of admissible solutions from different directions.

Let

$$g^0 = [g_1^0, ..., g_i^0, ..., g_k^0]^T \tag{8.16}$$

denote the ideal vector that contains the optimal solution for each objective function separately, determined after finding the corresponding extreme path, $d^{0(h)}$. With reference to k summable objective functions that must be minimized, the search procedure can be described by the following steps.

1) Read the network
2) Set $g_h^P = \infty$ for i = 1, 2, ...k, where g_h^P is the value of the h-th objective function for the Pareto optimal path d_n^P;
3) Find the extreme path $d^{0(h)}$ for each objective function separately, and the corresponding values of the objective function g_h^0 for h = 1, 2, ...k;
4) Fix the number N^a of optimal paths to be individuated;
5) Set N = 1;
6) Find the path $d^{(N)}$ that for N = 1 makes extreme the selected objective function, i.e. is such that

$$f_1(d_N) = \min_{d^{(N)}} \sum_{n_i, n_j \in d^{(N)}} f_1(n_i, n_j)$$

and for N > 1, is such that:

$$g_1\left(d^{(N)}\right) \geq g_1\left(d^{(N-1)}\right)$$

6) Determine the values $g_h(d^{(N)})$ of the objective functions for the path $d^{(N)}$;
7) Check if the path $d^{(N)}$ should be stored as Pareto optimal;
8) Set N = N +1
9) If $N < N^a$, go to 6); otherwise stop.

The number N^a of paths to consider is assumed a priori. Thus not all the Pareto optimal paths will be found, but only those which are contained in a selected region. If the solution individuated so far do not satisfy the decision-maker, the above procedure can be repeated for (i) a larger value of N^a or (ii) assuming another objective function to define the direction along which the investigation is carried out. Since an optimal allocation problem is dealt with in this study, only the admissible paths, i.e. those that satisfy the constraint on the amount of available economic resources, are considered.

8.7.2 Decision-making strategies

Once the Pareto optimal solutions have been obtained as described in Section 8.7.1, several decision-making strategies can be implemented. Two procedures have been selected here, namely: the *Utility Value Analysis* (UVA); the *concordance and discordance analysis* formulated in the ELECTRE method. They are described below.

8.7.2.1 Utility Value Analysis

The Utility Value Analysis [h] (whose logical diagram is shown in Fig.8.5) proceeds as follows.

For each Pareto optimal solution (named *alternative* in what follows) d_n^P and for each objective function g_h, define *criterion-related impact* e_{hh} the value assumed by the h-th objective function for that alternative.

The impacts are generally measured in various units (i.e. time unit, money, ...): in order to make them comparable, they are firstly transformed into non-dimensional *criterion utilities* u_{nh} by means of a *value* or *utility function* l_h.

In the development of the specific example, the criterion utilities u_{nh} are derived by the following relationships:

a) if the utility increases when the impact decreases (this is, for example, the case of a cost or a time objective function):

$$u_{nh}=\frac{\min(e_{nh})}{e_{nh}} \tag{8.17}$$

b) if the utility increases when the impact increases (this is, for example, the case of the network reliability)

$$u_{nh}=\frac{e_{nh}}{\max(e_{nh})} \tag{8.18}$$

Each objective function, and therefore the corresponding utilities, can be weighted by a factor w_h that reflects the relative importance of each objective function (the sum of the weights is usually taken equal to one). The weighted criterion utilities are called *partial utilities.* The partial utilities of the alternatives are then aggregated (for example, simply summed).

The *overall utility* N_n of each alternative d_n is defined as the sum of the weighted criterion utilities of that alternative. The *absolute optimum* corresponds to the path with the highest overall utility.

8.7.2.2 Concordance and discordance analyses

The ELECTRE - *ELimination Et Choix Traduisant la RÉalité* – methods [i] are based on a comparison of alternatives pair by pair.

The methods attempt to eliminate first a subset of less desirable alternatives from the complete set of alternatives (*elimination*), after which a complementary analysis is used to select the absolute optimal alternative, or a set of relatively good alternatives (*choice*). Let:

- $D^P=\left\{d_1^P,d_2^P,\dots,d_{N^a}^P\right\}$, the set of Pareto optimal solutions corresponding to a fixed maximum amount of economic resources;
- $G=\{g_1,g_2,\dots,g_k\}$, the set of objective functions taken into consideration;
- $W=\{w_1,w_2,\dots,w_k\}$, the weights associated to the considered objective functions;
- $g_h\left(d_n^P\right)=e_{nh}$, the value of the h-th objective function for the n-th optimal path;
- $G^+\left(d_r^P,d_s^P\right)=\left\{h\in G\Rightarrow g_h\left(d_r^P\right)\supset g_h\left(d_s^P\right)\right\}$, the set of objective functions according to which the alternative d_r^P is preferable to the alternative d_s^P;
- $G^=\left(d_r^P,d_s^P\right)=\left\{h\in G\Rightarrow g_h\left(d_r^P\right)=g_h\left(d_s^P\right)\right\}$, the set of objective functions according to which the alternative d_r^P is equivalent to the alternative d_s^P;
- $G^-\left(d_r^P,d_s^P\right)=\left\{h\in G\Rightarrow g_h\left(d_r^P\right)\subset g_h\left(d_s^P\right)\right\}$, the set of objective functions according to which the alternative d_s^P is preferable to the alternative d_r^P;
- $W^+\left(d_r^P,d_s^P\right),W^=\left(d_r^P,d_s^P\right),W^-\left(d_r^P,d_s^P\right)$, the sums of the weights associated to the objective

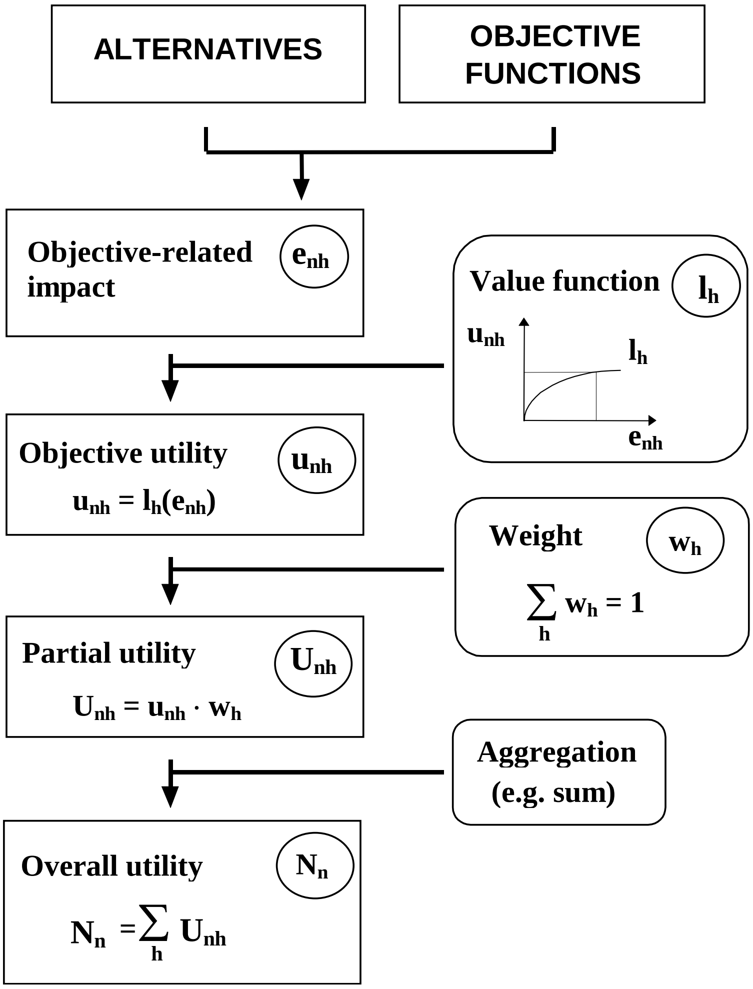

Figure 8.5 Logical diagram of Utility Value Analysis.

functions forming the sets $G^{+}\left(d_r^P, d_s^P\right), G^{=}\left(d_r^P, d_s^P\right), G^{-}\left(d_r^P, d_s^P\right)$.

The first step of the method consists in defining a *concordance index* for each pair of alternatives.

The concordance index CI(d_r^P, d_s^P) is a measure of the gain of the decision-makers if the alternative d_r^P is preferred to the alternative d_s^P. It is equal to the relative (weighted) frequency of objective functions according to which the alternative d_r^P is not worse than the competing alternative d_s^P:

$$CI\left(d_r^P, d_s^P\right) = \frac{W^{+}\left(d_r^P, d_s^P\right) + W^{=}\left(d_r^P, d_s^P\right)}{W^{+}\left(d_r^P, d_s^P\right) + W^{=}\left(d_r^P, d_s^P\right) + W^{-}\left(d_r^P, d_s^P\right)} \tag{8.20}$$

A complementary measure is given by the *discordance index* DI(d_r^P, d_s^P) that measures how much the impacts of alternative d_s^P are better than the impacts of alternative d_r^P. It can be expressed, for each pair of alternatives, in the form:

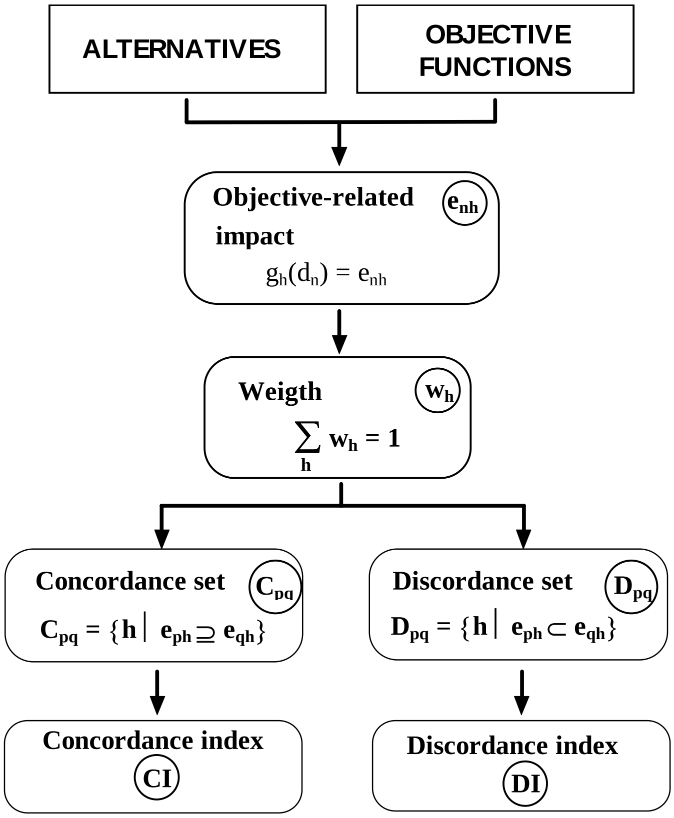

Figure 8.6 Definition of concordance and discordance indices.

$$DI\left(d_r^P, d_s^P\right) = \max_{h \in G^-} \frac{\left|g_h\left(d_s^P\right) - g_h\left(d_r^P\right)\right|}{L_h^{max}} \tag{8.21}$$

where L_h^{max} is the largest difference between the impacts of the objective function $g_h(d_s^P)$

The logical diagram of this analysis is shown in Fig.8.6.

Once the values of concordance and discordance indices have been derived for all pairs of alternatives, it is necessary to identify a criterion for evaluating the (set of) absolute optimal solution(s).

In general, it is possible to define threshold values of the indices, and to eliminate the alternatives characterized by a concordance smaller or a discordance larger than these critical values.

An alternative procedure can be followed. For each alternative, the *net concordance dominant value* can be calculated as:

$$CI_{net} = CI - CI^* = \sum_{\substack{d_r^P, d_s^P = 1 \\ s \neq r}}^{N^a} CI\left(d_r^P, d_s^P\right) - \sum_{\substack{d_r^P, d_s^P = 1 \\ s \neq r}}^{N^a} CI\left(d_s^P, d_r^P\right) \tag{8.22}$$

where CI is the sum of all concordance indices of alternative d_r^P with respect to the different alternatives, and CI^* is the degree of dominance of other alternatives with respect to alternative d_r^P. Analogously, the *net discordance dominance value* can be calculated as:

$$DI_{net} = DI - DI^{*} = \sum_{\substack{d_r^P, d_s^P = 1 \\ s \neq r}}^{N^a} DI\left(d_r^P, d_s^P\right) - \sum_{\substack{d_r^P, d_s^P = 1 \\ s \neq r}}^{N^a} DI\left(d_s^P, d_r^P\right) \tag{8.23}$$

where DI is the discordance dominant value and DI^{*} is the degree of discordance of other alternatives with respect to alternative d_r^P.

As a first indication, it can be noted that the alternative d_r^P is to be preferred as much as higher is the value of CI_{net}, and lower than 0 the value of DI_{net}. In numerical calculations, the alternative with the highest difference between the two terms can be considered.

8.8 SOME FINAL REMARKS

As underlined before, problems caused by wind cannot be neglected in a rational planning of our environment, even in Europe, a continent immune from great tropical disasters. Indeed, for a number of reasons (increased sensitivity of modern constructed facilities, increase of property values in windstorm-prone areas, climate changes and warming up of the atmosphere) each of three factors (*vulnerability*, *exposure* and *hazard*) that contribute to this environmental risk are steadily increasing.

It is high time to tackle all these problems in a rational way, if in the long run we want to reduce the risk and increase the comfort of our built-up environment. Some sensitivity indeed exists for seismic risk: numerical examples of the illustrated procedures have been developed for seismic action. Much smaller is the sensitivity towards “wind-oriented design”, that must become part of the cultural background of engineers, town planners, architects and policy makers in general, also in regions traditionally considered as characterised by a “well-behaved” wind climate.

Retrofitting and careful maintenance can reduce the *vulnerability*, but no intervention can modify the *hazard* of existing facilities; however, far-sighted land-use and town-planning policies can avoid future constructions of facilities and urban developments in sites with comparatively higher wind hazard. Thus, the wind *exposure* can be kept under control, or even be reduced. In any case, improved knowledge of the wind actions can help to develop better design theories and practices, thus decreasing the overall wind *risk* notwithstanding the increasing *vulnerability* of modern constructions.

With specific regard to the reduction of the vulnerability of existing facilities and lifeline networks, a specific optimal allocation problem has been tackled: the choice of a set of preventive upgrading interventions on the elements of a lifeline network, such as to optimize the benefit of the available resources.

The relevance of the problem arises from the usual shortage of public funds available for prevention programmes, and has been proved by the great advantages - amounting to orders of magnitude of the efficiency of the employed resources - found in the numerical examples between “rule-of-thumb” and optimized allocation strategies.

Moreover, it has been noted that the problem could require a *system approach*, *probabilistic* because of the many uncertainties involved, and the application of the procedures must combine several interdisciplinary competencies.

8.9 BASIC REFERENCES

[a] Bellman, R.E., Dreyfus, S.E.1962. *Applied Dynamic Programming*, Princeton University Press.

[b] Rao, S.S. 1992. *Reliability-Based Design*, McGraw-Hill, Inc.

[c] Ravindra, K.A., Magnanti, T.L., Oblin, J.B. 1993. *Network flows - Theory, Algorithms and Application*; Prentice-Hall, Inc., Englewoods Cliffs, New Jersey

[d] Cormen, T.H., Leiserson, C.E., Rivest, R.L. 1994. *Introduzione agli algoritmi*, Jackson Libri, Milan, Italy.

[e] Horn, W.A. 1972 Single-machine job sequencing with tree-like precedence ordering and linear delay penalties; *SIAM, Journal of Applied Mathematics*, **23**(2); 189-202;

[f] Nojima, N., Kameda, H. 1992. Optimal strategy by use of tree structures for post-earthquake restoration of lifeline network systems; *Proc. Tenth World Conference on Earthquake Engineering*, Madrid, Vol. 9, 5541-5546

[g] Osyczka, A. 1984. *Multicriterion Optimization in Engineering with FORTRAN programs*; Ellis Horwood Limited, Chichester

[h] Bielli, M., Gastaldi, M., Carotenuto, P. 1996. Multicriteria evaluation model of public transport networks; *Advanced Methods in Transportation Analysis* (L.Bianco and P.Toth Eds.), Springer Verlag, Berlin/Heidelberg.

[i] Benayoun, R., Roy, B., Sussman, N. 1966. *Manual de Référence du Programme Electre*, Note de Synthese et Formation, No.25, Direction Scientifique SEMA, Paris (mimeographed).

8.10 LIST OF PUBLICATIONS

[1] Augusti, G., Borri, A., Ciampoli, M. 1994. Optimal resource allocation for seismic reliability upgrading of existing structures and lifeline networks. *Reliability and Optimization of Structural Systems '94, Proceedings of 6th IFIP WG7.*, Assisi, Italy.

[2] Augusti, G., Ciampoli, M. 1998. Multi-objective optimal allocation of resources to increase the seismic reliability of highways. *Mathematical Methods of Operations Research*, **47** (1), 131-164.

[3] Augusti, G., Ciampoli, M. 1999. Further studies on the reduction of seismic risk in highway networks with limited resources. Optimizing Post-Earthquake Lifeline System Reliability, TCLEE Monograph No. 161 (a cura di W.M. Elliott & P. McDonough) ASCE, *Proc. 5th U.S. Conference on Lifeline Earthquake Protection*, Seattle, USA

[4] Augusti, G., Borri, C., Niemann, H.-J. 2001. Is Aeolian risk as significant as other environmental risks?. *Reliability Engineering & System Safety,* **74**, 227-237.

9 Control of the structural response

Giorgio Serino
University of Napoli Federico II

9.1 INTRODUCTION

In the course of the WINDERFUL project, the Research Units at the University of Napoli Federico II, at the University of Perugia and at the University of Bologna have been co-operating in the important field of the control of the response of structures subjected to wind, earthquakes and other types of dynamic loads. Some of the main results attained are summarized in the present chapter, while further details can be found in the publications listed at the end. Activities regarding the control of cables and cable supported systems carried out mainly at the University of Bologna are also reported in chapter 4.

The type of work performed during the two years of the project was theoretical (control algorithms and mechanical characterization of the devices), experimental (laboratory and in-situ tests) and numerical (FE models). Engineering design procedures have been also been developed for passive (viscoelastic and friction based), semi-active (mainly MR) and active (AMD) devices.

9.2 DESIGN OF PASSIVE SYSTEMS FOR HIGH-VOLTAGE EQUIPMENT

Recent world-wide seismic events have confirmed that, without appropriate precautions, a major earthquake may damage important parts of the electric transmission and distribution networks, involving the interruption of the electric power delivery for the essential time of repairs, with negative consequences on the social and economic activities of the area, as well as on the activities of rescue operations just during the emergency situation. From the seismic point of view, the most vulnerable points of an electric network are the High Voltage (HV, >150kV in a.c.) to Medium Voltage (MV, ≤150kV in a.c.) transformation open-air substation, because of the massive presence of HV equipment provided - both for electric insulation and for load bearing - with large porcelain insulators, a resistant but intrinsically brittle material, which is not suitable for resisting dynamic loads [a].

To improve the seismic behaviour of HV equipment some experts, in different parts of the world, have proposed the use of passive protection systems, even arriving in given cases at their effective implementation or at least at the construction and testing of prototypes [1]. These proposals have a common characteristic: the introduction of the isolation system at the base of the

Edited by Gianni Bartoli and Francesco Ricciardelli, WINDERFUL: Wind and INfrastructures: Dominating Eolian Risk
For Utilities and Lifelines, ISBN 88-8453-138-1, ©2004 Firenze University Press

equipment, that allows operating without modifying neither electrical functions nor dimensions of vertical structure. Main benefit of this type of solutions is the decrease of accelerations in the equipment and thus a strong reduction of structural damage.

9.2.1 Passive protection devices for HV equipment

For cantilevered electrical components, like the majority of those found in open-air substations, it has been proved that it is convenient to use 3D isolators, i.e. isolator devices endowed both with convenient deformability in the vertical direction and sufficient stiffness in the two horizontal directions, so that the equipment responds to seismic excitation mainly with rigid rotational motions around two main horizontal axes passing through the center of the base (rocking). In this paragraph consideration is given to two systems of this type judged to be particularly adequate from the technical and economical point of view: a system with helicoidal springs and visco-elastic dampers and Wire Rope system.

Systems with helicoidal springs and visco-elastic dampers have already been used for a long time for the isolation of vibrations produced by machinery containing rotating elements and by heavy machinery such as forging presses and power hammers, installing them at their base, as well as for the isolation from vibrations produced by motor-car traffic and underground trains. Helicoidal springs bear the weight of the structure and represent the purely filtering element of the isolation system, while visco-elastic dampers, typically consisting of a mobile part immersed in a highly viscous fluid, provide the dissipative force.

Isolators of the Wire Rope type have been used for a long time for isolation from vibrations and protection from the bumping of equipment in the military, electronic and air space fields. They consist of cables in stainless steel wound in the shape of a coil or an arc on drilled bars in aluminium alloy. Each cable consists of several plaited strands, while each strand in turn consists of several wires, the number of which varies according to the device in question. A peculiar characteristic of the Wire Rope isolators is that of being deformable in both the two horizontal and in the vertical directions, and of possessing at the same time a significant dissipation capacity due to the hysteretic damping achieved thanks to the friction produced by the rubbing of the individual strand wires and between one strand and another. The possibility of incorporating the filtering with the dissipative function in a single element makes these devices particularly interesting also for seismic isolation, and suitable in particular for the protection of light but costly equipment, in view of their quite considerable deformability in the vertical direction.

9.2.2 Exemplary application to a HV circuit breaker

To define the benefits, in terms of seismic action reduction, resulting from the use of base isolation, the study has been focused on a particular piece of electrical equipment: a 420 kV HV circuit breaker present in an electric substation near Benevento, for which results of static and dynamic experimental tests carried out by ISMES, under ENEL support, were available [b]. The analyzed circuit breaker (Fig. 9.1) is composed of a vertical pole, made of three porcelain insulators forming a vertical column supporting two interruption chambers inclined at 45° respect to vertical axis, each of them equipped, on one side, with a 500 pF condenser. The pole rests on a metallic structure, while the foundation is a reinforced concrete slab on which three circuit breakers, one for each phase, are installed, together with a single control cabinet.

In the Nineties ISMES carried out three types of tests on the circuit breaker:

- tests with forced sinusoidal excitation applied to the foundation in the horizontal direction, using a vibrodine installed near the metallic support. Its position and force amplitude were chosen to warrant that all fundamental modes of the circuit breaker were excited;

Figure 9.1 Analyzed HV circuit breaker

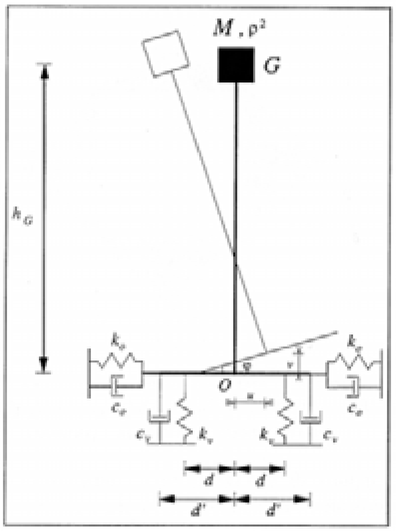

Figure 9.2 Simplified 2D design model

- transient response to wind gusts at a speed of 10-15 m/s;
- snap-back tests, performed on the circuit breaker and on the current transformer, connected to each other by an electric cable.

These tests showed that the participating mass is concentrated in the first six modes, while the higher modes do not give any significant contribution to the total dynamic response. We have then proceeded, using the FEM computer program SAP2000NL, to the development of a 3D model capable of adequately describe the significant components of the circuit breaker.

In a first phase of the analysis all the elements of the FEM model were treated as linear, and a comparison was made between the first frequencies pertaining to the model and those obtained in the experimental investigations carried out by ISMES. The flexibility of the rotational springs representing the connections between the porcelain insulators were calibrated comparing the eigenvalues and the pertaining modes of vibration obtained numerically with those experimentally available. This simple dynamic identification procedure allowed also to validate the geometry of the circuit breaker and the mechanical characteristics of the materials. Tab. 9.1 compares the first eight experimental and numerical frequencies of vibration of the switch-gear. A substantial agreement is observed.

Two passive seismic protection systems, based on the insertion of a flexible and dissipative isolation interface at the base, have been studied for this circuit breaker [2]. To design them it has been used, in both cases, a simplified 2D model of the switch-gear (supposed rigid), in which M=1933 kg is the total mass, G is the position of the center of mass, at the distance h_G=5.5 m from the base of equipment, and ρ=3.01 m its radius of gyration (Fig. 9.2).

The elastic and damping properties of the protection devices are represented by two linear springs, with stiffness k_v and k_o, and two viscous dampers, with constants c_v and c_o, inserted at the base of the equipment and acting in the vertical and horizontal directions. Indicating with 2d and 2d’ the distance between the springs and dampers, respectively, their values, together with k_v, k_o, c_v, c_o have been determined adopting the design procedure summarized in what follows.

Mode No.	Description	Experimental [Hz]	SAP2000 [Hz]
1	1st along Y	1.62	1.62
2	1st along X	1.75	1.70
3	Torsional	3.50	2.14
4	2nd along Y	9.07	9.10
5	2nd along X	10.60	10.23
6	Interr. chamb.	11.53	11.40
7	3rd along Y	13.46	12.59
8	3rd along X	15.51	15.90

Table 9.1 Comparison between experimental and numerical frequencies of HV circuit breaker.

Since it was noted that the dynamic behaviour of the 2D model was not significantly influenced by k_o and c_o, [c], the isolated equipment has been studied in the limit case $k_o \rightarrow \infty$, for which the number of dofs is reduced from three to two, the two undamped mode shapes are uncoupled and correspond to a rigid vertical translation and a rigid rotation around the middle point of the base, and their angular frequencies and viscous damping ratios are:

$$\omega_v = \sqrt{\frac{4k_v}{M}} \qquad \omega_\varphi = \sqrt{\frac{4k_v d^2}{M(h_G^2+\rho^2)}} = \omega_v \frac{d}{\sqrt{h_G^2+\rho^2}} \tag{9.1}$$

$$\xi_v = \frac{4c_v}{2M\omega_v} = \frac{c_v}{\sqrt{k_v M}} \qquad \xi_\varphi = \frac{4c_v d'^2}{2M(h_G^2+\rho^2)\omega_\varphi} = \xi_v \frac{1}{\sqrt{h_G^2+\rho^2}} \frac{d'^2}{d} \tag{9.2}$$

The first base isolation system is constituted by four coil springs and four visco-elastic dampers inserted, respectively, at each vertex and at the middle point of each side of a metallic square plate at the base of the equipment. The value of k_v has been obtained from the second of (9.1) adopting d=0.526 m (maximum value compatible with the plan dimensions of the metallic supporting frame) and $f_\varphi=\omega_\varphi/2\pi=0.5$ Hz for the rotational frequency. This gave k_v=678 kN/m and thus, from the first of (1), $f_v=\omega_v/2\pi=5.95$ Hz. A value of $\xi_\varphi=15\%$ has been assumed to determine damper constant, thus obtaining c_v=64.7 kN-s/m from the second of (9.2) and $\xi_v=179\%$ from the first.

The second isolation system is composed by four Wire Ropes placed with the longitudinal axis parallel to the diagonals of the metallic square plate at the base of the equipment, near its vertices. The selected Wire Rope devices have hysteretic behaviour (i.e. independent from frequency) under dynamic load and display as force-displacement curve (provided by the manufacturer):

$$F = ax^n \tag{9.3}$$

where n is 0.65 in compression, 1.54 in tension and 1.53 under horizontal load. The parameter a can be evaluated using the catalogue force-displacement logarithmic curve. The Wire Rope type has been chosen, according to the equipment weight and to the number of devices adopted. The vertical displacement due to its self weight results:

$$v_{pp} = \left(\frac{M \times g}{n_d \times a}\right)^{\frac{1}{0.65}} \tag{9.4}$$

where n_d=4 is the number of devices placed under the equipment, and the tangent stiffness corresponding to such displacement is

$$K^V = \left(\frac{dF}{dx}\right)_{x=v_{pp}} = 0.65 \times a \times (v_{pp})^{0.65-1} \qquad (9.5)$$

From the second of Eq. 9.1, adopting d=0.526 m and $f_\varphi=\omega_\varphi/2\pi$=0.5 Hz, the value of k_v=678 kN/m has been obtained, which allows to choose the device, among those available, having a tangent stiffness K^V closest to k_v. A value of equivalent viscous damping ratio $\xi_\varphi=\xi_V$=15% has been assumed, as suggested by the manufacturer according to the results of experimental cyclic tests.

9.2.3 Response of fixed base and base isolated HV circuit breaker

The SAP2000NL models of the fixed base and isolated circuit breaker have been used to assess equipment response under seismic action. Time-history analyses have been performed applying to the FE models the eight accelerograms recorded at different sites during the 1980 Irpinia earthquake (M=7.0) [2].

The records have been scaled according to the procedure proposed by Cornell [d], which states that an efficient way to predict the response of a non-linear structure given a scenario event is to use a representative ground motion attenuation law to evaluate the median spectral acceleration, for 5% damping, at the fundamental frequency of the initial tangent elastic structure, to select a set of records for the numerical analyses and to normalize them so as to have the same spectral acceleration at the same frequencies. The study assures that the response of the structure to the scaled records is not importantly dependent on ground motion parameters such as magnitude M, epicentral distance R and duration of the records. It has been observed that the scaled results reduce dispersion δ compared to that obtained from the unscaled records, thus reducing the number of runs necessary to estimate the median response by a factor of about 4.

The median spectral acceleration at the Benevento substation site has been evaluated using the attenuation law proposed by Pugliese and Sabetta [e], considered appropriate for Italy, with reference to the seismic event occurred in 1688 in the Sannio-Matese area (M=6.7, R=19.4 km), representing the seismic event having a 500 years return period for the selected area. It has been obtained:

$S_{a(f=1.62\ Hz)}=320\ m/s^2$ $\qquad \delta_{Sa}=0.276$

$S_{a(f=0.47\ Hz)}=320\ m/s^2$ $\qquad \delta_{Sa}=0.297$

$S_{a(f=0.53\ Hz)}=320\ m/s^2$ $\qquad \delta_{Sa}=0.296$

Calculations have been made assuming simultaneous actions in two horizontal (NS and WE) and vertical (UP) directions. For the fixed base model a 5% viscous damping ratio in all modes has been cautiously assumed.

Table 9.2 reports a summary of the results, in terms of median and dispersion, of the numerical analyses performed on the three different FE models: u_{Top} represents the maximum horizontal displacement at the top of the insulator pole, while M_{Base} the maximum bending moment at the critical section located at its base.

It is observed that with the coil springs and visco-elastic dampers isolation system, a reduction by a factor of 3.3 is obtained for the bending moment at the base of the pole, with the detriment of an increase of the top displacement by a factor of 3.7, compared to the fixed base model. Although smaller reductions in terms of stresses (of a factor of about 2) and lightly larger

Model	u_{Top}		M_{Base}	
	Median [cm]	δ_{uTop}	Median [kN-m]	δ_{MBase}
Fixed base	3.0	0.10	26.0	0.09
Spring + dampers isolation	11.0	0.17	7.8	0.19
Wire Rope isolation	12.9	0.11	13.1	0.34

Table 9.2 Results of the numerical FE analysis.

amplifications of top pole displacement are obtained adopting the Wire Rope isolation system, this solution can be considered overall preferable because of its simplicity and lower cost.

9.3 DESIGN OF SEMI-ACTIVE SYSTEMS WITH MR DAMPERS

In comparison with all the semi-active control devices employing some electrically controlled valves or mechanisms, that can be problematic in terms of reliability and maintenance, the class of semi-active controllable fluid devices using magnetorheological (MR) fluids has the basic advantage of containing no moving parts other than the piston, which makes them very reliable, and have been proved to be very rapid in their response and therefore particularly suited for semi-active earthquake engineering applications.

MR fluids are materials that respond to an applied magnetic field with a dramatic change in rheological behaviour: their essential characteristic is their ability to reversibly change from free-flowing linear viscous liquids to semi-solids having a yield strength controllable in milliseconds when exposed to a magnetic field. Although the initial discovery and development of MR fluids and devices can be credited to Jacob Rabinow at the US National Bureau of Standards [f], only recently a resurgence in interest in MR fluids has been seen in different Research Groups (University of Notre Dame with Prof. Spencer, Washington University with Prof. Dyke, University of Pavia with Prof. Casciati, Kajima Corporation with Prof. Kobori). MR fluids typically consist of non-colloidal micron-sized, magnetically polarizable particles dispersed in a non-magnetic carrier medium such as mineral/silicon oil or water. When a magnetic field is applied to the fluid, particle chains form, and the fluid becomes a semisolid exhibiting a viscoplastic behaviour: the mechanical energy needed to yield these chain-like structures increases as the applied magnetic field increases resulting in a field dependent yield stress; in the absence of an applied field, the MR fluids exhibit Newtonian-like behaviour. The so-called Bingham model [g], having a friction component augmented by a Newtonian viscosity component, is effective at describing the essential field dependent MR fluid characteristics:

$$\begin{aligned} &\tau = \eta\dot{\gamma} + \tau_y \operatorname{sgn}(\dot{\gamma}) && \text{if} \quad |\tau| > \tau_y \\ &\tau = G\gamma \ , \quad \dot{\gamma} = 0 && \text{if} \quad |\tau| < \tau_y \end{aligned} \tag{9.6}$$

where τ is the shear stress in fluid, h is the Newtonian viscosity, defined as the slope of the measured shear stress versus shear rate and independent of the applied magnetic field, $\dot{\gamma}$ is the shear strain rate, τ_y is the yielding shear stress controlled by the applied field and G is the complex material modulus. That is, the fluid is in a state of rest and behaves viscoelastically until the shear stress is lower than the critical value τ_y, and it moves as a Newtonian fluid as soon as such critical value is exceeded.

If a Bingham model for the fluid is assumed valid, a Bingham behaviour is obtained also for the MR damper (MRD) as a whole. In [h,i] it is shown how the force – velocity constitutive law of a MR damper can be derived through the study of a parallel-plate model of a MR fluid flow through a rectangular gap of total length L, leading to the following relation between the force F_d produced by the damper and the piston velocity U:

$$F_d(t) = F_\eta + F_\tau \cdot \mathrm{sgn}(U) = C_1 \frac{12\eta U L A_p}{bh^3} A_p + C_2 \frac{\tau_y L}{h} A_p \,\mathrm{sgn}(U) = C_d U + F_{dy}\,\mathrm{sgn}(U) \tag{9.7}$$

where F_η and F_τ represent the two components, in which the damping force can be decomposed, due to the fluid viscosity and to the field-induced yield stress, respectively; $C_1 = 1 - bh/(2A_p)$ and $C_2 \in (2.07, 3.07)$ are non-dimensional parameters, with b and h width and height of the rectangular gap, respectively, and A_p the piston cross-sectional area. Therefore the overall mechanical characteristics of the MR damper are:

$$C_d = C_1 \frac{12\eta L A_p}{bh^3} A_p\,,\quad F_{dy} = C_2 \frac{\tau_y L}{h} A_p \tag{9.8}$$

Clearly, C_d is independent of the applied field, while F_{dy} is function of the yielding shear stress and can be controlled through the applied field: F_{dy} constitutes just the controllable range of the damper, which is inversely proportional to the gap size h. This design variable has a great influence on the MRD mechanical characteristics, because an enlargement of it, besides reducing the viscous damping coefficient C_d, reduces the controllable force range, and consequently the effectiveness of the MR damper. It is worth to observe that in the force – velocity diagram of Fig. 9.3 the areas 1 and 2 are the upper and lower bounds of the device operation: in the first one, depending on the viscous coefficient C_d, the contribution F_0 of the friction force of the gaskets cannot be reduced; the second one is defined by the magnetic saturation line and the limit of force in the damper.

9.3.1 Response of dissipative braced frame to harmonic base motion

It is well known that for a steel frame structure, which is able to accommodate large interstorey drifts without significant damage, bracing systems equipped with energy dissipation devices are very well suited. In this section, the response to a harmonic base motion of a braced frame (Fig. 9.4), equipped with a passive viscous (VD) or rigid-plastic (RPD) damper, the latter representing devices based on friction mechanism or on the hysteretic behaviour of metals in the

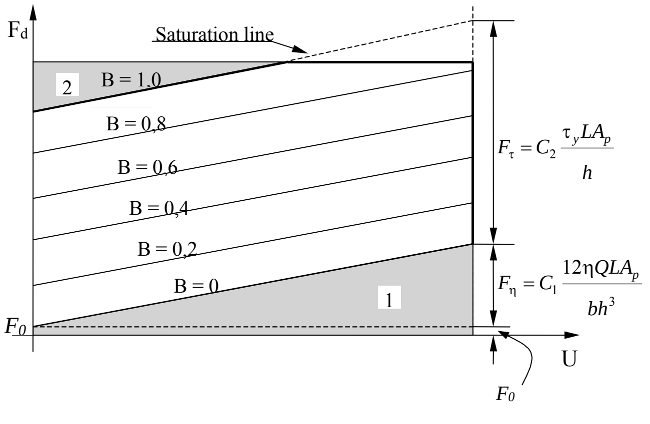

Figure 9.3 Force – velocity diagram of a MRD.

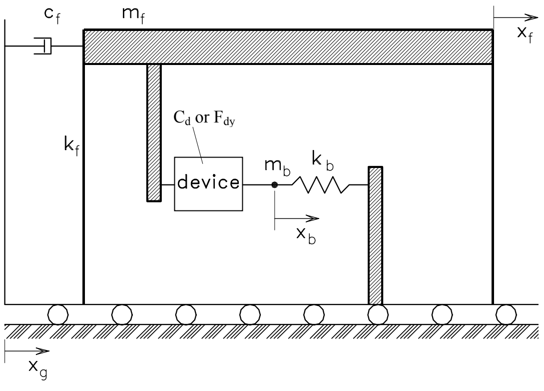

Figure 9.4 Dissipative braced frame.

plastic range, is analytically examined using a frequency domain approach, in order to single out the optimal viscous damping constant and yield strength, respectively, able to optimize the response in terms of top frame displacement.

9.3.2 Analytical definition of the optimal purely viscous damper's parameter

For the model in Fig. 9.4, where for simplicity $c_f = m_b = 0$, equipped with a linear viscous damper (Fig. 9.5a) and subjected to a harmonic base displacement $x_g(t) = x_{g,\max}\, e^{i\varpi t}$[j], the general expression of the equation of motion is the following:

$$m_f \cdot \ddot{x}_f + k_f \cdot x_f + F_d = m_f \varpi^2 x_{g,\max} \cdot e^{i\varpi t} \tag{9.9}$$

where $F_d = k_b \cdot x_b = C_d \cdot (\dot{x}_f - \dot{x}_b)$. The force – displacement relationship for the Maxwell element composed by the spring k_b and the viscous dashpot C_d in series is given by the well known expression $F_d(x_f) = K_d(\varpi) \cdot x_f$, where the complex stiffness $K_d(\varpi)$ is obtained as follows:

$$\begin{aligned} & x_f = x_b + \frac{\dot{x}_f - \dot{x}_b}{i\varpi} = F_d\left(\frac{1}{k_b} + \frac{1}{i\varpi C_d}\right) \quad \Rightarrow \quad F_d = \frac{k_b C_d^2 \varpi^2 + i k_b^2 C_d \varpi}{k_b^2 + \varpi^2 C_d^2} x_f \quad \Rightarrow \\ & \Rightarrow \quad K_d(\varpi) = \frac{k_b C_d^2 \varpi^2}{k_b^2 + \varpi^2 C_d^2} + i \frac{k_b^2 C_d \varpi}{k_b^2 + \varpi^2 C_d^2} = K'_d(\varpi) + i K''_d(\varpi) \end{aligned} \tag{9.10}$$

and $K'_d(\varpi)$ and $K''_d(\varpi)$ are respectively the storage and the loss modulus of the Maxwell element. Therefore Eq. (9.9) can be written as:

$$m_f \cdot \ddot{x}_f + \left[k_f + K'_d(\varpi) + i K''_d(\varpi)\right] \cdot x_f = m_f \varpi^2 x_{g,\max} \cdot e^{i\varpi t} \tag{9.11}$$

It is useful to write the above equation in non-dimensional form, by introducing the non-dimensional time $\tau = t \cdot \omega_b$, where $\omega_b = \sqrt{(k_f + k_b)/m_f}$ represents the circular frequency in the case of infinitely stiff damper ($C_d \to +\infty$), and the non-dimensional displacement $\zeta(\tau) = x_f(\tau)/x_{g,\max}$:

$$\zeta''(\tau) + f(\zeta) = \beta^2 e^{i\beta\tau} \tag{9.12}$$

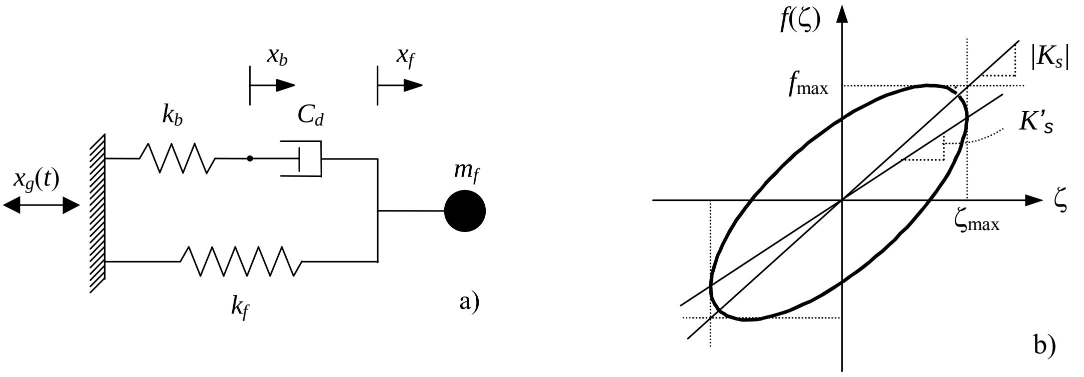

Figure 9.5 SDOF with purely viscous damper: a) scheme, b) $f(\zeta) - \zeta$ cycle.

where $\beta = \varpi/\omega_b$ and $f(\zeta) = \left[k_f \cdot x_f + F_d\left(x_f\right)\right] / \left(k_f x_{g,\max}\right) = K_s(\beta) \cdot \zeta(\tau)$ represents the normalized restoring force (Figure 9.5b). The force – displacement relationship is completely defined once the complex stiffness $\mathrm{K_s}(\beta)$ of the controlled structure is known:

$$K_s(\beta) = \frac{\kappa}{1+\kappa} + \frac{4\beta^2\nu^2\kappa(1+\kappa)}{(1+\kappa)\left[1+4\beta^2\nu^2\kappa(1+\kappa)\right]} + i\frac{2\beta\nu\sqrt{\kappa(1+\kappa)}}{(1+\kappa)\left[1+4\beta^2\nu^2\kappa(1+\kappa)\right]} = K_s'(\beta) + iK_s''(\beta) \tag{9.13}$$

where $K_s'(\varpi)$ and $K_s''(\varpi)$ are the overall storage and the loss modulus of the controlled structure, and the non-dimensional parameters $\kappa = k_f / k_b$ and $\nu = C_d \big/ 2\sqrt{k_f m_f}$ represent the frame/brace relative stiffness and the viscous damping ratio in the limit case $k_b \to +\infty$.

As the system is linear, an exact solution can be easily evaluated. The steady-state response is periodic with frequency β:

$$\zeta(\tau) = \zeta_{\max} \mathrm{e}^{\mathrm{i}\beta\tau} \tag{9.14}$$

and the amplitude of motion is the modulus of the complex number $\zeta_{\max}(\beta)$:

$$\left|\zeta_{\max}(\beta)\right| = \frac{\beta^2}{\sqrt{\left(\frac{\kappa}{1+\kappa} + \frac{4\beta^2\nu^2\kappa}{1+4\beta^2\nu^2\kappa(1+\kappa)} - \beta^2\right)^2 + \frac{4\beta^2\nu^2\kappa}{(1+\kappa)\left[1+4\beta^2\nu^2\kappa(1+\kappa)\right]^2}}} \tag{9.15}$$

The following limit cases can be considered:

- $\nu = 0 \;\Rightarrow\; C_d = 0$ (no damper) $\Rightarrow\; \left|\zeta_{\max}(\beta)\right| = \dfrac{\beta^2}{\left|\kappa/(1+\kappa) - \beta^2\right|}$;
- $\nu \to +\infty \;\Rightarrow\; C_d \to +\infty$ (infinitely stiff damper) $\Rightarrow\; \left|\zeta_{\max}(\beta)\right| = \dfrac{\beta^2}{\left|1-\beta^2\right|}$.

The quantity $\left|\zeta_{\max}(\beta)\right|$ as a function of β is plotted in Fig. 9.6 for $\kappa = 1, 0.1$ ($k_b = k_f$, $10k_f$) and for several different values of ν: the strong influence of the device damping coefficient on the system response comes out, i.e. a deep modification in the dynamic behaviour of the structure can be produced by a change in the viscous constant of the device. All the curves have a common

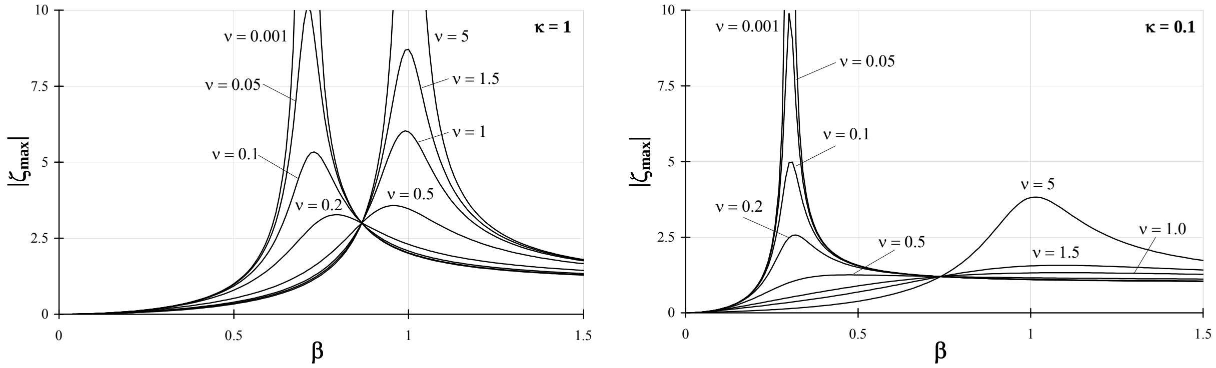

Figure 9.6 Transfer functions $\left|\zeta_{\max}(\beta)\right|$ for $\kappa = 1, 0.1$ (purely viscous damper case).

point, corresponding to the intersection of the two limit curves for $\nu = 0$ and $\nu \to +\infty$, whose coordinates are $\bar{\beta} = \sqrt{(1+2\kappa)/\left[2(1+\kappa)\right]}$ and $\left|\zeta_{\max}\left(\bar{\beta}\right)\right| = 1+2\kappa$. Among such curves, that one, for which the aforesaid point represents a maximum, i.e. the minimum resonance peak in the range $\nu = [0,+\infty]$, corresponds to the physically acceptable real root of the 3rd degree equation in the unknown ν^2:

$$8\kappa^2(1+\kappa)(1+2\kappa)^3\left(\nu^2\right)^3 + 4\kappa(1+2\kappa)^2(\kappa+2)\left(\nu^2\right)^2 - 2(1+2\kappa)(\kappa-1)\nu^2 - 1 = 0 \tag{9.16}$$

obtained by equating to zero the derivative of Eq 9.15 with respect to β computed for $\beta = \bar{\beta}$.

Such real solution, provided by the well known formula of Tartaglia-Cardano, represents the optimal (in the sense that it minimizes the amplitude of the resonance peak) value ν_{opt} of the parameter ν, for each assumed value of the parameter κ:

$$\nu^2_{opt,j+1} = \varepsilon^j \sqrt[3]{-\frac{q}{2} + \sqrt{\Delta}} + \varepsilon^{3-j} \sqrt[3]{-\frac{q}{2} - \sqrt{\Delta}} - a \quad j \in \{0,1,2\} \tag{9.17}$$

where:

$$-\frac{q}{2} = \frac{1}{216\kappa^3(1+\kappa)^3}, \quad \Delta = 0 \quad \forall\kappa, \quad a = \frac{\kappa+2}{6\kappa(1+\kappa)(1+2\kappa)} \tag{9.18}$$

and $\varepsilon^0 = 1$, $\varepsilon^1 = -1/2 + i\sqrt{3}/2$ and $\varepsilon^2 = -1/2 - i\sqrt{3}/2$ are the cubic roots of the unity. We can state that, as $\Delta = 0$, a simple root $2\sqrt[3]{-q/2} - a$ and a double root $-\sqrt[3]{-q/2} - a$ are obtained, both real and of opposite sign: the first one is always positive, the second one is always negative. Therefore ν_{opt} is given by the square root of the first one:

$$\nu_{opt} = \sqrt{2\sqrt[3]{-\frac{q}{2}} - a} = \sqrt{\frac{1}{2(1+\kappa)(1+2\kappa)}} \tag{9.19}$$

9.3.3 Analytical definition of the optimal purely friction damper's parameter

For the model in Fig. 9.4, where again $c_f = m_b = 0$, equipped with a friction damper (Fig. 9.7a) and subjected to an harmonic base displacement $x_g(t) = x_{g,\max} \cdot \cos(\varpi t)$, the general expression of the equation of motion is the following:

$$m_f \cdot \ddot{x}_f + k_f \cdot x_f + F_d = m_f \varpi^2 x_{g,\max} \cdot \cos(\varpi t) \tag{9.20}$$

where $F_d = k_b \cdot x_b$ always and $F_d = F_{dy}\,\text{sgn}(\dot{x}_f - \dot{x}_b)$ in the slip condition. It is useful to proceed as done in the previous case, by introducing the same non-dimensional parameters τ and $\zeta(\tau)$, leading to:

$$\zeta''(\tau) + f(\zeta) = \beta^2 \cos(\beta\tau) \tag{9.21}$$

where $\beta = \varpi/\omega_b$ and $f(\zeta) = \left[k_f \cdot x_f + F_d\right] / \left[\left(k_f + k_b\right) x_{g,\max}\right]$ represents the normalized restoring force. It is worth to note that in the normalized hysteretic cycle, shown in Fig. 9.7b, the initial

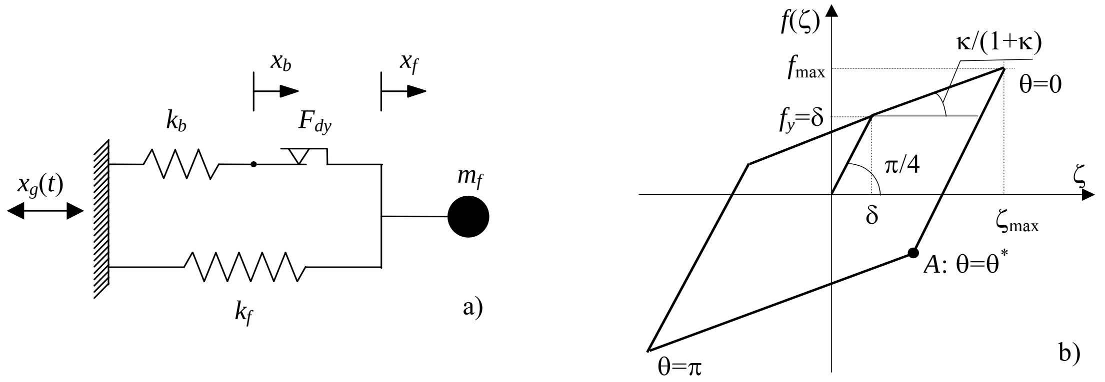

Figure 9.7 SDOF with purely friction damper: a) scheme, b) $f(\zeta)-\zeta$ cycle.

stiffness is reduced to unity so that the yield displacement $\delta = x_y/x_{g,\max} = F_{dy}/\left(k_b x_{g,\max}\right)$ and the yield strength f_y have the same value; furthermore the post-elastic stiffness is equal to κ/1+κ.

In this case the equation of motion is non-linear and only approximate analytical method can be used: in the following the slowly varying parameters method [k] will be adopted. It can be reasonably assumed that the steady-state response is periodic with frequency β:

$$\zeta(\tau) = \zeta_{\max}(\tau)\cos\left[\beta\tau + \phi(\tau)\right] = \zeta_{\max}\cos\theta \tag{9.22}$$

Using the slowly varying parameters method it is possible to assume the time derivative of the displacement and phase angle equal to zero ($d\zeta_{\max}(\tau)/d\tau = 0$, $d\phi(\tau)/d\tau = 0$) and then to approximate their value with their mean. Thus substituting Eq 9.22 in Eq 9.21 we get the following displacement and phase angle-frequency relationships:

$$\left[C(\zeta_{\max}) - \beta^2\zeta_{\max}\right]^2 + \left[S(\zeta_{\max})\right]^2 = \beta^4 \tag{9.23}$$

$$\tan\phi = \frac{S(\zeta_{\max})}{C(\zeta_{\max}) - \beta^2\zeta_{\max}} \tag{9.24}$$

where the functions $S(\zeta_{\max})$ and $C(\zeta_{\max})$ have the expressions:

$$\begin{cases} S(\zeta_{\max}) = -\dfrac{1}{1+\kappa}\dfrac{\zeta_{\max}}{\pi}\sin^2\theta^* & \text{if} \quad \zeta_{\max} > \delta \\ S(\zeta_{\max}) = 0 & \text{if} \quad \zeta_{\max} \le \delta \end{cases} \tag{9.25}$$

$$\begin{cases} C(\zeta_{\max}) = \dfrac{\zeta_{\max}}{\pi}\left[\dfrac{1}{1+\kappa}\theta^* + \dfrac{\kappa\pi}{1+\kappa} - \dfrac{1}{2(1+\kappa)}\sin 2\theta^*\right] & \text{if} \quad \zeta_{\max} > \delta \\ C(\zeta_{\max}) = \zeta_{\max} & \text{if} \quad \zeta_{\max} \le \delta \end{cases} \tag{9.26}$$

and $\theta^* = \cos^{-1}\left(1 - \dfrac{2\delta}{\zeta_{\max}}\right)$. The quantity $\zeta_{\max}$, which can be implicitly expressed as a function of β from Eq 9.18:

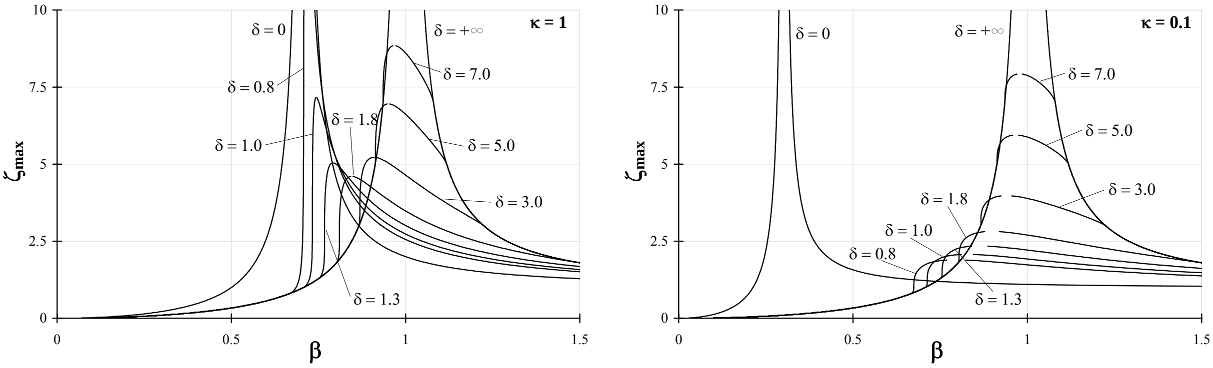

Figure 9.8 Transfer functions $\zeta_{\max}$ for $\kappa = 1, 0.1$ (purely friction damper case).

$$\beta^2 = \left[\zeta_{mac} C(\zeta_{mac}) \pm \sqrt{\zeta_{\max}^2 C^2(\zeta_{mac}) - \left(\zeta_{\max}^2 - 1\right)\left(C^2(\zeta_{mac}) + S^2(\zeta_{mac})\right)}\right] \Big/ \left(\zeta_{\max}^2 - 1\right) \qquad (9.27)$$

attains its maximum value for the value $\tilde{\zeta}_{\max}$ of $\zeta_{\max}$ which make void the radical quantity in Eq 9.27, i.e. satisfies the equation $\zeta_{\max}^2 = C^2(\zeta_{\max}) / S^2(\zeta_{\max}) + 1$, and the corresponding frequency is $\tilde{\beta} = S(\zeta_{\max})\sqrt{S^2(\zeta_{\max}) + C^2(\zeta_{\max})} \Big/ C(\zeta_{\max})$. The limit cases are the following:

- $\delta = 0 \;\Rightarrow\; \mathrm{F}_{dy} = 0$ (no damper) $\Rightarrow\; \beta^2 = \dfrac{\kappa\zeta_{\max}}{(1+\kappa)(\zeta_{\max} \mp 1)}$;
- $\nu \to +\infty \;\Rightarrow\; C_d \to +\infty$ (infinitely stiff damper) $\Rightarrow\; \beta^2 = \dfrac{\zeta_{\max}}{(\zeta_{\max} \mp 1)}$.

where now the two limit curves are expressed as $\beta = \beta(\zeta_{\max})$ instead of $\zeta_{\max} = \zeta_{\max}(\beta)$ as in the viscous damper case. The quantity $\zeta_{\max}$ as a function of β is plotted in Fig. 9.8 for κ=1,0.1 (k_b=k_f, 10k_f) and for several different values of δ: the point of co-ordinates $\bar{\beta} = \sqrt{(1+2\kappa) / [2(1+\kappa)]}$ and $\zeta_{\max}(\bar{\beta}) = 1 + 2\kappa$, represents again the intersection of the two limit curves but belongs only to them. One notes that a very low value of δ produces a peak of the curve near to the one of the undamped structure case, and its value decreases as far as the previous parameter increases; however a further increase of the yield displacement induces a shift of the resonance frequency toward β=1, with an increment, at the same time, of the peak amplitude. Therefore the resonance peak, within the range $\delta = [0, +\infty]$ has a minimum value, quite close to the one of the intersection point between the limit curves ($\bar{\beta}$).

9.3.4 Seismic protection of a steel frame through MR dampers

In the following, MR dampers are considered for seismically protecting a steel frame mock-up (MISS) selected as representative structure. MISS is a 4-storeys steel structure made of Fe430, composed by six vertical columns (HEB 100) bolted on a base frame made of HEB 140 beams and supporting four floor slabs manufactured using beam elements (HEB 100) only. On each slab it is possible to install up to 8 reinforced concrete blocks, each weighting 12.8 kN. Shaking table identification tests performed on the fixed base, unbraced configuration of the MISS structure, equipped with 4 reinforced concrete blocks on each floor, have indicated a first modal frequency along its short edge (transverse) direction ω_1=14.95 rad/s and an associated damping ratio

ξ_1=1.7%. Starting from these data, an equivalent single story frame (Fig. 9.4) has been deduced, characterized by: a mass m_f =17.50 t equal to the first transversal modal participating mass ratio (77.34%, from a numerical model of MISS structure) multiplied the total mass of the 4-storeys steel frame (m_{tot}=22.63 t), sum of the masses of the columns and the four floor slabs, and of that one of the concrete blocks; a frame stiffness k_f and a damping coefficient c_f obtained as $k_f = \omega_1^2 \cdot m_f = 3911\ kN/m$ and $c_f = \xi_1 \cdot 2\sqrt{k_f m} = 8.9\ kN/(m/s)$. A flexible brace equipped with a MR damper has then been introduced in the simplified model, thus obtaining what we called the 1+1-DOF reduced model of the MISS braced structure. C_d and F_{dy} are the MR damper's mechanical characteristics, the additional mass m_b=0.17 t representing the mass of the semi-active assembly (brace + MR damper) while the brace stiffness k_b has been chosen equal to the frame stiffness k_f because it has been shown that the implementation of a semi-active control system is more efficacious when these two stiffness values are comparable [1]. In what follows the results of a parametric investigation, performed on the 1+1-DOF simplified model of the MISS structure, are presented: non-linear time-history analyses have been performed on the reduced model subjected to three selected seismic inputs (the Tolmezzo NS record – 1976 Friuli earthquake, and two synthetic accelerograms generated according to EC8 for soft and medium soil conditions) in order to obtain numerically, through suitable software edited in Matlab language, its dynamic response in a passive configuration, with varying the mechanical characteristics of the MR damper. In Fig. 9.9, showing the response of the structure, for all the selected accelerograms, in terms of frame displacements x_f with varying the viscous damping coefficient C_d (F_{dy}=0), an interval of optimal values $C_{d,opt}$ =70 ÷400 kN/m/s is singled out. Moreover, Fig. 9.10 reports the same response quantity with varying the field-induced friction force F_{dy} (C_d=0), by pointing out an interval of optimal values $F_{dy,opt}$=10÷20 kN.

By applying the procedure shown in the previous section to the example case of the MISS reduced model, one obtains, for the assumed relative stiffness κ=1, the optimal values ν_{opt}=0.2887and δ_{opt}=1.8. The former optimal ratio corresponds to a purely viscous damping coefficient $C_{d,opt}$=76kN/(m/s), which falls within the range of the optimal viscous damping coefficients determined through the time-history analyses, while the latter provides an interval of values for $x_{g,max}$ =1.5 ÷ 3mm for the range of optimal friction force values obtained from the time domain analyses, considered acceptable for the selected earthquakes.

The response in terms of frame displacements x_f, to one of the considered earthquakes (EC8-C), of the uncontrolled structural configuration ($C_d = F_{dy} = 0$) has been compared with that one

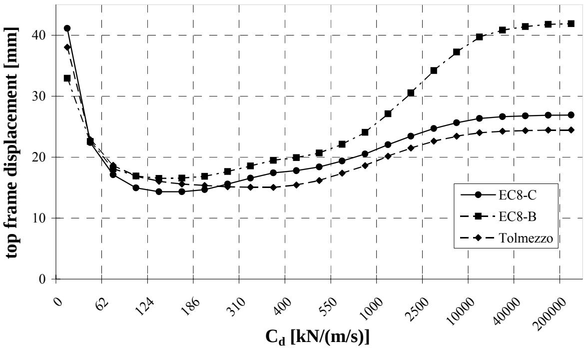

Figure 9.9 Response for a viscous damper.

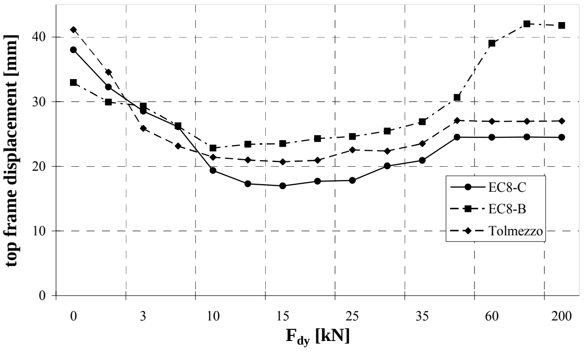

Figure 9.10 Response for a friction damper.

of the rigid-linked configuration ($C_d \to +\infty$ or $F_{dy} \to +\infty$) and that one of the best passive configuration (C_d=124kN/(m/s), F_{dy}=0kN). The response in terms of top frame displacement x_f of the above 1+1-DOF model in the optimal passive configuration, has been then compared with that one relating to the optimal mechanical properties of the semi-actively operating MR dampers ($C_d = 31 kN/(m/s)$, $F_{dy} = 1 \div 25 kN$), singled out from a careful parametric investigation performed by using two different control algorithms suitable for MR dampers ("Clipped" Linear Quadratic Regulator and Minimized Energy Input), with the aim to estimate the effectiveness of the semi-active control strategies [3].

9.4 MECHANICAL CHARACTERIZATION OF MR DAMPERS FROM EXPERIMENTAL TESTS

As stated above, the 2-parameters Bingham model can describe qualitatively the behaviour of a MR damper. However, some authors found that this model may not satisfactorily capture the behaviour of a real MR device. Even if a number of alternate models can be found in literature, the experimental tests described in the following have been designed so as to provide answers to some issues regarding the physical behaviour of semi-active MR devices still needing some clarification [4]:

- The model of a MR damper has to be included in a more general numerical representation of the main structure hosting the device(s). Therefore, there is a need for a reasonably accurate model relying on a limited number of parameters.
- The dependence of the viscous force and of the magnetorheological effect on the current feeding the device, i.e., on the applied magnetic field, is still unclear.

9.4.1 Experimental set up

Four prototype semi-active MR dampers have been designed and manufactured in the framework of the EU funded SPACE (Semi-active and PAssive Control of the dynamic behaviour of structures subjected to Earthquakes, wind and vibrations) Research Project [m]. One of these full-scale MR dampers is shown in figure 9.11: it looks pretty much like a conventional viscous damper, with the exception of some extra wiring needed to feed the coils inside the body. The overall dimensions of the device are 712mm × 200mm × 250mm and its mass is approximately 16 kg. It can develop a maximum damping force of 50 kN along its longitudinal axis, while the absence of bending, shear and torsional moment in the piston rod is obtained through special spherical pin joints at both ends of the device. Therefore, only forces along the longitudinal axis of the piston rod are applied on the device, although limited transverse forces can also be sustained. The damper has a stroke of ± 25 mm, and the external diameters of the piston head and of the piston rod are 82.2 mm and 40 mm, respectively. The gap between the piston head and the cylinder housing is 0.9 mm wide and 76 mm long. The magnetic field produced in the device is generated by a magnetic circuit composed by three coils, each of them with a resistance $R = 1.15\ \Omega$ and an inductivity $L = 92$ mH. The design features an innovative idea about the way in which the magnetic circuit is implemented as well as about its interaction with the flow of the fluid inside the body. The current in the circuit, in the range of $i = 0 \div 3$ A is provided by a power supply commanded by a voltage input signal.

The monoaxial shaking table "Ariete", located at the Structural Dynamic Testing Laboratory of ENEL.Hydro – ISMES in Seriate (Bergamo, Italy), has been used to perform different experimental tests on the MR damper. The experimental set up, shown in figure 9.12, included a rigid steel frame locked to the shaking table, to which the main body of the damper was firmly connected, while the device piston was connected to a rigid plate clamped to the ground.

Two different types of dynamic tests were performed, i.e., imposed harmonic displacement tests and imposed constant velocity tests. In the harmonic displacement tests a number of sinusoidal displacement cycles of constant amplitude was imposed: six different frequencies (0.5, 1, 2, 2.4, 3 and 4 Hz) with two different displacement amplitudes (± 10 and ± 20 mm) and nine different current levels (0, 0.5, 0.75, 1.0, 1.5, 2.0, 2.25, 2.5 and 3 A) were considered. In the constant velocity tests a number of triangular displacement cycles of constant amplitude was imposed: four different constant velocities (10, 50, 100 and 300 mm/s) with two displacement amplitudes (± 10 and ± 20 mm) and six different current levels (0, 0.75, 1.5, 2.25, 2.5 and 3 A) were considered.

9.4.2 Numerical analysis of the experimental results

As a first step, the effective force–displacement and force–velocity cycles obtained during the tests have been compared to the cycles obtained numerically by properly choosing the mechanical properties of the Bingham model. This model allows to fit the experimental cycle through the sum of the rectangular loop of a rigid-perfectly plastic element and the elliptical cycle of a linear viscous element. Therefore, in the fitting procedure $F_{dy,\min}$ can be determined by visually estimating the friction component in the tests performed at 0 A, $F_{dy,\max}$ can be estimated by observing at each current level the plastic threshold depending on the applied magnetic field, and C_d can be found from the amplitude of the elliptical part of the cycles. In the numerical analysis, the velocity U has been obtained as numerical derivative of the experimental displacement D2.

The numerical force–displacement loops shown in Fig. 9.11 refer to the sinusoidal tests at 2.4 Hz and ± 20 mm amplitude, and correspond to three different levels of current inside the damper, namely 0, 1.5 and 2.5 A. The figure shows the experimental data as well as the curves corresponding to the following numerical model:

$$F_d = C_d \cdot U + \left[F_{dy,\min} + \left(F_{dy,\max} - F_{dy,\min} \right) \cdot i/i_{\max} \right] \cdot \operatorname{sgn}\left(U\right) \qquad (9.28)$$

being C_d=18 kNs/m, $F_{\mathrm{dy,min}}$ and $F_{\mathrm{dy,max}}$ set to 0.6 kN and 28 kN, respectively, and $i_{\max}$ the maximum current in the working range of the device (3 A). The numerical and experimental data shown in Fig. 9.11 demonstrate that: a) the standard, 2-parameter Bingham model can describe the behaviour of the MR damper with reasonable accuracy, b) the variable plastic threshold F_{dy} can be assumed linearly dependent on the current *i* and c) the weaker part of the numerical model is the assumed independence of the viscous damping constant C_d from the current *i*.

In fact, the viscous component of the loops seems to be overestimated at i = 0 A and underestimated at i = 2.5 A. Therefore, by including a dependency of the damping constant on the magnetic field inside the damper and, in turn, on the feeding current *i*, the Bingham model can be modified in the following constitutive law:

$$F_d = C_d\left(i\right) \cdot U + \left[F_{dy,\min} + \left(F_{dy,\max} - F_{dy,\min} \right) \cdot i/i_{\max} \right] \cdot \operatorname{sgn}\left(U\right) \qquad (9.29)$$

The experimental and numerical force-displacement loops corresponding to the sinusoidal tests at 2.4 and 1.0 Hz and to 0 and 2.5 A levels of current inside the damper, having set in the numerical model the viscous damping constant C_d to 6 kNs/m at i = 0 A and to 22 kNs/m at i = 2.5 A, shows a rather satisfactory agreement for the tests at 2.4 Hz, thus confirming the better accuracy of a model including the dependence of the viscous damping constant on the current inside the coils. However, the parameters chosen to fit the tests at 2.4 Hz yield a lower level of accuracy when adopted to analyze the tests at 1.0 Hz.

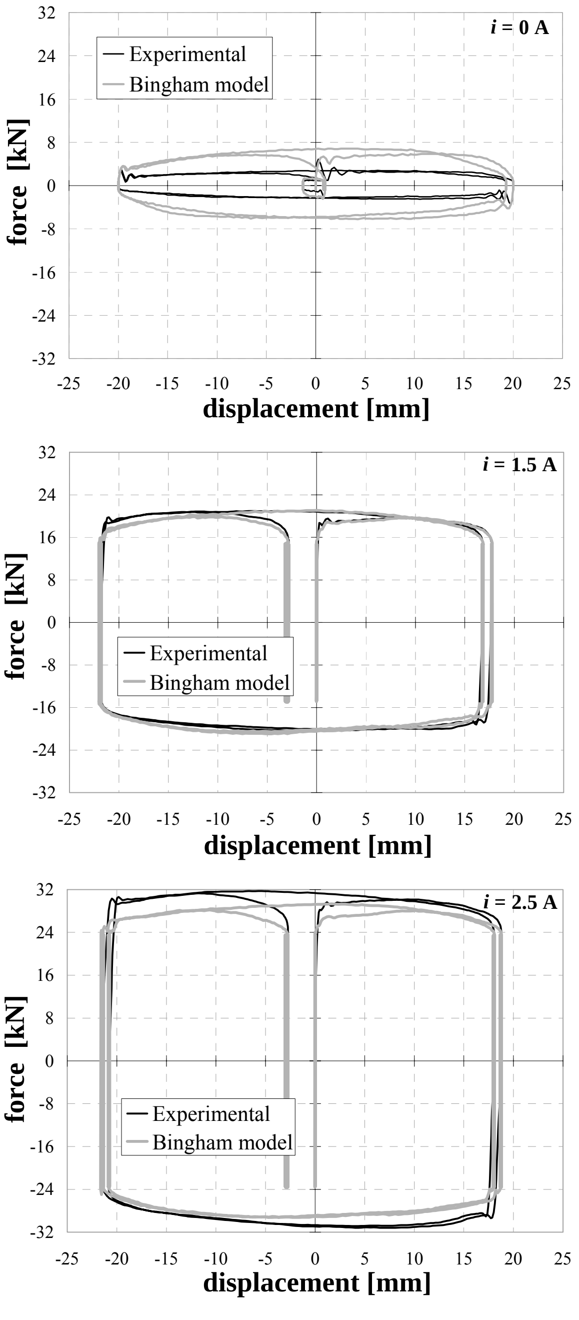

Figure 9.11 Experimental and numerical (Bingham model) cycles in harmonic displacement tests at 2.4 and ± 20 mm amplitude with 0, 1.5 and 2.5 A current level.

Nevertheless, it was found that, by applying the fitting procedure described before, it is always possible to find out a value of C_d which results in a good agreement of experimental data and numerical simulations based on Eq. 9.29. This means that the viscous damping component of the total force in the damper cannot be considered linearly dependent on the velocity, but it is more correct to assume the following non-linear relationship between the viscous damping force and the velocity:

$$F_\eta = C(i)\cdot|U|^{\alpha(i)}\cdot\mathrm{sgn}(U) \qquad (9.30)$$

Hence, the force–velocity constitutive law of the MR damper is characterized by three mechanical parameters C, α and F_{dy}, all of them dependent on the current intensity i. The experimental data have been fitted by properly selecting the couples (C, α) for any given level of current intensity inside the damper. The result of the comprehensive numerical fitting of the experimental data measured during the tests described in section 9.4.1, carried out by continuously varying the parameters C and α in order to obtain the best laws able to describe the damper's mechanical behaviour, leads to the following "improved model":

$$F_d = C(i)\cdot|U|^{\alpha(i)}\cdot\mathrm{sgn}(U) + \\ +\left[F_{dy,\min} + \left(F_{dy,\max} - F_{dy,\min}\right)\cdot i/i_{\max}\right]\cdot\mathrm{sgn}(U) \qquad (9.31)$$

where $C(i)$=5.5+5.0 i [kNs/m], $\alpha(i)$=0.0795 i^2-0.3475 i+0.9, and $F_{dy,\min}$ and $F_{dy,\max}$ set to 0.6 kN and 28 kN, respectively, as before. This model allows a very good interpretation of the experimental data relative to tests performed at different test velocities and current levels, as shown in Fig. 9.12.

9.5 CONTROL ALGORITHMS FOR SEMI-ACTIVE CONTROL DEVICES

When dealing with passive control, designing a device usually means to fix a set of boundary conditions and to choose a device optimized for that set of conditions. The controlled system will

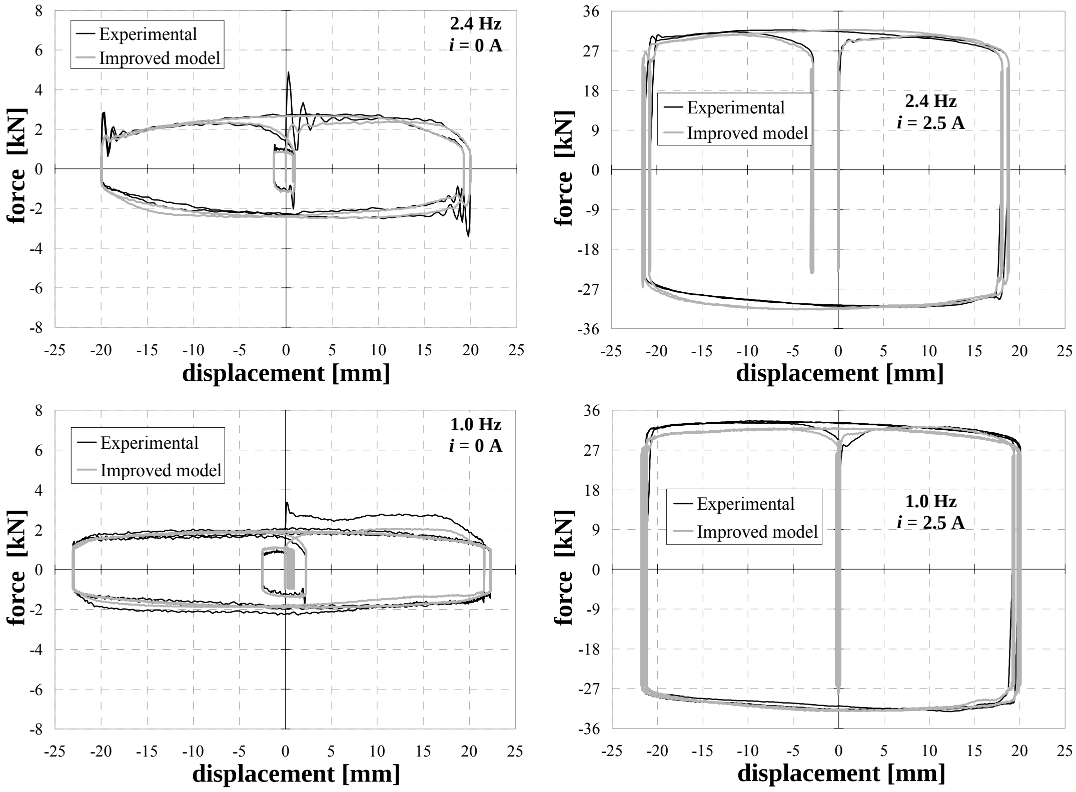

Figure 9.12 Experimental and numerical (improved model) cycles in harmonic displacement tests at 2.4 and 1.0 Hz, ± 20 mm amplitude with 0 and 2.5 A current level.

behave as designed as long as the operating environment closely fits the design hypoteses. By exploiting properly designed operating criteria, semi-active control may enhance the performances of passive systems, adapting their properties to the actual operating conditions. From this perspective, a semi-active control system can be looked at as a self-optimizing passive device. This basic idea is usually hidden behind virtually any operating criterion, i.e., algorithm, found in the scientific literature.

The control algorithms proposed in the scientific literature can be indexed into two main categories. The first one includes control algorithms originally proposed for fully active control systems, whereas algorithms based on the physical interpretation of the damper behaviour belong to the second one. The next section describes some algorithms representative of both families.

Consider the 1+1 degree of freedom model shown in Fig. 9.13. It is made up by a simple linear shear frame and a control system composed of an MR damper, a mass and an elastic element. The equations of motion are:

$$\begin{bmatrix} m_f & 0 \\ 0 & m_b \end{bmatrix}\begin{bmatrix}\ddot{x}_f \\ \ddot{x}_b\end{bmatrix} + \begin{bmatrix} c_f & 0 \\ 0 & 0 \end{bmatrix}\begin{bmatrix}\dot{x}_f \\ \dot{x}_b\end{bmatrix} + \begin{bmatrix} k_f & 0 \\ 0 & k_b \end{bmatrix}\begin{bmatrix}x_f \\ x_b\end{bmatrix} = -\begin{bmatrix} m_f & 0 \\ 0 & m_b \end{bmatrix}\begin{bmatrix}1 \\ 1\end{bmatrix}\ddot{x}_g + \begin{bmatrix}1 \\ -1\end{bmatrix} f$$

(9.32)

$$\mathbf{M}_s\ddot{\mathbf{x}} + \mathbf{C}_s\dot{\mathbf{x}} + \mathbf{K}_s\mathbf{x} = -\mathbf{M}_s\mathbf{i}\,\ddot{x}_g + \mathbf{l}\,f$$

By adopting a Bingham model for the magnetorheological damper, the force *f* is described by the following inequality:

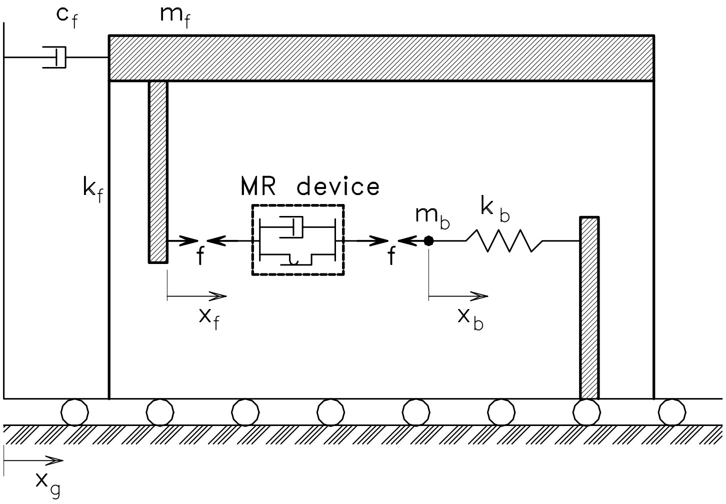

Figure 9.13 1+1 DOF structural model.

$$f \le u_y\left(i\right)\mathrm{sgn}(\dot{x}_b - \dot{x}_f) + c_b(\dot{x}_b - \dot{x}_f) \tag{9.33}$$

being u_y and c_b the parameters which characterize the MR damper and $i(t)$ the current signal controlling the level of the yield stress in the device. If we assume the absolute accelerations of the masses as output of the system, the state-space representation is the following:

$$\begin{cases} \begin{bmatrix} \dot{\mathbf{x}} \\ \ddot{\mathbf{x}} \end{bmatrix} = \begin{bmatrix} \mathbf{0}_{2\times2} & \mathbf{I}_{2\times2} \\ -\mathbf{M}_s^{-1}\mathbf{K}_s & -\mathbf{M}_s^{-1}\mathbf{C}_s \end{bmatrix} \begin{bmatrix} \mathbf{x} \\ \dot{\mathbf{x}} \end{bmatrix} + \begin{bmatrix} \mathbf{0}_{2\times1} \\ -\mathbf{i} \end{bmatrix} \ddot{x}_g + \begin{bmatrix} \mathbf{0}_{2\times1} \\ \mathbf{M}_s^{-1}\mathbf{l} \end{bmatrix} f \\ \\ \left[\ddot{\mathbf{x}}_{\mathrm{T}}\right] = \left[-\mathbf{M}_s^{-1}\mathbf{K}_s \quad -\mathbf{M}_s^{-1}\mathbf{C}_s\right] \begin{bmatrix} \mathbf{x} \\ \dot{\mathbf{x}} \end{bmatrix} + \left[\mathbf{M}_s^{-1}\mathbf{l}\right] f \end{cases} \tag{9.34}$$

or, in a more syntetic notation,

$$\begin{cases} \dot{\mathbf{z}} = \mathbf{A}\mathbf{z} + \mathbf{e}\ddot{x}_g + \mathbf{b}f \\ \mathbf{y} = \mathbf{C}\mathbf{z} + \mathbf{d}f \end{cases}$$

A particular case of optimal control, a linear quadratic regulator [n] is an analytical tool to find out a control law $f_{opt}(t)$ such as to minimize a scalar "cost" functional:

$$J = \int_0^t [\mathbf{z}^T\mathbf{Q}\mathbf{z} + r\, f_{opt}^{\ 2}]d\tau \tag{9.35}$$

Provided that t approaches infinite and f_{opt} is unbounded, denoting by **P** the solution of the algebraic Riccati equation, the feedback control law minimizing the index J is given by:

$$f_{opt}\left(t\right) = -r^{-1}\mathbf{b}^T\mathbf{P}\ \mathbf{z}\left(t\right) = -\mathbf{G}_{LQR}\ \mathbf{z}\left(t\right) \tag{9.36}$$

It is not always possible to make the semi-active MR damper produce the optimal control force described by Eq. 9.36. The goal is then to keep the available force f that can be acted by the device as close as possible to f_{opt} (clipped optimal control). In a bang-bang control scheme, the algorithm controlling the current in the MR damper is given by:

$$i(t) = i_{\max}\ \mathrm{H}\left[\left(f_{opt} - f\right)\cdot f\right] \tag{9.37}$$

being H the Heavyside function.

A different approach to the design of control algorithms for semi-active devices in based on the exploitation of Lyapunov stability theory, usually adopted to check if an active control algorithm results in a stable system. The stability assessment involves the definition of a positive, real scalar and lower bounded function V of the whole state **z**. The Barbalat's Lemma can be used to demonstrate that, in a wide range of hypoteses, the negativeness of the time derivative d*V*/d*t* guarantees the system stability in the bounded input-bounded output sense. Thus, a semi-active device may be driven by an algorithm that tries to minimize the value of that derivative. An interesting application of this concept can be obtained by assuming a Lyapunov function made up of the sum of the kinetic and elastic stored energy in the structure:

$$V(\mathbf{z}) = \frac{1}{2}\left(\mathbf{x}^T\mathbf{K}_s\mathbf{x} + \dot{\mathbf{x}}_T{}^T\mathbf{M}_s\dot{\mathbf{x}}_T\right) \tag{9.38}$$

The time derivative of Eq. 9.38 in a structural system described by Eq. 9.32 is:

$$\dot{V} = \mathbf{x}^T\mathbf{K}_s\dot{\mathbf{x}} + \dot{\mathbf{x}}_T{}^T\left(-\mathbf{C}_s\dot{\mathbf{x}} - \mathbf{K}_s\mathbf{x} + \mathbf{l}\,f\right) \tag{9.39}$$

The only term that can be directly changed by the control action *f* is the last one. Therefore, the control algorithm would be based on the sign of the scalar quantity:

$$\dot{\mathbf{x}}_T{}^T\mathbf{l}\,f = \begin{bmatrix}\dot{x}_{fT} & \dot{x}_{bT}\end{bmatrix}\begin{bmatrix}1\\-1\end{bmatrix} f = f(\dot{x}_{fT} - \dot{x}_{bT}) = f(\dot{x}_f - \dot{x}_b) \tag{9.40}$$

If Eq. 9.40 is negative, the only directly controllable term of Eq. 9.39 is negative and, in order to make the time derivative of *V* as negative as possible, *f* must be assigned its maximum value. The corresponding control law can be written as follows:

$$i(t) = i_{\max}\mathrm{H}\left[f(\dot{x}_b - \dot{x}_f)\right] \tag{9.41}$$

Eq. 9.41 allows an energy interpretation of the control law: the force in the MR damper has to be maximum as long as the istantaneous work done on the device is positive. However, being the control device a passive one, the argument of the Heavyside function in Eq. 9.41 can never be negative. In this case, the Lyapunov analysis can only confirm that a passive device can never make the structure unstable. If we look at the subsystem made up by MR damper, mass and spring, a more effective energy-based control algorithm can be defined as follows. The subsystem can be used to temporarily store a fraction of the energy flowing from the ground to the structure during an earthquake and to release that energy during properly-tuned, fast dissipation processes. The storing phase corresponds to time intervals where the power flowing from the structure into the subsystem is positive, i.e., when:

$$f\ \dot{x}_f < 0 \tag{9.42}$$

In the storing phase, the subsystem has to be tuned so as to achive the maximum possible strain in the elastic element and, therefore, the value of *f* has to be set as high as possible. When the sign of Eq. 9.42 changes to positive, the power starts flowing from the device into the structure. At this point, by switching u_y to its minimum value, the dissipation phase is invoked to let the MR

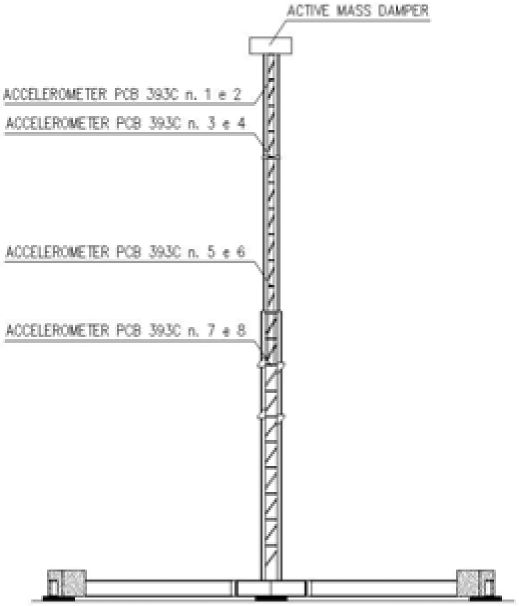

Figure 9.14 The aluminium mast used for the experimental tests and active mass damper and accelerometers location.

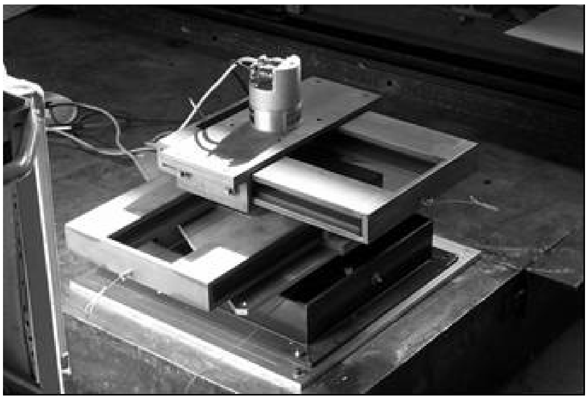

Figure 9.15 The AMD placed on top of the structure.

damper dissipate the elastic energy stored in the elastic spring. If the control subsytem is properly designed, the spring displacement x_b goes to zero, thus dissipating the elastic energy stored therein in a time interval that is short if compared to the natural period of the structural frame. The corresponding control law is as follows:

$$i(t) = i_{\max} \mathrm{H}\left[f\ (-\dot{x}_f) \right] \tag{9.43}$$

9.6 ACTIVE CONTROL EXPERIMENTS ON A WIND EXCITED MAST

Within a multidiscipline project, an aluminium mast was realized by the University of Perugia to verify the applicability of the active control methodology to flexible structure subjected to wind loads (Fig. 9.14). Active control technique can, in fact, be used to reduce the effect of the environmental actions according to different control strategies [o, p]. The active control system (Fig. 9.15) is an active mass damper (AMD) controlled by a dedicated PC and is placed on the top of the structure (Fig. 9.14). It is made up of two rotating engines connected to two steel masses, whose weight is approximately 122 N, that can move along two perpendicular directions. An optical encoder connected to the rotating engine allows us to know the relative displacement between the mass and the top of the structure. The acquisition system is composed of 8 accelerometers type PCB 393 C disposed on 4 levels (Fig. 9.14).

Several experimental tests have been planned and carried out to identify the dynamic characteristics of the structure and to put in evidence the positive effect of the control device in reducing the vibration due to external time dependent forces.

A proportional and derivative algorithm (PD) has been used to command the AMD. The feedback parameters used in the closed loop control strategy are the relative displacement (proportional term) and the relative velocity (derivative term) between the top of the mast and the moveable steel mass. Thus the control force can be expressed in the following way:

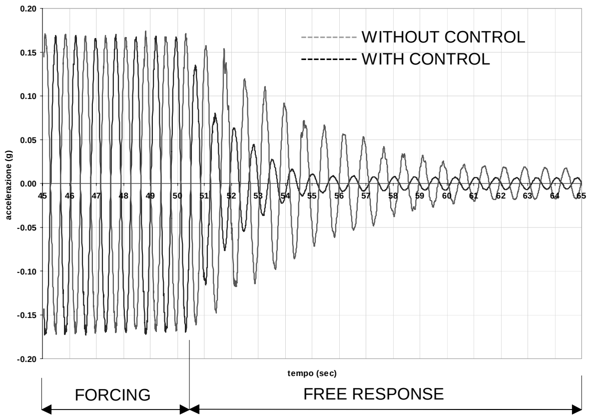

Figure 9.16 Free response of uncontrolled and controlled structure.

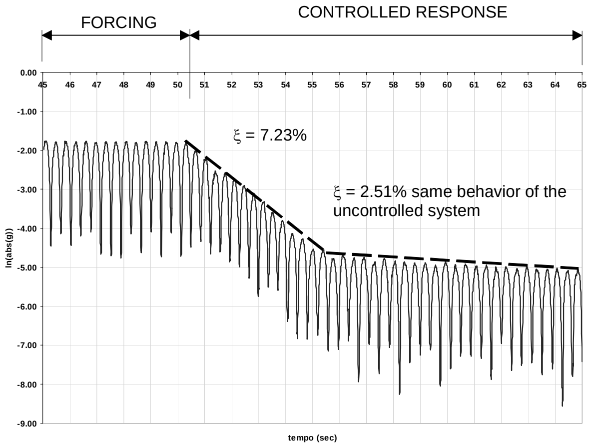

Figure 9.17 Logarithmic decrement of the controlled free response.

$$u(t) = K_P x(t) + K_D \dot{x}(t) \tag{9.44}$$

During the first phase of this research a set of forced vibration tests have been carried out. In these tests the control device was used initially to excite the structure applying a sinusoidal force on the top of the mast for a prescribed time interval (30 sec). This sinusoidal force was a 1,35 Hz frequency force, close to the first eigenfrequency. It is worth to note that to apply this force the software that command the AMD was written with a higher frequency to take into account the time delay caused by the limited computing velocity.

Passed this initial period the law that command the AMD changes and the device starts to work as an active control device. Several attempts were made to find the couple of control gains K_P and K_D that maximize the effect of control, based on the evaluation of the damping of the first mode. It turned out that this parameter are $K_P = 16$ and $K_D = 24$. With these parameters the damping increased from 2.51% to 7.23%, calculated using the logarithmic decrement of acceleration and the free oscillations of the mast were reduced faster as can be seen from the acceleration data acquired by accelerometer no. 1 (Fig. 9.16). Moreover the effect of control is negligible for small vibration as can be seen in Fig. 9.17 where is plotted the acceleration time history in a semi-logarithmic scale. In fact, after an initial phase where the oscillations were strongly and promptly reduced, the dynamic response of the system turns to be the same of the uncontrolled structure. This behaviour is due to the friction present in the mechanism: for small vibration the relative displacement and the relative velocity between the AMD masses and the top of the structure are small and the corresponding control force is smaller than the friction. In this way the AMD masses move together with the antenna and the effect of active control disappears.

Other tests were executed during windstorms to evaluate the reduction of oscillation using the active control. Each test was one hour long, divided in six equally long intervals. The control is used during intervals no. 1, 3 and 5 while during intervals no. 2, 4 and 6 the response of the uncontrolled structure is recorded.

Since it wasn’t possible to contemporarily check the controlled and uncontrolled response a ultrasonic anemometer was installed close to the antenna. The data obtained from the anemometer were used to statistically compare the wind velocities time histories during the six intervals. The structural response was recorded with 100 Hz sampling frequency while for the wind velocity a 4 Hz sampling frequency was employed.

From the 1st test two portions with duration 327.68 sec (corresponding to 2^{15} points) were extracted respectively at the beginning (controlled system) and at the end (uncontrolled system) while from the 2nd test two 163.84 sec long portion (corresponding to 2^{14} points) were obtained at the beginning (controlled system) and at the end (uncontrolled system). In Tab. 9.3 are summarized the results of the two tests in term of velocities and acceleration standard deviation. The subscript *c* indicates the controlled phase while *nc* is for the uncontrolled phase.

	$\frac{\sigma(u)_c}{\sigma(u)_{nc}}$	$\frac{\sigma(v)_c}{\sigma(v)_{nc}}$	$\frac{\sigma(acc)_c}{\sigma(acc)_{nc}}$
Test no. 1	1.16	1.09	0.55
Test no. 2	1.09	0.7626	0.38

Table 9.3 Summary of the wind load vibration tests.

It can be noticed that in both tests the ratio between the standard deviation of the acceleration in the controlled phase and the one relative to the uncontrolled phase is 0.55 for the 1st test and 0.38 for the 2nd tests while the analogous ratio for the wind components velocities are generally bigger than 1. In Fig. 9.18 and 9.19 are depicted the acceleration probability densities (bars) of the analyzed time history portions. In each figure are represented the controlled (narrow bars) and uncontrolled (wide bars) responses. The solid line describes a gaussian process with zero mean and standard deviation equal to that experimentally determined. It is clear that the presence of the control reduce the tails of the distributions, reducing also the stress peaks caused by the time varying forces.

Both tests (free response and wind load tests) confirmed that the introduction of this type of control device ensures a significant increment of the structural damping with the consequent reduction of the wind-induced vibrations. This latter aspect causes positive effects for both ultimate (peak stresses reduction, fatigue) and service limit states (deflection and vibrations reduction). Moreover, during the free response tests, a numerical analysis made possible to detect the effects of friction, imperfections, time delay and other aspects, always present in real systems, that can affect the control device performances. The efficiency of the active control system was observed through a relevant reduction of the maximum of the floating part of the dynamic response.

9.7 BASIC REFERENCES

[a] Schiff A.J. (Ed.), 1999. Guide to improved earthquake performance of electric power systems. *Electric Power and Communications Commitee - Technical Council on Lifeline Earthquake Engineering*. ASCE Manuals and Reports on Engineering Practice no. 96.

[b] Camensig C., Bresesti L., Clementel S., Mucciarelli M., Salvetti M. 1993. Evaluation of seismic risk of HV electric substation" (in Italian), *Proceedings 6th Italian National Conference on Seismic Engineering*, Perugia, Italy, **3**, pp. 1029-1038.

[c] Mazzolani F.M., Serino G. 1994. Innovative techniques for seismic retrofit: design methodologies and recent applications, *Proceedings Italian-French Symposium on Strengthening and Repair of Structures in Seismic Area*, Nice, France, pp. 211-220.

[d] Shome N., Cornell C.A., Bazzurro P., Carballo J.E. 1998. Earthquakes, records and nonlinear responses, *Earthquake Spectra*, **14**(3), pp. 469-500.

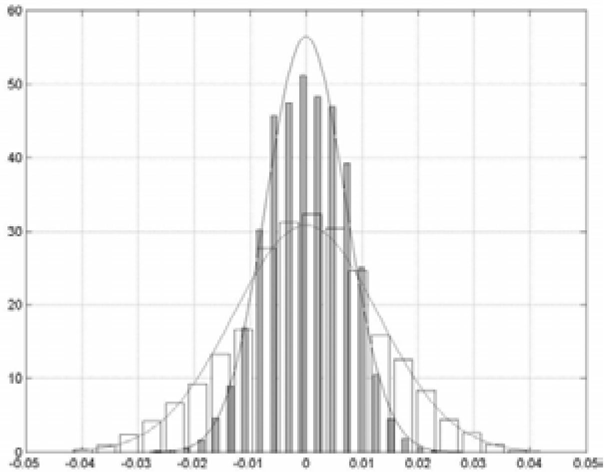

Figure 9.18 Test no. 1: acceleration probability density

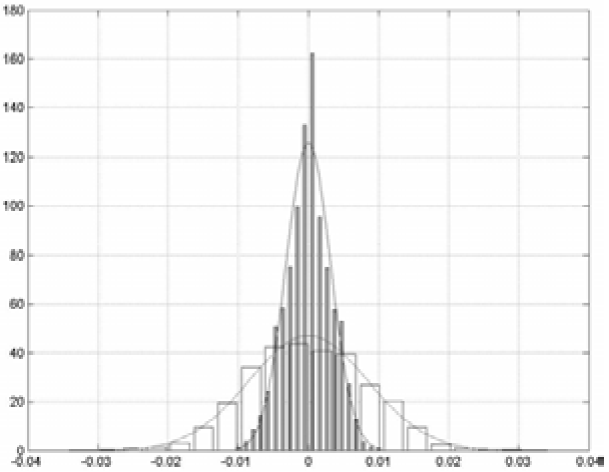

Figure 9.19 Test no. 2: acceleration probability density

[e] Pugliese A., Sabetta F. 1989. Prediction of response spectra from strong Italian records (in Italian), *Ingegneria sismica*, **2**(6), pp. 3-14.

[f] Rabinow J. 1948. The magnetic fluid clutch. *AIEE Transactions*, 67: 1308-1315.

[g] Carlson J.D., Jolly M.R. 2000. MR fluid, foam and elastomer devices. *Mechatronics*, 10: 555-569.

[h] Spencer Jr. B.F., Yang G., Carlson J.D., Sain M.K. 1998. Smart dampers for seismic protection of structures: a full-scale study. *Proc. 2nd World Conference on Structural Control*, Kyoto, Japan, 1: 417-26.

[i] Spizzuoco M., Serino G. 2001. Design of MR dampers' mechanical properties for the seismic response control of a steel frame structure. *Proc. of 7th Int. Seminar on Seismic Isolation, Passive Energy Dissipation and Active Control of Vibrations of Structures*, Assisi, Italy.

[j] Spizzuoco M. 2000. *Modelling, testing and design of non-linear viscous devices for structural control*. Ph.D. Dissertation.

[k] Caughey T.K. 1960. Sinusoidal excitation of a system with bilinear hysteresis. *Journal of Applied Mechanics*, 27: 640-643.

[l] Inaudi J.A. 2000. Performance of variable-damping systems: theoretical analysis and simulation. *Proc. 3rd Int. Workshop on Structural Control*, Paris, France, 301-316.

[m] Medeot R et al. 2001. The EC-funded project SPACE. *Proc. 7th Int. Seminar on Seismic Isolation, Passive Energy Dissipation and Active Control of Vibrations of Structures*, Assisi, Italy, pp 447-75.

[n] Luenberger D.G. 1979. *Introduction to Dynamic Systems*, John Wiley & Sons, New York, 394-416.

[o] Housner G.W. et al. 1997. Structural control: past, present, and future. *J. of Eng. Mech.*, Special Issue, ASCE, **123**(9).

[p] Soong, T.T. 1990. *Active structural control: theory and practice. Harlow*, Longman Scient. & Tech, UK.

9.8 LIST OF PUBLICATIONS

[1] Di Donna M., Serino G., Giannini R. 2002. Advanced earthquake protection systems for high voltage electric equipment. *Proc. 12th European Conf. on Earthquake Engineering*, London, U.K.

[2] Di Donna M., Serino G. 2002. Base isolation of high voltage equipment: comparison between two different solutions. *Proc. of Probabilistic Methods Applied to Power Systems (PMAS 2002)*, Napoli, Italy.

[3] Serino G., Spizzuoco M. 2002. About the design of passive and semi-active MR dampers for seismic protection of buildings. *Proc. 12th European Conf. on Earthquake Engineering*, London, U.K.

[4] Occhiuzzi A., Spizzuoco M. and Serino G. 2003. Experimental analysis of magnetorheological dampers for structural control. *Smart Materials and Structures*, vol. 12, n. 5, 2003, 703-711.

[5] Renzi E., Serino G. 2004. Testing and modelling a semi-actively controlled steel frame structure equipped with MR dampers. *Structural Control and Health Monitoring*, vol. 11.

[6] Spizzuoco M., Occhiuzzi A., Serino G. 2003. Experimental validation of a semi-active control system based on magnetorheological dampers, *Proc. ERES 2003*.

[7] Paolacci F., Serino G. 2002. Experimental characterization of a semiactive MR damper, *Proc. 3rd World Conf. on Structural Control*, Como, Italy.

[8] Occhiuzzi A., Serino G. 2002. Control strategies for semi-active structural control devices, *Proc. 3rd World Conf. on Structural Control*, Como, Italy.

[9] Spizzuoco M., Seiler C. 2002. Numerical evaluation of the earthquake response of semi-actively controlled building and bridge structures, *Proc. 3rd World Conf. on Structural Control*, Como, Italy.

[10] Serino G., Occhiuzzi A., Spizzuoco M., Seiler C., Fischer O. 2002. Semi-active control via MR dampers: algorithms, numerical modelling and prediction of the resulting response of structures, *Proc. 3rd World Conf. on Structural Control*, Como, Italy.

[11] Occhiuzzi A., Spizzuoco M. 2003. Semi-active magnetorheological dampers applied to a steel building. *Proc. 4th Int. Conf. on Behaviour of Steel Structures in Seismic Areas*, Napoli, Italy.

[12] Occhiuzzi A., Spizzuoco M., Serino G. 2002. Semi-active MR dampers in TMD's for vibration control of footbridges - part 1: numerical modelling and control algorithm. *Proc. of the Footbridge Conference*, Paris, France.

[13] Breccolotti M., Gusella V., Materazzi A.L. 2002. PD control experiment on a mast subjected to wind loads. *Proc. 7th Wind Engineering National Congress*, Milan, Italy. (in Italian).

[14] Breccolotti M., Materazzi A.L. 2001. Active control experiments on deformable structures. *Proc. Workshop on vibration problems on civil structures and mechanical construction*, Perugia, Italy. (in Italian).

[15] Breccolotti M., Gusella V., Materazzi A.L. 2003. Active control of a wind excited mast. *Proc. ISEC-02 Conference*, Rome, Italy.

WITH CONTRIBUTION FROM:

Marco Breccolotti, Università degli Studi di Perugia
Vittorio Gusella, Università degli Studi di Perugia
Annibale Luigi Materazzi, Università degli Studi di Perugia
Antonio Occhiuzzi, Università degli Studi di Napoli Federico II
Mariacristina Spizzuoco, Università degli Studi di Napoli Federico II

10 Monitoring of structures

Massimiliano Pieraccini
Universiy of Firenze

10.1 INTRODUCTION

In this chapter the physical principles and the experimental results of the application of microwave radar systems to the monitoring of vibration state of the structures are described. Specific microwave radar techniques, continuous-wave single-frequency (CW-SF) and multi-frequency (CW-MF) approach, for the measurement of large structure vibration are presented. After a description of the theoretical background the experimental results performed in three different cases: a vertical steel structure, subjected both to artificial solicitation through a vibrodina and to wind, a reinforced concrete building and a bridge are reported .

10.2 THEORETICAL BACKGROUND

10.2.1 Introduction

Monitoring techniques based on measured changes of dynamic properties of structures are pervasive throughout the civil, mechanical and aerospace engineering communities [a]. They are based on measurement of natural frequencies and amplitude changes of the structure under test [b]. The most popular types of sensors used for vibration testing are piezoelectric accelerometers [a]. Although accurate, reliable and relatively inexpensive, they must be mounted at the appropriate locations, and access may represent a problem in some cases. Accelerometer mounting and wiring are typically the hardest and most time consuming task associated with the test. Non contact systems for vibration measurement both laser [c] and microwave [d] based are described in the literature. The use of active microwave remote sensing apparatus for monitoring structures subject of the activity carried out by this unit, is based on the measurement of the variation induced on radar response by mechanical vibration.

10.2.2 Working Principle

The radar response of a single vibrating target in the field of view of the antennas at distance *R* from a Continuous Wave transceiver operating at Single Frequency (CW-SF) is:

$$E = C\,Se^{-j\frac{4\pi}{c}f\left(R+\frac{\underline{\underline{R}}\cdot\underline{\underline{d}}(t)}{R}+R_{inst}\right)} \tag{10.1}$$

Edited by Gianni Bartoli and Francesco Ricciardelli, WINDERFUL: Wind and INfrastructures: Dominating Eolian Risk
For Utilities and Lifelines, ISBN 88-8453-138-1, ©2004 Firenze University Press

with C as instrumental constant, S reflection coefficient of the target, c speed of light, f microwave frequency, $\underline{d}(t)$ displacement caused by vibration, and R_{inst} additional path introduced by cables and instrumentation. By calculating the Fast Fourier Transform of the angle of the measured in-phase and quadrature response in time, the amplitude and the frequency of the vibration is obtained. In some practical cases this can be an effective method for vibration measurement of a large structure, as is shown in the next section. Nevertheless, by using a single frequency it is not possible to separate the contributions of different targets in the field of view. This can be a problem in some cases.

Consider a set of targets vibrating at the same frequency f_m. In general, each target k is vibrating with a different amplitude vector $\underline{A}_k$ and phase ϕ_k. Let the radar transmit continuous waves at increasing discrete frequency values (CW-MF: Continuous Wave Multi Frequency) by scanning a bandwidth $B=f_2-f_1$, in a sweep time t_{sweep}.
The measured signal E_i at i-th frequency is given by the following:

$$E_i = C\sum_k S_k \exp\left(-j\frac{4\pi f_i}{c}\left(R_k + \frac{\underline{A}_k \cdot \underline{R}_k}{R_k}\sin\left(2\pi f_v t_{sweep}\frac{f_i - f_1}{B} + \phi_k\right) + R_{inst}\right)\right) \tag{10.2}$$

with S_k reflection coefficient of the k-th target, f_i i-th frequency, R_k distance from the k-th target to the n-th radar position.
Eq. (10.2) can be viewed as a frequency modulation (FM) of the microwave carrier caused by the vibration frequency f_v, so its Fourier Transform can be written as

$$F(R) = C\sum_k \sum_{m=-\infty}^{m=\infty} S_k \exp\left(-j\left(\frac{4\pi}{c} f_0\left(R_k + R_{inst}\right) + m\phi_k\right)\right)\; J_m(\beta)\; \mathrm{sinc}\left(\frac{2B}{c}\left(R - R_k - mr_v\right)\right) \tag{10.3}$$

where $J_m(\beta)$ is the Bessel function of m order, $\beta = 2\pi\left(f_1 + f_2\right)\underline{A}_v \cdot \underline{R}/(cR)$, $r_v = ct_{sweep} f_v / 2\pi B$.

For example, consider a scenario constituted of two targets vibrating at 1.5 Hz frequency with amplitude 1 mm and 2 mm at distances 10 m and 12 m from the radar respectively. Figure 10.1 shows the calculated $F(R)$. As an effect of vibration, the signal relative to the targets decreases by a factor equal to zero order Bessel function of β; furthermore, a symmetric set of secondary peaks appears at distances R_i+mr_v, with m integer. The amplitudes of these secondary peaks are proportional to m-th order Bessel function of β. Afterwards, the vibration amplitude of a target positioned at distance R_k from the radar can be evaluated from the ratio ρ_k between the amplitude $F\left(R_k \pm r_v\right)$ of the secondary peaks of the first order and the amplitude $F(R_k)$ of the main peak, using the following eq.

$$\beta = K^{-1}\left(\left|\rho_k\right|\right) \tag{10.4}$$

with $K(x) = J_1(x)/J_o(x)$. The plot in Figure 10.2 shows the numerically calculated behaviour of $K^{-1}(x)$. Finally, from eq. (10.3) it is evident that the phase of the vibration of the target k is the argument of ρ_k .

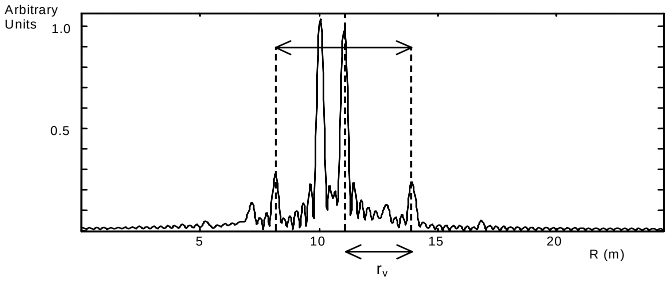

Figure 10.1 Simulated response of a scenario constituted by two targets at distances 10 m and 12 m from the radar vibrating at 1.5 Hz frequency with amplitude 1 mm and 2 mm respectively.

The described method is able to separate the contributions of a set of targets, provided that vibration frequency is known. This can be adequately measured by calculating the Fast Fourier Transform of the angle of the measured response in time normalized with respect to the instantaneous microwave frequency.

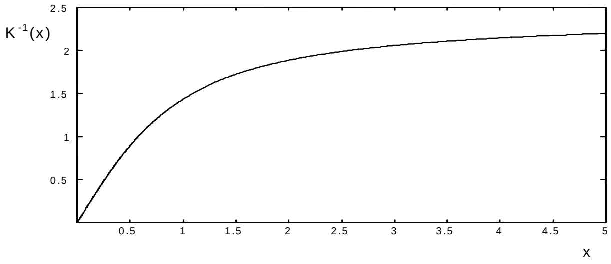

Figure 10.2 Plot of *K*-1(*x*)

10.3 EXPERIMENTAL CAMPAIGN ON A VERTICAL FRAME AT UNIVERSITY OF PERUGIA

The proposed radar technique has been tested at a facility of the Department of Civil and Environmental Engineering at the University of Perugia. The test structure was a vertical steel frame 10 m in height. A mechanical vibrodina was positioned on the summit (Figure 10.3). The CW radar was a prototype based on a Network Analyser (HP 8753D) that operated as a coherent microwave transmitter and receiver, with a couple of horn antennas as described in [e]. The radar system was positioned in front of the structure, at a 8 m distance. An accelerometer was installed on the structure at 6 m in height.

Figure 10.3 Photograph of the experimental set-up

CWSF measurement was carried out both with the structure artificially shaken by the vibrodina, and naturally stirred by a light breeze. Figure 10.4 shows the plots of the FFT of the radar angular response in time of the structure naturally stirred. CWMF measurement was carried out with the structure artificially shaken. Figure 10.5 shows the plot of the expression in eq. (10.2). Table 10.1 summarizes the results of the radar measurements and compares them to the reference data obtained with the accelerometer installed on the structure. The agreement between CWSF tests and accelerometer measurements is rather qualitative. As the radar performs a global displacement measurement, the comparison with a punctual sensor is poor significant.

On the contrary, as the CWMF technique is able to separate the contribution of the structure section where the accelerometer was installed, the agreement between CWMF tests and accelerometer measurements is more satisfactory.

Radar technique	**Microwave Band**	**Stimulus**	**Radar measured frequency (Hz)**
CWSF	**6 GHz**	**Vibrodina**	**1.53**
CWSF	**6 GHz**	**Wind**	**1.37**
CWMF	**5.5-6 GHz**	**Vibrodina**	**1.45**
CWMF	**5.5-6 GHz**	**Vibrodina**	**1.45**

Table 10.1 Comparison between experimental results and stimulating mean.

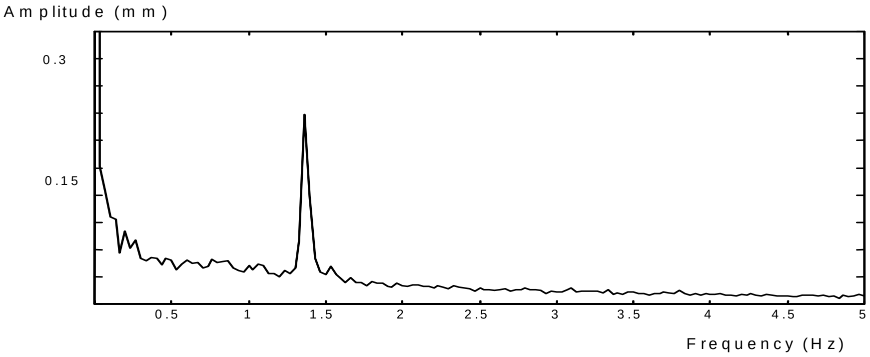

Figure 10.4 measurement carried out on the structure stirred by a light breeze. Plot of the FFT of the angular response.

10.4 EXPERIMENTAL CAMPAIGN ON A BUILDING

With the aim to verify the working principle on a building, the laboratory prototype based on the Network Analyzer that operated as a coherent microwave transceiver, with a couple of horn antennas with 15° of half power beam width (HPBW) was mounted on a linear mechanical guide of three meters length. The radar system realizes now a synthetic aperture moving an antenna along a linear mechanical guide and makes available an image of a building.

The radar transmits Continuous-Wave Step-Frequency (CW-SF) waveform scanning a bandwidth $B=f_2-f_1$, at increasing discrete values in a sweep time t_{sweep}. At each frequency f_i, the instrumentation measures the in-phase (I) and quadrature (Q) components of the received signal; thus, a

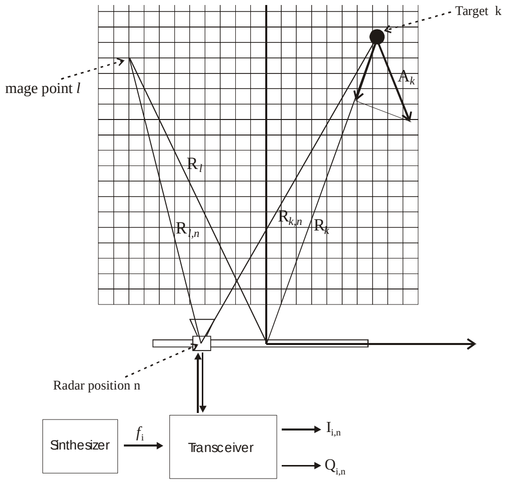

Figure 10.5 Imaging Working Principle

single measurement consists of a complex matrix $E_{i,n} = I_{i,n} + jQ_{i,n}$ of $N_f \times N_p$ values, with N_f number of frequencies and N_p number of positions along the scan length.

A synthetic radar image can be obtained from measurement matrix $E_{i,k}$ by coherently adding all signal contributions taken at different frequency and position, taking in account their phase history. With this aim, a set of image points $\left\{\vec{R}_l\right\}$ with R_l distance of the l-point from the central point of the linear scan, has to be defined. These points could build a grid, as shown in Figure 10.5, or constitute a sparse set. In the latter case they should be projected and interpolated on a planar grid in order to obtain a readable map.

Therefore, the value of the complex radar image at point l (M_l) of the set $\left\{\underline{R}_l\right\}$ is:

$$M_l = \frac{1}{N_f N_p} \sum_n^{N_p} R_{l,n}^2 F_{l,n} \tag{10.5}$$

$$F_{l,n} = \sum_i^{N_f} E_{i,n} \exp\Big(j2k_i \left(R_{l,n} - R_{inst} \right)\Big) \tag{10.6}$$

where $R_{l,n}$ is the distance between the image point l and the n-th position on the rail. k_i is the wave number relative to the frequency f_i ($k_i = 2\pi f_i / c$ with c speed of light). The constant R_{inst} (dimensionally a distance) takes into account the RF system internal delay introduced by components and cables. Figure 10.6 shows the block scheme of the radar instrumentation. A directional coupler before the transmitting antenna provided the reference signal to the Network Analyzer. A Personal Computer controlled both the Network Analyzer by a GPIB link and the mechanical guide by the serial port. The radar technique described above has been tested in the laboratories of ENEL.HYDRO – ISMES company in Bergamo (Italy).

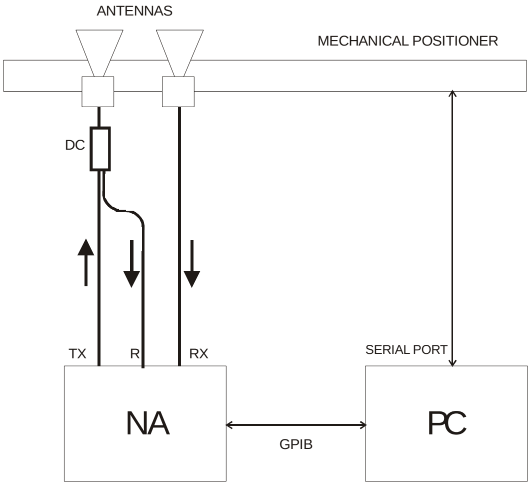

Figure 10.6: Block scheme of the radar prototype. DC: Directional Coupler, NA: Network Analyzer, TX: transmit channel, RX: Receive channel, R: Reference channel, PC: Personal Computer

The test facility consisted of a three-storey masonry and concrete frame 10 m in height, 9 m in width and 8 m in depth. A vibrodina was positioned on the top floor in order to force a controlled horizontal vibration. The radar system was positioned at about 18 m distance. The mechanical guide was both horizontally and vertically oriented to obtain radar images with resolution in the horizontal and vertical plane respectively. Eight accelerometers were located at the girder-column joints.

First, a radar acquisition of the static scenario was performed according to measurement parameters in Table 10.2 with the mechanical guide horizontally positioned.

Linear scan length (L)	2.00 m
Linear scansion point number (N_p)	161
Number of frequencies (N_f)	1601
Central frequency (f_c)	5.75 GHz
Bandwidth (B)	500 MHz
Linear scan length (L)	2.00 m

Table 10.2 Measurements parameters

Figure 10.7 shows a picture and the radar image of the structure. The picture is taken from the point of view of the radar installation. In the radar image several features are recognizable: the corner of the vertical metallic column, the four external walls and an internal wall. The coordinate system has origin in the center of the mechanical guide. The amplitudes in radar image are in linear scale. It should be noted that as this radar image is obtained through a horizontal scan, it has no synthetic resolution in z direction and each pixel in the image is relative to the entire aperture in z direction of the antenna lobe (about 15° of half-aperture) that pointed the half-height of the structure.

Afterwards, the structure was excited at 2.85 Hz vibration frequency by the vibrodina, and a radar acquisition of the scenario in dynamic steady-state was carried out. From the pixel by pixel ratio between the static and dynamic images, the amplitude pattern image shown in Figure 10.8

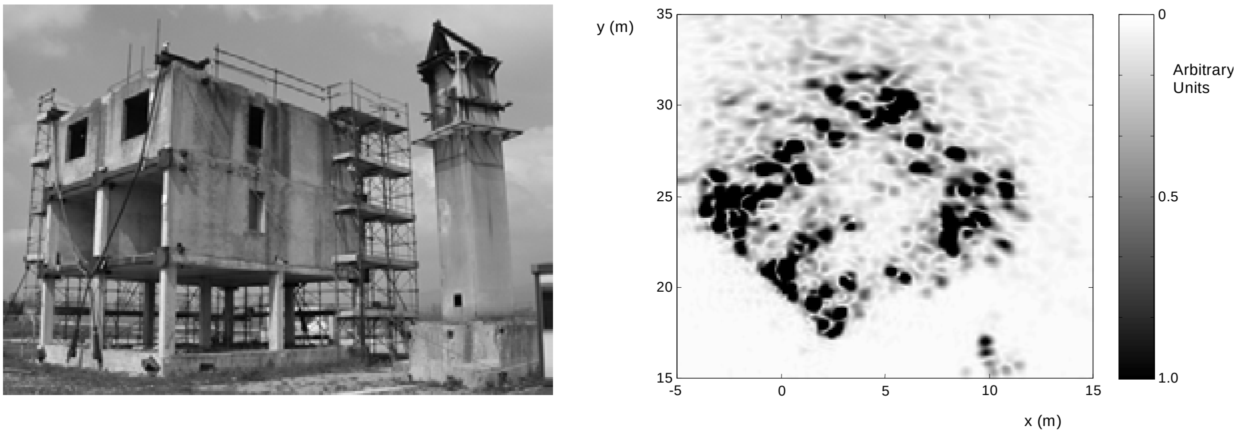

Figure 10.7 Picture of the structure and radar image acquired through a horizontal scan

was obtained. A Vibration amplitude map was obtained through a horizontal antenna scan during the test at 2.85 Hz. The mean amplitude was 1.33 mm to be compared with 1.15 mm vibration amplitude measured by the accelerometers installed at the height of the first floor. The vibration frequency has been measured through the Fourier Transform of the phase of the measured response in time normalized with respect to the instantaneous microwave frequency.

10.5 EXPERIMENTAL CAMPAIGN ON A BRIDGE

10.5.1 Introduction

A test based on the same principle introduced in section 10.2 but devoted to evaluate the capability of the radar techniques to monitor the vibration state of the structures also in a non stationary case, was carried out at the end of 2003. The observation of the complete time evolution of the vibrating structure compel us to employ a new specific instrument. The test was carried out on a bridge: the “Indiano bridge” of Florence. The structure built from 1973 to 1978 by Florence Municipality is devoted to vehicular traffic; it is a stayed steel bridge not anchored, with a 206m

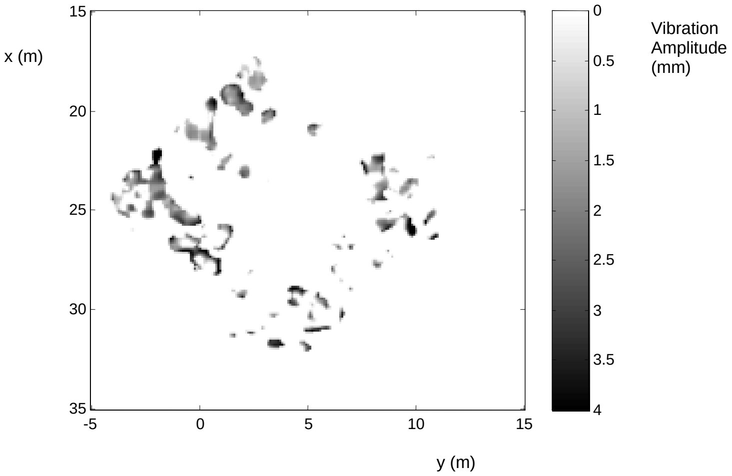

Figure 10.8 Vibration amplitude map obtained through a horizontal antenna scan during the test at 2.85 Hz

span, reinforced by two girders.

10.5.2 The radar system

We designed and realized a CW Stepped Frequency Radar with performances focused towards the suggested application: a short measurement time (< 100ms) and a high accuracy in displacement estimation (< 0.1 mm) as demanded for a better understanding of building deformations in non stationary case. The choice of a higher frequency allows also to reduce noticeably the system encumbrance. The system is a fully programmable digital transceiver whose RF subsystem can be changed *ad hoc* for different applications. Main radar features are: a maximum bandwidth of 400MHz centered at 16.8GHz: the transmitted signal is obtained through two multiplier stages.

The minimum frequency step is some tenths of Hertz. The output RF power can be adjusted in 10dBm step from 0dBm to 30dBm. The dynamic range allows to work up to a 2 Km maximum distance for any scenario. By using a 400MHz bandwidth with 4KHz steps we can achieve a 37cm range resolution, 1Km of non ambiguous range; the sampling is 20Hz. The hardware is divided in six main modules and is connected to PC via USB. The transmitter is based on a high speed signal synthesizer: a 300MHz clocked DDS (Direct Digital Synthesizer); an adequate frequency hopping speed with frequency and phase accuracy is available. The acquisition subsystem is based on a 16BIT 250KHz maximum sample rate A/D converter.

Figure 10.9 Sight of the bridge from below.

Figure 10.11 photograph of the Ku band interferometer

10.5.3 Experimental results

Many data were collected on the bridge in different configurations. Here we show some preliminary results demonstrating the effectiveness of the proposed technique. The measurement were realized sending 5120 frequencies separated by 80KHz. The chosen band and frequency step allow a range resolution of 36.62cm and a non-ambiguous range of 937.5m. Time acquisition was maximized: 5120 frequency steps are collected in 51.21 ms that is to say 19.53 scan per second. A scan consists of a capture of the instantaneous position of the structure: typical resonance frequencies of such structures are not lower than fractions of Hertz and not more than few Hertz. We are interested to vertical displacements due to the effect on the bridge of the vehicular traffic so the optimal observation position is from below of the bridge: we recall that radar observation can estimate displacements along the line of sight (LOS). It is possible to observe targets within 1 kilometer (8µs is the maximum time of flight of this range to which about 4µs must be added for the overall system functioning) . Data were acquired for 2.5 minutes; IFFT was calculated for each frequency scan. Samples represent single resolution cell 36cm wide. The modulus of each sample is related to the intensity of the echo from the selected one; phase indicates the delay between transmitted and received signal at centre frequency and can be used to measure the differential displacement of the cell. The plot of the modulus of such samples indicates the distribution along range direction of the different single scattering points on the bridge and it is similar for each scan, except when for large displacement there is a change of the resolution cell. The plot of the phase must be considered in relation with previous or successive scans. The phase difference between two sequential scans is proportional to the occurred displacement. If we select a specific pixel, the plot of its phase versus time corresponds to a time representation of the displacements. Figures 10.12 and 10.13 show data corresponding to resolution cell #100 e #182. Each point is far "50ms" and the global time duration is 150 seconds.

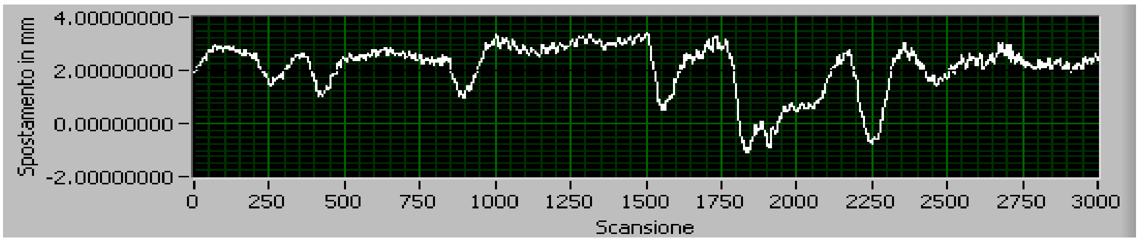

Figure 10.12 Resolution cell #100 = 36.6 m from the antennas (time evolution).

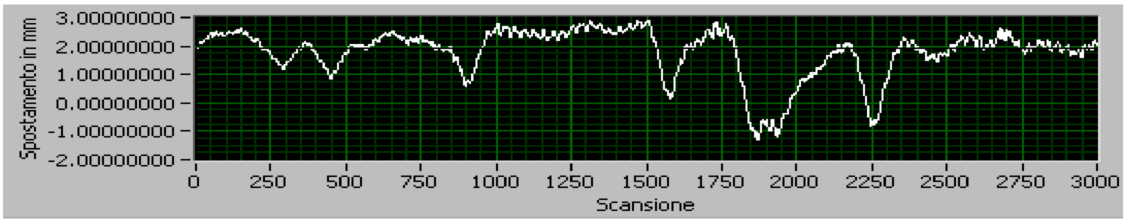

Figure 10.13 Resolution cell #182 = 66.6 m from the antennas (time evolution).

The measured displacements are of the order of millimeters; evaluating the grazing angle the effective displacement is one order of magnitude larger. By means of the time evolution of the displacements of the bridge we can calculate the FFT and to investigate the spectrum of vibration. In particular we can calculate the natural oscillation frequency of the structure and the potential periodical solicitations. The FFT corresponding to pixel #100 and # 182 are shown in fig. 10.14 and fig. 10.15.

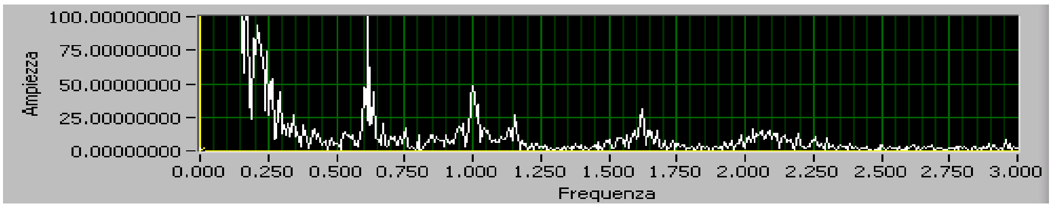

Figure 10.14 Displacement spectra measured on cell #100

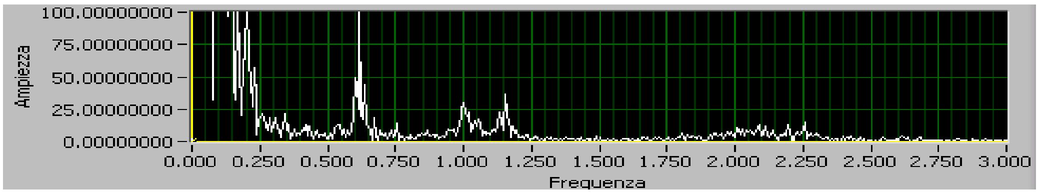

Figure 10.15 Displacement spectra measured on cell #182.

Both measurements showed a strong and neat 0.62Hz component which can be ascribed to the bridge itself, confirm the effectiveness of the proposed technique.

10.6 BASIC REFERENCES

[a] Doebling S.W., Farrar C.R., Prime M.B., Shevitz D.W. 1996. Damage identification and health monitoring of structural and mechanical systems from change in their vibration characteristics: a literature review. *Los Alamos National Laboratory Report LA-13070-MS*, available at http://lib-www.lanl.gov/

[b] Hearn G., Testa R.B. 1991. Modal analysis for damage detection in structures. *Journal of Structural Engineering*, **117**, 3042-3063

[c] Tomasini E. P. 2002. Special issues on advances and application in vibration measurement by laser techniques. *Optics and Lasers in Engineering*, **38**(3-4)

[d] Farrar C.R., Darling T.W., Migliorini A., Baker W.E. 1991. Microwave interferometer for non-contact vibration measurements on large structures. *Mechanical Systems and Signal Processing*, **13**, 241-253

[e] Pieraccini M., Luzi G., Atzeni C. 2001. Terrain mapping by ground-based interferometric radar. *IEEE Transactions on Geoscience and Remote Sensing*, **39**, 2176-2181

10.7 LIST OF PUBLICATIONS

[1] Pieraccini M., Mecatti D., Noferini L., Luzi G., Franchioni G., Atzeni C. 2002. SAR Interferometry for detecting the effects of earthquakes on buildings. *NDT&E international*,, **34**, 615-625

[2] Pieraccini M., Luzi G., Mecatti D., Noferini L., Atzeni C. 2003. A microwave radar technique for dynamic testing of large structure. *IEEE Transactions on Microwave Theory and Technique*, **51**(5), 1603-1609

[3] Pieraccini M., Luzi G., Mecatti D., Gusella V., Atzeni C. 2003. Microwave techniques for measurement of large structure vibration. *Microwave and Optical Technology Letters*, **37**(3), 216-218

WITH CONTRIBUTION FROM:

Guido Luzi, Università degli Studi di Firenze